12-16-2015

Motion and Noise Artifact Detection and Vital Signal Reconstruction in ECG/PPG based Wearable Devices

Seyed Mohamad Amin Salehizadeh
Biomedical Engineering, seyed.salehizadeh@uconn.edu

Motion and Noise Artifact Detection and Vital Signal Reconstruction in ECG/PPG based Wearable Devices

Seyed Mohamad Amin Salehizadeh, PhD

University of Connecticut, 2015

Abstract – The design and development of wearable biosensor systems for health and wellness monitoring has garnered lots of attention in the scientific community and the industry during the past decade. When it comes to health and wellness monitoring, accurate measurements, analysis and estimations would be vital. One major challenge in achieving a high performance wearable health monitoring system is motion and noise artifacts. This consideration was the basis for this dissertation. This study presents different algorithms and signal processing techniques to address motion and noise artifact detection and vital signal reconstruction from electrocardiogram/photoplethysmogram recordings. Five vital signals including ECG, PPG, Heart Rate, HRV and SpO2 are in the scope of the present dissertation. Accurate estimation of Heart Rates and Oxygen Saturation from photoplethysmogram (PPG) and Heart Rate from electrocardiogram (ECG) signals during daily physical activity is a very challenging problem. On the other hand motion and noise artifact in PPG and ECG recordings introduce challenges in early detection of heart failure diseases including Atrial Fibrillation and congestive heart failure. We address the problem of motion and noise artifact in three levels (1) “Motion and Noise Corrupted Data Removal”, and (2) “MA Corrupted Signal Usability Index Measurement” and (3) “Motion and Noise Corrupted Data Reconstruction”. Nine novel signal processing techniques (TDV, RepMA, RAFMA, IMAR, DyParaM, TifMA, OxiMA, SpaMa and SegMA) are introduced in this study to cope with the motion and noise artifact in PPG and ECG based wearable sensors. It will be shown that the proposed techniques are able to meet major aims of this study and to address the problem of motion and noise artifacts corresponding to each of the three scenarios. The results show that the algorithms presented in this study have potential for PPG or ECG based HR or SpO2 monitoring in wearable devices for fitness tracking and health monitoring during daily physical activities.

Motion and Noise Artifact Detection and Vital Signal Reconstruction in ECG/PPG based Wearable Devices

Seyed Mohamad Amin Salehizadeh

B.A., K. N. Toosi University of Technology, 2006

M.Sc., Amirkabir University of Technology, 2009

A Dissertation

Submitted in Partial Fulfillment of the

Requirements for the Degree of

Doctor of Philosophy

at the

University of Connecticut

2015

APPROVAL PAGE

Doctor of Philosophy Dissertation

Motion and Noise Artifact Detection and Vital Signal Reconstruction in ECG/PPG based Wearable Devices

Presented by

Seyed Mohamad Amin Salehizadeh, B.Sc., M.Sc.

Major Advisor _____

Dr. Ki H. Chon

Associate Advisor _____

Dr. Kazunori Hoshino

Associate Advisor _____

Dr. Sabato Santaniello

University of Connecticut

2015

Acknowledgements

First and foremost I wish to express my special appreciation and thanks to my advisor Professor Ki Chon. I am so deeply grateful for his help, professionalism, valuable guidance and support throughout the PhD program. His advice on both research as well as on my career have been invaluable.

I would like to thank the US Army Medical Research and Materiel Command (USAMRMC) for their support and sponsorship of this project.

I would like to thank my committee members, Prof. Kazunori Hoshino and Prof. Sabato Santaniello for serving as my committee members. I would also like to thank my lab mates in Chon Lab: Dr. Jowoon Chong, Dr. Yeonsik Noh, Dr. Relijn, Chae Cho, Duy Dao, Jeffery Bolkhovsky, Bersain Reyes, Hugo Posada and Justin Bales for their help and collaborations. Every result described in this thesis cannot be accomplished without the help and support of my fellow lab mates and friends.

A special gratitude to my parents. Words cannot express how grateful I am to my mother and father for all of the sacrifices that they've made on my behalf. Their prayer for me was what sustained me thus far. This accomplishment would not have been possible without them. Thank you.

Finally I would like to thank to my beloved Mina for supporting me and encouraging me throughout this experience. I could never have accomplished this dissertation without her love, support, and understanding.

Table of Contents

ACKNOWLEDGEMENTS ..... **V**

TABLE OF CONTENTS ..... **VI**

TABLE OF FIGURES ..... **X**

TABLE OF TABLES ..... **XIII**

CHAPTER 1: INTRODUCTION TO WEARABLE TECHNOLOGY AND VITAL SIGNAL MONITORING **1**

1.1. INTRODUCTION 1

1.1.1. Vital Sign Monitoring *5*

1.1.2. Wearable Technology Applications *6*

1.1.3. ELECTROCARDIOGRAM 10

1.1.4. PHOTOPLETHYSMOGRAM 13

Photoplethysmography *19*

REFERENCES 23

CHAPTER 2: PROBLEM STATEMENT, AIMS AND SCOPE **28**

2.1. PROBLEM STATEMENT AND BACKGROUND 28

2.1.1. Motion and Noise Artifact and PPG *28*

2.1.2. Motion and Noise Artifact and ECG *36*

2.2. THESIS AIMS AND SCOPE 41

REFERENCES 46

CHAPTER 3: TDV – A TIME-DOMAIN MOTION AND NOISE ARTIFACT DETECTION ALGORITHM **54**

3.1. INTRODUCTION 54

3.2. MATERIALS AND METHOD 54

3.2.1. Experimental Protocol and Preprocessing *54*

3.2.2. Parameters from PPG Signals *57*

3.2.3. SVM-based Detection of Motion/Noise Artifacts *59*

3.2.4. Enhancement of MNA Detection by Major Votes *61*

3.3. RESULTS 62

3.3.1. Reference: Clean vs. corrupted *63*

3.3.2. Classification Accuracy *64*

3.3.3. Performance Comparison of MNA detection Algorithms *69*

3.3.4. HR and SpO2 Estimation *70*

3.4. DISCUSSION 72

REFERENCES 76

CHAPTER 4: REPMA – A NOVEL MOTION AND NOISE DETECTION ALGORITHM **87**

4.1. INTRODUCTION 87

4.2. MATERIALS AND EXPERIMENTS 88

4.2.1. Reference signal for MNA Detection *90*

4.3. METHODOLOGY 91
4.3.1. Transforming PPG 1-D signal to 2-D image using Recurrence Plot 92
4.3.2. Recurrence Image Processing 95
4.4. RESULTS 100
4.5. DISCUSSION 102
REFERENCES 103

CHAPTER 5: RAFMA – A NOVEL MOTION AND NOISE ARTIFACT DETECTION AND ATRIAL FIBRILLATION DETECTION ALGORITHM 106

5.1. INTRODUCTION 106
5.2. MATERIALS AND EXPERIMENTS 109
5.3. METHODOLOGY 111
5.4. RESULTS 121
5.5. DISCUSSION 122
REFERENCES 124

CHAPTER 6: IMAR – A TIME-DOMAIN MOTION AND NOISE ARTIFACT REDUCTION ALGORITHM 127

6.1. INTRODUCTION 127
6.1. MATERIALS AND METHOD 128
6.1.1. Experimental Protocol and Preprocessing 128
6.1.2. Motion Artifact Reduction 129
6.2. RESULTS 136
6.2.1. NOISE SENSITIVITY ANALYSIS 136
6.2.2. HEART RATE AND SPO2 ESTIMATION FROM FOREHEAD SENSOR 139
6.2.3. PPG SIGNAL RECONSTRUCTION PERFORMANCE IN FINGER EXPERIMENT 145
6.2.4. PPG SIGNAL RECONSTRUCTION PERFORMANCE FOR THE WALKING AND STAIR CLIMBING EXPERIMENTAL DATA 146
6.3. DISCUSSION 147
REFERENCES 149

CHAPTER 7: DYPARAM – A TIME-DOMAIN MOTION AND NOISE ARTIFACT REDUCTION ALGORITHM 152

7.1. INTRODUCTION 152
7.2. MATERIALS AND METHOD 153
7.2.1. EXPERIMENTAL PROTOCOL AND PREPROCESSING 153
7.2.2. DYNAMIC PARAMETRIC MODELING 154
7.2.3. PPG SIGNAL MODELING: TIME-VARYING REGRESSION MODEL 156
7.2.4. MODEL ORDER DETERMINATION AND PARAMETER ESTIMATION: OPTIMAL PARAMETER SEARCH (OPS) ALGORITHM 158
7.3. RESULTS 160
7.3.1. NOISE SENSITIVITY ANALYSIS 160
7.3.2. APPLICATION OF THE REGRESSION MODELS IN REAL EXPERIMENTS 163
FINGER EXPERIMENT 163
HEAD EXPERIMENT 166
UMASS EXPERIMENT 166
7.4. DISCUSSION 170
REFERENCES 172

CHAPTER 8: TIFMA – A NOVEL ALGORITHM FOR MOTION AND NOISE ARTIFACT CORRUPTED DATA USABILITY INDEX MEASUREMENT 176

8.1. INTRODUCTION 176
8.2. MATERIAL AND METHODS 177
8.2.1. EXPERIMENTAL PROTOCOL AND PREPROCESSING 177
8.2.2. REFERENCE SIGNAL FOR MNA DETECTION 180
8.2.3. REFERENCE SIGNAL FOR DATA USABILITY DETECTION 180
8.2.4. TIFMA 181
TifMA Phase (1): MNA Detection 182
TifMA Phase (2): Usability Detection 188
8.3. RESULTS 193
8.3.1. MNA DETECTION RESULTS 193
8.3.2. USABILITY DETECTION RESULTS 198
8.5. DISCUSSION 199
REFERENCES 202

CHAPTER 9: OXIMA: A NOVEL MOTION AND NOISE ARTIFACT REDUCTION FOR THE PURPOSE OF SPO2 AND HR RECONSTRUCTION 205

9.1. INTRODUCTION 205
9.2. EXPERIMENTS AND MATERIALS 206
9.4. METHODOLOGY 207
9.4.1. TIME-VARYING SPECTRAL ANALYSIS OF PPG 208
9.4.2. SIGNAL DECOMPOSITION 209
9.4.3. SPECTRAL FILTERING 211
9.4.4. HEART RATE TRACKING AND EXTRACTION 213
9.4.5. OXYGEN SATURATION ESTIMATION 214
9.5. RESULTS 216
9.6. DISCUSSION 217
REFERENCES 220

CHAPTER 10: SPAMA – A NOVEL MOTION AND NOISE ARTIFACT REDUCTION FOR HR RECONSTRUCTION FROM PPG RECORDINGS 223

10.1. INTRODUCTION 223
10.2. MATERIALS AND EXPERIMENTS 225
10.3. METHODOLOGY 227
10.3.1. TIME-VARYING SPECTRAL ANALYSIS OF PPG AND ACCELEROMETER DATA 227
10.3.2. SPECTRAL FILTERING 231
10.3.3. MOTION ARTIFACT DETECTION 232
10.3.4. HEART RATE TRACKING & EXTRACTION 233
10.3.5. PPG SIGNAL RECONSTRUCTION FOR HRV ANALYSIS 236
10.4. RESULTS 238
10.5. DISCUSSION 242
REFERENCES 245

CHAPTER 11: SEGMA – A NOVEL MOTION AND NOISE ARTIFACT REDUCTION FOR HR RECONSTRUCTION FROM ECG RECORDINGS 248

11.1. Introduction 248
11.2. Materials and Experiments 252
11.3. Methodology 252
11.3.1. ECG Preprocessing 254
11.3.2. Time-Varying Spectral Analysis of ECG data 255
11.3.3. Spectral Filtering 256
11.3.4. Heart Rate Tracking & Extraction 259
11.3.5. Heart Rate Variability analysis 261
11.4. Results 261
11.5. 4. Discussion 265
References 267
CHAPTER 12: DISCUSSION, CONCLUSIONS AND FUTURE WORK 271
12.1. Discussion and Conclusions 271

Table of Figures

Figure 1.1 - Illustration of a remote health monitoring system based on wearable sensors. 3
Figure 1.2 - Main morphological features of ECG [56]. 11
Figure 1.3 - Oxygen saturation in blood:. 14
Figure 1.4 - Finger Pulse Oximeter 16
Figure 1.5 - Pulse Oximeter Properties 17
Figure 1.6 - Beer-Lambert Law Feasibility. 18
Figure 1.7 - How pulse oximeter address ambient light problem. 19
Figure 1.8 - Light absorbance difference due to tissue difference, ... 20
Figure 1.9 - How pulse oximeter measures pulsatile blood 20
Figure 1.10 - Pulse Oximeter Light absorption Through Tissue and Blood 21
Figure 2.1 – Motion and Noise Artifact Using Finger Pulse Oximeter. 28
Figure 2.2 – Illustration of the effect of motion on PPGs. 31
Figure 2.3 – ECG recordings. 37
Figure 2.4 – Diagram of the methodology of this research. 45
Figure 3.1 - PPG signals recorded during voluntary motion artifact conducted in a laboratory setting. 56
Figure 3.2 - Training phase of the proposed SVM-based motion detection algorithm. 60
Figure 3.3 - Test phase of the proposed SVM-based motion detection algorithm 61
Figure 3.4 - Enhancement of MNA detection by diversity. 62
Figure 3.5 - A sample forehead recorded PPG signal 65
Figure 3.6 - Trained SVM classification 66
Figure 3.7 - Validation: pairs of parameters for clean and corrupted PPG signals 66
Figure 3.8 - A representative PPG signal with detected peaks (red) 69
Figure 3.9 - Detection Probability of Corruption by additive white Gaussian noise (AWGN) 70
Figure 3.10 - Classification performance comparison between our SVM algorithm, Hjorth (H1, H2), Kurtorsis and Shanon Entropy (K, SE) parameters. 71
Figure 3.11 - Comparison of mean errors and detection error fraction between original signal (labeled “None”) and artifact removed signal from five detection methods (SVM, H1, H2, K, and SE). 72
Figure 3.11 - Mean error comparison between our SVM algorithm, Hjorth (H1, H2), Kurtorsis and Shanon Entropy (K, SE) parameters. 74
Figure 4.1 – Recurrence time-time Plot of a single frequency sinusoid signal. 93
Figure 4.2 – Recurrence time-time Plot of 4 sec PPG segment of recordings#3 from the first dataset. 94
Figure 4.3 – Recurrence time-time Plot of a 4 sec PPG signal. 95
Figure 4.4 – A typical Clean vs. Corrupted PPG segment from recording #3. 97
Figure 4.5 – Removing edge objects from left-diagonal recurrence image 97
Figure 4.6 – Removing edge objects from left-diagonal recurrence image 98
Figure 4.7 – Objects alignment and MA criteria calculations 99
Figure 4.6 – Detection Results of Subject#3. 100

Figure 5.1 – ECG recordings 112
Figure 5.2 – Recurrence time-time Plot of a single frequency sinusoid signal. 114
Figure 5.3 – Recurrence time-time Plot of a 4 sec ECG signal. 115
Figure 5.4 – Recurrence Plot as a tool for peak detection in 20 sec ECG data 116
Figure 5.5 – Motion Artifact Detection using Recurrence Plot of 3 sec ECG segment..... 118
Figure 5.6 – Atrial Fibrillation Detection using Recurrence Plot of 3 sec ECG segment..... 119
Figure 5.7 – Flowchart of RAFMA Algorithm..... 120
Figure 5.8 – RAFMA MNA Detection Results for Subject 9 (Chon Lab Dataset)..... 121
Figure 5.9 – Noise-contaminated ECG segments from a non-AF subject (top) and an AF 123
Figure 6.1 - Typical infrared PPG signal. 133
Figure 6.2 - The first 12 eigenvector components of the PPG signal for..... 134
Figure 6.3 - Iterative reconstruction of a corrupted eigenvector with frequency of 0.967 Hz..... 135
Figure 6.4 - (Odd#) HR estimated from reconstructed PPG for different additive white noise levels; (Even#) SpO2 estimated from reconstructed PPG for different levels of additive white noise. 141
Figure 6.5 - (Odd#) HR estimated from reconstructed PPG for different additive colored noise levels; (Even#) SpO2 estimated from reconstructed PPG for different levels of additive colored noise. 142
Figure 6.5 -HR estimated from IMAR-reconstructed PPG compared to reference and corrupted PPG 143
Figure 7.1 - Training and Prediction results obtained by using 4 different models on the simulated signal with -20dB additive color noise..... 161
Figure 7.2 - Training and prediction performance of the 4 models on subject#2 164
Figure 7.3 - HR estimations from the output of the 4 models on a typical segment from subjects #2, ... 166
Figure 7.4 - Training and prediction performance of the 4 models on a typical IR segment from subject #10 167
Figure 7.5 - HR and SpO2 estimations from the output of the 4 models on a typical PPG segment from subject #10,..... 168
Figure 7.6 - Training and prediction performance of the 4 models on a typical IR segment from patient #2 169
Figure 7.7 - HR and SpO2 estimations from the output of the 4 models on a typical segment from patient #2. 170
Figure 8.1 - Time-Frequency Spectrum produced by VFCDM in 8sec PPG window (L = 4s). 184
Figure 8.2 - Trace-back strategy to find the start (A) and end (B) points of MNA. 187
Figure 8.3 - An example of MNA detection using VFCDM. 188
Figure 8.4 - An example of MNA detection using our VFCDM method versus other methods: 189
Figure 8.5 - Subject # 7 from dataset (3)..... 190
Figure 8.6 - VFCDM Time-Frequency Spectrum of Subject #7 from dataset (3)..... 191
Figure 8.7 - Example of usable and non-usable PPG data 192
Figure 8.8 - Filtered TFS 193
Figure 8.9 - Reference usability index 194
Figure 8.10 - TifMA Algorithm Flowchart..... 195
Figure 8.11 - Receiver-operative-curves (ROCs) of all the features used in MNA detection algorithms. 198

Figure 8.11 - An example showing Accelerometer vs. TifMA based methods performance on a typical PPG signal recorded from a subject during walking. 202
Figure 9.1 - Time-Frequency spectra of recording #5 210
Figure 9.2 - VFCDM Signal Decomposition on subject 5's data 211
Figure 9.3 - Three scenarios of HR frequency estimation 213
Figure 9.4 - Filtered TFS and HR Extraction. 215
Figure 9.5 - PPG signal reconstruction and SpO2 estimation 216
Figure 9.6 - Subject 5. (a-b) Reconstructed infrared and red PPG vs. actual PPG recordings. 218
Figure 10.1 - Time-Frequency spectra of recording #8 from dataset (1). 230
Figure 10.2 - Spectral Filtering. PPG time-frequency spectrum 232
Figure 10.3 - Motion Artifact Detection in the PPG spectrum. 233
Figure 10.4 - Flowchart of HR Tracking and Extraction 235
Figure 10.5 - Comparison of reconstructed HR obtained from SpaMA to reference HR obtained from simultaneous ECG recordings. 236
Figure 10.6 - PPG signal reconstruction 237
Figure 10.7 - Heart Rate Variability Analysis. 238
Figure 10.8 - Subject 9 (IEEE Competition Training Dataset) 239
Figure 10.9 - Reconstructed HR vs. reference HR 239
Figure 10.10 - Subject 30 (Chon Lab Dataset) 240
Figure 11.1 - ECG recordings and estimated HR from subject #3. 257
Figure 11.2 - Time-Frequency spectra of recording #3. 258
Figure 11.3 - Spectral Filtering. 258
Figure 11.4 - Comparison of reference HR to the HR tracking from filtered time-frequency spectrum of ECG recordings from subject #3 labeled with type of activities 260
Figure 11.5 - Comparison of reconstructed HR obtained from SegMA to reference HR estimated from simultaneous ECG recordings#3. 261
Figure 11.6 - Heart Rate Variability Analysis. 262
Figure 11.7 – Results of Subject 8. 263
Figure 11.8 – Reconstructed HR vs. reference HR. 264
Figure 11.9 – Results of Subject 4 264

Table of Tables

Table 1.1 – Vital Signals **5**
Table 3.2. C obtained by 9 fold cross-validation and grid search method **67**
Table 3.3. Detection accuracy, specificity and sensitivity (Mean ± SD) for 7-seonds segment **68**
Table 3.4. Detection accuracy (Mean ± SD) for varying window length **68**
Table 4.1 Averaged Cohen's κ Coefficients representing the agreement between inspectors' decision on PPG labels **90**
Table 4.2. RepMA Algorithm Steps **91**
Table 4.3 Recurrence Image Processing Procedure in RepMA Algorithm **95**
Table 4.4. MA Detection Performance on dataset #1: Lab Controlled Forehead PPG Recordings **101**
Table 4.5. MA Detection Performance on dataset #2: Lab Controlled Finger PPG Recordings **101**
Table 4.6. MA Detection Performance on dataset #3: UMASS Hospital Forehead PPG Recordings **101**
Table 4.7. MA Detection Performance on dataset #4: UMASS Hospital Finger PPG Recordings **102**
Table 4.8. Comparison of Detection Algorithms' Average DTT error from all recordings **102**
Table 5.1. ECG Datasets and Experiments Settings **111**
Table 5.2. Chon Lab Experiment Settings **111**
Table 5.3. MNA Detection Performance Comparison **122**
Table 5.4. AF Detection Performance Comparison on all 33 (23 with AF and 10 healthy) subjects **122**
Table 6.1. Iterative Motion Artifact Reduction (IMAR) Procedure **137**
Table 6.2. Comparison & Statistical Analysis of HR Estimations from IMAR-reconstructed PPG for Different Levels of Additive White Noise. * represents p<0.05. ..... **138**
Table 6.3. Comparison & Statistical Analysis of Estimations from IMAR-reconstructed PPG for Different Levels of Additive White Noise. * represents p<0.05. ..... **138**
Table 6.4. Comparison & Statistical Analysis of HR Estimations from IMAR-reconstructed PPG for Different Levels of Additive Colored Noise. * represents p<0.05. ..... **139**
Table 6.5. Comparison & Statistical Analysis of SpO2 Estimations from IMAR-reconstructed PPG for Different Levels of Additive Colored Noise. * represents p<0.05. ..... **139**
Table 6.6. Comparison & Statistical Analysis of HR Estimations from IMAR-reconstructed PPG for 10 Different Subjects (Head Experiment). * represents p<0.05. ..... **144**
Table 6.7. Comparison & Statistical Analysis of SpO2 Estimations from IMAR-reconstructed PPG for 10 Different Subjects (Head Experiment). * represents p<0.05. ..... **144**
Table 6.8. Comparison & Statistical Analysis of HR Estimations from IMAR-reconstructed PPG for 10 Different Subjects (Finger Experiment). * represents p<0.05. ..... **145**
Table 6.9. Comparison & Statistical Analysis of HR Estimations from IMAR-reconstructed PPG for 9 Different Subjects (Walking & Stair Climbing Experiment). * represents p<0.05. ..... **146**
Table 6.10. Comparison & Statistical Analysis of SpO2 Estimations from IMAR-reconstructed PPG for 9 Different Subjects (Walking & Stair Climbing Experiment) **147**
Table 7.1. Predictive Optimal Parameter Search Algorithm **159**
Table 7.2. Frequency Varying Scenario. NMSE Comparison Results (additive white noise) **162**
Table 7.3. Frequency Varying Scenario. NMSE Comparison Results (additive color noise) **163**

Table 7.4. Real Experiment (1). NMSE Comparison Results 165
Table 7.5. Real Experiment (1). Estimated Heart Rate Comparison Results..... 165
Table 7.6. Real Experiment (2). Estimated Heart Rate Comparison Results..... 167
Table 7.7. Real Experiment (2). Estimated SpO2 Comparison Results 168
Table 7.8. Real Experiment (3). Estimated Heart Rate Comparison Results..... 169
Table 7.9. Real Experiment (3). Estimated SpO2 Comparison Results 170
Table 8.1. PPG Datasets and Experiments Settings..... 179
Table 8.2. Averaged Cohen's κ coefficients representing the agreement between inspectors' decision on PPG labels..... 180
Table 8.3. VFCDM Algorithm Procedure 181
Table 8.4. Frequently used MNA Detection Methods in Literature..... 186
Table 8.5. Mean ± Std. Deviation of Performance Metrics of Our Proposed TifMA Using Various Window Length. 196
Table 8.6. Mean ± Std. Deviation of Performance Metrics of Our Proposed TifMA, Other Methods. (*) Indicate Statistical Significance (p<0.05) BETWEEN Our Method vs. the Others. 197
Table 8.7. Mean ± Std. Detection of Transition Time (DTT) of TifMA and Other Methods. 197
Table 8.8. TifMA Usability Detection Performance. 199
Table 9.1. PPG Datasets and Experiments Settings..... 207
Table 9.2. Experiment Protocol 207
Table 9.3. The proposed OxiMA algorithm: HR and SpO2 Reconstruction..... 208
Table 9.4. VFCDM Algorithm Procedure 209
Table 9.5. OxiMA Algorithm Performance Comparison 217
Table 9.6. OxiMA Algorithm Improvement Rate 219
Table 10.1. PPG Datasets and Experiments Settings..... 226
Table 10.2. The proposed SpaMA algorithm: HR and PPG signal reconstruction 228
Table 10.3. SpaMA Algorithm Performance Comparison..... 241
Table 10.4. Frequency Domain HRV analysis Comparison: PSD of estimated vs. reference..... 242
Table 10.5. Time Domain HRV analysis Comparison: estimated vs. reference HRV 242
Table 11.1. ECG Wearable Devices..... 253
Table 11.2. ECG Datasets and Experiments Settings 253
Table 11.3. Experiment Protocol 254
Table 11.4. The proposed SegMA algorithm: HR and ECG signal reconstruction..... 254
Table 11.5. SegMA Algorithm Performance Comparison 262
Table 11.6. Correlation between PSD of estimated SegMA and reference HRV..... 265

Chapter 1: Introduction to Wearable Technology and Vital Signal Monitoring

1.1. Introduction

The US health care system faces daunting challenges. With the improvements in health care in the last few decades, residents of industrialized countries are now living longer, but with multiple, often complex, health conditions [3-5]. Survival from acute trauma has also improved, but this is associated with an increase in the number of individuals with severe disabilities [6]. The number of patients now requiring continuous monitoring has raised proportionally with increase in population and, by 2025, the elderly group will number approximately 1.2 billion. By 2050, there will be 2 billion of this age group, with 80 % in developing countries [7]. Moreover, in developed countries the older adult will constitute nearly 20 % of the overall population according to the population reference bureau [8]. In 2006, in the US, the 75 Age group accounted for 41 % of the population of state pensionable age. However, by 2056, with the increase in the age for state pension entitlement, this group will account for 67% of the pensionable population [9]. From an epidemiological standpoint, the cohort of “baby boomers” in the US is now reaching an age at which they will begin to severely stress the Medicare system. Finally, recent health care reform efforts may add 32 million newly insured patients to the health care system in the next few years [10]. These altered demographics raise some fundamental questions

- How do we care for an increasing number of individuals with complex medical conditions?
- How do we provide quality care to those in areas with reduced access to providers?
- How do we maximize the independence and participation of an increasing number of individuals with disabilities?

Cleary, answers to these questions will be complex and will require changes into how we organize and pay for health care. However, part of the solution may lie in how and to what extent we take advantage of recent advances in information technology and related fields. Currently, there exist technologies that hold great promise to expand the capabilities of the health care system, extending its range into the

community, improving diagnostics and monitoring, and maximizing the independence and participation of individuals.

Wearable sensors have diagnostic, as well as monitoring applications. Their current capabilities include physiological and biochemical sensing, as well as motion sensing [11, 12]. It is hard to overstate the magnitude of the problems that these technologies might help solve. Physiological monitoring could help in both diagnosis and ongoing treatment of a vast number of individuals with neurological, cardiovascular and pulmonary diseases such as seizures, hypertension, dysrthymias, and asthma. Nearly 20% of those in the US live in rural areas, but only

9% of physicians work in rural areas [13]. Access may get worse over time as many organizations are predicting a shortfall in primary care providers as health care reform provides insurance to millions of new patients [14]. There is a large body of literature that describes the disparities in care faced by rural residents [13]. Compared to those in urban areas, those in rural areas travel 2 to 3 times farther to see a physician, see fewer specialists, and have worse outcomes for such common conditions as diabetes, and heart attack [14, 15]. Wearable sensors and remote monitoring systems have the potential to extend the reach of specialists in urban areas to rural areas and decrease these disparities.

A conceptual representation of a system for remote monitoring is shown in Figure 1. Wearable sensors are used to gather physiological and movement data thus enabling patient's status monitoring. Sensors are deployed according to the clinical application of interest. Sensors to monitor vital signs (e.g. heart rate and respiratory rate) would be deployed, for instance, when monitoring patients with congestive heart failure or patients with chronic obstructive pulmonary disease undergoing clinical intervention. Sensors for movement data capturing would be deployed, for instance, in applications such as monitoring the effectiveness of home-based rehabilitation interventions in stroke survivors or the use of mobility assistive devices in older adults.

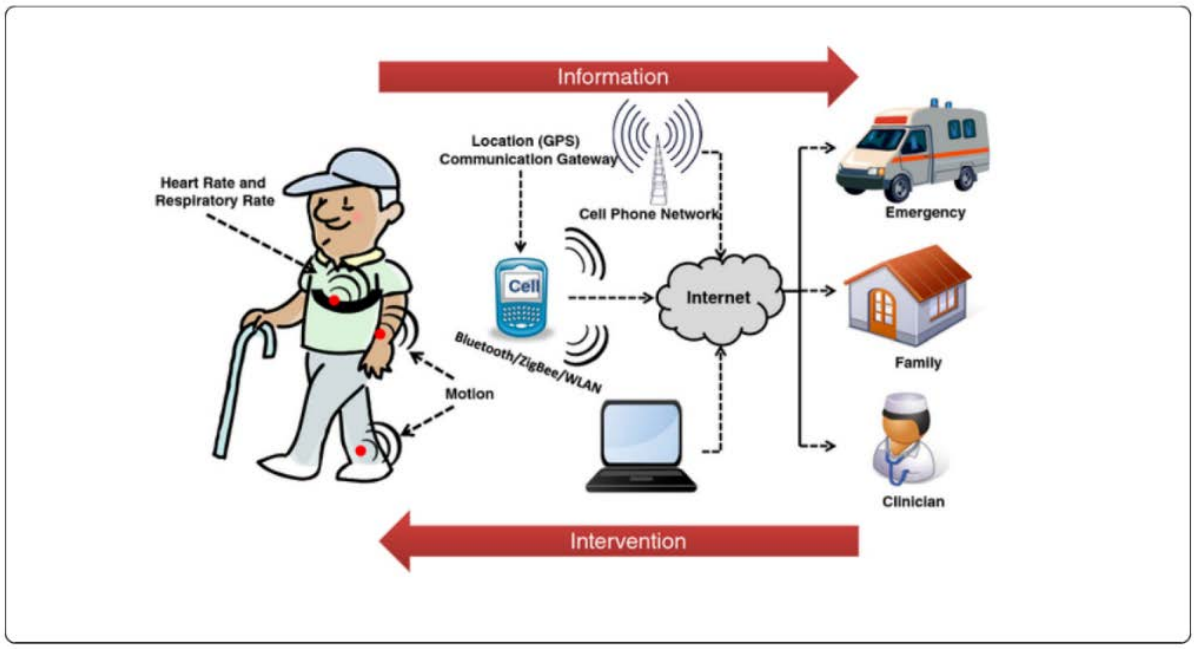

Figure 1.1 - Illustration of a remote health monitoring system based on wearable sensors. Health related information is gathered via bodyworn wireless sensors and transmitted to the caregiver via an information gateway such as a mobile phone. Caregivers can use this information to implement interventions as needed [1].

Wireless communication is relied upon to transmit patient's data to a mobile phone or an access point and relay the information to a remote center via the Internet. Emergency situations (e.g. falls) are detected via data processing implemented throughout the system and an alarm message is sent to an emergency service center to provide immediate assistance to patients. Family members and caregivers are alerted in case of an emergency but could also be notified in other situations when the patient requires assistance with, for instance, taking his/her medications. Clinical personnel can remotely monitor patient's status and be alerted in case a medical decision has to be made.

Wearable systems for patients' remote monitoring consist of three main building blocks: 1) the sensing and data collection hardware to collect physiological and movement data, 2) the communication hardware and software to relay data to a remote center, and 3) the data analysis techniques to extract clinically-relevant information from physiological and movement data. Recent advances in sensor technology, microelectronics, telecommunication, and data analysis techniques have enabled the

development and deployment of wearable systems for patients' remote monitoring. Researchers have relied upon advances in the above-mentioned fields to address shortcomings of ambulatory technologies (e.g. Holter monitors) that had previously prevented long-term monitoring of patients' status in the home and community settings.

Health monitoring applications of wearable systems most often employ multiple sensors that are typically integrated into a sensor network either limited to bodyworn sensors or integrating body-worn sensors and ambient sensors. In the early days of body-worn sensor networks (often referred to as "body sensor networks"), the integration of wearable sensors was achieved by running "wires" in pockets created in garments for this purpose to connect body-worn sensors. An example of this technology is the MIThril system [16]. Such systems by design were not suitable for long-term health monitoring. Recently developed wearable systems integrate individual sensors into the sensor network by relying on modern wireless communication technology. During the last decade, we have witnessed tremendous progress in this field and the development of numerous communication standards for low-power wireless communication. These standards have been developed keeping in mind three main requirements: 1) low cost, 2) small size of the transmitters and receivers, and 3) low power consumption. With the development of IEEE 802.15.4/ZigBee [17] and Bluetooth, tethered systems have become obsolete. The recently developed IEEE 802.15.4a standard based on Ultra-wide-band (UWB) impulse radio opens the door for low-power, low-cost but high data rate sensor network applications with the possibility of highly accurate location estimation [18].

Most monitoring applications require that data gathered using sensor networks be transmitted to a remote site such as a hospital server for clinical analysis. This can be achieved by transmitting data from the sensor network to an information gateway such as a smart phone smart watch or personal computer. Data analysis techniques such as signal processing, pattern recognition, data mining and other artificial intelligence-based methodologies have enabled remote monitoring applications that would have been otherwise impossible.

1.1.1. Vital Sign Monitoring

Physiological measures of interest in rehabilitation include heart rate, respiratory rate, blood pressure, blood oxygen saturation, and muscle activity. Parameters extracted from such measures can provide indicators of health status and have tremendous diagnostic value. Until recently, continuous monitoring of physiological parameters was possible only in the hospital setting. But today, with developments in the field of wearable technology, the possibility of accurate, continuous, real-time monitoring of physiological signals is a reality.

Vital sign monitoring systems will, therefore, involve monitoring one or more of the following [19]:

Table 1.1 – Vital Signals

Electrocardiograph (ECG)	Pulse Rate (Heart Rate)
Photoplethysmogram (PPG)	Heart Rate Variability (HRV)
Blood Glucose Level	Respiration Rate;
Blood Pressure	Blood Oxygen Saturation (SpO_2)

Out of above 8 vital signs, 5 signals including ECG, PPG, Heart Rate, HRV and SpO2 are in the scope of the present dissertation.

Integrating physiological monitoring in a wearable system often requires ingenious designs and novel sensor locations. For example, Asada et al. [20] presented a ring sensor design for measuring blood oxygen saturation (SpO2) and heart rate. The ring sensor was completely self-contained. Worn on the base of the finger (like a ring), it integrated techniques for motion artifact reduction, which were designed to improve measurement accuracy. Applications of the ring sensor ranged from the diagnosis of hypertension to the management of congestive heart failure. A self-contained wearable cuff-less photoplethysmographic (PPG) based blood pressure monitor was subsequently developed by the same research group [21]. The sensor integrated a novel height sensor based on two MEMS accelerometers for measuring the hydrostatic pressure offset of the PPG sensor relative to the heart. The mean arterial blood pressure was derived from

the PPG sensor output amplitude by taking into account the height of the sensor relative to the heart. Another example of ingenious design is the system developed by Corbishley et al. [22] to measure respiratory rate using a miniaturized wearable acoustic sensor (i.e. microphone). The microphone was placed on the neck to record acoustic signals associated with breathing, which were band-pass filtered to obtain the signal modulation envelope. By developing techniques to filter out environmental noise and other artifacts, the authors managed to achieve accuracy greater than 90% in the measurement of breathing rate. The authors also presented an algorithm for the detection of apneas based on the above-described sensing technology. In recent years, physiological monitoring has benefited significantly from developments in the field of flexible circuits and the integration of sensing technology into wearable items [23]. An ear-worn, flexible, low-power PPG sensor for heart rate monitoring was introduced by Patterson et al. [24]. The sensor is suited for long-term monitoring due to its location and unobtrusive design. Although systems of this type have shown promising results, additional work appears to be necessary to achieve motion artifact reduction [25, 26]. Proper attenuation of motion artifacts is essential to the deployment of wearable sensors. Nonetheless, further advances in signal processing techniques to mitigate motion artifacts are needed.

1.1.2. Wearable Technology Applications

- Health & wellness monitoring
- Safety monitoring
- Home rehabilitation
- Assessment of treatment efficacy
- Early detection of disorders

Health & wellness monitoring

With increase in population and changing life styles there is urgency to develop a system that can monitor patient activities and daily routines to prevent them from serious health related disorders [19]. Advancements in wearable sensors and wireless technologies create huge impact on health-care monitoring

system. Now we have facilities to monitor patients from remote location on continuous basis by using wearable sensors and wireless systems. Different types of sensors available for specific applications.

Long-term monitoring of physiological data can lead to improvements in the diagnosis and treatment, for instance, of cardiovascular diseases. Commercially available technology provides one with the ability to achieve long-term monitoring of heart rate, blood pressure, oxygen saturation, respiratory rate, body temperature and galvanic skin response. Clinical studies are currently carried out to evaluate and validate the performance of wearable sensor platforms to monitor physiological data over long periods of time and improve the clinical management of patients, for instance, with congestive heart failure [27, 28]. LifeGuard is a custom data logger designed to monitor health status of individuals in extreme environments (space and terrestrial) [29]. The system has undergone testing in hostile environments with good results. As part of the FP5 program of the European Commission, a project named AMON resulted in the development of a wrist-worn device capable of monitoring blood pressure, skin temperature, blood oxygen saturation, and ECG. The device was developed to monitor high risk patients with cardio-respiratory problems [30]. Other projects worth mentioning that have been carried out as part of different programs of the European Commission are: MyHeart [31], WEALTHY [32], and MagIC [33]. Samsung created a research wearable health monitoring system prototype, “Simband”, for continuous monitoring of ECG and PPG signals [34]. These projects led to the development of garment-based wearable sensors aiming at general health monitoring of people in the home and community settings.

Safety monitoring

A number of devices have been developed for safety monitoring applications, such as detecting falls and relaying alarm messages to a caregiver or an emergency response team. The Life Alert Classic by Life Alert Emergency Response Inc [35] and the AlertOne medical alert system [36] are examples of commercially-available devices designed for safety monitoring. These devices are simple emergency response devices consisting of a pendant or watch with a push button. Pressing the button, one has the ability to wirelessly relaying an alarm message to operators located in a remote call center. Other systems

integrate sensors into the body-worn unit. For instance, the Wellcore system [37] employs advanced microprocessors and accelerometers to monitor the body's position. The system detects falls as distinct events from normal movements, and automatically relays a message to the designated response center or nurse call station. Another device in this category is the MyHalo™ by Halo Monitoring ™. The system is worn as a chest strap and detects falls, while it monitors heart rate, skin temperature, sleep/ wake patterns, and activity levels [38]. The BrickHouse system [39] equipped with an automatic fall detector and a manual panic button. Finally, among the numerous commercially available systems, it is worth mentioning the ITTM EasyWorls [40], a system based on a mobile phone that is equipped with balance sensors which trigger automatic dialing SOS numbers if the system detects a sudden impact.

Home rehabilitation

An emerging area of application of wearable technology is the use of wearable sensors to facilitate the implementation of home-based rehabilitation interventions. Systems that aim to facilitate the implementation of rehabilitation exercise programs often leverage the combination of sensing technology and interactive gaming or virtual reality (VR) environments. For example, The Rehabilitation Engineering Research Center at the University of Southern California [41] is building on VR gaming to address compliance and motivation challenges [42]. VR simulation technology using specialized interface devices has been applied to improve motor skills in subjects undergoing rehabilitation to address functional deficits including reaching, hand function and walking. It has been proposed that such VR-based activities could be delivered in the home via a tele-rehabilitation approach to support patients' increased access to rehabilitation and preventive exercise programming.

Assessment of treatment efficacy

A quantitative way of assessing treatment efficacy can be a valuable tool for clinicians in disease management. By knowing what happens between outpatient visits, treatment interventions can be fine-tuned to the needs of individual patients [43]. Another important application would be for use in randomized clinical trials. By gathering accurate and objective measures of symptoms, one could reduce the number of

subjects and the duration of treatment required to observe an effect in a trial of a new therapy. Intensive long-term rehabilitation post-stroke is an important factor in ensuring motor function recovery. Tracking changes in motor function can be used as a feedback tool for guiding the rehabilitation process. Uswatte et al. [44, 45] have shown that accelerometer data can provide objective information about real-world arm activity in stroke survivors. In their study, 169 stroke survivors undergoing constraint-induced movement therapy wore an accelerometer on both wrists for a period of 3 days. The results indicated good patient compliance and showed that by simply taking the ratio of activity recorded on impaired and unimpaired arm using accelerometers, one can gather clinically-relevant information about upper extremity motor status.

Early detection of disorders

An area of growing interest in the field of wearable technology is the use of wearable sensors and systems to achieve early detection of changes in patient's status requiring clinical intervention. An example of this type of application of wearable technology is the management of patients with chronic heart failure diseases like atrial fibrillation [46].

Atrial fibrillation (AF) is the most common diagnosed dysrhythmia affecting approximately 3 millions of Americans. AF is the most common arrhythmia among the elderly, with the median age of those affected to be around 75 years of age. Prevalence of AF increases with age and reaches 8% of people in the United States over the age of 80 years [47]. Atrial fibrillation is an independent risk factor for death (relative risk in men 1.5 and in women 1.9) [48] and a major cause of ischemic stroke whose impact increases with age, reaching 23.5% in patients older than 80 years [49]. Although the 12-lead electrocardiogram remains the gold-standard diagnostic test for AF, a major challenge in the diagnosis of this arrhythmia is its paroxysmal nature, particularly in its early stages [50].

Diagnostic testing is one method of detection and is usually the result of symptomatic patients. Some of these tests include long-term Holter monitoring, electrocardiogram interpretation and blood tests.

Use of ECG monitors (e.g., Holter monitors) is common in the diagnosis and management of patients with, or at risk for, AF, given the paroxysmal, short-lived, and frequently asymptomatic nature of this serious arrhythmia. Biological imaging is a method that involves the analysis of images obtained from echocardiograms and chest x-rays. The prevalence of asymptomatic AF found incidentally on clinical examination is 20%, [50, 51] even higher with Holter or event recorders [52, 53]. Given these difficulties, a recent National Health Heart Lung & Blood Institute Expert panel has emphasized the pressing need to develop new methods for accurate AF detection and monitoring [54]. One study of patients with implantable pacemakers for AF detection found an incidence of 50% of asymptomatic AF [55]. Given the significant risk of mortality and morbidity and the fact that asymptomatic AF is not detected unless specifically looked for, there is a strong impetus for ambulatory monitoring. With the greater need for ambulatory monitoring, accurate and automated detection of asymptomatic AF becomes an important task. If atrial fibrillation can be easily and automatically detected early in their pathology, the risk of complications that are consequential due to late detection can be drastically reduced. Early detection could also potentially save billions of dollars spent on health care costs and research directly related to the heart conditions. A method to automatically detect atrial fibrillation and atrial flutter will save lives, improve quality of life of millions of people at-risk, and reduce the economic burden placed by AF.

1.1.3. Electrocardiogram

Electrocardiogram (ECG) is a diagnostic tool that measures and records the electrical activity of the heart in detail. Interpretation of these details enables the diagnosis of a wide range of heart conditions from minor to life threatening [56].

It is important to know the heart's structure and blood flow to understand the ECG. The heart is a hollow muscle which is divided into four chambers: the right atrium, the right ventricle and the left atrium and the left ventricle [57]. The right atrium receives venous blood which passes via the tricuspid valve to the right ventricle, which propels it through the pulmonary artery to the lungs. In the lungs venous blood

comes in contact with inhaled air, picks up oxygen, and loses carbon dioxide. Oxygenated blood is returned to the left atrium through the pulmonary veins. Passage of blood through the left atrium, bicuspid valve, into the left ventricle. Via the aortic valve the blood is pumped in the aorta and the arterial branches of the whole body. ECG refers to the recording of electrical changes occurring in the cardiac muscle during the cardiac cycle. ECG signals can be resolved into heartbeats, each of which represents, from a physiological point of view, a cardiac cycle. A heartbeat is segmented into smaller functional standard waves, designated as P, Q, R, S and T. Generally, these waves declare depolarization and repolarization phases of the heart muscle [58]. A heartbeat also contains inter-wave time segments, specifically, PR interval, QRS complex, QT interval and ST segment in addition to the refractory period. The latter extends from the end of a T wave of the preceding heartbeat to the beginning of next heartbeat P wave. This period guarantees enough time for heart muscle to relax. When dealing with multiple heartbeats, the R-R interval, which is the time taken between each ventricular blood ejection, or the time between each two consecutive heartbeats, is a significantly important feature [58]. These waves and time segments are illustrated in Fig.2.

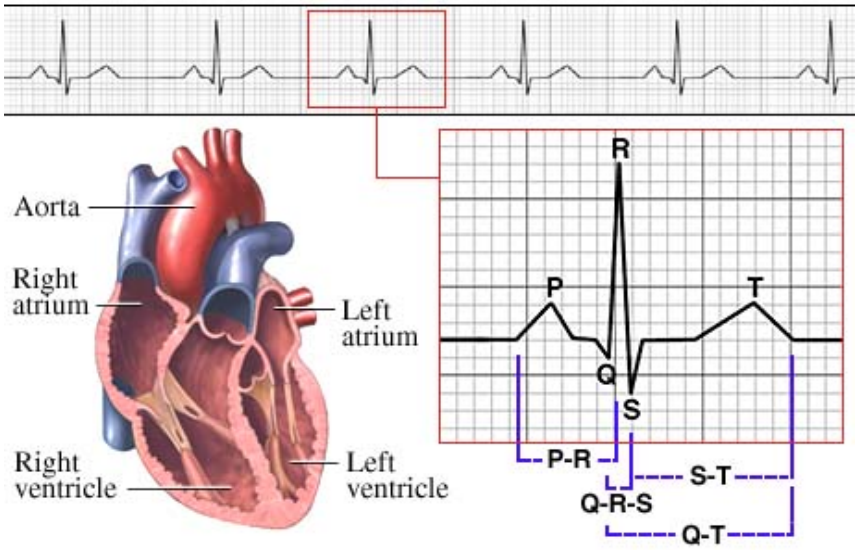

Figure 1.2 - Main morphological features of ECG [56].

ECG Monitoring Systems from Past to Present

In 1980s, a review of computer-based systems for the analysis of ambulatory ECG recordings was reported by Pahlm and Sornmo [59], a historical review of diagnostics problem solving by computer, from its inception in the 1950s, was presented by Benjamin [60] as well as syntactic ECG processing by Skordalakis [61]. In the past decade, research in the development and implementation through innovative technology as well as a critical review of knowledge-based approaches to ECG pattern interpretation [62], reviewed wearable monitoring systems in smart homes [63], comprehensive surveys and reviews of wireless body area networks [93], wireless sensor networks for healthcare [64] and mobile telemedicine [65] was also reported. The review of the ECG signal collection, analysis, technologies used, limitations and future recommendations from 2000 to 2007 can be found in [66-68] and from 2008 to 2011 can be found in [69]. Although Holter monitors are capable of providing continuous monitoring, the central unit of these monitors is bulky and each electrode is connected to the central unit with wires. Therefore, use of the Holter monitor interrupts the daily routine of the patient and is not feasible for unobtrusive continuous monitoring. Over the past few years, with the advancement in wireless technologies, Holter monitors have been miniaturized and evolved into complete wire-free monitoring devices. Although ambulatory wire-free devices look promising for continuous monitoring, there is still a need for further development of such devices.

Current trends in wearable ECG monitoring systems have produced an innovative and versatile approach to wearable smart shirt, vest, watch and band monitoring systems. ECG data have been collated using smart shirts [70] and/or T-shirts [71]. One of the most important modules of smart wearable monitoring technology is wearable biomedical sensors which are attached directly to the patient or to electrode-embedded wearable garment. LOBIN [72] is a combination of e-textile and wireless sensor network integrated into a smart shirt for ECG monitoring. Mobile personal trainer (MOPET) is a wearable system that supervises a physical fitness activity for better training and motivating users [73]. Blue Box [74] is a novel hand-held device capable of collecting and wirelessly transmitting key cardiac parameters

of ECG, photoplethysmography and bio-impedance. It also measures RR interval and QRS duration, heart rate (HR) and systolic time intervals. A commercially available biofeedback device was designed to enhance heart rate variability, called StressEraserTM [75]. A smart vest in [76] is a wearable physiological monitoring system, incorporated in a vest which uses a variety of sensors integrated into the garment's fabric to simultaneously collect certain bio-signals in a non-invasive and unobtrusive way. Researchers in [77, 78] developed an ultra-low-power ECG platform and a low-power wireless ECG necklace. Samsung created a research wearable health monitoring system prototype, "Simband", for continuous monitoring of ECG and PPG signals [34].

1.1.4. Photoplethysmogram

It is important to monitor the perfusion of the circulation. The most important cardiopulmonary parameter is blood pressure, but monitoring it is complicated. A second important parameter is blood flow, which is related to blood pressure [79]. We can monitor the blood perfusion in large vessels using ultrasound devices, but it is not practical to use these routinely. The perfusion of blood flow can be determined easily using a pulse rate monitor [79, 80].

Wearable pulse rate sensors based on photoplethysmography (PPG) have become increasingly popular, with more than ten companies producing these sensors commercially. The principle behind PPG sensors is optical detection of blood volume changes in the microvascular bed of the tissue [79]. The sensor system consists of a light source and a detector, with red and infrared (IR) light-emitting diodes (LEDs) commonly used as the light source. The PPG sensor monitors changes in the light intensity via reflection from or transmission through the tissue. The changes in light intensity are associated with small variations in blood perfusion of the tissue and provide information on the cardiovascular system, in particular, the pulse rate.

Using spectrophotometric methodology, pulse oximetry measures oxygen saturation by illuminating the skin and measuring changes in light absorption of oxygenated (oxyhemoglobin) and

deoxygenated blood [80]. Pulse oximeters measure how much of the hemoglobin in blood is carrying oxygen (oxygen saturation). Oxygen enters the lungs and then is passed on into blood. The blood carries the oxygen to the various organs in our body. The main way oxygen is carried in our blood is by means of hemoglobin. You can imagine hemoglobin molecules (Hb) as “cars” and the “roads” being our blood vessels. The oxygen molecules get into these cars and travel around the body till they reach their destination [81].

The hemoglobin without oxygen we will call de oxygenated hemoglobin (deoxy Hb). The hemoglobin with oxygen, we will call oxygenated hemoglobin (oxy Hb) [81]. Oxygen saturation simply refers to the percentage of the available hemoglobin that carries oxygen (see Fig .3).

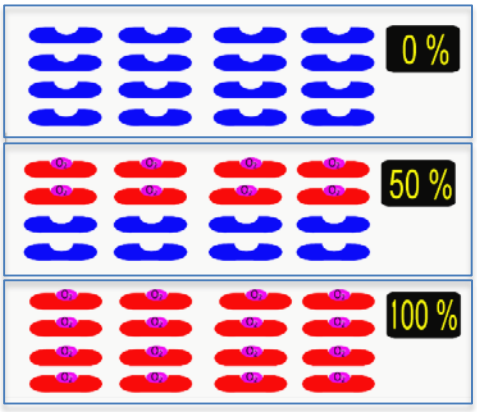

Figure 1.3 - Oxygen saturation in blood: [top] 0% saturation since none of the hemoglobin that carries oxygen, [middle] 50% saturation, [bottom] 100% saturation when all hemoglobin units have oxygen.

Pulse oximeters uses light to work out oxygen saturation and they come in two types: reflectance and transmittance. In a transmittance PO, light is emitted from light sources which goes across the pulse oximeter probe and reaches the light detector. If a finger is placed in between the light source and the light detector, the light will now have to pass through the finger to reach the detector. Part of the light will be absorbed by the finger and the part not absorbed reaches the light detector.

The amount of light that is absorbed by the finger depends on the following properties and these properties are used by the pulse oximeter to calculate the oxygen saturation [80, 81]

1. **Concentration of the light absorbing substance:** Amount of light absorbed is proportional to the concentration of the light absorbing substance. Hemoglobin (Hb) absorbs light. The amount of light absorbed is proportional to the concentration of Hb in the blood vessel. In the diagram below, the blood vessels in both fingers have the same diameter. However, one blood vessel has a low Hb concentration (i.e. low number of Hb in each unit volume of blood) and the other blood vessel has a high Hb concentration (i.e. high number of Hb in each unit volume of blood). Each single Hb absorbs some of the light, so more the Hb per unit area, more is the light is absorbed. This property is described in a law in physics called "Beer's Law: Amount of light absorbed is proportional to the concentration of the light absorbing substance".
2. **Length of the light path in the absorbing substance:** Amount of light absorbed is proportional to the length of the light path. The light emitted from the source has to travel through the artery. The light travels in a shorter path in the narrow artery and travels through a longer path in the wider artery (paths are shown as green lines below). Though the concentration of Hb is the same in both arteries, the light meets more Hb in the wider artery, since it travels in a longer path. Therefore, longer the path the light has to travel, more is the light absorbed. This property is described in a law in physics called "Lambert's Law: Amount of light absorbed is proportional to the length of the path that the light has to travel in the absorbing substance".
3. **Oxyhemoglobin and deoxyhemoglobin absorbs red and infrared light differently:** oxyhemoglobin absorbs more infrared light than red light & deoxyhemoglobin absorbs more red light than infrared light. Different "colors" of light have their own wavelength.

The physical properties that a pulse oximeter employs is illustrated in Fig.5 (a-d) using the transmission pulse oximeter shown in Fig.4. A finger is shown inserted into the probe. Above the finger are the light sources that emit light. In the finger is an artery which carries the blood the pulse oximeter is interested in and a vein through which the blood leaves the finger. Below the finger is the light detector.

The pulse oximeters typically come it two types—transmission and reflectance. In transmission mode, the light transmitted through the medium is detected by a detector opposite the LED source, while in reflectance mode, the detector detects light that is back-scattered or reflected from tissue, bone and/or blood vessels [81].

Figure 1.4 - Finger Pulse Oximeter

The transmission type is capable of obtaining a relatively good signal, but the measurement site may be limited. To be effective, the sensor must be located on the body at a site where transmitted light can be readily detected, such as the fingertip, nasal septum, cheek, tongue, or earlobe [79]. Sensor placement on the nasal septum, cheek or tongue is only effective under anesthesia. The fingertip and earlobe are the preferred monitoring positions; however, these sites have limited blood perfusion. In addition, the fingertip and earlobe are more susceptible to environmental extremes, such as low ambient temperatures (e.g., for military personnel or athletes in training). The greatest disadvantage is that the fingertip sensor interferes with daily activates [79].

Reflectance mode eliminates the problems associated with sensor placement, and a variety of measurement sites (e.g. finger, forehead, ear lobe) can be used [79]. However, reflection-mode PPG is affected by motion artifacts and pressure disturbances. Any movement, such as physical activity, may lead to motion artifacts that corrupt the PPG signal and limit the measurement accuracy of physiological parameters. Pressure disturbances acting on the probe, such as the contact force between the pulse oximeter sensor and measurement site, can deform the arterial geometry by compression [79]. Thus, in the reflected PPG signal, the AC amplitude may be influenced by the pressure exerted on the skin.

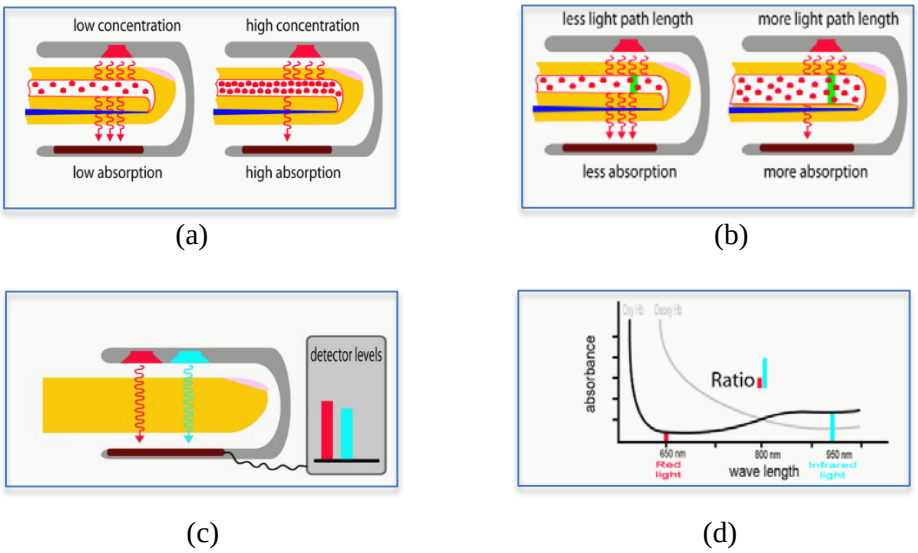

Figure 1.5 - Pulse Oximeter Properties: (a) first property: Beer' Law, (b) second property: Lambert's Law, (c) third property: Oxyhemoglobin and deoxyhemoglobin absorbs red and infrared light differently, (d) Oxyhemoglobin (HbO2) absorbs more infrared light while deoxyhemoglobin (Hb) absorbs more red light.

The pulse oximeter uses two lights to analyze hemoglobin. One is a red light, which has a wavelength of approximately 650 nm. The other is an infrared light, which has a wavelength of 950 nm. The pulse oximeter works out the oxygen saturation by comparing how much red light and infrared light is absorbed by the blood. Depending on the amounts of oxy Hb and deoxy Hb present, the ratio of the amount of red light absorbed compared to the amount of infrared light absorbed changes [80, 81].

Early on, we discussed how the pulse oximeter uses Beer's and Lambert's Law (absorbance depends on concentration and path length) as part of its factors that it uses to compute oxygen saturation. Unfortunately, in physics, the Beer and Lambert law have very strict criteria to be accurate. However, in real life, this does not happen. Blood is not a neat red liquid. Instead, it is full of various irregular objects such as red cells etc. (See Fig. 6). This makes the light scatter, instead of going in a straight line. Therefore Beer and Lamberts Law cannot be applied strictly [81]. Because Beer and Lamberts law cannot be applied strictly, there would be errors if they were used to directly calculate oxygen saturation. A solution to this is to use a "calibration graph" to correct for errors [79-81]. A test pulse oximeter is first calibrated using human volunteers. The test pulse oximeter is attached to the volunteer and then the volunteer is asked to

breathe lower and lower oxygen concentrations. At intervals, arterial blood samples are taken. As the volunteer's blood desaturates, direct measurements made on the arterial blood are compared simultaneously with the readings shown by the test pulse oximeter. In this way, the errors due to the inability of applying Beers and Lamberts law strictly are noted and a correction calibration graph is made.

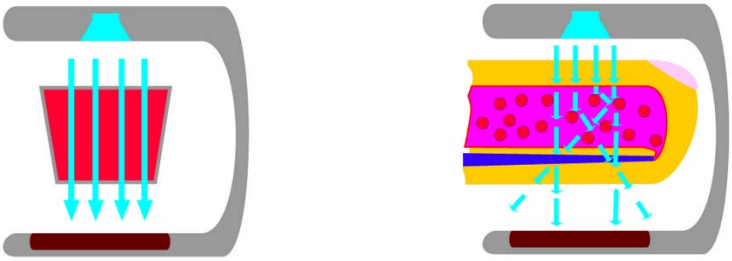

(a) (b)

Figure 1.6 - Beer-Lambert Law Feasibility. (a) In physics the light that goes through the sample should go straight through, (b) In real life blood is not a neat red liquid, thus the light scatter, instead of going in a straight line.

However, in order to not harm the volunteers, the oxygen saturation is not allowed to drop below about 75 – 80 %. For saturations below this, the calibration curve is mathematically estimated .Therefore, pulse oximeters are typically less accurate below saturations of about 75 – 80 %.

A typical transmittance pulse oximeter has one red LED and one infrared LED. On the other side there is a light detector. However, although there are only two LEDs, the light detector is exposed to three sources of light. In addition to the red and infrared LED light sources, there is also light in the room (ambient light) that the pulse oximeter is working in [79, 81]. Some of this room light can also reach the detector. The pulse oximeter has to work with these three sources of light. It requires both the red and infrared light to calculate oxygen saturation. On the other hand, the room light is unwanted "noise", and needs to be taken account of. In reality, both LEDs are never lit together. Instead, the pulse oximeter rapidly switches the LED's on and off in a particular sequence. First, the pulse oximeter activates the red LED light. The red light goes through the finger and reaches the detector. Stray room light also reaches the detector. The detector therefore records red light and room light that falls on it. Next, the pulse oximeter switches off the red LED light and switches on the infrared LED light. The infrared light goes through the finger (not shown)

and reaches the detector. Stray room light also reaches the detector. The detector therefore records infrared light and room light that falls on it. Finally the pulse oximeter switches off both the red and infrared LED lights. Now the only light that falls on the detector is the room light. The pulse oximeter now records the room light level. Since the pulse oximeter now knows the level of room light, it is able to subtract it from the readings to get the actual red and infrared light levels (See Fig.7).

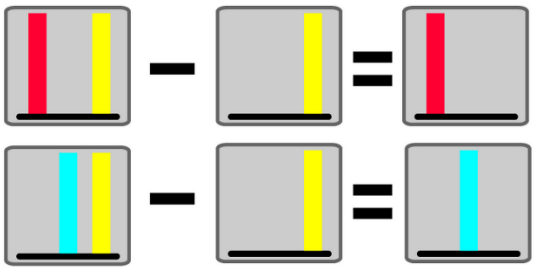

Figure 1.7 - How pulse oximeter address ambient light problem. Colors red and blue represent Pulse oximeter red and blue LEDs, while yellow indicates the ambient light.

If the ambient light is too strong, the LED light signal gets "submerged" in the noise of the ambient light. This can lead to erroneous readings. Therefore, it is important to minimize the amount of ambient light falling on the detector. One can try and move away strong sources of room light. One can also try and cover the pulse oximeter probe and finger with a dark cloth [81].

Photoplethysmography

In a body part such as a finger, arterial blood is not the only thing that absorbs light [79-81]. Skin and other tissues also absorb some light. This poses a problem, because the pulse oximeter should only analyze arterial blood while ignoring the absorbance of light by surrounding tissues. For an example of how tissues can interfere, take the two situations shown in Fig.8. One is a thin finger and the other is a fat finger. The tissues in the thin finger absorbs only a little extra light, while the fatter finger shown on the right absorbs much more light. However, the pulse oximeter has no way to measure if the finger is fat or thin, and therefore has the potential to get confused because it doesn't know how much light is absorbed by blood and how much is absorbed by the tissues surrounding blood [81].

(a) (b)

Figure 1.8 - Light absorbance difference due to tissue difference, (a) Thin finger, (b) Fat finger.

Fortunately, there is a clever solution to the problem [81]. The pulse oximeter wants to only analyze arterial blood, ignoring the other tissues around the blood. Luckily, arterial blood is the only thing pulsating in the finger. Everything else is non-pulsating. Any "changing absorbance" must therefore be due to arterial blood. On the other hand, the pulse oximeter knows that any absorbance that is not changing, must be due to non-pulsatile things such as skin and other "non-arterial" tissues [81].

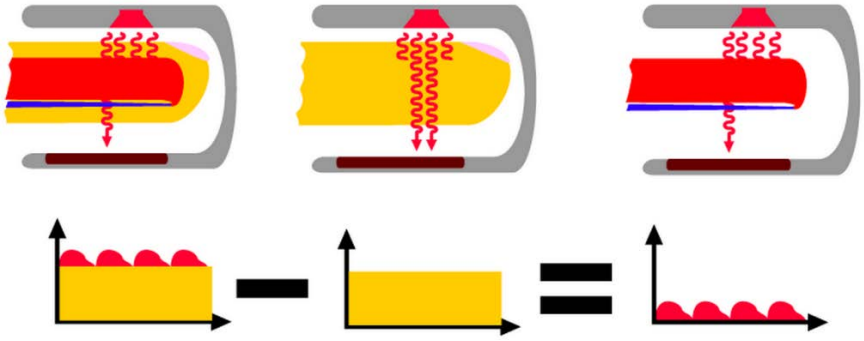

Figure 1.9 - How pulse oximeter measures pulsatile blood

However the pulsatile signal is very small and typically only about 2 % of the total signal is pulsatile. Off all the light that passes through the finger, it is only the small pulsatile part that the pulse oximeter analyses (see Fig.10). Because it is such a small amount of the total light, the pulse oximeter is very susceptible to errors if for an example, the sensor is not placed properly or if the patient moves the sensor [79-81].

The pulsatile signal from pulse oximeter is called "photoplethysmogram", PPG [79-81]. Heart rate and oxygen saturation can be calculated and estimated from PPG signals [79-81]. PPG is affected by factors

that affect the peripheral blood flow. For an example, low blood pressure or peripheral cold temperature can reduce it [80].

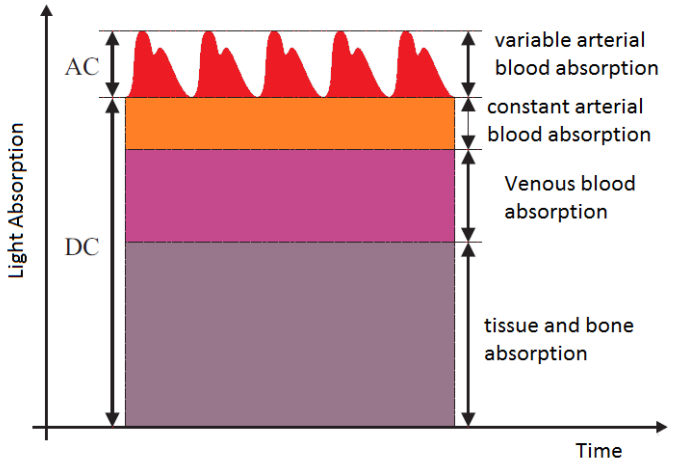

Figure 1.10 - Pulse Oximeter Light absorption Through Tissue and Blood

Utilizing a pulse oximeter as a multi-purpose vital sign monitor has clinical appeal, since it is familiar to clinicians and comfortable for the patient [82]. In healthy, uninjured persons, SpO2 is typically near 98%. A lower reading indicates a level of hypoxia.

A good peripheral blood flow makes the arteries in fingers nicely pulsatile. As discussed before, it is the pulsatile change in absorbance that is used in the calculation of oxygen saturation. When the peripheral perfusion is poor (e.g. in hypotension), the arteries are much less pulsatile. The change in absorbance is therefore less and the pulse oximeter may then find the signal inadequate to correctly calculate oxygen saturation.

At present, use of pulse oximeters is spreading in low-acuity ambulatory settings, e.g., to obtain temporal SpO2 patterns of chronic lung disease (CLD) patients during activities of daily living. Temporal SpO2 patterns can be used to advance understanding of CLD, and to improve oxygen therapy [82-84]. In addition, heart rate variability (HRV) can be derived from a PPG, e.g., to assess dynamic characteristics of the patient's autonomic nervous system [85].

Heart Rate Variability

Heart Rate Variability (HRV), which has been for long used as a screening tool for diagnostic purposes, is another physiological signal that reveals the state cases of having non-consistent Peak-Peak durations/intervals over a number of cardiac cycles per unit time [58, 86]. The origin of heart beating is the electric initiation caused by the SA node that generates about 100-120 pulses per minute during rest [58]. However, when subject is in equilibrium, Heart Rate (HR) will never reach this rate because of the continuous non-voluntary control provided by the Autonomic Nervous System (ANS). The ANS has two main branches, namely, the Sympathetic Nervous System (SNS) that triggers and escalates body responses and the Parasympathetic Nervous System (PNS), which contradicts or reverses actions caused by the sympathetic ANS in order to reach an optimized stable state. Sympathetic and parasympathetic systems control all body organs [58].

Analysis of heart rate variability (HRV) is a powerful tool used to evaluate the regulation of cardiac activity by the autonomic nervous system (ANS). Since its inception HRV has been proven to index foetal distress [87], reveal diabetic neuropathy [88] and uncover ANS pathology [89]. Importantly, HRV has also been shown to predict the mode of death in chronic heart failure [90], raising the prospect that HRV may prove a valuable guide to clinical intervention in cardiovascular disease [91]. Blood Pressure (BP) alterations may increase the risks of having abnormalities in the cardiovascular system, especially in hypertensive individuals. Electrocardiographic evidences show that HRV is significantly decreased in cases with cardiovascular abnormalities such as Left Ventricular Hypertrophy (LVH), aortic valve disease and hypertension. A strong correlation was found between HRV and arterial baroreflex, which is reduced in the case of diabetes and hypertension [92]. Diabetes can cause severe autonomic dysfunction. Decreased beat-to-beat variability causes lowered HRV as a complication of poorly controlled diabetes. It was also concluded that cardiac PNS activity is diminished in diabetic patients [93-95]. Many tests were run on patients with renal failure. Five-minute HRV analysis experiments on patients with chronic renal failure showed a negative correlation between the mean of Peak-Peak intervals and calcium ions concentration

after hemodialysis. In renal failure cases, HR power spectral density analysis exhibited a strong reduction of power spectral density in all frequency ranges, which dictates reduction of HRV [96, 97].

References

1. Patel, S., et al., A review of wearable sensors and systems with application in rehabilitation. Journal of NeuroEngineering and Rehabilitation, 2012. 9(1): p. 1-17.
2. P. A. Muennig and S. A. Glied, What Changes in Survival Rates Tell Us About U.S. Health Care. Health Affairs Web 2010. First.
3. Gulley, S.P., E.K. Rasch, and L. Chan, If we build it, who will come? Working-age adults with chronic health care needs and the medical home. Med Care, 2011. 49(2): p. 149-55.
4. Gulley, S.P., E.K. Rasch, and L. Chan, Ongoing coverage for ongoing care: access, utilization, and out-of-pocket spending among uninsured working-aged adults with chronic health care needs. Am J Public Health, 2011. 101(2): p. 368-75.
5. Goonewardene, S.S., et al., Road traffic collisions-case fatality rate, crash injury rate, and number of motor vehicles: time trends between a developed and developing country. Am Surg, 2010. 76(9): p. 977-81.
6. Organization, W.H. Active Aging a Policy Framework. Available from: http://www.who.int/ageing/publications/active_ageing/en/.
7. Kinsella, K.G., D.R. Phillips, and P.R. Bureau, Global Aging: The Challenge of Success. 2005: Population Reference Bureau.
8. Bray, H., National population projections, O.f.N. Statistics, Editor. 2008.
9. Axelrod, D.A., D. Millman, and M.M. Abecassis, US Health Care Reform and Transplantation. Part I: overview and impact on access and reimbursement in the private sector. Am J Transplant, 2010. 10(10): p. 2197-2202.
10. Teng, X.F., et al., Wearable medical systems for p-Health. IEEE Rev Biomed Eng, 2008. 1: p. 62-74.
11. Bonato, P., Wearable sensors and systems. From enabling technology to clinical applications. IEEE Eng Med Biol Mag, 2010. 29(3): p. 25-36.
12. Health Care Disparities in Rural Areas. Available from: http://archive.ahrq.gov/research/ruraldisp/ruraldispar.htm.
13. Caudill, T.S., et al., Commentary: Health care reform and primary care: training physicians for tomorrow's challenges. Acad Med, 2011. 86(2): p. 158-60.
14. Chan, L., L.G. Hart, and D.C. Goodman, Geographic access to health care for rural Medicare beneficiaries. J Rural Health, 2006. 22(2): p. 140-6.
15. DeVaul, R., et al., MIThril 2003: Applications and Architecture, in Proceedings of the 7th IEEE International Symposium on Wearable Computers. 2003, IEEE Computer Society. p. 4.
16. ZigBee Alliance. Available from: http://www.zigbee.org.
17. Jinyun, Z., et al., UWB Systems for Wireless Sensor Networks. Proceedings of the IEEE, 2009. 97(2): p. 313-331.
18. Yilmaz, T., R. Foster, and Y. Hao, Detecting Vital Signs with Wearable Wireless Sensors. Sensors, 2010.
19. Asada, H.H., et al., Mobile monitoring with wearable photoplethysmographic biosensors. IEEE Eng Med Biol Mag, 2003. 22(3): p. 28-40.
20. Shaltis, P.A., A. Reisner, and H.H. Asada, Wearable, cuff-less PPG-based blood pressure monitor with novel height sensor. Conf Proc IEEE Eng Med Biol Soc, 2006. 1: p. 908-11.
21. Corbishley, P. and E. Rodriguez-Villegas, Breathing Detection: Towards a Miniaturized, Wearable, Battery-Operated Monitoring System. Biomedical Engineering, IEEE Transactions on, 2008. 55(1): p. 196-204.

22. Barbaro, M., et al., Active devices based on organic semiconductors for wearable applications. IEEE Trans Inf Technol Biomed, 2010. 14(3): p. 758-66.
23. Patterson, J.A.C., D.G. McIlwraith, and Y. Guang-Zhong. A Flexible, Low Noise Reflective PPG Sensor Platform for Ear-Worn Heart Rate Monitoring. in Wearable and Implantable Body Sensor Networks, 2009. BSN 2009. Sixth International Workshop on. 2009.
24. Yan, Y.S. and Y.T. Zhang, An efficient motion-resistant method for wearable pulse oximeter. IEEE Trans Inf Technol Biomed, 2008. 12(3): p. 399-405.
25. Wood, L.B. and H. Asada, Low variance adaptive filter for cancelling motion artifact in wearable photoplethysmogram sensor signals. Conf Proc IEEE Eng Med Biol Soc, 2007. 2007: p. 652-5.
26. Merilahti, J., et al., Compliance and technical feasibility of long-term health monitoring with wearable and ambient technologies. J Telemed Telecare, 2009. 15(6): p. 302-9.
27. Sciacqua, A., et al. Validation of a flexible and innovative platform for the home monitoring of heart failure patients: Preliminary results. in Computers in Cardiology, 2009. 2009.
28. Mundt, C.W., et al., A multiparameter wearable physiologic monitoring system for space and terrestrial applications. IEEE Trans Inf Technol Biomed, 2005. 9(3): p. 382-91.
29. Anliker, U., et al., AMON: a wearable multiparameter medical monitoring and alert system. IEEE Trans Inf Technol Biomed, 2004. 8(4): p. 415-27.
30. Habetha, J., The MyHeart project--fighting cardiovascular diseases by prevention and early diagnosis. Conf Proc IEEE Eng Med Biol Soc, 2006. Suppl: p. 6746-9.
31. Paradiso, R. Wearable health care system for vital signs monitoring. in Information Technology Applications in Biomedicine, 2003. 4th International IEEE EMBS Special Topic Conference on. 2003.
32. Di Rienzo, M., et al., MagIC System: a New Textile-Based Wearable Device for Biological Signal Monitoring. Applicability in Daily Life and Clinical Setting. Conf Proc IEEE Eng Med Biol Soc, 2005. 7: p. 7167-9.
33. Samsung. Simband. Available from: https://www.simband.io/.
34. Life Alert Classic. Available from: http://www.halomonitoring.com.
35. AlertOne medical alert system.
36. Automatic Fall Detection. Available from: http://www.wellcore.com/learn/automatic-falldetection.
37. myHalo.
38. BrickHouse. Available from: http://www.brickhousealert.com/personal-emergency-medicalalarm.html.
39. EASY WORLS. Available from: http://www.ttmmonaco.com/en/default.htm.
40. USC Rehabilitation Engineering Research Center. Available from: http://www.isi.edu/research/rerc.
41. Rizzo, A., et al., Virtual reality applications for addressing the needs of those aging with disability. Stud Health Technol Inform, 2011. 163: p. 510-6.
42. Vincent, C., et al., Rehabilitation needs for older adults with stroke living at home: perceptions of four populations. BMC Geriatr, 2007. 7: p. 20.
43. Uswatte, G., et al., Ambulatory monitoring of arm movement using accelerometry: an objective measure of upper-extremity rehabilitation in persons with chronic stroke. Arch Phys Med Rehabil, 2005. 86(7): p. 1498-501.
44. Uswatte, G., et al., Validity of accelerometry for monitoring real-world arm activity in patients with subacute stroke: evidence from the extremity constraint-induced therapy evaluation trial. Arch Phys Med Rehabil, 2006. 87(10): p. 1340-5.
45. Patel, S., et al., A review of wearable sensors and systems with application in rehabilitation. J Neuroeng Rehabil, 2012. 9: p. 21.
46. Heeringa, J., et al., Prevalence, incidence and lifetime risk of atrial fibrillation: the Rotterdam study. European Heart Journal, 2006. 27(8): p. 949-953.
47. Benjamin, E.J., et al., Impact of atrial fibrillation on the risk of death: the Framingham Heart Study. Circulation, 1998. 98(10): p. 946-52.

48. Wolf, P.A., R.D. Abbott, and W.B. Kannel, Atrial fibrillation as an independent risk factor for stroke: the Framingham Study. Stroke, 1991. 22(8): p. 983-8.
49. Humphries, K.H., et al., New-onset atrial fibrillation: sex differences in presentation, treatment, and outcome. Circulation, 2001. 103(19): p. 2365-70.
50. Kerr, C., et al., Follow-up of atrial fibrillation: The initial experience of the Canadian Registry of Atrial Fibrillation. Eur Heart J, 1996. 17 Suppl C: p. 48-51.
51. Kinlay, S., et al., Cardiac event recorders yield more diagnoses and are more cost-effective than 48-hour Holter monitoring in patients with palpitations. A controlled clinical trial. Ann Intern Med, 1996. 124(1 Pt 1): p. 16-20.
52. Roche, F., et al., Frequent and prolonged asymptomatic episodes of paroxysmal atrial fibrillation revealed by automatic long-term event recorders in patients with a negative 24-hour Holter. Pacing Clin Electrophysiol, 2002. 25(11): p. 1587-93.
53. Benjamin, E.J., et al., Prevention of atrial fibrillation: report from a national heart, lung, and blood institute workshop. Circulation, 2009. 119(4): p. 606-18.
54. Defaye, P., F. Dournaux, and E. Mouton, Prevalence of supraventricular arrhythmias from the automated analysis of data stored in the DDD pacemakers of 617 patients: the AIDA study. The AIDA Multicenter Study Group. Automatic Interpretation for Diagnosis Assistance. Pacing Clin Electrophysiol, 1998. 21(1 Pt 2): p. 250-5.
55. Electrocardiogram. Available from: http://www.emedicinehealth.com/electrocardiogram_ecg/article_em.htm.
56. ECG Features. Available from: http://www.davita-shop.co.uk/ecg-instruments.html.
57. Oweis, R.J. and B.O. Al-Tabbaa, QRS Detection and Heart Rate Variability Analysis: A Survey. Biomedical Science and Engineering, 2014. 2(1): p. 13-34.
58. Pahlm, O. and L. Sornmo, Software QRS detection in ambulatory monitoring--a review. Med Biol Eng Comput, 1984. 22(4): p. 289-97.
59. Kleinmuntz, B., Diagnostic problem solving by computer: a historical review and the current state of the science. Comput Biol Med, 1984. 14(3): p. 255-70.
60. Skordalakis, E., Syntactic ECG processing: a review. Pattern Recogn., 1986. 19(4): p. 305-313.
61. Kundu, M., M. Nasipuri, and D. Kumar Basu, Knowledge-based ECG interpretation: a critical review. Pattern Recognition, 2000. 33(3): p. 351-373.
62. Chan, M., et al., A review of smart homes-Present state and future challenges. Comput. Methods Prog. Biomed., 2008. 91(1): p. 55-81.
63. Alemdar, H. and C. Ersoy, Wireless sensor networks for healthcare: A survey. Computer Networks, 2010. 54(15): p. 2688-2710.
64. Lin, C.-F., Mobile Telemedicine: A Survey Study. Journal of Medical Systems, 2012. 36(2): p. 511-520.
65. Paul, S.A., Wavelet transforms and the ECG: a review. Physiological Measurement, 2005. 26(5): p. R155.
66. Davenport, C., et al., Assessing the diagnostic test accuracy of natriuretic peptides and ECG in the diagnosis of left ventricular systolic dysfunction: a systematic review and meta-analysis. Br J Gen Pract, 2006. 56(522): p. 48-56.
67. Poli, S., et al., Prediction of atrial fibrillation from surface ECG: review of methods and algorithms. Ann Ist Super Sanita, 2003. 39(2): p. 195-203.
68. Baig, M.M., H. Gholamhosseini, and M.J. Connolly, A comprehensive survey of wearable and wireless ECG monitoring systems for older adults. Med Biol Eng Comput, 2013. 51(5): p. 485-95.
69. Lee, Y.-D. and W.-Y. Chung, Wireless sensor network based wearable smart shirt for ubiquitous health and activity monitoring. Sensors and Actuators B: Chemical, 2009. 140(2): p. 390-395.
70. Bianchi, A.M., M.O. Mendez, and S. Cerutti, Processing of signals recorded through smart devices: sleep-quality assessment. IEEE Trans Inf Technol Biomed, 2010. 14(3): p. 741-7.

71. Lopez, G., V. Custodio, and J.I. Moreno, LOBIN: E-textile and wireless-sensor-network-based platform for healthcare monitoring in future hospital environments. IEEE Trans Inf Technol Biomed, 2010. 14(6): p. 1446-58.
72. Buttussi, F. and L. Chittaro, MOPET: a context-aware and user-adaptive wearable system for fitness training. Artif Intell Med, 2008. 42(2): p. 153-63.
73. Pollonini, L., et al., A novel handheld device for use in remote patient monitoring of heart failure patients--design and preliminary validation on healthy subjects. J Med Syst, 2012. 36(2): p. 653-9.
74. Heilman, K.J., et al., Accuracy of the StressEraser in the detection of cardiac rhythms. Appl Psychophysiol Biofeedback, 2008. 33(2): p. 83-9.
75. Pandian, P.S., et al., Smart Vest: wearable multi-parameter remote physiological monitoring system. Med Eng Phys, 2008. 30(4): p. 466-77.
76. Yazicioglu, R.F., et al., Ultra-low-power wearable biopotential sensor nodes. Conf Proc IEEE Eng Med Biol Soc, 2009. 2009: p. 3205-8.
77. J Penders, J.v.d.M., M Altini, F Yazicioglu, C Van Hoof. A low-power wireless ECG necklace for reliable cardiac activity monitoring on-the-move. in Proceedings of the International Conference of the IEEE Engineering in Medicine and Biology Society. 2011.
78. Tamura, T.M., Y.; Sekine, M.; Yoshida, M., Wearable Photoplethysmographic Sensors—Past and Present. Electronics, 2014. 3(2): p. 282-302.
79. Jubran, A., Pulse oximetry. Intensive Care Med, 2004. 30(11): p. 2017-20.
80. Tilakaratna, P., How pulse oximeters work explained simply.
81. Zhu, Z., et al., Continuous oxygen monitoring--a better way to prescribe long-term oxygen therapy. Respir Med, 2005. 99(11): p. 1386-92.
82. Barratt, C.W., et al., Detection of previously unrecognized daytime desaturation in children with chronic lung disease. J Med Eng Technol, 2007. 31(2): p. 101-8.
83. Cutaia, M., Ambulatory Monitoring of Oxygen Saturation in Chronic Lung Disease: Optimizing Long-Term Oxygen Therapy. Clinical Pulmonary Medicine, 2002. 9(6): p. 297-305.
84. Lu, S., et al., Can photoplethysmography variability serve as an alternative approach to obtain heart rate variability information? J Clin Monit Comput, 2008. 22(1): p. 23-9.
85. Lu, G., et al., A comparison of photoplethysmography and ECG recording to analyse heart rate variability in healthy subjects. J Med Eng Technol, 2009. 33(8): p. 634-41.
86. Hon, E.H. and S.T. Lee, ELECTRONIC EVALUATION OF THE FETAL HEART RATE. VIII. PATTERNS PRECEDING FETAL DEATH, FURTHER OBSERVATIONS. Am J Obstet Gynecol, 1963. 87: p. 814-26.
87. Ewing, D.J., et al., The value of cardiovascular autonomic function tests: 10 years experience in diabetes. Diabetes Care, 1985. 8(5): p. 491-8.
88. Tulen, J.H., et al., Sleep patterns and blood pressure variability in patients with pure autonomic failure. Clin Auton Res, 1991. 1(4): p. 309-15.
89. Guzzetti, S., et al., Different spectral components of 24 h heart rate variability are related to different modes of death in chronic heart failure. Eur Heart J, 2005. 26(4): p. 357-62.
90. Chattipakorn, N., et al., Heart rate variability in myocardial infarction and heart failure. International Journal of Cardiology, 2007. 120(3): p. 289-296.
91. de Boer, R.W., J.M. Karemaker, and J. Strackee, Relationships between short-term blood-pressure fluctuations and heart-rate variability in resting subjects. I: A spectral analysis approach. Med Biol Eng Comput, 1985. 23(4): p. 352-8.
92. Pfeifer, M.A., et al., Quantitative evaluation of cardiac parasympathetic activity in normal and diabetic man. Diabetes, 1982. 31(4 Pt 1): p. 339-45.
93. Singh, J.P., et al., Association of hyperglycemia with reduced heart rate variability (The Framingham Heart Study). Am J Cardiol, 2000. 86(3): p. 309-12.
94. Wheeler, T. and P.J. Watkins, Cardiac Denervation in Diabetes. British Medical Journal, 1973. 4(5892): p. 584-586.

95. Chan, C.T., et al., Effects of daily hemodialysis on heart rate variability: results from the Frequent Hemodialysis Network (FHN) Daily Trial. Nephrol Dial Transplant, 2014. 29(1): p. 168-78.
96. Zoccali, C., M. Ciccarelli, and Q. Maggiore, Defective reflex control of heart rate in dialysis patients: evidence for an afferent autonomic lesion. Clin Sci (Lond), 1982. 63(3): p. 285-92.

Chapter 2: Problem Statement, Aims and Scope

2.1. Problem Statement and Background

Despite the potential advantages of a remote monitoring system relying on wearable sensors like the one described above, there are significant challenges ahead before such a system can be utilized on a large scale. These challenges include technological barriers such as limitations of currently available battery technology as well as motion and noise artifacts. Vital signals are very vulnerable to motion, such as a patient moving his hand or body or simply doing any typical physical activities.

2.1.1. Motion and Noise Artifact and PPG

Consider an example of a finger pulse oximeter, as the finger moves, the light levels change dramatically. Such a poor signal makes it difficult for the pulse oximeter to calculate oxygen saturation and also heart rate.

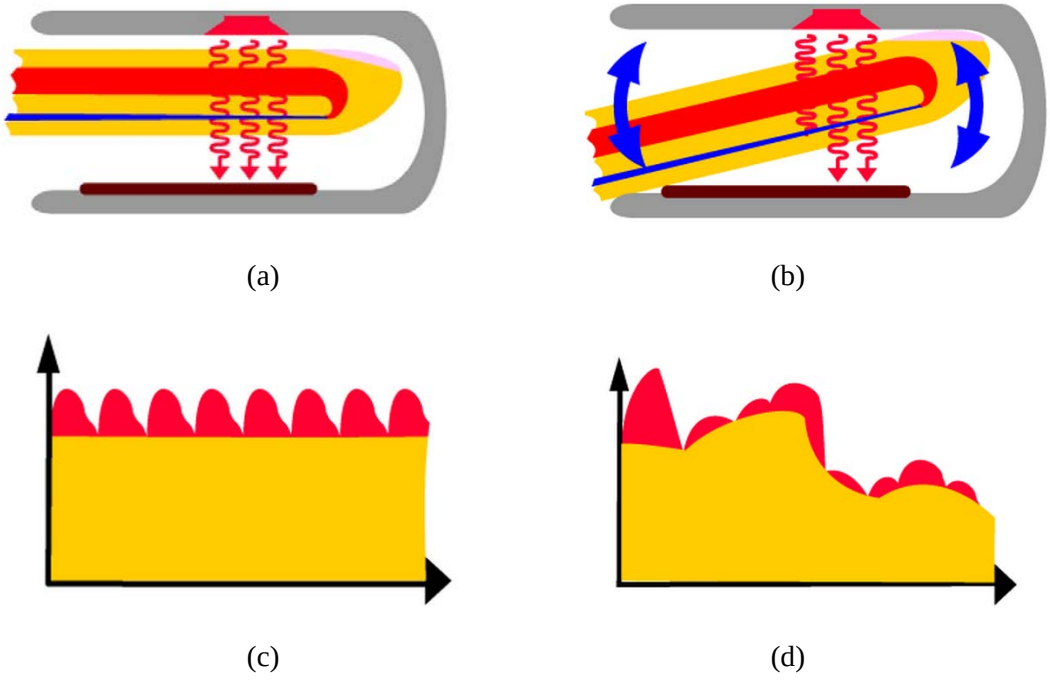

Figure 2.1 – Motion and Noise Artifact Using Finger Pulse Oximeter. (a) Fixed finger in a pulse oximeter, (b) Moving finger in a pulse oximeter, (c) light absorbance and photoplethysmogram during no movement, (d) light absorbance and photoplethysmogram during motion

Previous research has identified several factors that affect PPG recordings, including the measurement site (i.e., probe attachment site), the contact force, mechanical movement artifacts, subject posture, and breathing, as well as ambient temperature [79]. The location of the LED and PD is an important design issue that affects the signal quality and robustness against motion artifacts [79, 81]. Therefore, suitable measurement sites must be located to optimize sensor performance [79]. PPG sensors are commonly worn on the fingers due to the high signal amplitude that can be achieved in comparison with other sites [98]. However, this configuration is not well suited to pervasive sensing, as most daily activities involve the use of the fingers. In recent years, different measurement sites for PPG sensors have been explored extensively, including the ring finger [99], wrist [34, 100, 101], brachia [102], earlobe [103-105], external ear cartilage [106], and the superior auricular region [24]. In addition, the esophageal region has been used in clinical practice [107-109]. Commercial clinical PPG sensors commonly use the finger, earlobe and forehead [110]. In addition, use of a glass-type wireless PPG has been examined [111]. The perfusion values of 52 anatomical sites in healthy subjects showed that the fingers, palm, face, and ears offer much higher perfusion values compared with other measurement sites [112]; the transmitted PPG signal amplitude from the earlobe provides the largest perfusion value. Wristwatch-type pulse oximetry and blood pressure sensors have been developed and commercialized by several companies. These devices, although much easier to wear, are not usually used in clinical settings, due to several technical issues like motion and noise artifacts. Samsung recently developed a wrist band “Simband” device for continuous monitoring of ECG and PPG signals [34]. Forehead sensors have shown greater sensitivity to pulsatile signal changes under low perfusion conditions, compared with other peripheral body locations [110]. The thin-skin layer of the forehead, coupled with a prominent bone structure, helps to direct light back to the PD. Sensor placement on the forehead has been shown to result in decreased motion artifacts during certain types of physical activity.

In reflectance-type PPG, the PPG signal waveform may be affected by the contact force between the sensor and the measurement site. The waveform of the obtained PPG signal differs depending on the PPG probe contact pressure. A number of studies have suggested that the PPG waveform coincides with arterial stiffness and vascular reactivity. Several studies have shown that moderate pressure on the sensor can improve the PPG signal. Ideally, the best PPG signal can be obtained under conditions of transmural pressure, defined as the pressure difference between the inside and outside of the blood vessel (i.e., the pressure across the wall of the blood vessel). Insufficient pressure results in inadequate contact and consequently low AC signal amplitude. However, PPG signal recording under excessive pressure conditions can also lead to low AC signal amplitude, as well as distorted waveforms caused by the occluded artery beyond the PPG probe. Optimal contact pressure corresponds to the maximal pulsatile amplitude; this occurs when the transmural pressure approaches zero (i.e., under maximal arterial compliance). Studies have shown that contact pressures ranging from 8 to 12 kPa (60–90 mmHg) resulted in the largest PPG amplitude for a reflectance sensor attached to the forehead region above the eye, although the signal-to-noise ratio (SNR) did not improve significantly [113].

Motion artifacts mainly consist of random low-frequency interference. Therefore, most artifact reduction is accomplished by signal processing. In the present thesis, the problem of motion and noise artifact detection and signal reconstruction is addressed.

The moving average method is commonly used to reduce motion artifacts and works well for a limited artifact range. However, this method does not account for sudden changes. The periodic moving average filter (PMAF), based on the quasi-periodicity of the PPG signals, segments the PPG signal into periods and resamples each period [114].

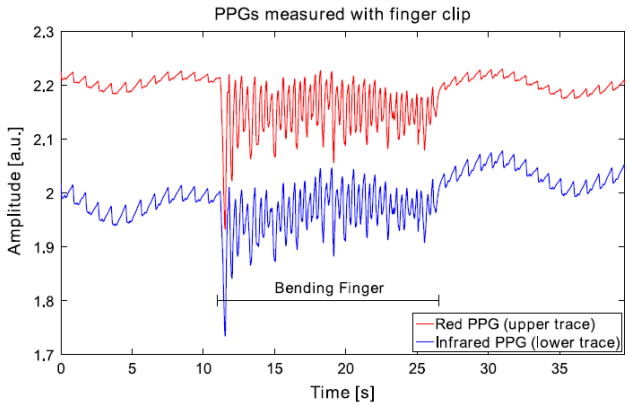

(a)

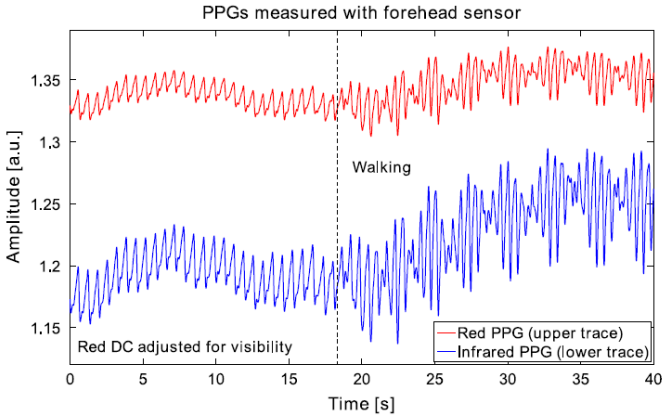

(b)

Figure 2.2 – Illustration of the effect of motion on PPGs. (a) PPGs obtained using a transmissive finger clip. The motion artifacts are caused by repetitive slight bending of the finger. (b) PPGs obtained using a reflective forehead sensor. Walking causes the motion artifacts [2].

Filtering Methods

Instead, motion artifacts can be removed using a filter bank and a matched filter consisting of several frequency bands [115]. In this case, the adaptive filter exhibited many variations and errors due to amplitude variations during convergence when measuring PPG in real-time, whereas the moving average filter exhibited a more stable output. Compared with traditional adaptive filtering methods, the ratio variation was 50% lower than that of the moving average filter, allowing more stable measurement of oxygen saturation, despite the patient's movement [115].

The basic function of a filter is to remove the unwanted signal from the signal of interest. A commonly used filtering technique separates the signal from noise using the peak frequencies of the signal and artifact [79]. In addition, the mean square of the error signal (the difference between the desired response and actual response of the filter) can be minimized. However, when the peak frequency of the pulse rate is similar to the noise frequency, the pulse rate cannot be separated from the noise [79]. In PPG measurements, active noise cancellation with acceleration-based adaptive filters has been attempted by several researchers [79]. Obtaining the best design usually requires a priori knowledge of certain statistical parameters (such as the mean and correlation functions) within the useful signal. With this information, an optimal filter can be designed that minimizes the unwanted signals according to statistical criteria. The least mean square (LMS) adaptive algorithm removes motion artifact noise by estimating the synthetic noise reference signal and adapting the filter coefficients based on filter order [79]. LMS algorithms are a class of adaptive filters used to mimic the desired filter by finding the filter coefficients that relate to producing the least mean square of the error signal [116].

Many adaptive techniques have been applied to the reduction of motion artifacts from PPG signals, including the normalized least mean squares (NLMS) method, recursive least squares (RLS) filter, time varying step-size LMS (TVS-LMS), adaptive step-size LMS (AS-LMS), and Kalman filters [117]. A LMS filter with automatic step-size control was used to mitigate the effects of motion artifacts in PPG recordings for long-term patient monitoring [118]. The experimental results indicated that the proposed variable step-size LMS filter provided better performance than the LMS filter with a fixed step-size. In another study, a two-dimensional (2-D) active noise cancellation algorithm was applied to compensate for motion-distorted signals using directional accelerometer data [119]; a NLMS adaptive filter (fourth-order) was used in the algorithm, resulting in a reduction in signal distortion from 52.34% to 3.53% over the frequency range of 1–2.5 Hz (the frequency range for daily motion, such as walking and jogging). A Laguerre series was implemented to compactly represent the system dynamics for joggers using a few parameters, such as the

heart rate [120]. This study determined that the standard artifact reduction scheme does not work when the physiological signal is correlated with wearer motion. Thus, adaptive blind-source separation techniques can be used to recover the physiological signal. However, the success of this method is currently limited.

Blind Source Separation Techniques

Blind signal separation, also known as blind source separation, is the separation of a set of source signals from a set of mixed signals, without the aid of information (or with very little information) about the source signals or the mixing process [121]. One of the blind source separation techniques is principle component analysis (PCA). The basic concept of PCA-based noise reduction is to observe the noisy data in a large m-dimensional space of delayed coordinates [79]. As the noise is assumed to be random, it extends in an approximately uniform manner in all directions in this space. In contrast, the dynamics of deterministic systems underlying the data confine the trajectories of useful signals to a lower dimensional subspace of dimension $p < m$. Consequently, the eigenspace of the observed noisy mixtures is partitioned into a noise and a signal-plus-noise subspace. In this case, noise reduction is performed by projecting the noisy mixtures onto the signal and noise subspace [79].

Another technique in BSS family is independent component analysis. The independent component analysis (ICA) model describes generation of the observed data in terms of mixing of components. ICA is attractive as it does not require prior knowledge of the system [79]. However, ICA assumes that all source signal component pairs are mutually independent. It is important to assess the statistical independence of the source components in PPG data, especially if ICA is to be applied in ambulatory monitoring environments, where motion artifacts can have a substantial effect on the quality of data received from light-based sensors [79]. Analyses have indicated that motion significantly affects arterial flow, so care must be taken when applying ICA to light-based sensor data acquired from wearable platforms [122]. In addition, by exploiting the independence between PPG and motion artifacts, Kim and Yoo proposed that

the combination of ICA and block interleaving with a low-pass filter can reduce the motion artifacts under the conditions used in general dual-wavelength measurements [123].

In Chapter (6) of this study, we propose a novel motion and noise artifact reduction technique (IMAR) using singular spectrum analysis (SSA), another BSS technique.

Model based Algorithms

An active noise cancellation method using a MEMS accelerometer was developed to recover corrupted wearable sensor signals from a finger ring PPG sensor [124], the signal of which is susceptible to the hand motion of the wearer. A MEMS accelerometer embedded in the PPG sensor detected hand acceleration. The correlation between acceleration and distorted PPG signal was analyzed, and a low-order FIR model relating the signal distortion to the hand acceleration was obtained. The model parameters were identified in real-time using the RLS method [124].

In Chapter (7) a new tool (DyParaM) for modeling dynamics of photoplethysmogram (PPG) data is introduced. The idea is to use a nonlinear model to identify the clean PPG signal and then using the model to retrieve the PPG signal information from the MNA corrupted PPG readings from pulse oximeter.

Time-Frequency Methods

Due to the nature of biological systems, biological signals tend to be non-stationary and their properties can change substantially over time. Thus, time–frequency methods (e.g. wavelet transforms [125] and smoothed pseudo Wigner-Ville distributions [126], Variable Frequnecy Complex Demodulation [127], Spectrogram [128], Sparse time-frequency spectrum [129-131]) may provide better signal enhancement for PPG signals than traditional methods.

Lee et al. (2003) [125] proposed a wavelet ―denoising approach for the reduction of motion artifacts from PPG recordings, in which the stationary wavelet transform (SWT) and wavelet transform modulus maxima (WTMM) were used to remove motion artifacts. In the experimental set-up, two identical

PPG circuits were used. One of these circuits was attached to the subject's left index finger that was held in a stable position to obtain a reference signal as standard. Meanwhile, the second circuit was attached to the right index finger that moved vertically or circularly to introduce motion artifacts. The corrupted PPG signals were decomposed by a seven-level SWT for circular motion. The signal was then reconstructed by applying the inverse of the SWT and WTMM to remove signal noise. By applying the proposed method, the researchers observed an 87% (61%) reduction in heart rate estimation error and a 66% (46%) reduction in instantaneous heart rate error for vertical motion (circular motion).

The smoothed pseudo Wigner-Ville distribution (SPWVD) has been applied to reduce motion artifacts affecting pulse oximetry [126]. The SPWVD approach was compared with two other techniques commonly used in this field: the weighted moving average (WMA) and FFT. SpO2 and pulse rate were estimated from a PPG signal recorded when the subject was in the resting state, as well as when performing four types of motion: horizontal and vertical movements of the hand, and bending and pressing motions of the finger. For each condition, 24 sets of 30-s PPG signals were collected from six subjects. These signals were evaluated with respect to a PPG reference signal recorded simultaneously from the subject's other hand that was stationary at all times. The SPWVD approach showed significant improvement in performance ($p < 0.05$), compared with traditional approaches, when subjects bent their finger or pressed their finger against the sensor. In addition, the SPWVD approach also significantly reduced the mean absolute pulse rate error ($p < 0.05$) from 16.4 bpm and 11.2 bpm for the WMA and FFT approaches, respectively, to 5.62 bpm [126].

Two noteworthy algorithms recently published are TROIKA and JOSS [129, 130] in which sparsity-based spectrum estimation and spectral peak tracking with verification, are used to estimate and monitor heart rate during intensive physical activity, respectively. Both approaches make use of PPG and accelerometer information to obtain an accurate estimation of heart rate while running on a treadmill. TROIKA has two extra stages of signal decomposition and reconstruction using singular spectrum analysis

(SSA) and it then applies temporal difference operations on the SSA-reconstructed PPG. SSA components are compared to the accelerometer signals and those components with close frequencies to the accelerometer signals are discarded and the rest are used to reconstruct the signal. In JOSS and TROIKA, spectral peak tracking with verification aims to select the spectral peaks corresponding to HR. JOSS, which has been shown to estimate HR more accurately than TROIKA, is based on the idea that the spectra of PPG signals and simultaneous acceleration signals have some common spectrum structures, and thus formulates the spectrum estimation of these signals into a joint sparse signal recovery model using the multiple measurement vector (MMV) model. MMV is used for joint spectrum estimation based on PPG and accelerometer data, which is in contrast to the single measurement vector (SMV) model that was used in TROIKA and was based on only a single PPG signal. Although JOSS has been shown to be much more accurate than previous methods for reconstruction of heart rate from MA-contaminated PPG signals, the main disadvantage of the method is it can merely provide smoothed HR reconstruction estimations. Neither time-domain PPG signal reconstruction nor heart rate variability analysis can be done using JOSS or TROIKA.

In the present dissertation (Chapters 8-10) we propose two time-frequency based motion and noise artifact detection and reduction methods (TifMA, OxiMA and SpaMA) for PPG signals.

2.1.2. Motion and Noise Artifact and ECG

With an ambulatory ECG monitoring devices the ECG signal can be recorded or monitored in ambulatory conditions where the patient can perform all the routine activity. However, the effectiveness of ECG device can be significantly impaired by motion artifacts which contaminates the signal and that can lead to errors in estimation of cardiac parameters and trigger false alarms. Detection and reduction of noises and artifacts in the cardiovascular monitoring are two of the greatest challenges for enhancing signal quality [13, 132-136].

Skin stretching due to body or limb movement or physical activity (PA) is a main cause of motion artifacts in ECG signals. Skin stretching causes modifications in the distribution of charges at the interface between the skin and electrode. Since skin can be considered a current generator that actively produces a potential difference between the in- and out-side of the skin, stretching causes disturbance in the distribution of charges at the electrode-electrolyte interface. It induces a temporary change in the half-cell potential, providing a variation of the involved potentials and reducing its magnitude [137-139].

The motion artifact induced due PA has a spectral overlap with ECG signal in 1-10 Hz [140]. Many important cardiac features of ECG signal like P and T wave has significant energy content in this overlapping band of 1-10Hz. So it is very difficult to separate or eliminate motion artifact completely without affecting these cardiac features in ECG [140].

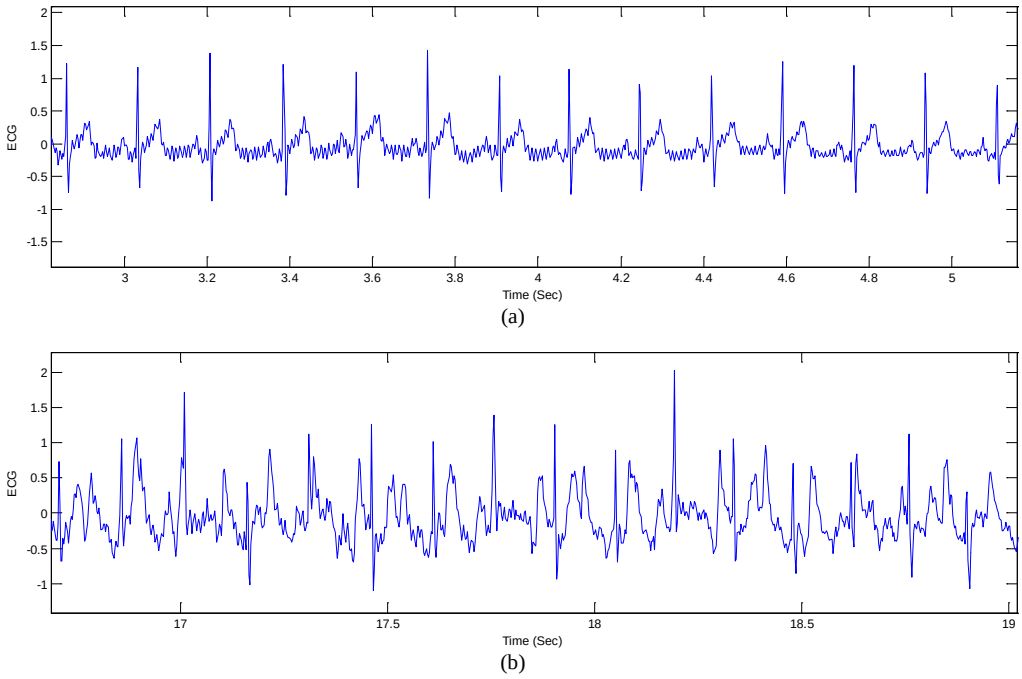

Figure 2.3 – ECG recordings (a) clean signal form healthy subject with prominent-waves and regular, consistent RR-interval, (b) MA corrupted signal from healthy subject which shows irregular pattern with indistinguishable P-waves and RR-interval.

Several efforts have been made to obtain robust ECG against MAs [141-146], but MAs remain one of the major problems in both short- and long- term cardiovascular monitoring [147-150]. There are two possible approaches to compensating MAs. The first, is the modification of supports and materials involved in the skin-electrode interface, while the second implements models and algorithms for reducing MA contribution. The first approach is based on reducing skin-electrode discontinuity. It is achieved by cleaning or grazing the part of the skin in contact with the electrode and modifying material or form of the electrode itself [151, 152]. An example of the latter approach is the use of textile electrodes, which are made of conductive yarns integrated into textile substrates. They exhibit the advantage of having a bigger surface in contact with the skin than the standard electrodes decreasing the skin-electrode impedance. Moreover, textile electrodes offer a greater dynamical adaptation to anatomical profiles [151]. The second approach includes procedures and algorithms which aim at detecting and removing artifacts from the acquired signals. Several techniques have been used in biomedical applications compensate for MAs.

Filtering

Among these, one of the most used and effective is the adaptive filtering cancellation technique [153-155]. It uses a "primary" input containing the corrupted signal (signal with artifacts) and a "reference" input containing artifacts correlated in some unknown way with the primary noise [156]. This adaptive filtering adjusts its parameters automatically, requiring a little a priori knowledge of noise characteristics. More specifically, the reference input is derived from a noise field where the signal is weak or undetectable, and is subtracted from a primary input containing both signal and noise. In this way, the primary noise is attenuated or eliminated by cancellation. Successive implementations were then improved with the introduction of recursivity [157].

In [158] a simple and efficient normalized LMS algorithm is proposed for removal of noise from ECG signal that is suitable for application requiring large signal to noise ratio with less computationally complexity using simple addition and shift operation and achieves considerably speed-up over other LMS

based realization. In [133] block LMS algorithm is used to remove artifact preserving low frequency component of ECG. In [159] the problem of noise cancellation from ECG signal using error normalization-based adaptive filters, their block-based versions are proposed and tested on real signals with different artifacts obtained from the MIT-BIH database. For this, the input and the desired response signals are properly chosen in such a way that the filter output is the best least squared estimate of the original ECG signal. Among the six algorithms, the BB-ENSRLMS performs better than the other. From the simulated results, it is clear that these algorithms remove the artifacts efficiently present in the ECG signal In [155] an Adaptive Kalman Filter for ECG Signal Enhancement used, filter operates by sequentially estimating the measurement and process noise covariance and uses these covariance to estimate the Kalman gain and update the estimated ECG complexes.

Wavelet based Methods

The wavelet based methods are extensively used in pre-processing, denoising and analysis of ECG signals. In [160] DWT method is used to extract ECG parameters in a three-step processes: first, the low frequency components are removed using DWT transformation, second the noise in the signal is suppressed using the DWT based denoising techniques and finally ECG parameter are extracted. In [161] the morphology of ECG is used for classification of the ECG beats. To extract the shape related features from the ECG signal, three-level Daubechies-1 DWT is used after noise suppression in the ECG signal through a digital filter. After that principal component analysis and support vector machines are trained to formulate a classifier. In [162] undecimated wavelet transform was used for denoising ECG. In [163] spatial correlation filtering and stationary wavelet transform is proposed to eliminate the noise in ECG signal. The spatial correlation filtering is applied to shrink the wavelet coefficient, and the stationary wavelet transform used to decompose the noisy signal. In [164] stationary wavelet transform used to optimal denoise ECG signal in which signal to noise ratio is adjusted from 1 to 10 dB and result is evaluated by visual inspection then conclude using symlet4,decomposition at level5 and hard shrinkage function with empirical bayesian

threshold can get superior denoise performance. In [165] an integrated electrocardiogram (ECG) signal processing scheme is proposed. Using a systematic wavelet transform (WT) algorithm, this signal processing scheme can realize multiple functions in real-time, including baseline drift removal, noise suppression, QRS detection, heart beat rate (HBR) prediction & classification, and clean ECG reconstruction. In [166] wavelet-based denoising technique is investigated for suppressing EMG noise and motion artifact in ambulatory ECG. EMG noise is reduced by thresholding the wavelet coefficients using an improved thresholding function combining the features of hard and soft thresholding. Motion artifact is reduced by limiting the wavelet coefficients. Thresholds for both the denoising steps are estimated using the statistics of the noisy signal. Denoising of simulated noisy ECG signals resulted in an average SNR improvement of 11.4 dB, and its application on ambulatory ECG recordings resulted in L2 norm and max-min based improvement indices close to one. It significantly improved R-peak detection in both the cases.

Blind Source Separation Techniques

In [164] in the time domain the cardiac activity mean and the motion artifact noise of the ECG signal are modeled by Hermite polynomial expansion and principal component analysis, a set of time domain accelerometer feature is also extracted. A support vector machine is employed for supervised classification using these time domain feature, motivated by their potential for convolution noise, cepstral features extracted from ECG and accelerometer signals based on frame level analysis are modeled using Gaussian mixture models (GMM). To reduce dimension of tri-axial accelerometer cepstral features which are concatenated and fused at the feature level hetroscaedastic linear discrimination analysis is performed.

The ECG is analyzed beat-by-beat using a recursive principal component analysis (RPCA) based method in [140]. The RPCA based method can follow the slow changes in cardiac cycle, while detecting abrupt changes in motion artifact signal due to the transition to a different type of PA. The RPCA algorithm is useful for temporal segmentation of ECG beats with respect to the type of PA. In [167, 168] the separability of motion artifacts due to different types of PA is tested by classifying them automatically

based on the nature of PA. A principal component analysis (PCA) based method is used for supervised learning of the classifiers for the same purpose. It has also been observed in [169] that different pace levels of the PA have different impact on the generation of motion artifact in AECG. The RPCA based error signal is derived from ECG as an index of motion artifacts and also as a measure of impact of different pace levels on ECG, simply referred as an impact signal [169].

Moreover, other techniques such as independent component (ICA) analysis [149, 170-172] as well as Empirical Mode Decomposition (EMD) [173-175] have been explored.

2.2. Thesis Aims and Scope

In order to address the problem of motion and noise artifact in PPG and ECG vital signals we investigate the problem from different point of views and domains. In general the scope of the present study is to address the following aims:

Aim 1. Accurate and reliable HR estimations from ECG/PPG during movement and physical activities.

Aim 2. Accurate and reliable SpO_2 estimations from ECG/PPG during movement and physical activities.

Aim 3. Beat-to-Beat Heart Rate Estimations and being able to perform Heart Rate Variability Analysis from ECG/PPG during movement and physical activities.

Aim 4. Reconstruction of the ECG/PPG vital signs during movement and physical activities.

Aim 5. Being able to analyze the ECG/PPG recordings for detection of Atrial Fibrillation even during movement and physical activities.

Aim 6 Being able to implement the algorithms in real-time.

We categorize the application and scenario to address the challenges in the way of achieving the above aims and objectives as

(1) “Motion and Noise Corrupted Data Removal”, and

(2) “MA Corrupted Signal Usability Index Measurement” and

(3) “Motion and Noise Corrupted Data Reconstruction”.

(1) All of the above aims except number 4 can be met by removing the motion and noise corrupted segments of data if the information of vital signs during the period of motion and noise can be ignored. Any algorithm that is designed to estimate HR, Oxygen Saturation or to perform HRV analysis or detection of AF from ECG/PPG recordings might work properly as long as we analyze the segments of the data that is not corrupted by motion and noise artifacts. To this end, one might develop signal processing techniques to detect MA corrupted segments of recordings and disregard them in the next phase of the analysis. In this study we propose three techniques TDV, RepMa and RAFMA (chapters 3-5 of this thesis) that belong to this category of methods. TDV is a time-domain MA detection algorithm that can provide a clean versus corrupted decision on each successive PPG segment. Four time-domain parameters are computed: (1) standard deviation of peak-to-peak intervals (2) standard deviation of peak-to-peak amplitudes (3) standard deviation of systolic and diastolic interval ratios, and (4) mean standard deviation of pulse shape. A support vector machine (SVM) is adopted to automatically classify clean and corrupted data using the above four parameters. In Chapter 4, a new algorithm for MA detection based on recurrence quantification of PPG signal is presented. The idea is by using recurrence plots we convert the signal into a binary image that can be processed later for distortion and corruption. The algorithm runs on each 4 sec segments of the signal and the recurrence plot (image) of each segment is then preprocessed and analyzed to determine if the

segment is clean or corrupted by noise. The point is MAs change the signal recurrence behavior and makes irregular recurrence patterns that can be utilized to distinguish between clean and corrupted PPG segment. Next in Chapter 5, a novel MA detection and Atrial Fibrillation detection algorithm (RAFMA) for ECG signals is presented. The idea is to process the ECG time series in time-time domain by transforming the 1-D signal to a 2-D image using recurrence quantification and then to analyze the image for MNA detection and AF diagnosis. The discriminative features for MNA and AF detection will be more prominent in time-time domain and make it easier to find out when the ECG recordings are corrupted by or clean from movement and when AF episodes occur.

(2) However, removing the MA corrupted data is not desirable for most of the applications and eventually a more advanced algorithm might be needed. Sometimes a recording might be corrupted by motion and noise but the level of corruption is still can be tolerated for HR or SpO2 estimations, HRV analysis or AF detection. So the next idea that might come up is to investigate the corruption segment for its usability for HR/SpO2/HR/AF applications. In Chapter (8) of the thesis we propose a novel approach TifMA based on Time-frequency spectrum of PPG that has the potential to perform MA detection and also measures usability of the corrupted data for HR estimations. The term “usable” refers to those type of PPG data of which HR signal can be recovered accurately even if the signal is not free from MA. Two sequential classification procedures were included in TifMA algorithm. The first classifier detect between MNA corrupted and MNA free PPG data. Once a segment of data belong to MNA corrupted category, a new classifier is adopted to determine whether the HR can be recovered from the corrupted segment or not. Features from time-frequency spectrum of PPG were extracted to build the detection model.

(3) Finding out if a recording is corrupted by motion and noise artifact is one story, but reconstructing the corrupted information during movement and physical activities is a whole new story. Eventually, it is desired to recover the inaccurate information and estimations from a MA corrupted ECG/PPG signal. The rest of the present thesis (Chapters 6, 7 and 9-11) is dedicated to address the

reconstruction of vital signals during movement and physical activities. Depending on the target vital sign, the reconstruction algorithm can be designed differently.

In Chapters 6 and 7 we propose IMAR and DyParaM algorithms that are designed to reconstruct the PPG signal in time-domain. IMAR algorithm is based on an iterative motion artifact removal (IMAR) approach, which utilizes the singular spectral analysis (SSA) algorithm to reduce MNA artifacts so that more accurate estimates of uncorrupted heart rates (HR) and arterial oxygen saturation values (SpO2) values recorded by a pulse oximeter can be derived. In Chapter (7) a new tool (DyParaM) for modeling dynamics of photoplethysmogram (PPG) data is introduced. The idea is to use a nonlinear model to identify the clean PPG signal and then using the model to retrieve the PPG signal information from the MNA corrupted PPG readings from pulse oximeter. We propose two different regression models, one is Sinusoidal Frequency which utilizes sinusoids as the basis functions and the other model is Autoregressive model in which the basis function is the past historical values of the signal. The basis functions in both models are then projected onto sets of Legendre and Walsh functions in order to capture the nonstationary dynamics of the PPG signal. Time varying optimal search (TV-OPS) algorithm is then used to estimate the parameters of the proposed sinusoidal frequency and autoregressive models. Chapter (9) presents a new algorithm OxiMA based on time-frequency spectrum that can be used to reconstruct HR and SpO2 from PPG signals. The idea of OxiMA is to decompose the signal into its frequency components by using a complex demodulation based technique and choosing the components with frequencies close to the HR frequency for reconstructing the clean PPG signal. Next, SpO2 is estimated from the reconstructed PPG signal.

SpaMA and SegMA (Chapters 10 and 11) are the two algorithm mainly designed to reconstruct beat-to-beat HR values for HRV analysis from PPG and ECG respectively. The idea of SpaMA is to calculate power spectral density of both PPG and accelerometer signals for each time shift of a windowed data segment. By comparing time-varying spectra of PPG and accelerometer data, those frequency spectra belonging to the accelerometer can be distinguished from the PPG spectrum. By preserving the spectrum

of PPG and discarding that of the motion artifacts, the most dominant frequency component of the resulting spectrum in each window will represent HR and it will be extracted for each window segment.

In SegMA the idea is to calculate time-frequency spectrum of ECG for each time shift of a windowed data segment. By analyzing time-varying spectra of ECG and those frequency spectra belonging to the HR can be distinguished from the ECG spectrum. By preserving the spectra corresponds to highest power in the time-frequency spectrum, the most dominant frequency components of the resulting spectrum in each window will represent HR and it will be extracted for each window segment.

Finally Chapter 12 summarizes the main findings of this dissertation as well as the limitations and areas of future development and application of the methods proposed in this research.

Fig.5 illustrates the relation between the methods that presented in this study to the aims and scope of the present thesis.

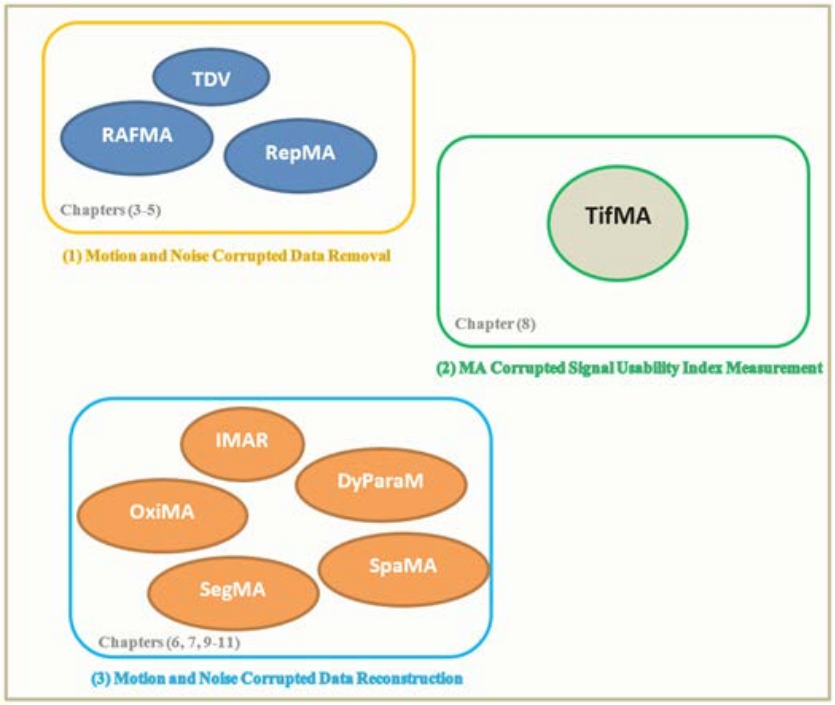

Figure 2.4 – Diagram of the methodology of this research.

References

1. Patel, S., et al., A review of wearable sensors and systems with application in rehabilitation. Journal of NeuroEngineering and Rehabilitation, 2012. 9(1): p. 1-17.
2. Wijshoff, R.W., et al., Reducing motion artifacts in photoplethysmograms by using relative sensor motion: phantom study. J Biomed Opt, 2012. 17(11): p. 117007.
3. P. A. Muennig and S. A. Glied, What Changes in Survival Rates Tell Us About U.S. Health Care. Health Affairs Web 2010. First.
4. Gulley, S.P., E.K. Rasch, and L. Chan, If we build it, who will come? Working-age adults with chronic health care needs and the medical home. Med Care, 2011. 49(2): p. 149-55.
5. Gulley, S.P., E.K. Rasch, and L. Chan, Ongoing coverage for ongoing care: access, utilization, and out-of-pocket spending among uninsured working-aged adults with chronic health care needs. Am J Public Health, 2011. 101(2): p. 368-75.
6. Goonewardene, S.S., et al., Road traffic collisions-case fatality rate, crash injury rate, and number of motor vehicles: time trends between a developed and developing country. Am Surg, 2010. 76(9): p. 977-81.
7. Organization, W.H. Active Aging a Policy Framework. Available from: http://www.who.int/ageing/publications/active_ageing/en/.
8. Kinsella, K.G., D.R. Phillips, and P.R. Bureau, Global Aging: The Challenge of Success. 2005: Population Reference Bureau.
9. Bray, H., National population projections, O.f.N. Statistics, Editor. 2008.
10. Axelrod, D.A., D. Millman, and M.M. Abecassis, US Health Care Reform and Transplantation. Part I: overview and impact on access and reimbursement in the private sector. Am J Transplant, 2010. 10(10): p. 2197-2202.
11. Teng, X.F., et al., Wearable medical systems for p-Health. IEEE Rev Biomed Eng, 2008. 1: p. 62-74.
12. Bonato, P., Wearable sensors and systems. From enabling technology to clinical applications. IEEE Eng Med Biol Mag, 2010. 29(3): p. 25-36.
13. Hamilton, P.S., et al. Comparison of methods for adaptive removal of motion artifact. in Computers in Cardiology 2000. 2000.
14. Caudill, T.S., et al., Commentary: Health care reform and primary care: training physicians for tomorrow's challenges. Acad Med, 2011. 86(2): p. 158-60.
15. Chan, L., L.G. Hart, and D.C. Goodman, Geographic access to health care for rural Medicare beneficiaries. J Rural Health, 2006. 22(2): p. 140-6.
16. DeVaul, R., et al., MIThril 2003: Applications and Architecture, in Proceedings of the 7th IEEE International Symposium on Wearable Computers. 2003, IEEE Computer Society. p. 4.
17. Raya, M.A.D. and L.G. Sison. Adaptive noise cancelling of motion artifact in stress ECG signals using accelerometer. in Engineering in Medicine and Biology, 2002. 24th Annual Conference and the Annual Fall Meeting of the Biomedical Engineering Society EMBS/BMES Conference, 2002. Proceedings of the Second Joint. 2002.
18. Jinyun, Z., et al., UWB Systems for Wireless Sensor Networks. Proceedings of the IEEE, 2009. 97(2): p. 313-331.
19. Yilmaz, T., R. Foster, and Y. Hao, Detecting Vital Signs with Wearable Wireless Sensors. Sensors, 2010.
20. Asada, H.H., et al., Mobile monitoring with wearable photoplethysmographic biosensors. IEEE Eng Med Biol Mag, 2003. 22(3): p. 28-40.
21. Shaltis, P.A., A. Reisner, and H.H. Asada, Wearable, cuff-less PPG-based blood pressure monitor with novel height sensor. Conf Proc IEEE Eng Med Biol Soc, 2006. 1: p. 908-11.

22. Corbishley, P. and E. Rodriguez-Villegas, Breathing Detection: Towards a Miniaturized, Wearable, Battery-Operated Monitoring System. Biomedical Engineering, IEEE Transactions on, 2008. 55(1): p. 196-204.
23. Barbaro, M., et al., Active devices based on organic semiconductors for wearable applications. IEEE Trans Inf Technol Biomed, 2010. 14(3): p. 758-66.
24. Patterson, J.A.C., D.G. McIlwraith, and Y. Guang-Zhong. A Flexible, Low Noise Reflective PPG Sensor Platform for Ear-Worn Heart Rate Monitoring. in Wearable and Implantable Body Sensor Networks, 2009. BSN 2009. Sixth International Workshop on. 2009.
25. Yan, Y.S. and Y.T. Zhang, An efficient motion-resistant method for wearable pulse oximeter. IEEE Trans Inf Technol Biomed, 2008. 12(3): p. 399-405.
26. Wood, L.B. and H. Asada, Low variance adaptive filter for cancelling motion artifact in wearable photoplethysmogram sensor signals. Conf Proc IEEE Eng Med Biol Soc, 2007. 2007: p. 652-5.
27. Merilahti, J., et al., Compliance and technical feasibility of long-term health monitoring with wearable and ambient technologies. J Telemed Telecare, 2009. 15(6): p. 302-9.
28. Sciacqua, A., et al. Validation of a flexible and innovative platform for the home monitoring of heart failure patients: Preliminary results. in Computers in Cardiology, 2009. 2009.
29. Mundt, C.W., et al., A multiparameter wearable physiologic monitoring system for space and terrestrial applications. IEEE Trans Inf Technol Biomed, 2005. 9(3): p. 382-91.
30. Anliker, U., et al., AMON: a wearable multiparameter medical monitoring and alert system. IEEE Trans Inf Technol Biomed, 2004. 8(4): p. 415-27.
31. Habetha, J., The MyHeart project--fighting cardiovascular diseases by prevention and early diagnosis. Conf Proc IEEE Eng Med Biol Soc, 2006. Suppl: p. 6746-9.
32. Paradiso, R. Wearable health care system for vital signs monitoring. in Information Technology Applications in Biomedicine, 2003. 4th International IEEE EMBS Special Topic Conference on. 2003.
33. Di Rienzo, M., et al., MagIC System: a New Textile-Based Wearable Device for Biological Signal Monitoring. Applicability in Daily Life and Clinical Setting. Conf Proc IEEE Eng Med Biol Soc, 2005. 7: p. 7167-9.
34. Samsung. Simband. Available from: https://www.simband.io/.
35. Reyes, B.A., et al., Novel electrodes for underwater ECG monitoring. IEEE Trans Biomed Eng, 2014. 61(6): p. 1863-76.
36. AlertOne medical alert system.
37. Automatic Fall Detection. Available from: http://www.wellcore.com/learn/automatic-falldetection.
38. myHalo.
39. BrickHouse. Available from: http://www.brickhousealert.com/personal-emergency-medicalalarm.html.
40. EASY WORLS. Available from: http://www.ttmmonaco.com/en/default.htm.
41. USC Rehabilitation Engineering Research Center. Available from: http://www.isi.edu/research/rerc.
42. Rizzo, A., et al., Virtual reality applications for addressing the needs of those aging with disability. Stud Health Technol Inform, 2011. 163: p. 510-6.
43. Vincent, C., et al., Rehabilitation needs for older adults with stroke living at home: perceptions of four populations. BMC Geriatr, 2007. 7: p. 20.
44. Uswatte, G., et al., Ambulatory monitoring of arm movement using accelerometry: an objective measure of upper-extremity rehabilitation in persons with chronic stroke. Arch Phys Med Rehabil, 2005. 86(7): p. 1498-501.
45. Uswatte, G., et al., Validity of accelerometry for monitoring real-world arm activity in patients with subacute stroke: evidence from the extremity constraint-induced therapy evaluation trial. Arch Phys Med Rehabil, 2006. 87(10): p. 1340-5.

46. Patel, S., et al., A review of wearable sensors and systems with application in rehabilitation. J Neuroeng Rehabil, 2012. 9: p. 21.
47. Heeringa, J., et al., Prevalence, incidence and lifetime risk of atrial fibrillation: the Rotterdam study. European Heart Journal, 2006. 27(8): p. 949-953.
48. Benjamin, E.J., et al., Impact of atrial fibrillation on the risk of death: the Framingham Heart Study. Circulation, 1998. 98(10): p. 946-52.
49. Wolf, P.A., R.D. Abbott, and W.B. Kannel, Atrial fibrillation as an independent risk factor for stroke: the Framingham Study. Stroke, 1991. 22(8): p. 983-8.
50. Humphries, K.H., et al., New-onset atrial fibrillation: sex differences in presentation, treatment, and outcome. Circulation, 2001. 103(19): p. 2365-70.
51. Kerr, C., et al., Follow-up of atrial fibrillation: The initial experience of the Canadian Registry of Atrial Fibrillation. Eur Heart J, 1996. 17 Suppl C: p. 48-51.
52. Kinlay, S., et al., Cardiac event recorders yield more diagnoses and are more cost-effective than 48-hour Holter monitoring in patients with palpitations. A controlled clinical trial. Ann Intern Med, 1996. 124(1 Pt 1): p. 16-20.
53. Roche, F., et al., Frequent and prolonged asymptomatic episodes of paroxysmal atrial fibrillation revealed by automatic long-term event recorders in patients with a negative 24-hour Holter. Pacing Clin Electrophysiol, 2002. 25(11): p. 1587-93.
54. Benjamin, E.J., et al., Prevention of atrial fibrillation: report from a national heart, lung, and blood institute workshop. Circulation, 2009. 119(4): p. 606-18.
55. Defaye, P., F. Dournaux, and E. Mouton, Prevalence of supraventricular arrhythmias from the automated analysis of data stored in the DDD pacemakers of 617 patients: the AIDA study. The AIDA Multicenter Study Group. Automatic Interpretation for Diagnosis Assistance. Pacing Clin Electrophysiol, 1998. 21(1 Pt 2): p. 250-5.
56. Electrocardiogram. Available from: http://www.emedicinehealth.com/electrocardiogram_ecg/article_em.htm.
57. ECG Features. Available from: http://www.davita-shop.co.uk/ecg-instruments.html.
58. Oweis, R.J. and B.O. Al-Tabbaa, QRS Detection and Heart Rate Variability Analysis: A Survey. Biomedical Science and Engineering, 2014. 2(1): p. 13-34.
59. Pahlm, O. and L. Sornmo, Software QRS detection in ambulatory monitoring--a review. Med Biol Eng Comput, 1984. 22(4): p. 289-97.
60. Kleinmuntz, B., Diagnostic problem solving by computer: a historical review and the current state of the science. Comput Biol Med, 1984. 14(3): p. 255-70.
61. Skordalakis, E., Syntactic ECG processing: a review. Pattern Recogn., 1986. 19(4): p. 305-313.
62. Kundu, M., M. Nasipuri, and D. Kumar Basu, Knowledge-based ECG interpretation: a critical review. Pattern Recognition, 2000. 33(3): p. 351-373.
63. Chan, M., et al., A review of smart homes-Present state and future challenges. Comput. Methods Prog. Biomed., 2008. 91(1): p. 55-81.
64. Alemdar, H. and C. Ersoy, Wireless sensor networks for healthcare: A survey. Computer Networks, 2010. 54(15): p. 2688-2710.
65. Lin, C.-F., Mobile Telemedicine: A Survey Study. Journal of Medical Systems, 2012. 36(2): p. 511-520.
66. Paul, S.A., Wavelet transforms and the ECG: a review. Physiological Measurement, 2005. 26(5): p. R155.
67. Davenport, C., et al., Assessing the diagnostic test accuracy of natriuretic peptides and ECG in the diagnosis of left ventricular systolic dysfunction: a systematic review and meta-analysis. Br J Gen Pract, 2006. 56(522): p. 48-56.
68. Poli, S., et al., Prediction of atrial fibrillation from surface ECG: review of methods and algorithms. Ann Ist Super Sanita, 2003. 39(2): p. 195-203.

69. Baig, M.M., H. Gholamhosseini, and M.J. Connolly, A comprehensive survey of wearable and wireless ECG monitoring systems for older adults. Med Biol Eng Comput, 2013. 51(5): p. 485-95.
70. Lee, Y.-D. and W.-Y. Chung, Wireless sensor network based wearable smart shirt for ubiquitous health and activity monitoring. Sensors and Actuators B: Chemical, 2009. 140(2): p. 390-395.
71. Bianchi, A.M., M.O. Mendez, and S. Cerutti, Processing of signals recorded through smart devices: sleep-quality assessment. IEEE Trans Inf Technol Biomed, 2010. 14(3): p. 741-7.
72. Lopez, G., V. Custodio, and J.I. Moreno, LOBIN: E-textile and wireless-sensor-network-based platform for healthcare monitoring in future hospital environments. IEEE Trans Inf Technol Biomed, 2010. 14(6): p. 1446-58.
73. Buttussi, F. and L. Chittaro, MOPET: a context-aware and user-adaptive wearable system for fitness training. Artif Intell Med, 2008. 42(2): p. 153-63.
74. Pollonini, L., et al., A novel handheld device for use in remote patient monitoring of heart failure patients--design and preliminary validation on healthy subjects. J Med Syst, 2012. 36(2): p. 653-9.
75. Heilman, K.J., et al., Accuracy of the StressEraser in the detection of cardiac rhythms. Appl Psychophysiol Biofeedback, 2008. 33(2): p. 83-9.
76. Pandian, P.S., et al., Smart Vest: wearable multi-parameter remote physiological monitoring system. Med Eng Phys, 2008. 30(4): p. 466-77.
77. Yazicioglu, R.F., et al., Ultra-low-power wearable biopotential sensor nodes. Conf Proc IEEE Eng Med Biol Soc, 2009. 2009: p. 3205-8.
78. J Penders, J.v.d.M., M Altini, F Yazicioglu, C Van Hoof. A low-power wireless ECG necklace for reliable cardiac activity monitoring on-the-move. in Proceedings of the International Conference of the IEEE Engineering in Medicine and Biology Society. 2011.
79. Tamura, T.M., Y.; Sekine, M.; Yoshida, M., Wearable Photoplethysmographic Sensors—Past and Present. Electronics, 2014. 3(2): p. 282-302.
80. Jubran, A., Pulse oximetry. Intensive Care Med, 2004. 30(11): p. 2017-20.
81. Tilakaratna, P., How pulse oximeters work explained simply.
82. Zhu, Z., et al., Continuous oxygen monitoring--a better way to prescribe long-term oxygen therapy. Respir Med, 2005. 99(11): p. 1386-92.
83. Barratt, C.W., et al., Detection of previously unrecognized daytime desaturation in children with chronic lung disease. J Med Eng Technol, 2007. 31(2): p. 101-8.
84. Cutaia, M., Ambulatory Monitoring of Oxygen Saturation in Chronic Lung Disease: Optimizing Long-Term Oxygen Therapy. Clinical Pulmonary Medicine, 2002. 9(6): p. 297-305.
85. Lu, S., et al., Can photoplethysmography variability serve as an alternative approach to obtain heart rate variability information? J Clin Monit Comput, 2008. 22(1): p. 23-9.
86. Lu, G., et al., A comparison of photoplethysmography and ECG recording to analyse heart rate variability in healthy subjects. J Med Eng Technol, 2009. 33(8): p. 634-41.
87. Hon, E.H. and S.T. Lee, ELECTRONIC EVALUATION OF THE FETAL HEART RATE. VIII. PATTERNS PRECEDING FETAL DEATH, FURTHER OBSERVATIONS. Am J Obstet Gynecol, 1963. 87: p. 814-26.
88. Ewing, D.J., et al., The value of cardiovascular autonomic function tests: 10 years experience in diabetes. Diabetes Care, 1985. 8(5): p. 491-8.
89. Tulen, J.H., et al., Sleep patterns and blood pressure variability in patients with pure autonomic failure. Clin Auton Res, 1991. 1(4): p. 309-15.
90. Guzzetti, S., et al., Different spectral components of 24 h heart rate variability are related to different modes of death in chronic heart failure. Eur Heart J, 2005. 26(4): p. 357-62.
91. Chattipakorn, N., et al., Heart rate variability in myocardial infarction and heart failure. International Journal of Cardiology, 2007. 120(3): p. 289-296.

92. de Boer, R.W., J.M. Karemaker, and J. Strackee, Relationships between short-term blood-pressure fluctuations and heart-rate variability in resting subjects. I: A spectral analysis approach. Med Biol Eng Comput, 1985. 23(4): p. 352-8.
93. Pfeifer, M.A., et al., Quantitative evaluation of cardiac parasympathetic activity in normal and diabetic man. Diabetes, 1982. 31(4 Pt 1): p. 339-45.
94. Singh, J.P., et al., Association of hyperglycemia with reduced heart rate variability (The Framingham Heart Study). Am J Cardiol, 2000. 86(3): p. 309-12.
95. Wheeler, T. and P.J. Watkins, Cardiac Denervation in Diabetes. British Medical Journal, 1973. 4(5892): p. 584-586.
96. Chan, C.T., et al., Effects of daily hemodialysis on heart rate variability: results from the Frequent Hemodialysis Network (FHN) Daily Trial. Nephrol Dial Transplant, 2014. 29(1): p. 168-78.
97. Zoccali, C., M. Ciccarelli, and Q. Maggiore, Defective reflex control of heart rate in dialysis patients: evidence for an afferent autonomic lesion. Clin Sci (Lond), 1982. 63(3): p. 285-92.
98. Hertzman, A.B., The Blood Supply of Various Skin Areas as Estimated by the Photoelectric Plethysmograph. 1938.
99. Rhee, S., B.H. Yang, and H.H. Asada, Artifact-resistant power-efficient design of finger-ring plethysmographic sensors. IEEE Trans Biomed Eng, 2001. 48(7): p. 795-805.
100. Jung, J.Y. and J.W. Lee. ZigBee Device Access Control and Reliable Data Transmission in ZigBee Based Health Monitoring System. in Advanced Communication Technology, 2008. ICACT 2008. 10th International Conference on. 2008.
101. Yongkwi, L., et al. Development of a wristwatch-type PPG array sensor module. in Consumer Electronics - Berlin (ICCE-Berlin), 2011 IEEE International Conference on. 2011.
102. Maeda, Y., M. Sekine, and T. Tamura, Relationship between measurement site and motion artifacts in wearable reflected photoplethysmography. J Med Syst, 2011. 35(5): p. 969-76.
103. Vogel, S., et al., In-ear vital signs monitoring using a novel microoptic reflective sensor. IEEE Trans Inf Technol Biomed, 2009. 13(6): p. 882-9.
104. Shin, K., et al., A Novel Headset with a Transmissive PPG Sensor for Heart Rate Measurement, in 13th International Conference on Biomedical Engineering, C. Lim and J.H. Goh, Editors. 2009, Springer Berlin Heidelberg. p. 519-522.
105. Poh, M.-Z., N.C. Swenson, and R.W. Picard, Motion-tolerant magnetic earring sensor and wireless earpiece for wearable photoplethysmography. Trans. Info. Tech. Biomed., 2010. 14(3): p. 786-794.
106. Ming-Zher, P., et al., Cardiovascular Monitoring Using Earphones and a Mobile Device. Pervasive Computing, IEEE, 2012. 11(4): p. 18-26.
107. Kyriacou, P.A., et al., A system for investigating oesophageal photoplethysmographic signals in anaesthetised patients. Med Biol Eng Comput, 1999. 37(5): p. 639-43.
108. Kyriacou, P.A., et al., Esophageal pulse oximetry utilizing reflectance photoplethysmography. IEEE Trans Biomed Eng, 2002. 49(11): p. 1360-8.
109. Kyriacou, P.A., Direct pulse oximetry within the esophagus, on the surface of abdominal viscera, and on free flaps. Anesth Analg, 2013. 117(4): p. 824-33.
110. Mendelson, Y. and C. Pujary. Measurement site and photodetector size considerations in optimizing power consumption of a wearable reflectance pulse oximeter. in Engineering in Medicine and Biology Society, 2003. Proceedings of the 25th Annual International Conference of the IEEE. 2003.
111. Lee, E.M., et al. Glass-type wireless PPG measuring system. in Engineering in Medicine and Biology Society (EMBC), 2010 Annual International Conference of the IEEE. 2010.
112. Tur, E., et al., Basal Perfusion of the Cutaneous Microcirculation: Measurements as a Function of Anatomic Position. J Investig Dermatol, 1983. 81(5): p. 442-446.
113. Dresher, R.M., Y. . Attachment of a wearable skin reflectance pulse oximeter. in In Proceedings of the 2005 BMES Annual Fall Meeting. 2005. Baltimore, MD, USA.

114. Lee, H.-W.L., J.-W.; Jung, W.-C.; Lee, G.-K. , The periodic moving average filter for removing motion artifacts from PPG signals. Int. J. Ctrl. Autom. Syst. , 2007. 5: p. 701-706.
115. Lee, J., et al., Design of filter to reject motion artifact of pulse oximetry. Computer Standards & Interfaces, 2004. 26(3): p. 241-249.
116. Harry Asada, H., H.H. Jiang, and P. Gibbs, Active noise cancellation using MEMS accelerometers for motion-tolerant wearable bio-sensors. Conf Proc IEEE Eng Med Biol Soc, 2004. 3: p. 2157-60.
117. Lee, B., et al., Adaptive comb filtering for motion artifact reduction from PPG with a structure of adaptive lattice IIR notch filter. Conf Proc IEEE Eng Med Biol Soc, 2011. 2011: p. 7937-40.
118. Chan, K.W. and Y.T. Zhang. Adaptive reduction of motion artifact from photoplethysmographic recordings using a variable step-size LMS filter. in Sensors, 2002. Proceedings of IEEE. 2002.
119. Han, H., M.J. Kim, and J. Kim, Development of real-time motion artifact reduction algorithm for a wearable photoplethysmography. Conf Proc IEEE Eng Med Biol Soc, 2007. 2007: p. 1538-41.
120. Wood, L. and I.o.T. Massachusetts, Motion Artifact Reduction for Wearable Photoplethysmogram Sensors Using Micro Accelerometers and Laguerre Series Adaptive Filters. 2008.
121. Jutten, C. and P. Comon, Chapter 1 - Introduction, in Handbook of Blind Source Separation, P. Comon and C. Jutten, Editors. 2010, Academic Press: Oxford. p. 1-22.
122. Yao, J. and S. Warren, A short study to assess the potential of independent component analysis for motion artifact separation in wearable pulse oximeter signals. Conf Proc IEEE Eng Med Biol Soc, 2005. 4: p. 3585-8.
123. Kim, B.S. and S.K. Yoo, Motion artifact reduction in photoplethysmography using independent component analysis. IEEE Trans Biomed Eng, 2006. 53(3): p. 566-8.
124. Wood, L. and H. Harry Asada, Active motion artifact reduction for wearable sensors using laguerre expansion and signal separation. Conf Proc IEEE Eng Med Biol Soc, 2005. 4: p. 3571-4.
125. Lee, C.M. and Y.T. Zhang. Reduction of motion artifacts from photoplethysmographic recordings using a wavelet denoising approach. in Biomedical Engineering, 2003. IEEE EMBS Asian-Pacific Conference on. 2003.
126. Yan, Y.S., C.C. Poon, and Y.T. Zhang, Reduction of motion artifact in pulse oximetry by smoothed pseudo Wigner-Ville distribution. J Neuroeng Rehabil, 2005. 2(1): p. 3.
127. Chon, K.H., S. Dash, and J. Kihwan, Estimation of Respiratory Rate From Photoplethysmogram Data Using Time–Frequency Spectral Estimation. Biomedical Engineering, IEEE Transactions on, 2009. 56(8): p. 2054-2063.
128. Baumgartner, C., et al., Discussion of "time-frequency techniques in biomedical signal analysis: a tutorial review of similarities and differences". Methods Inf Med, 2013. 52(4): p. 297-307.
129. Zhilin, Z., P. Zhouyue, and L. Benyuan, TROIKA: A General Framework for Heart Rate Monitoring Using Wrist-Type Photoplethysmographic Signals During Intensive Physical Exercise. Biomedical Engineering, IEEE Transactions on, 2015. 62(2): p. 522-531.
130. Zhang, Z., Photoplethysmography-Based Heart Rate Monitoring in Physical Activities via Joint Sparse Spectrum Reconstruction. Biomedical Engineering, IEEE Transactions on, 2015. PP(99): p. 1-1.
131. Gardner, T.J. and M.O. Magnasco, Sparse time-frequency representations. Proceedings of the National Academy of Sciences, 2006. 103(16): p. 6094-6099.
132. Aase, S.O., et al., CPR artifact removal from human ECG using optimal multichannel filtering. IEEE Trans Biomed Eng, 2000. 47(11): p. 1440-9.
133. Rahman, M.Z.U., R.A. Shaik, and D.V.R.K. Reddy. Adaptive noise removal in the ECG using the Block LMS algorithm. in Adaptive Science & Technology, 2009. ICAST 2009. 2nd International Conference on. 2009.
134. Deepu, C.J., et al. An ECG-on-Chip for Wearable Cardiac Monitoring Devices. in Electronic Design, Test and Application, 2010. DELTA '10. Fifth IEEE International Symposium on. 2010.

135. Zito, D., et al., Feasibility Study and Design of a Wearable System-on-a-Chip Pulse Radar for Contactless Cardiopulmonary Monitoring. Int J Telemed Appl, 2008: p. 328597.
136. Lanata, A., E.P. Scilingo, and D. De Rossi, A Multimodal Transducer for Cardiopulmonary Activity Monitoring in Emergency. Information Technology in Biomedicine, IEEE Transactions on, 2010. 14(3): p. 817-825.
137. Webster, J.G. and J.W. Clark, Medical Instrumentation: Application and Design. 1995: Wiley.
138. Thakor N, W.J. The origin of skin potential and its variations. in In: Proc. Ann. Conf. Eng. Biol. Med. 1987.
139. de Talhouet H, W.J., The origin of skin-stretch-caused motion artifacts under electrodes. Physiological Measurement, 1996. 17(2).
140. Chaudhuri, S., T.D. Pawar, and S. Duttagupta, Ambulation Analysis in Wearable ECG. 2010: Springer US.
141. Yunfeng, W. and R.M. Rangayyan. An Algorithm for Evaluating the Performance of Adaptive Filters for the Removal of Artifacts in ECG Signals. in Electrical and Computer Engineering, 2007. CCECE 2007. Canadian Conference on. 2007.
142. Shoker, L., S. Sanei, and J. Chambers, Artifact removal from electroencephalograms using a hybrid BSS-SVM algorithm. Signal Processing Letters, IEEE, 2005. 12(10): p. 721-724.
143. Velazquez, R. An optimal adaptive filtering approach for stress-tests motion artifacts removal: application on an ECG for telediagnosis. in Signal Processing, 2002 6th International Conference on. 2002.
144. Hedley, M. and H. Yan, Motion artifact suppression: a review of post-processing techniques. Magn Reson Imaging, 1992. 10(4): p. 627-35.
145. Greco, A., et al., On the deconvolution analysis of electrodermal activity in bipolar patients. Conf Proc IEEE Eng Med Biol Soc, 2012. 2012: p. 6691-4.
146. Lanata, A., et al., How the Autonomic Nervous System and Driving Style Change With Incremental Stressing Conditions During Simulated Driving. Intelligent Transportation Systems, IEEE Transactions on, 2015. 16(3): p. 1505-1517.
147. Serteyn, A., et al., Using an injection signal to reduce motion artifacts in capacitive ECG measurements. Conf Proc IEEE Eng Med Biol Soc, 2013. 2013: p. 4795-8.
148. Lim, Y.G., K.K. Kim, and K.S. Park, ECG recording on a bed during sleep without direct skin-contact. IEEE Trans Biomed Eng, 2007. 54(4): p. 718-25.
149. Sameni, R., C. Jutten, and M.B. Shamsollahi, Multichannel electrocardiogram decomposition using periodic component analysis. IEEE Trans Biomed Eng, 2008. 55(8): p. 1935-40.
150. Sameni, R. and G.D. Clifford, A Review of Fetal ECG Signal Processing; Issues and Promising Directions. Open Pacing Electrophysiol Ther J, 2010. 3: p. 4-20.
151. Tam, H.W. and J.G. Webster, Minimizing electrode motion artifact by skin abrasion. IEEE Trans Biomed Eng, 1977. 24(2): p. 134-9.
152. Burbank, D.P. and J.G. Webster, Reducing skin potential motion artefact by skin abrasion. Med Biol Eng Comput, 1978. 16(1): p. 31-8.
153. Yelderman, M., et al., ECG enhancement by adaptive cancellation of electrosurgical interference. IEEE Trans Biomed Eng, 1983. 30(7): p. 392-8.
154. Ferrara, E.R. and B. Widrow, Fetal electrocardiogram enhancement by time-sequenced adaptive filtering. IEEE Trans Biomed Eng, 1982. 29(6): p. 458-60.
155. Vullings, R., B. de Vries, and J.W. Bergmans, An adaptive Kalman filter for ECG signal enhancement. IEEE Trans Biomed Eng, 2011. 58(4): p. 1094-103.
156. Widrow, B., et al., Adaptive noise cancelling: Principles and applications. Proceedings of the IEEE, 1975. 63(12): p. 1692-1716.
157. Thakor, N.V. and Y.S. Zhu, Applications of adaptive filtering to ECG analysis: noise cancellation and arrhythmia detection. IEEE Trans Biomed Eng, 1991. 38(8): p. 785-94.

158. Rahman, M.Z.U., R.A. Shaik, and D.V.R.K. Reddy. Noise cancellation in ECG signals using normalized Sign-Sign LMS algorithm. in Signal Processing and Information Technology (ISSPIT), 2009 IEEE International Symposium on. 2009.
159. Rahman, M.Z.U., R.A. Shaik, and D.V.R.K. Reddy, Efficient and Simplified Adaptive Noise Cancelers for ECG Sensor Based Remote Health Monitoring. Sensors Journal, IEEE, 2012. 12(3): p. 566-573.
160. Elbuni, A., et al. ECG Parameter Extraction Algorithm using (DWTAE) Algorithm. in Computer Technology and Development, 2009. ICCTD '09. International Conference on. 2009.
161. Thanapatay, D., C. Suwansaroj, and C. Thanawattano. ECG beat classification method for ECG printout with Principle Components Analysis and Support Vector Machines. in Electronics and Information Engineering (ICEIE), 2010 International Conference On. 2010.
162. Akshay, N., et al. ECG noise removal and QRS complex detection using UWT. in Electronics and Information Engineering (ICEIE), 2010 International Conference On. 2010.
163. Wentao, S. and Z. Dan. Noise reduction of ECG using spatial correlation filtering and stationary wavelet transform. in Computer Science and Education (ICCSE), 2010 5th International Conference on. 2010.
164. Suyi, L. and L. Jun. The Optimal De-noising Algorithm for ECG Using Stationary Wavelet Transform. in Computer Science and Information Engineering, 2009 WRI World Congress on. 2009.
165. Liu, X., et al., Multiple Functional ECG Signal is Processing for Wearable Applications of Long-Term Cardiac Monitoring. Biomedical Engineering, IEEE Transactions on, 2011. 58(2): p. 380-389.
166. Mithun, P., et al. A wavelet based technique for suppression of EMG noise and motion artifact in ambulatory ECG. in Engineering in Medicine and Biology Society, EMBC, 2011 Annual International Conference of the IEEE. 2011.
167. Pawar, T., S. Chaudhuri, and S.P. Duttagupta. Analysis of Ambulatory ECG Signal. in Engineering in Medicine and Biology Society, 2006. EMBS '06. 28th Annual International Conference of the IEEE. 2006.
168. Pawar, T., S. Chaudhuri, and S.P. Duttagupta, Body Movement Activity Recognition for Ambulatory Cardiac Monitoring. Biomedical Engineering, IEEE Transactions on, 2007. 54(5): p. 874-882.
169. Pawar, T., et al., Impact analysis of body movement in ambulatory ECG. Conf Proc IEEE Eng Med Biol Soc, 2007. 2007: p. 5453-6.
170. Barros, A.K., A. Mansour, and N. Ohnishi, Removing artifacts from electrocardiographic signals using independent components analysis. Neurocomputing, 1998. 22(1–3): p. 173-186.
171. Milanesi, M., et al., Independent component analysis applied to the removal of motion artifacts from electrocardiographic signals. Med Biol Eng Comput, 2008. 46(3): p. 251-61.
172. Chawla, M.P.S., PCA and ICA processing methods for removal of artifacts and noise in electrocardiograms: A survey and comparison. Applied Soft Computing, 2011. 11(2): p. 2216-2226.
173. Lee, J., et al., Automatic motion and noise artifact detection in Holter ECG data using empirical mode decomposition and statistical approaches. IEEE Trans Biomed Eng, 2012. 59(6): p. 1499-506.
174. Chang, K.M., Arrhythmia ECG noise reduction by ensemble empirical mode decomposition. Sensors (Basel), 2010. 10(6): p. 6063-80.
175. Maji, U., M. Mitra, and S. Pal, Automatic Detection of Atrial Fibrillation Using Empirical Mode Decomposition and Statistical Approach. Procedia Technology, 2013. 10: p. 45-52.

Chapter 3: TDV – A Time-Domain Motion and Noise Artifact Detection Algorithm

3.1. Introduction

In this chapter, we propose an accurate and comprehensive MNA detection algorithm which detects MNA in PPG under various types of motion. We first introduce time-domain parameters quantifying MNA in the recorded PPG signal. We then consider their statistical measures as input variables for a machine learning-based MNA detection algorithm. Our MNA detection algorithm is self-trained by the SVM with clean and corrupted PPG data sets, and then the trained SVM tests the unknown PPG data. We tested the efficacy of our proposed algorithm on PPG data sets recorded from the finger and forehead pulse oximeters in simulations, laboratory-controlled and walking/stair-climbing experiments, respectively.

3.2. Materials and Method

3.2.1. Experimental Protocol and Preprocessing

PPG signals were obtained from custom reflectance-mode prototype pulse oximeters. PPG data with laboratory-controlled head and finger movement, daily-activity movement, or simulated movement were collected respectively from healthy subjects recruited from the student community of Worcester Polytechnic Institute (WPI). This study was approved by WPI's IRB and all subjects were given informed consent prior to data recording.

In laboratory-controlled head movement data, motion artifacts were induced by head movements for specific time intervals in both horizontal and vertical directions. 11 healthy volunteers were asked to wear a forehead reflectance pulse oximeter along with a reference Masimo Radical (Masimo SET®, Masimo Corporation, CA, USA) finger type transmittance pulse oximeter. After baseline recording for 5 minutes without any movement, subjects were instructed to introduce motion artifacts for specific time intervals varying from 10 to 50% within a 1 minute segment as shown in Fig. 1a. For example, if a subject

was instructed to perform left-right movements for 6 seconds, an 1 min segment of data would contain 10% noise. MNA amplitudes varied for each subject as shown in Fig. 1b. Specifically, mean amplitude ratios the deviation ratios (between 75th mean and 25th percentile values) between corrupted and clean signals are in the ranges of [0.9935 3.0092] and [1.3375 11.1250], respectively. The right middle finger with the sensor attached to the Masimo pulse oximeter was kept stationary. HR and SpO2 signals were acquired by the Masimo pulse oximeter at 80Hz and 1Hz, respectively, and were acquired synchronously with the PPG signals recorded from the forehead sensor.

In laboratory-controlled finger movement data, motion artifacts were induced by left-right movements of the index finger. 9 healthy volunteers were asked to sit and wear two reflection type PPG pulse oximeters (TSD200, BIOPAC Systems Inc., CA, USA) on their index and middle fingers, respectively. After baseline recording for 5 minutes without any movement to acquire clean data, motion artifacts were induced by left-right movements of the index finger while the middle finger was kept stationary as a reference.

Similar to the head movement data, motion was induced at specific time intervals corresponding to 10-50% duration in a 1 minute segment. Such controlled movement was repeated five times per subject. MNA amplitudes are varied for each subject as shown in Fig. 1c. Mean amplitude ratios and deviation ratios (between 75th mean and 25th percentile values) between corrupted and clean signals are in the range of [0.9360 4.0226] and [1.3892 32.2647], respectively. The pulse oximeters were connected to a biopotential amplifier (PPG100, BIOPAC Systems Inc., CA, USA) having a gain of 100 and cut-off frequencies of 0.05-10Hz. The MP1000 (BIOPAC Systems Inc., CA, USA) was used to acquire finger PPG signals at 100 Hz.

The daily-activity movement PPG data were recorded while subjects were walking straight or climbing stairs for 45 min. 9 subjects were asked to walk or climb stairs after wearing a forehead reflectance

pulse oximeter along with a Holter electrocardiogram (ECG) monitor (Rozinn RZ153+, Rozinn Electronics, Inc., NY, USA) at 180Hz and a Masimo Rad-57 pulse oximeter (Masimo Corporation, CA, USA)at 0.5Hz.

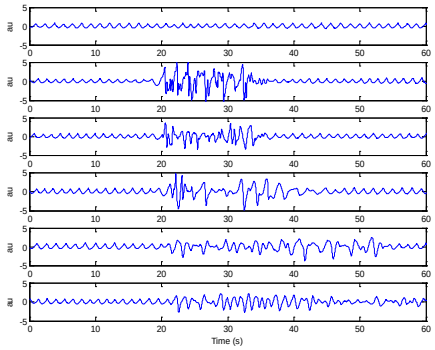

(a)

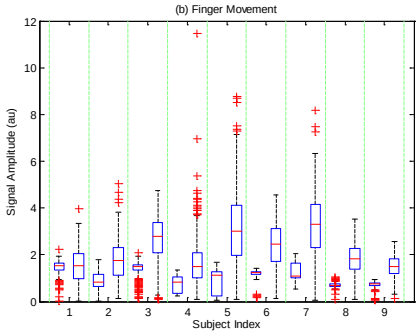

(b)

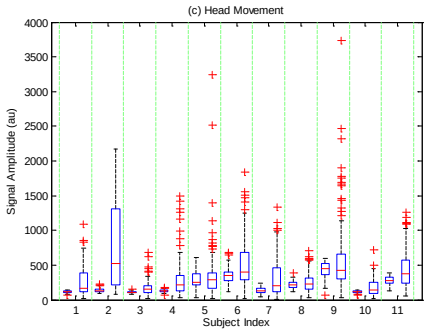

(c)

Figure 0.1 - PPG signals recorded during voluntary motion artifact conducted in a laboratory setting. (a) A representative clean forehead-PPG signal recorded during voluntary motion artifact conducted in a laboratory setting (1st row). The mixed (up-down and left-right) movement of the forehead to which the PPG probe was attached for predetermined time interval induced 10% to 50% noise (2nd – 6th row) within a 60s PPG segment (b) amplitudes of clean (left) and MNA-corrupted (right) finger-PPG signals of 9 subjects, and (c) amplitudes of clean (left) and MNA-corrupted (right) forehead-PPG signals of 11 subjects. The central line on each box corresponds to the median; the edges of the box correspond to the 25th and 75th percentiles, the whiskers extend to the most extreme data points not considered as outliers, and outliers are plotted individually.

The reference ECG was obtained from the Holter ECG monitor while HR and SpO2 readings were measured from the Masimo pulse oximeter connected to the subject's right index finger, which was held against the chest to minimize motion artifacts. Finally, the simulation movement PPG data were generated by the addition of white noise to the clean PPG data. PPG data were preprocessed by a 6th order infinite impulse response (IIR) band pass filter with cut-off frequencies of 0.5 Hz and 12Hz. Zero-phase forward and reverse filtering was applied to account for the non-linear phase of the IIR filter. After these preprocessing, the following parameters for classifying clean and corruption were derived.

3.2.2. Parameters from PPG Signals

Motion corrupted PPG signals are observed to have noticeably different pulse amplitudes, pulse widths and trough depth differences compared to clean PPG signals [193]. Moreover, morphology and amplitude ratios of corrupted PPG signals differ from those of clean ones. It was found that some PPG signals show strong similarity among good pulses, but large variation among successive poor and bad quality pulses [193]. Based on our observations on measured clean/corrupted PPG signals in Fig. 1 as well as above previous research results, we consider pulse amplitude, pulse width and pulse shape with applying standard deviation to them in order to clearly quantize successive differences among these features. We additionally considered systolic/diastolic ratio since systolic/diastolic ratio is observed to be within a certain range for clean PPG pulses [200].

1. Standard deviation of peak-to-peak interval (STD_{HR}):

   The $STD_{HR,n}$ of the n^{th} segment is defined by:

$$STD_{HR,n} = \sqrt{\frac{1}{N}\sum_{i=1}^{N}\left(D_{n,j} - \overline{D}_n\right)^2} \qquad (1)$$

where $D_{n,j}$ is peak-to-peak interval at the i^{th} pulse of the n^{th} segment and $\overline{D}_n$ is mean peak-to-peak interval of the n^{th} segment. The $D_{n,j}$ is calculated by the difference $T_{peak,n,i} - T_{peak,n,i-1}$ between two successive peak times.

2. Standard deviation of peak-to-peak amplitude (STD_{AMP}):

$STD_{AMP,n}$ is calculated by substituting $D_{n,i}$ and $\overline{D}_n$ in (1) with $A_{n,i}$ and $\bar{A}_n$, respectively, where $A_{n,i}$ is peak amplitude at the i^{th} pulse of the n^{th} segment and $\bar{A}_n$ is mean peak-to-peak interval of the n^{th} segment. The $A_{n,i}$ is defined by the difference between the i^{th} peak and the forthcoming $(i+1)^{th}$ trough amplitude values.

3. Standard deviation of systolic and diastolic ratio (STD_{SD}): $STD_{SD,n}$ is derived by replacing $D_{n,i}$ and $\overline{D}_n$ in (1) by $R_{SD,n,i}$ and $\bar{R}_{SD,n}$ and, respectively, where $R_{SD,n,i}$ is systolic and diastolic time interval ratio at the i^{th} pulse of the n^{th} segment and $\bar{R}_{SD,n}$ is the mean systolic and diastolic time interval ratio of the n^{th} segment. The $R_{SD,n,i}$ is calculated by

$$R_{SD,n,i} = \left(T_{trough,n,i} - T_{peak,n,i}\right) / \left(T_{peak,n,i} - T_{trough,n-1,i}\right) \quad (2)$$

where $T_{trough,n,i}$ denotes the trough (or lowest point) times at the i^{th} pulse of the n^{th} segment.

4. Mean-standard deviation of pulse shape (STD_{WAV}):

To derive pulse shape, we take N sample points of a pulse. The $STD_{WAV,n}$ of the n^{th} segment is derived by taking average of the standard deviation at each sample point as follows:

$$STD_{WAV,n} = E\left[STD_{WAV,n,m}\right] \quad (3)$$

where $STD_{WAV,n,m}$ is calculated by substituting $D_{n,i}$ and $\overline{D}_n$ with $D_{n,i}$ and $q_{n,i}(m)$ and $\bar{q}_n(m)$, respectively, where $q_{n,i}(m)$ is the m^{th} sample at the i^{th} pulse of the n^{th} segment and $\overline{q_n(m)}$ the mean at the m^{th} sample of the n^{th} segment.

3.2.3. SVM-based Detection of Motion/Noise Artifacts

Classification by Support Vector Machine (SVM)

SVM was applied to build a decision boundary classifying motion corruption from clean PPG signals. SVM is widely used in classification and regression due to its accuracy and robustness to noise [201]. The SVM consists of training and test phases described in the following sections.

Training phase:

A flow chart of the training phase in the SVM-based MNA detection algorithm is shown in Fig. 2. An SVM first derives the parameter values from clean and corrupted PPG training segments which are labeled separately (clean: 0, corrupted: 1). The SVM then trains itself with the labeled parameter values and finds the support vectors among the parameter values which maximize the margin (or the distance) between different classes. Finally, the SVM builds a decision boundary from the support vectors. If the estimated decision from the decision boundary is different from its known label, the decision is regarded as a training error.

We consider a soft-margin SVM which can set the boundary even when the data sets are mixed and cannot be separated. In the soft-margin SVM algorithm, slack variables are introduced to minimize the training error with maximizing the margin. Soft-margin SVM uses the following equation to find the support vectors [202].

$$Min\ C \sum_{sv=1}^{N} \delta_{sv} + \frac{1}{2}\langle W_s, W_s \rangle \qquad (4)$$

$$Subject\ to\ T_{sv}(\langle W_s, W_s \rangle + b_s) \geq 1 = \delta_{sv} \text{ for } sv = 1,2, \dots, N \text{ and } \delta_{sv} \geq 0.$$

Where C is regularization parameter, N is the number of vectors, δ_{sv} is the slack variable, W_s is weight vector and $\langle .,. \rangle$ is the inner product operation. The T_{sv} is the svth target variable, y_{sv} and the sv^{th} input vector data, and b_s is the bias. The SVM decision boundary F_{sv} is derived as

$$F_{sv} = \langle W_s^*, y \rangle + b_s^* = 0 \qquad (5)$$

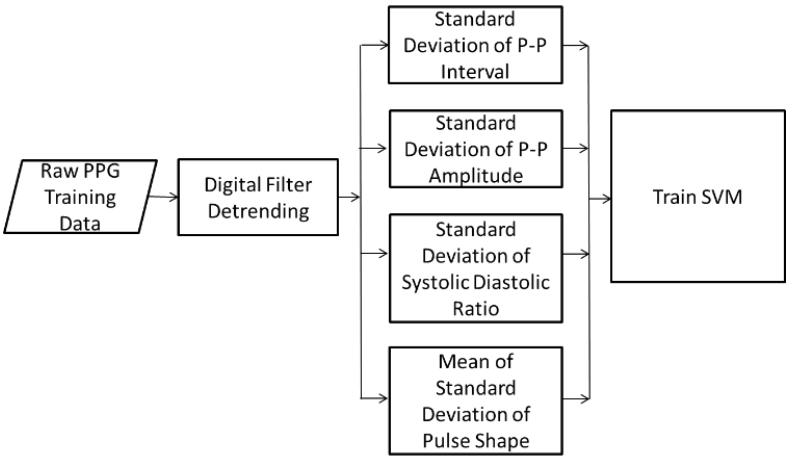

Figure 0.2 - Training phase of the proposed SVM-based motion detection algorithm. Four time-domain features corresponding to (1) standard deviation of peak-to-peak intervals (2) standard deviation of peak-to-peak amplitudes (3) standard deviation of systolic and diastolic interval ratio, and (4) mean standard deviation of pulse shape, are candidate input variables to the SVM.

where W_s^* and b_s^* are weight factor and bias, respectively, obtained from Eq. (7) and y is the input point.

By transforming the y_{sv} and y term to $\Phi(y_{sv})$ andΦ(y), the non-linear SVM can be transformed to a linear SVM. For nonlinear SVM, Eq. (4) is modified as

$$T_{sv}(\langle W_s, \Phi(y_{sv}) \rangle + b_s) \geq 1 \qquad (2)$$

To facilitate the operation in nonlinear SVM, a kernel function $K_s(.,.)$, which is a dot-product in the transformed feature space as follows, is used,

$$K_s(y_{sv}, y_{sv}) = \langle \Phi(y_{sv}), \Phi(y_{sv}) \rangle \qquad (3)$$

Where $sv = 1,2,\ldots,N$.

Test phase:

Fig. 3 shows a flow chart of the test phase in the SVM-based MNA detection algorithm. We partition PPG data into many 7-second segments, and derive parameters from each PPG portion to examine if it is corrupted by motion artifact or not.

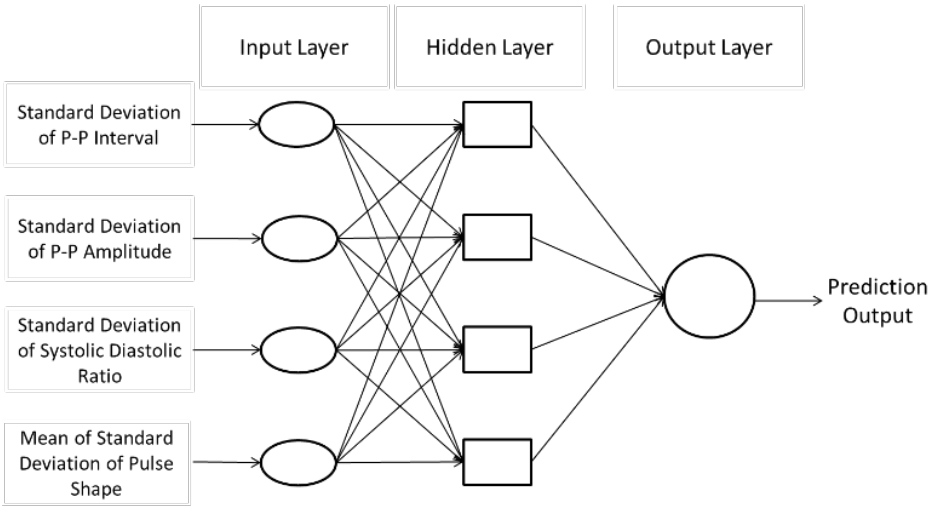

Figure 0.3 - Test phase of the proposed SVM-based motion detection algorithm. The hidden layers correspond to kernel function of the SVM. The function between hidden layer and output layer is a linear operator.

3.2.4. Enhancement of MNA Detection by Major Votes

To enhance MNA detection performance, the proposed algorithm incorporates multiple decisions on a set of neighbor segments in deciding whether a "target" segment is clean or corrupted. Neighbor segment is defined as a segment surrounding a target segment within ± Tneighbor seconds. Decision on a

neighbor segment is highly likely to be the same as the decision on a target segment since PPG pulses in the neighbor segments are most likely to exhibit similar dynamics to the target segment.

The algorithm gathers the decisions of neighbor segments as well as target segment (see Fig. 4) and makes a final decision on the target segment based on a majority vote concept.

3.3. Results

We evaluated the performance of the MNA detection algorithm for various types (simulated, laboratory controlled, and daily activities) of motion-corrupted PPGs to validate its performance in a wide range of scenarios.

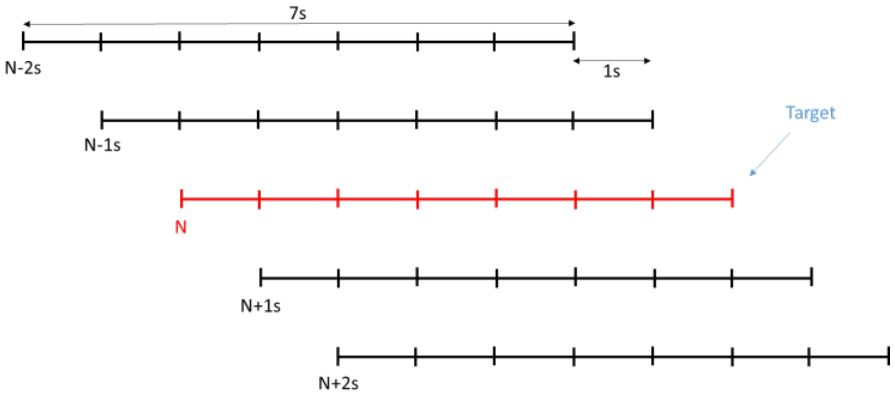

Figure 0.4 - Enhancement of MNA detection by diversity. Neighbor segments are the segments surrounding a target segment within ± 2 seconds. Decisions on the target segment are based on a majority vote from the decisions of neighbor segments as well as the one of the target segment (red).

For all types of motions, the PPG recordings were divided into 7-second segments to compare our algorithm with the conventional detection algorithm which is applied to 7-second PPG segments [42]. We also compared the proposed algorithm with four recently published MNA detection algorithms based on kurtosis (K), Shannon entropy (SE), Hjorth 1 (H1), and Hjorth 2 (H2) metrics [203, 204], respectively. As performance metrics, we considered classification accuracy, sensitivity and specificity. We also investigated mean HR and SpO2 errors as well as detection error ratio.

3.3.1. Reference: Clean vs. corrupted

The following are criteria which we adopted to reference PPG segments (clean or corrupted) for each experiment. A visual reference was excluded to avoid subjective decisions by visual inspectors; for subtle MNA there were large disagreements among visual inspectors. Instead, we performed objective decisions based on controlled corruption start ($Tcorr_{start}$) and end ($Tcorr_{end}$) time points, ECG-derived heart rate (HR_{PPG}), PPG-derived heart rate (HR_{PPG}), and SpO2 ($SpO2_{PPG}$) from PPG signals. HRs from ECG signals and pulse rates (PRs) from PPG signals are shown to have high agreement when the subjects do not move [205]. Specifically, the difference between HRs and PRs for 10 subjects is within around 5 bpm on average. Even during heavy exercise, sudden HR increases or drops between successive beats are within 20 bpm [206] while sudden SpO2 increases or drops between successive beats are around 2% [207]. Since subjects' movements in this research are less severe than heavy exercise, sudden HR and SpO2 changes are expected to be smaller than 20 bpm and 10% (with additional margin to 2%) which are larger values than the maximum HR and SpO2 changes during heavy exercise. Based on these experimental observations, we set PPG clean versus motion-corrupted classification criteria for PPG segments as follows.

- If more than 85% of a segment is outside of [$Tcorr_{start}$, $Tcorr_{end}$], the segment was considered clean. Otherwise, the segment was referenced to be corrupted.

- If $SpO2_{PPG}$ deviates by 10 % from the mean of $SpO2_{PPG}$ in a segment, then the segment was referenced to be corrupted [207].

- Successive difference, $|HR_{PPG}(i+1) - HR_{PPG}(i)|$, from PPG signals is larger than 20 bpm for at least one pulse during a segment, then the segment was referenced to be corrupted [206].

Daily activity data (Walking and stair-climbing)

- Successive difference, $|HR_{ECG}(i+1) - HR_{ECG}(i)|$, from ECG signals is larger than 20 bpm for at least one pulse during a segment, then the segment was excluded [206].

- If $SpO2_{PPG}$ deviates by 10 % from the mean of $SpO2_{PPG}$ in a segment, then the segment was referenced to be corrupted [207].

- If $|HR_{PPG}(i+1) - HR_{PPG}(i)|$is larger than 20 bpm for at least one pulse during a segment, then the segment was referenced to be corrupted [206].

- If $|HR_{ECG}(i+1) - HR_{ECG}(i)| < 5$ bpm during more than 85 % of a segment, the segment was considered clean. Otherwise, the segment was referenced to be corrupted [205].

Table I describes the number of clean and corrupted PPG segments for each motion type used in the experiment as determined by the criteria defined above.

Table 3.1. Numbers of Subjects and Numbers of Clean and Corrupted Segments for Each Motion Artifact

Type	Subtype	# of Subjects	# Clean	# Corrupted
Simulation	Simulation	N/A	N/A	N/A
Laboratory Controlled	Finger	13	195	105
	Forehead	11	190	110
Daily-Activity	Walking/ Stair-climbing	9	125	175

3.3.2. Classification Accuracy

A sample forehead PPG signal and its corresponding 56-85 seconds have larger parameter values compared to clean segments between 1-56 seconds and 85-112 seconds. We sampled 17 points (N = 17) of

each pulse using spline interpolation irrespective of test subjects and conditions to derive pulse shape in Fig. 5f. This enables pulse shape comparisons within and among test subjects.

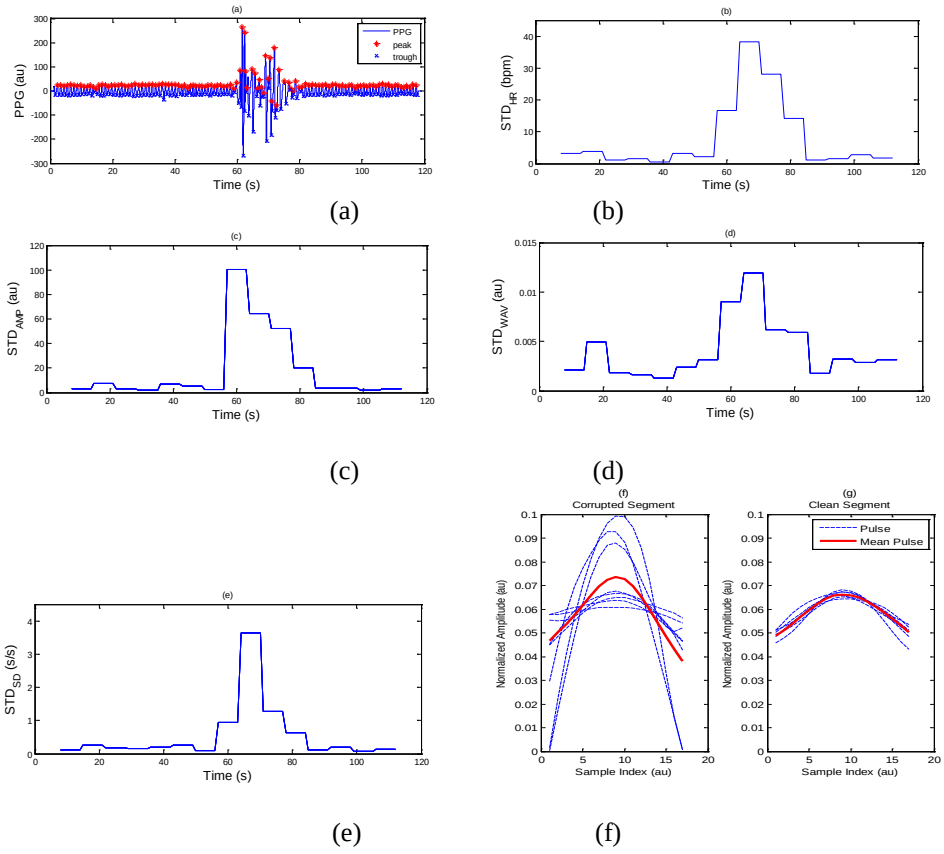

Figure 0.5 - A sample forehead recorded PPG signal (a) along with the (b) standard deviation of P-P intervals (c) standard deviation of P-P amplitudes (d) standard deviation of systolic and diastolic time ratio, and (e) mean standard deviation of pulse shape, computed for each segment. The normalized sampled corrupt and clean PPGs for mean standard deviation of pulse shape (N =17) are given in (f).

Fig. 6a-b show (STD_{HR}, STD_{AMP}) and (STD_{SD}, STD_{WAV}) of clean (circle) and corrupted (star) forehead signals, respectively, with corresponding SVM boundaries (black line). To lower computational complexity, a linear kernel was considered for the SVM in the experiment. We adopted inverse k-fold cross-validation which selects one fold for training and k-1 for testing [208]. We trained SVM with data from one subject and tested data from 10 subjects. There were little differences among test errors of different inverse cross-validation cases. As a training data, however, we selected the training subject which has the least test

error. Re-training was not performed since each subject generated enough number of clean and corrupted PPG data and the SNRs of clean PPG signals were usually higher than algorithm's sensitivity level. We optimized regularization parameter value (C) of the linear kernel SVM in terms of minimizing the training error rate. We adopted a 11-fold cross-validation and grid search ($C = \{10^{-3}, 10^{-2}, 10^{-1}, 1, 10^{1}, 10^{2}, 10^{3}\}$) which is widely used to determine C [209].

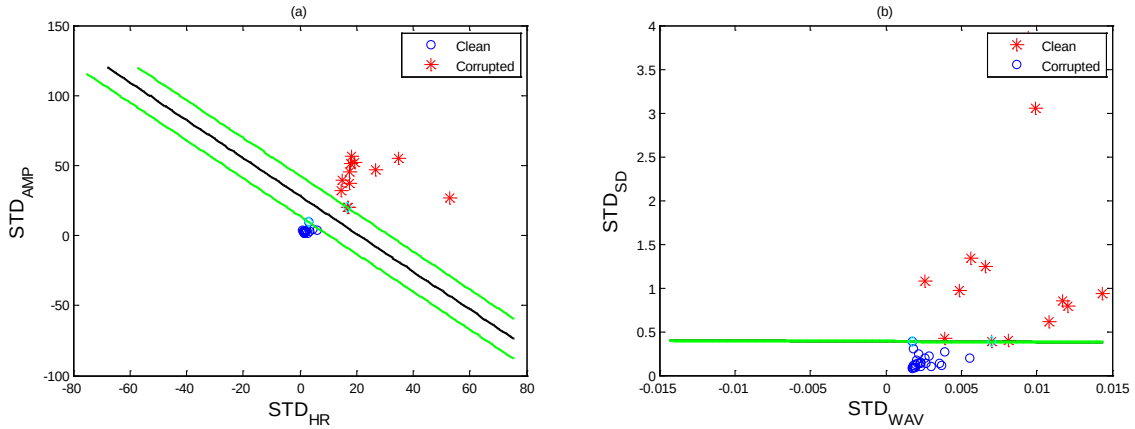

(a) (b)

Figure 0.6 - Trained SVM classification with a sample training finger recorded PPG signal is given with (a)-(b) pairs of two parameters. The SVM decision and margin boundaries are marked by black and green lines, respectively.

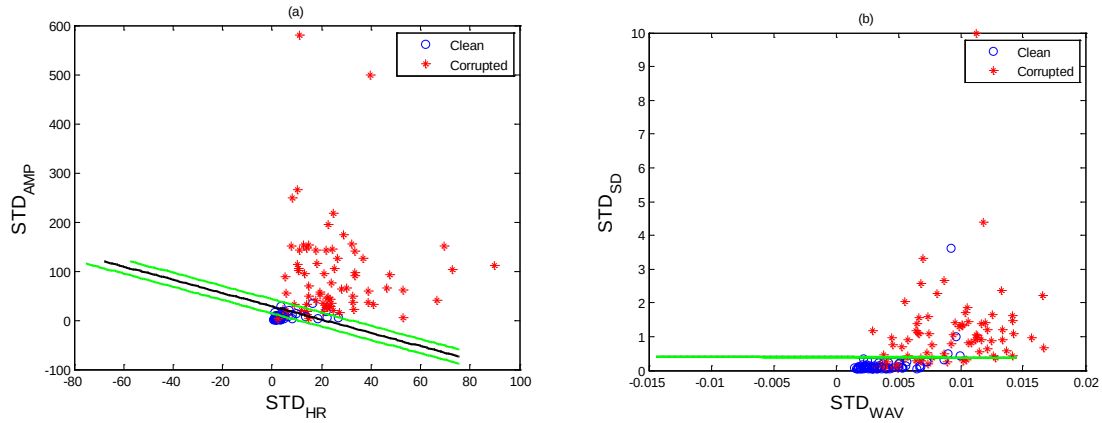

(a) (b)

Figure 0.7 - Validation: pairs of parameters for clean and corrupted PPG signals

Fig. 7 shows classification results by the SVM boundaries obtained from Fig. 6. Fig. 8 shows a representative PPG signal with detected peaks (red) along with the corresponding statistical parameter values. Note the corrupted PPG signal interval between 21 to 31 seconds. The discrepancy between corrupted and clean portions is reflected by parameters$(STD_{HR}, STD_{AMP}, STD_{SD}, STD_{WAV})$. The parameter values from the corrupted PPG segments exhibit larger variability and consequently have higher standard deviation value compared to those from clean data segments. The STD_{HR}, STD_{AMP} and STD_{WAV} have large values between 21-35 seconds (see Fig. 8b-d), while STD_{SD} has large value only between 21-28 seconds (see Fig. 8e). Using SVM with these parameter values, the proposed algorithm correctly discriminated MNA corrupted segment between 21-35 seconds (see Fig. 8f). Table (2) presents C for finger, forehead, and walking/stair-climbing data. We tested our algorithm to different segment lengths varying from 3 to 11 seconds and calculated their mean classification accuracies, which are provided in Table (3).

Table 3.2. C obtained by 9 fold cross-validation and grid search method

Type	Subtype	*C*
Simulation	Simulation	100
Laboratory Controlled	Finger	1000
	Forehead	1
Daily-Activity	Walking/ Stair-climbing	0.01

Among the different data segment lengths tested, the 7-second segment provided the highest classification accuracies for all data: finger, forehead and walking/stair-climbing PPG signals. Accuracy, specificity, and sensitivity for each dataset are presented in Table (4).

Table 3.3. Detection accuracy, specificity and sensitivity (Mean ± SD) for 7-seonds segment

Type	Accuracy	Specificity	Sensitivity
Finger	94.4 ± 3.3	94.7 ± 4.5	94.7 ± 3.4
Forehead	93.4 ± 3.5	96.7 ± 3.0	88.8 ± 7.9
Walking/ Stair-climbing	93.7 ± 2.7	91.4 ± 2.0	93.9 ± 5.0

Table 3.4. Detection accuracy (Mean ± SD) for varying window length

Type	Window Length				
	3	5	7	9	11
Finger	0.883±0.042	0.906±0.035	0.944±0.033	0.944±0.033	0.875±0.042
Forehead	0.883±0.023	0.880±0.027	0.934±0.035	0.856±0.045	0.805±0.044
Walk-Stair Climbing	0.813±0.033	0.871±0.039	0.937±0.026	0.867±0.052	0.856±0.056

On average, the SVM performance using the 7-second segment showed a 93.9% accuracy, 92.4% specificity, and 94.3% sensitivity. To derive lower bound of our algorithm's performance [[210]] as well as evaluate the sensitivity of our MNA detection algorithm to a combination of various noise or noise itself [211, 212] (e.g., thermal noise), we added Gaussian white noise (GWN) of varying signal-to-noise (SNR) levels to a representative non-MNA corrupted PPG signal. For each SNR, 50 independent realizations of clean PPG signal with GWN are generated.

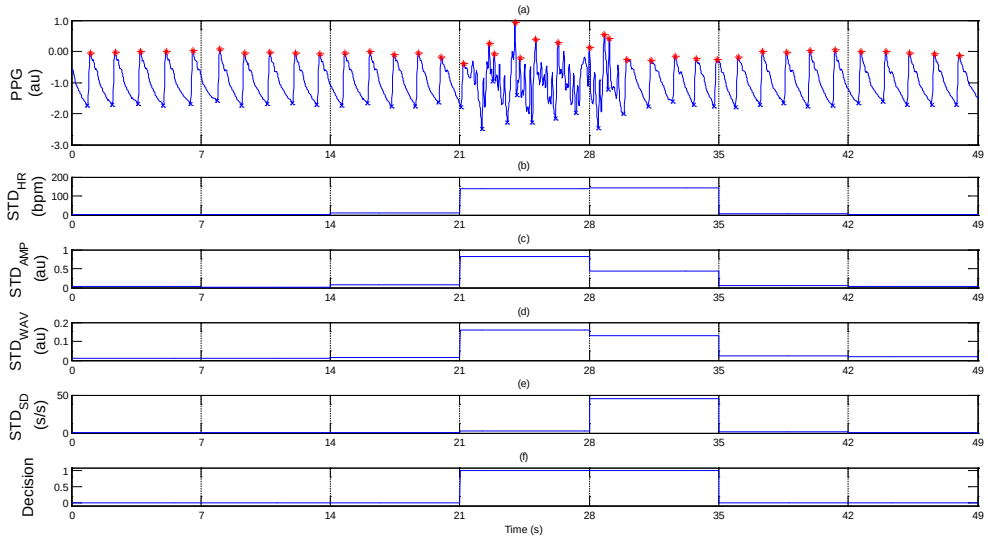

Figure 0.8 - A representative PPG signal with detected peaks (red) (a) along with the (b) standard deviation of P-P intervals (c) standard deviation of P-P amplitudes (d) mean standard deviation of pulse shape and (e) standard deviation of systolic and diastolic time ratio, computed for each segment.

As shown in Fig. 9, the PPG signals with a SNR below -10 dB are detected as corrupted data with our algorithm. For a SNR of -20 dB, every segment was detected as corrupted.

3.3.3. Performance Comparison of MNA detection Algorithms

Our algorithm was compared with other artifact detection methods based on H1, H2 , K and SE since these methods have been shown to provide good detection accuracies [203, 213, 214]. The H1 and H2 parameters represent the central frequency and half of bandwidth, respectively, and are defined as follows:

$$H_1 = \sqrt{\frac{\bar{v}_2(n)}{\bar{v}_0(n)}} \quad \text{and } H_2 = \sqrt{\frac{\bar{v}_4(n)}{\bar{v}_2(n)} - \frac{\bar{v}_2(n)}{\bar{v}_0(n)}} \qquad (11)$$

Where $\bar{v}_i(n) = \int_{-\pi}^{\pi} v^i S_y(e^{jv}) dv$. Here, $S_y(e^{jv})$is the power spectrum of signal y.

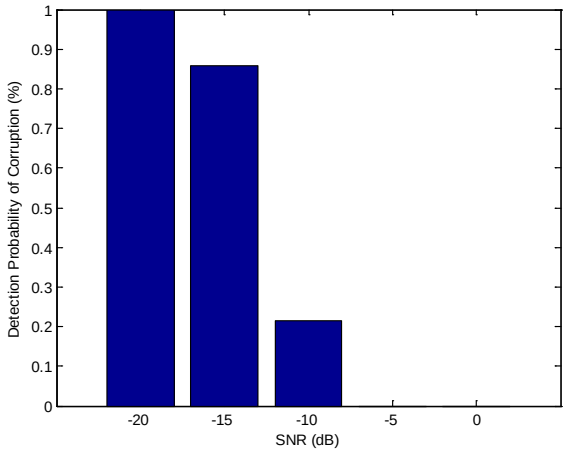

Figure 0.9 - Detection Probability of Corruption by additive white Gaussian noise (AWGN) for varying SNR from -20 to 0 dB. 50 AWGN realizations for each SNR level are separately added to a non-MNA corrupted PPG. Each realization is tested by the proposed MNA detection algorithm to compute the detection probability of corruption.

For a fair comparison, all detection methods used 7 second data segments. Figs. 10a-c compare the medians and 25th and 75th percentiles of detection accuracy, sensitivity, and specificity, which are obtained from each subject, for all five detection methods for the finger, head and walking/stair-climbing data sets. In general, our SVM method consistently yielded higher performance with a mean accuracy of 94%, sensitivity of 97%, and a specificity of 92%; whereas other methods showed fluctuations depending on which datasets were used. In the finger recorded data, H1 yielded a slightly higher accuracy than all other methods due to higher specificity, but the detection sensitivity was lower.

3.3.4. HR and SpO2 Estimation

Fig. 11a compares the mean HR error and detection error fraction from five MNA detection methods for walking/stair-climbing data. The HR errors were defined by the difference between the estimated HR derived from the PPG and the reference HR readings while the detection error fraction is

defined by a ratio of the number of erroneous detection events to that of total detection events. Low mean HR error and low detection error fraction values would reflect an effective artifact detection algorithm.

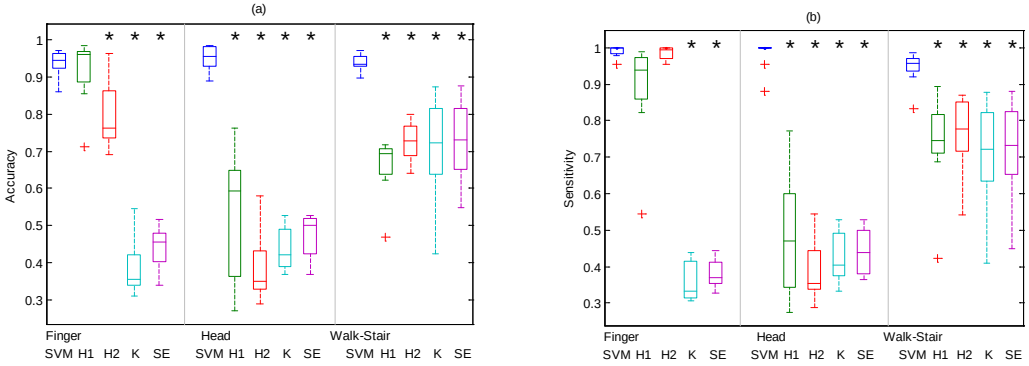

(a) (b)

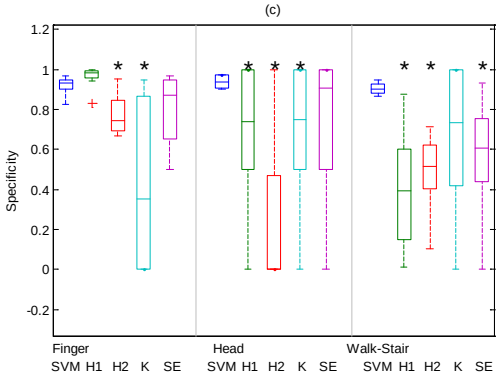

(c)

Figure 0.10 - Classification performance comparison between our SVM algorithm, Hjorth (H1, H2), Kurtorsis and Shanon Entropy (K, SE) parameters. (a) Accuracy; (b) Sensitivity; (c) Specificity. The central mark on each box corresponds to the median; the edges of the box correspond to the 25th and 75th percentiles, the whiskers extend to the most extreme data points not considered outliers, and outliers are plotted individually. (*) indicate the mean is significantly different ($p<0.05$ at 95% CI) between SVM and other methods used for comparison.

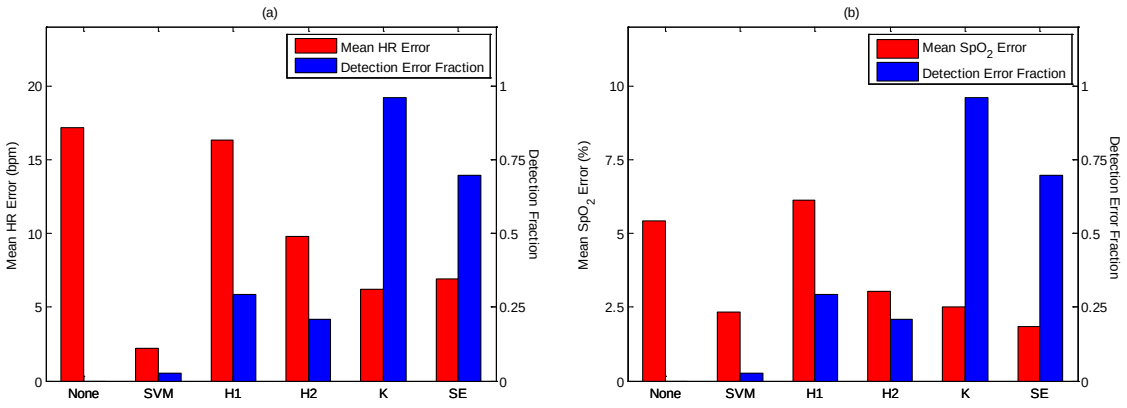

(a) (b)

Figure 0.11 - Comparison of mean errors and detection error fraction between original signal (labeled "None") and artifact removed signal from five detection methods (SVM, H1, H2, K, and SE). (a) HR error; (b) SpO2 error.

Our algorithm yielded the lowest HR error and detection error fraction among the other MNA methods we compared. Fig. 11b compares mean SpO2 error and detection error fraction from five MNA detection methods. The SE based detection method showed a lower mean SpO2 error than our algorithm, but its detection error fraction was very high (>70%), indicating that the SpO2 error was computed based on only 30% of clean data. On the other hand, the proposed SVM algorithm resulted in a mean SpO2 error of 2.7 with a detection error of only 6.3%. Fig. 12 compares five MNA detection methods in terms of paired-t test results of HR and SpO2 estimation and detection accuracy. On average, the SVM algorithm outperformed the K, SE, H1 and H2 methods with HR errors of 2.3 bpm, SpO2 errors of 2.7% and detection error fraction of 6.3%.

3.4. Discussion

Robust real-time MNA detection algorithms for raw PPG signals have been elusive to date. In this study, an SVM-based method is introduced to detect MNA-corrupted PPG data. Reconstruction of MNA-corrupted PPG segments was described in the companion chapter. The aim of the current chapter is to detect the MNA corrupted PPG segments as accurate as possible. The question is how to detect MNA in an

adaptive and cognitive way with enhancing detection and minimizing the signal distortions in PPG segments. To address this question, we use four parameters: (a) standard deviation of peak-to-peak intervals (b) standard deviation of peak-to-peak amplitudes (c) standard deviation of systolic and diastolic time ratios, and (d) mean-standard deviation of pulse shapes; and use them as inputs to an SVM-based MNA detection method with sliding with a major vote concept. We use these parameters since motion corrupted PPG signals are observed to have noticeably different values and have large variations for successive pulses compared to clean PPG signals.[193] We are currently researching on finding more parameters to enhance detection performance on diverse types of MNA-corrupted PPG signals.

MNA detection algorithms have been proposed to detect MNAs or quantize signal quality of PPG pulses. Various approaches use a set of several parameters to detect MNA and but the test data was confined to several types of motions.[180, 193-197, 199] Given that conventional methods give a certain amount of MNA detection performance, we have evaluated our proposed algorithm by comparing it to the conventional detection methods.

The results demonstrated that our proposed SVM-based MNA detection algorithm has offered higher classification accuracy as well as lower HR and SpO2 errors compared to the conventional detection methods. The paired-t test was performed to determine whether there is a significant difference between classification errors obtained from our SVM approach compared with other published methods. For the finger recorded PPG segments, Fig. 10a indicate that the mean classification accuracy is significantly different ($p<0.05$ at 95% CI) between our SVM and K, SE and H2 methods (except for H1). K, SE, H1 and H2 methods were significantly different from our SVM method for forehead and walking/stair-climbing PPG data. Kurtosis and Shannon entropy based detection methods' low performance may be caused by clean PPG signals' variations in amplitude and pulse. These variations can be induced unintentionally during the measurement due to small movement or physiological artifacts which is not severe but varies between test subjects or test conditions. Since H1 is estimating central frequency, H1 method is expected to high performance as the clean PPG signal gets more stable in frequency domain.

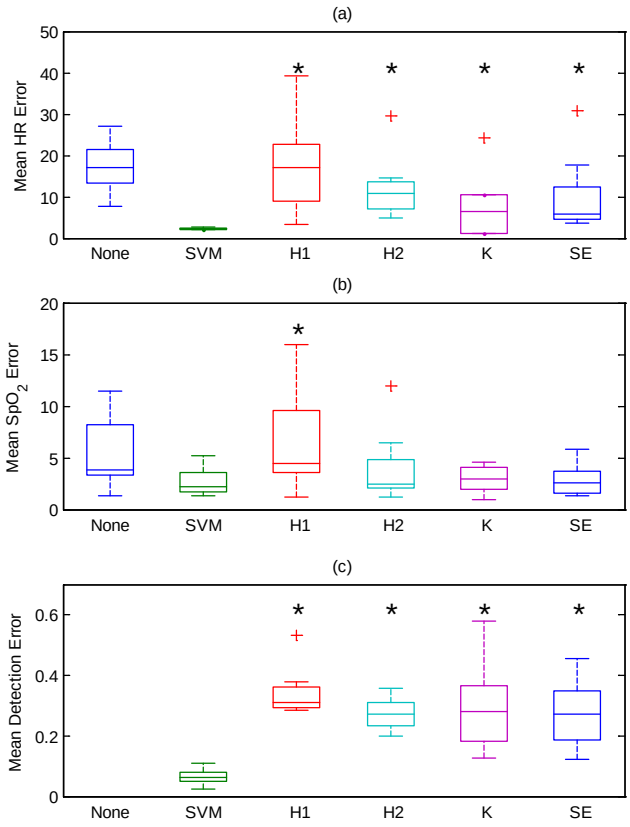

Figure 0.12 - Mean error comparison between our SVM algorithm, Hjorth (H1, H2), Kurtorsis and Shanon Entropy (K, SE) parameters. (a) Heart rate; (b) SpO2; (c) detection error for walk/stair-climbing data. The central mark on each box corresponds to the median; the edges of the box correspond to the 25th and 75th percentiles, the whiskers extend to the most extreme data points not considered outliers, and outliers are plotted individually. (*) indicate the mean is significantly different ($p<0.05$ at 95% CI) between SVM and other methods used for comparison. The x-axis labelled "None" in all panels refers to the mean errors when compared to the reference signals without removing the MNA detected segments as identified by any of the five computational methods.

Hence, H1 shows high performance for finger movement whose clean PPG signals are measured in the most stable conditions among clean finger, head and walking/stair-climbing PPG measurements as

shown in Fig. 10a-c. H1 performs worse for head and walking/stair-climbing PPGs since slight movement and physiological artifacts get larger. Similarly, H2 methods estimating half of the bandwidth shows comparable performance for finger PPG signals as shown in Fig. 10a-c. However, H2 performs worse for head and walking/stair-climbing PPGs. Fig. 12a-c summarizes paired-t test results of HR and SpO2 estimations as well as detection accuracy for walking/stair-climbing data. As shown in Fig. 12a-c, SVM is significantly different from H1, H2, K, and SE in terms of HR estimation and detection accuracy (see Figs. 11a and c), while SpO2 derived from the SVM method is significantly different from only H1(see Fig. 12b).

To enhance decision accuracy of our MNA detection algorithm, we adopted a major vote concept which is widely used in other engineering fields to fuse the decisions from multiple entities[215]. The major vote concept in our algorithm took a role of giving a decision on a target PPG segment after fusing the decisions of neighbor PPG segments as well as that of target segment. This is enabled based on the observation that the decision on target segment (clean or corrupted) is highly correlated to those of neighbor segments.

The advantage of the our MNA detection algorithm is that it can classify MNA-corrupted PPG from clean PPG in an adaptive and cognitive manner. Hence, it can be applied to either controlled or daily-activity moving scenarios. The MNA detection algorithm coded with Matlab (2012a) takes only 7 ms on an Intel Xeon 3.6 GHz computer for the 7-second data segment. Hence, the algorithm is real-time realizable especially when it is coded in either C or C++. Our proposed MNA algorithm, incorporating it with reconstruction algorithm, can also provide information whether the signal is good originally (detected as clean), good after reconstruction (detected as corrupted but succeeded in reconstruction) or bad (detected as bad and failed in reconstruction). In conclusion, the proposed algorithm with a pulse oximeter device may have significant implications for real-time clinical applications and especially for ambulatory monitoring of vital signs.

References

1. Patel, S., et al., *A review of wearable sensors and systems with application in rehabilitation.* Journal of NeuroEngineering and Rehabilitation, 2012. **9**(1): p. 1-17.
2. Wijshoff, R.W., et al., *Reducing motion artifacts in photoplethysmograms by using relative sensor motion: phantom study*. J Biomed Opt, 2012. **17**(11): p. 117007.
3. P. A. Muennig and S. A. Glied, *What Changes in Survival Rates Tell Us About U.S. Health Care.* Health Affairs Web 2010. **First**.
4. Gulley, S.P., E.K. Rasch, and L. Chan, *If we build it, who will come? Working-age adults with chronic health care needs and the medical home.* Med Care, 2011. **49**(2): p. 149-55.
5. Gulley, S.P., E.K. Rasch, and L. Chan, *Ongoing coverage for ongoing care: access, utilization, and out-of-pocket spending among uninsured working-aged adults with chronic health care needs.* Am J Public Health, 2011. **101**(2): p. 368-75.
6. Goonewardene, S.S., et al., *Road traffic collisions-case fatality rate, crash injury rate, and number of motor vehicles: time trends between a developed and developing country.* Am Surg, 2010. **76**(9): p. 977-81.
7. Organization, W.H. *Active Aging a Policy Framework*. Available from: http://www.who.int/ageing/publications/active_ageing/en/.
8. Kinsella, K.G., D.R. Phillips, and P.R. Bureau, *Global Aging: The Challenge of Success*. 2005: Population Reference Bureau.
9. Bray, H., *National population projections*, O.f.N. Statistics, Editor. 2008.
10. Axelrod, D.A., D. Millman, and M.M. Abecassis, *US Health Care Reform and Transplantation. Part I: overview and impact on access and reimbursement in the private sector.* Am J Transplant, 2010. **10**(10): p. 2197-2202.
11. Teng, X.F., et al., *Wearable medical systems for p-Health.* IEEE Rev Biomed Eng, 2008. **1**: p. 62-74.
12. Bonato, P., *Wearable sensors and systems. From enabling technology to clinical applications.* IEEE Eng Med Biol Mag, 2010. **29**(3): p. 25-36.
13. Hamilton, P.S., et al. *Comparison of methods for adaptive removal of motion artifact*. in *Computers in Cardiology 2000*. 2000.
14. Caudill, T.S., et al., *Commentary: Health care reform and primary care: training physicians for tomorrow's challenges.* Acad Med, 2011. **86**(2): p. 158-60.
15. Chan, L., L.G. Hart, and D.C. Goodman, *Geographic access to health care for rural Medicare beneficiaries.* J Rural Health, 2006. **22**(2): p. 140-6.
16. DeVaul, R., et al., *MIThril 2003: Applications and Architecture*, in *Proceedings of the 7th IEEE International Symposium on Wearable Computers*. 2003, IEEE Computer Society. p. 4.
17. Raya, M.A.D. and L.G. Sison. *Adaptive noise cancelling of motion artifact in stress ECG signals using accelerometer*. in *Engineering in Medicine and Biology, 2002. 24th Annual Conference and the Annual Fall Meeting of the Biomedical Engineering Society EMBS/BMES Conference, 2002. Proceedings of the Second Joint*. 2002.
18. Jinyun, Z., et al., *UWB Systems for Wireless Sensor Networks.* Proceedings of the IEEE, 2009. **97**(2): p. 313-331.
19. Yilmaz, T., R. Foster, and Y. Hao, *Detecting Vital Signs with Wearable Wireless Sensors.* Sensors, 2010.
20. Asada, H.H., et al., *Mobile monitoring with wearable photoplethysmographic biosensors.* IEEE Eng Med Biol Mag, 2003. **22**(3): p. 28-40.
21. Shaltis, P.A., A. Reisner, and H.H. Asada, *Wearable, cuff-less PPG-based blood pressure monitor with novel height sensor.* Conf Proc IEEE Eng Med Biol Soc, 2006. **1**: p. 908-11.

22. Corbishley, P. and E. Rodriguez-Villegas, *Breathing Detection: Towards a Miniaturized, Wearable, Battery-Operated Monitoring System.* Biomedical Engineering, IEEE Transactions on, 2008. **55**(1): p. 196-204.
23. Barbaro, M., et al., *Active devices based on organic semiconductors for wearable applications.* IEEE Trans Inf Technol Biomed, 2010. **14**(3): p. 758-66.
24. Patterson, J.A.C., D.G. McIlwraith, and Y. Guang-Zhong. *A Flexible, Low Noise Reflective PPG Sensor Platform for Ear-Worn Heart Rate Monitoring*. in *Wearable and Implantable Body Sensor Networks, 2009. BSN 2009. Sixth International Workshop on*. 2009.
25. Yan, Y.S. and Y.T. Zhang, *An efficient motion-resistant method for wearable pulse oximeter.* IEEE Trans Inf Technol Biomed, 2008. **12**(3): p. 399-405.
26. Wood, L.B. and H. Asada, *Low variance adaptive filter for cancelling motion artifact in wearable photoplethysmogram sensor signals.* Conf Proc IEEE Eng Med Biol Soc, 2007. **2007**: p. 652-5.
27. Merilahti, J., et al., *Compliance and technical feasibility of long-term health monitoring with wearable and ambient technologies.* J Telemed Telecare, 2009. **15**(6): p. 302-9.
28. Sciacqua, A., et al. *Validation of a flexible and innovative platform for the home monitoring of heart failure patients: Preliminary results*. in *Computers in Cardiology, 2009*. 2009.
29. Mundt, C.W., et al., *A multiparameter wearable physiologic monitoring system for space and terrestrial applications.* IEEE Trans Inf Technol Biomed, 2005. **9**(3): p. 382-91.
30. Anliker, U., et al., *AMON: a wearable multiparameter medical monitoring and alert system.* IEEE Trans Inf Technol Biomed, 2004. **8**(4): p. 415-27.
31. Habetha, J., *The MyHeart project--fighting cardiovascular diseases by prevention and early diagnosis.* Conf Proc IEEE Eng Med Biol Soc, 2006. **Suppl**: p. 6746-9.
32. Paradiso, R. *Wearable health care system for vital signs monitoring*. in *Information Technology Applications in Biomedicine, 2003. 4th International IEEE EMBS Special Topic Conference on*. 2003.
33. Di Rienzo, M., et al., *MagIC System: a New Textile-Based Wearable Device for Biological Signal Monitoring. Applicability in Daily Life and Clinical Setting.* Conf Proc IEEE Eng Med Biol Soc, 2005. **7**: p. 7167-9.
34. Samsung. *Simband*. Available from: https://www.simband.io/.
35. Reyes, B.A., et al., *Novel electrodes for underwater ECG monitoring.* IEEE Trans Biomed Eng, 2014. **61**(6): p. 1863-76.
36. *AlertOne medical alert system.*
37. *Automatic Fall Detection*. Available from: http://www.wellcore.com/learn/automatic-falldetection.
38. *myHalo.*
39. *BrickHouse*. Available from: http://www.brickhousealert.com/personal-emergency-medicalalarm.html.
40. *EASY WORLS*. Available from: http://www.ttmmonaco.com/en/default.htm.
41. *USC Rehabilitation Engineering Research Center*. Available from: http://www.isi.edu/research/rerc.
42. Rizzo, A., et al., *Virtual reality applications for addressing the needs of those aging with disability.* Stud Health Technol Inform, 2011. **163**: p. 510-6.
43. Vincent, C., et al., *Rehabilitation needs for older adults with stroke living at home: perceptions of four populations.* BMC Geriatr, 2007. **7**: p. 20.
44. Uswatte, G., et al., *Ambulatory monitoring of arm movement using accelerometry: an objective measure of upper-extremity rehabilitation in persons with chronic stroke.* Arch Phys Med Rehabil, 2005. **86**(7): p. 1498-501.
45. Uswatte, G., et al., *Validity of accelerometry for monitoring real-world arm activity in patients with subacute stroke: evidence from the extremity constraint-induced therapy evaluation trial.* Arch Phys Med Rehabil, 2006. **87**(10): p. 1340-5.

46. Patel, S., et al., *A review of wearable sensors and systems with application in rehabilitation.* J Neuroeng Rehabil, 2012. **9**: p. 21.
47. Heeringa, J., et al., *Prevalence, incidence and lifetime risk of atrial fibrillation: the Rotterdam study.* European Heart Journal, 2006. **27**(8): p. 949-953.
48. Benjamin, E.J., et al., *Impact of atrial fibrillation on the risk of death: the Framingham Heart Study.* Circulation, 1998. **98**(10): p. 946-52.
49. Wolf, P.A., R.D. Abbott, and W.B. Kannel, *Atrial fibrillation as an independent risk factor for stroke: the Framingham Study.* Stroke, 1991. **22**(8): p. 983-8.
50. Humphries, K.H., et al., *New-onset atrial fibrillation: sex differences in presentation, treatment, and outcome.* Circulation, 2001. **103**(19): p. 2365-70.
51. Kerr, C., et al., *Follow-up of atrial fibrillation: The initial experience of the Canadian Registry of Atrial Fibrillation.* Eur Heart J, 1996. **17 Suppl C**: p. 48-51.
52. Kinlay, S., et al., *Cardiac event recorders yield more diagnoses and are more cost-effective than 48-hour Holter monitoring in patients with palpitations. A controlled clinical trial.* Ann Intern Med, 1996. **124**(1 Pt 1): p. 16-20.
53. Roche, F., et al., *Frequent and prolonged asymptomatic episodes of paroxysmal atrial fibrillation revealed by automatic long-term event recorders in patients with a negative 24-hour Holter.* Pacing Clin Electrophysiol, 2002. **25**(11): p. 1587-93.
54. Benjamin, E.J., et al., *Prevention of atrial fibrillation: report from a national heart, lung, and blood institute workshop.* Circulation, 2009. **119**(4): p. 606-18.
55. Defaye, P., F. Dournaux, and E. Mouton, *Prevalence of supraventricular arrhythmias from the automated analysis of data stored in the DDD pacemakers of 617 patients: the AIDA study. The AIDA Multicenter Study Group. Automatic Interpretation for Diagnosis Assistance.* Pacing Clin Electrophysiol, 1998. **21**(1 Pt 2): p. 250-5.
56. *Electrocardiogram*. Available from: http://www.emedicinehealth.com/electrocardiogram_ecg/article_em.htm.
57. *ECG Features*. Available from: http://www.davita-shop.co.uk/ecg-instruments.html.
58. Oweis, R.J. and B.O. Al-Tabbaa, *QRS Detection and Heart Rate Variability Analysis: A Survey.* Biomedical Science and Engineering, 2014. **2**(1): p. 13-34.
59. Pahlm, O. and L. Sornmo, *Software QRS detection in ambulatory monitoring--a review.* Med Biol Eng Comput, 1984. **22**(4): p. 289-97.
60. Kleinmuntz, B., *Diagnostic problem solving by computer: a historical review and the current state of the science.* Comput Biol Med, 1984. **14**(3): p. 255-70.
61. Skordalakis, E., *Syntactic ECG processing: a review.* Pattern Recogn., 1986. **19**(4): p. 305-313.
62. Kundu, M., M. Nasipuri, and D. Kumar Basu, *Knowledge-based ECG interpretation: a critical review.* Pattern Recognition, 2000. **33**(3): p. 351-373.
63. Chan, M., et al., *A review of smart homes-Present state and future challenges.* Comput. Methods Prog. Biomed., 2008. **91**(1): p. 55-81.
64. Alemdar, H. and C. Ersoy, *Wireless sensor networks for healthcare: A survey.* Computer Networks, 2010. **54**(15): p. 2688-2710.
65. Lin, C.-F., *Mobile Telemedicine: A Survey Study.* Journal of Medical Systems, 2012. **36**(2): p. 511-520.
66. Paul, S.A., *Wavelet transforms and the ECG: a review.* Physiological Measurement, 2005. **26**(5): p. R155.
67. Davenport, C., et al., *Assessing the diagnostic test accuracy of natriuretic peptides and ECG in the diagnosis of left ventricular systolic dysfunction: a systematic review and meta-analysis.* Br J Gen Pract, 2006. **56**(522): p. 48-56.
68. Poli, S., et al., *Prediction of atrial fibrillation from surface ECG: review of methods and algorithms.* Ann Ist Super Sanita, 2003. **39**(2): p. 195-203.

69. Baig, M.M., H. Gholamhosseini, and M.J. Connolly, *A comprehensive survey of wearable and wireless ECG monitoring systems for older adults.* Med Biol Eng Comput, 2013. **51**(5): p. 485-95.
70. Lee, Y.-D. and W.-Y. Chung, *Wireless sensor network based wearable smart shirt for ubiquitous health and activity monitoring.* Sensors and Actuators B: Chemical, 2009. **140**(2): p. 390-395.
71. Bianchi, A.M., M.O. Mendez, and S. Cerutti, *Processing of signals recorded through smart devices: sleep-quality assessment.* IEEE Trans Inf Technol Biomed, 2010. **14**(3): p. 741-7.
72. Lopez, G., V. Custodio, and J.I. Moreno, *LOBIN: E-textile and wireless-sensor-network-based platform for healthcare monitoring in future hospital environments.* IEEE Trans Inf Technol Biomed, 2010. **14**(6): p. 1446-58.
73. Buttussi, F. and L. Chittaro, *MOPET: a context-aware and user-adaptive wearable system for fitness training.* Artif Intell Med, 2008. **42**(2): p. 153-63.
74. Pollonini, L., et al., *A novel handheld device for use in remote patient monitoring of heart failure patients--design and preliminary validation on healthy subjects.* J Med Syst, 2012. **36**(2): p. 653-9.
75. Heilman, K.J., et al., *Accuracy of the StressEraser in the detection of cardiac rhythms.* Appl Psychophysiol Biofeedback, 2008. **33**(2): p. 83-9.
76. Pandian, P.S., et al., *Smart Vest: wearable multi-parameter remote physiological monitoring system.* Med Eng Phys, 2008. **30**(4): p. 466-77.
77. Yazicioglu, R.F., et al., *Ultra-low-power wearable biopotential sensor nodes.* Conf Proc IEEE Eng Med Biol Soc, 2009. **2009**: p. 3205-8.
78. J Penders, J.v.d.M., M Altini, F Yazicioglu, C Van Hoof. *A low-power wireless ECG necklace for reliable cardiac activity monitoring on-the-move*. in *Proceedings of the International Conference of the IEEE Engineering in Medicine and Biology Society*. 2011.
79. Tamura, T.M., Y.; Sekine, M.; Yoshida, M., *Wearable Photoplethysmographic Sensors—Past and Present.* Electronics, 2014. **3**(2): p. 282-302.
80. Jubran, A., *Pulse oximetry.* Intensive Care Med, 2004. **30**(11): p. 2017-20.
81. Tilakaratna, P., *How pulse oximeters work explained simply*.
82. Zhu, Z., et al., *Continuous oxygen monitoring--a better way to prescribe long-term oxygen therapy.* Respir Med, 2005. **99**(11): p. 1386-92.
83. Barratt, C.W., et al., *Detection of previously unrecognized daytime desaturation in children with chronic lung disease.* J Med Eng Technol, 2007. **31**(2): p. 101-8.
84. Cutaia, M., *Ambulatory Monitoring of Oxygen Saturation in Chronic Lung Disease: Optimizing Long-Term Oxygen Therapy.* Clinical Pulmonary Medicine, 2002. **9**(6): p. 297-305.
85. Lu, S., et al., *Can photoplethysmography variability serve as an alternative approach to obtain heart rate variability information?* J Clin Monit Comput, 2008. **22**(1): p. 23-9.
86. Lu, G., et al., *A comparison of photoplethysmography and ECG recording to analyse heart rate variability in healthy subjects.* J Med Eng Technol, 2009. **33**(8): p. 634-41.
87. Hon, E.H. and S.T. Lee, *ELECTRONIC EVALUATION OF THE FETAL HEART RATE. VIII. PATTERNS PRECEDING FETAL DEATH, FURTHER OBSERVATIONS.* Am J Obstet Gynecol, 1963. **87**: p. 814-26.
88. Ewing, D.J., et al., *The value of cardiovascular autonomic function tests: 10 years experience in diabetes.* Diabetes Care, 1985. **8**(5): p. 491-8.
89. Tulen, J.H., et al., *Sleep patterns and blood pressure variability in patients with pure autonomic failure.* Clin Auton Res, 1991. **1**(4): p. 309-15.
90. Guzzetti, S., et al., *Different spectral components of 24 h heart rate variability are related to different modes of death in chronic heart failure.* Eur Heart J, 2005. **26**(4): p. 357-62.
91. Chattipakorn, N., et al., *Heart rate variability in myocardial infarction and heart failure.* International Journal of Cardiology, 2007. **120**(3): p. 289-296.

92. de Boer, R.W., J.M. Karemaker, and J. Strackee, *Relationships between short-term blood-pressure fluctuations and heart-rate variability in resting subjects. I: A spectral analysis approach.* Med Biol Eng Comput, 1985. **23**(4): p. 352-8.
93. Pfeifer, M.A., et al., *Quantitative evaluation of cardiac parasympathetic activity in normal and diabetic man.* Diabetes, 1982. **31**(4 Pt 1): p. 339-45.
94. Singh, J.P., et al., *Association of hyperglycemia with reduced heart rate variability (The Framingham Heart Study).* Am J Cardiol, 2000. **86**(3): p. 309-12.
95. Wheeler, T. and P.J. Watkins, *Cardiac Denervation in Diabetes.* British Medical Journal, 1973. **4**(5892): p. 584-586.
96. Chan, C.T., et al., *Effects of daily hemodialysis on heart rate variability: results from the Frequent Hemodialysis Network (FHN) Daily Trial.* Nephrol Dial Transplant, 2014. **29**(1): p. 168-78.
97. Zoccali, C., M. Ciccarelli, and Q. Maggiore, *Defective reflex control of heart rate in dialysis patients: evidence for an afferent autonomic lesion.* Clin Sci (Lond), 1982. **63**(3): p. 285-92.
98. Hertzman, A.B., *The Blood Supply of Various Skin Areas as Estimated by the Photoelectric Plethysmograph*. 1938.
99. Rhee, S., B.H. Yang, and H.H. Asada, *Artifact-resistant power-efficient design of finger-ring plethysmographic sensors.* IEEE Trans Biomed Eng, 2001. **48**(7): p. 795-805.
100. Jung, J.Y. and J.W. Lee. *ZigBee Device Access Control and Reliable Data Transmission in ZigBee Based Health Monitoring System*. in *Advanced Communication Technology, 2008. ICACT 2008. 10th International Conference on*. 2008.
101. Yongkwi, L., et al. *Development of a wristwatch-type PPG array sensor module*. in *Consumer Electronics - Berlin (ICCE-Berlin), 2011 IEEE International Conference on*. 2011.
102. Maeda, Y., M. Sekine, and T. Tamura, *Relationship between measurement site and motion artifacts in wearable reflected photoplethysmography*. J Med Syst, 2011. **35**(5): p. 969-76.
103. Vogel, S., et al., *In-ear vital signs monitoring using a novel microoptic reflective sensor.* IEEE Trans Inf Technol Biomed, 2009. **13**(6): p. 882-9.
104. Shin, K., et al., *A Novel Headset with a Transmissive PPG Sensor for Heart Rate Measurement*, in *13th International Conference on Biomedical Engineering*, C. Lim and J.H. Goh, Editors. 2009, Springer Berlin Heidelberg. p. 519-522.
105. Poh, M.-Z., N.C. Swenson, and R.W. Picard, *Motion-tolerant magnetic earring sensor and wireless earpiece for wearable photoplethysmography*. Trans. Info. Tech. Biomed., 2010. **14**(3): p. 786-794.
106. Ming-Zher, P., et al., *Cardiovascular Monitoring Using Earphones and a Mobile Device.* Pervasive Computing, IEEE, 2012. **11**(4): p. 18-26.
107. Kyriacou, P.A., et al., *A system for investigating oesophageal photoplethysmographic signals in anaesthetised patients.* Med Biol Eng Comput, 1999. **37**(5): p. 639-43.
108. Kyriacou, P.A., et al., *Esophageal pulse oximetry utilizing reflectance photoplethysmography.* IEEE Trans Biomed Eng, 2002. **49**(11): p. 1360-8.
109. Kyriacou, P.A., *Direct pulse oximetry within the esophagus, on the surface of abdominal viscera, and on free flaps.* Anesth Analg, 2013. **117**(4): p. 824-33.
110. Mendelson, Y. and C. Pujary. *Measurement site and photodetector size considerations in optimizing power consumption of a wearable reflectance pulse oximeter*. in *Engineering in Medicine and Biology Society, 2003. Proceedings of the 25th Annual International Conference of the IEEE*. 2003.
111. Lee, E.M., et al. *Glass-type wireless PPG measuring system*. in *Engineering in Medicine and Biology Society (EMBC), 2010 Annual International Conference of the IEEE*. 2010.
112. Tur, E., et al., *Basal Perfusion of the Cutaneous Microcirculation: Measurements as a Function of Anatomic Position.* J Investig Dermatol, 1983. **81**(5): p. 442-446.
113. Dresher, R.M., Y. . *Attachment of a wearable skin reflectance pulse oximeter*. in *In Proceedings of the 2005 BMES Annual Fall Meeting*. 2005. Baltimore, MD, USA.

114. Lee, H.-W.L., J.-W.; Jung, W.-C.; Lee, G.-K. , *The periodic moving average filter for removing motion artifacts from PPG signals.* Int. J. Ctrl. Autom. Syst. , 2007. **5**: p. 701-706.
115. Lee, J., et al., *Design of filter to reject motion artifact of pulse oximetry.* Computer Standards & Interfaces, 2004. **26**(3): p. 241-249.
116. Harry Asada, H., H.H. Jiang, and P. Gibbs, *Active noise cancellation using MEMS accelerometers for motion-tolerant wearable bio-sensors.* Conf Proc IEEE Eng Med Biol Soc, 2004. **3**: p. 2157-60.
117. Lee, B., et al., *Adaptive comb filtering for motion artifact reduction from PPG with a structure of adaptive lattice IIR notch filter.* Conf Proc IEEE Eng Med Biol Soc, 2011. **2011**: p. 7937-40.
118. Chan, K.W. and Y.T. Zhang. *Adaptive reduction of motion artifact from photoplethysmographic recordings using a variable step-size LMS filter*. in *Sensors, 2002. Proceedings of IEEE*. 2002.
119. Han, H., M.J. Kim, and J. Kim, *Development of real-time motion artifact reduction algorithm for a wearable photoplethysmography.* Conf Proc IEEE Eng Med Biol Soc, 2007. **2007**: p. 1538-41.
120. Wood, L. and I.o.T. Massachusetts, *Motion Artifact Reduction for Wearable Photoplethysmogram Sensors Using Micro Accelerometers and Laguerre Series Adaptive Filters*. 2008.
121. Jutten, C. and P. Comon, *Chapter 1 - Introduction*, in *Handbook of Blind Source Separation*, P. Comon and C. Jutten, Editors. 2010, Academic Press: Oxford. p. 1-22.
122. Yao, J. and S. Warren, *A short study to assess the potential of independent component analysis for motion artifact separation in wearable pulse oximeter signals.* Conf Proc IEEE Eng Med Biol Soc, 2005. **4**: p. 3585-8.
123. Kim, B.S. and S.K. Yoo, *Motion artifact reduction in photoplethysmography using independent component analysis.* IEEE Trans Biomed Eng, 2006. **53**(3): p. 566-8.
124. Wood, L. and H. Harry Asada, *Active motion artifact reduction for wearable sensors using laguerre expansion and signal separation.* Conf Proc IEEE Eng Med Biol Soc, 2005. **4**: p. 3571-4.
125. Lee, C.M. and Y.T. Zhang. *Reduction of motion artifacts from photoplethysmographic recordings using a wavelet denoising approach*. in *Biomedical Engineering, 2003. IEEE EMBS Asian-Pacific Conference on*. 2003.
126. Yan, Y.S., C.C. Poon, and Y.T. Zhang, *Reduction of motion artifact in pulse oximetry by smoothed pseudo Wigner-Ville distribution.* J Neuroeng Rehabil, 2005. **2**(1): p. 3.
127. Chon, K.H., S. Dash, and J. Kihwan, *Estimation of Respiratory Rate From Photoplethysmogram Data Using Time–Frequency Spectral Estimation.* Biomedical Engineering, IEEE Transactions on, 2009. **56**(8): p. 2054-2063.
128. Baumgartner, C., et al., *Discussion of "time-frequency techniques in biomedical signal analysis: a tutorial review of similarities and differences".* Methods Inf Med, 2013. **52**(4): p. 297-307.
129. Zhilin, Z., P. Zhouyue, and L. Benyuan, *TROIKA: A General Framework for Heart Rate Monitoring Using Wrist-Type Photoplethysmographic Signals During Intensive Physical Exercise.* Biomedical Engineering, IEEE Transactions on, 2015. **62**(2): p. 522-531.
130. Zhang, Z., *Photoplethysmography-Based Heart Rate Monitoring in Physical Activities via Joint Sparse Spectrum Reconstruction.* Biomedical Engineering, IEEE Transactions on, 2015. **PP**(99): p. 1-1.
131. Gardner, T.J. and M.O. Magnasco, *Sparse time-frequency representations.* Proceedings of the National Academy of Sciences, 2006. **103**(16): p. 6094-6099.
132. Aase, S.O., et al., *CPR artifact removal from human ECG using optimal multichannel filtering.* IEEE Trans Biomed Eng, 2000. **47**(11): p. 1440-9.
133. Rahman, M.Z.U., R.A. Shaik, and D.V.R.K. Reddy. *Adaptive noise removal in the ECG using the Block LMS algorithm*. in *Adaptive Science & Technology, 2009. ICAST 2009. 2nd International Conference on*. 2009.
134. Deepu, C.J., et al. *An ECG-on-Chip for Wearable Cardiac Monitoring Devices*. in *Electronic Design, Test and Application, 2010. DELTA '10. Fifth IEEE International Symposium on*. 2010.

135. Zito, D., et al., *Feasibility Study and Design of a Wearable System-on-a-Chip Pulse Radar for Contactless Cardiopulmonary Monitoring.* Int J Telemed Appl, 2008: p. 328597.
136. Lanata, A., E.P. Scilingo, and D. De Rossi, *A Multimodal Transducer for Cardiopulmonary Activity Monitoring in Emergency.* Information Technology in Biomedicine, IEEE Transactions on, 2010. **14**(3): p. 817-825.
137. Webster, J.G. and J.W. Clark, *Medical Instrumentation: Application and Design*. 1995: Wiley.
138. Thakor N, W.J. *The origin of skin potential and its variations*. in *In: Proc. Ann. Conf. Eng. Biol. Med.* 1987.
139. de Talhouet H, W.J., *The origin of skin-stretch-caused motion artifacts under electrodes.* Physiological Measurement, 1996. **17**(2).
140. Chaudhuri, S., T.D. Pawar, and S. Duttagupta, *Ambulation Analysis in Wearable ECG*. 2010: Springer US.
141. Yunfeng, W. and R.M. Rangayyan. *An Algorithm for Evaluating the Performance of Adaptive Filters for the Removal of Artifacts in ECG Signals*. in *Electrical and Computer Engineering, 2007. CCECE 2007. Canadian Conference on*. 2007.
142. Shoker, L., S. Sanei, and J. Chambers, *Artifact removal from electroencephalograms using a hybrid BSS-SVM algorithm.* Signal Processing Letters, IEEE, 2005. **12**(10): p. 721-724.
143. Velazquez, R. *An optimal adaptive filtering approach for stress-tests motion artifacts removal: application on an ECG for telediagnosis*. in *Signal Processing, 2002 6th International Conference on*. 2002.
144. Hedley, M. and H. Yan, *Motion artifact suppression: a review of post-processing techniques.* Magn Reson Imaging, 1992. **10**(4): p. 627-35.
145. Greco, A., et al., *On the deconvolution analysis of electrodermal activity in bipolar patients.* Conf Proc IEEE Eng Med Biol Soc, 2012. **2012**: p. 6691-4.
146. Lanata, A., et al., *How the Autonomic Nervous System and Driving Style Change With Incremental Stressing Conditions During Simulated Driving.* Intelligent Transportation Systems, IEEE Transactions on, 2015. **16**(3): p. 1505-1517.
147. Serteyn, A., et al., *Using an injection signal to reduce motion artifacts in capacitive ECG measurements.* Conf Proc IEEE Eng Med Biol Soc, 2013. **2013**: p. 4795-8.
148. Lim, Y.G., K.K. Kim, and K.S. Park, *ECG recording on a bed during sleep without direct skin-contact.* IEEE Trans Biomed Eng, 2007. **54**(4): p. 718-25.
149. Sameni, R., C. Jutten, and M.B. Shamsollahi, *Multichannel electrocardiogram decomposition using periodic component analysis.* IEEE Trans Biomed Eng, 2008. **55**(8): p. 1935-40.
150. Sameni, R. and G.D. Clifford, *A Review of Fetal ECG Signal Processing; Issues and Promising Directions.* Open Pacing Electrophysiol Ther J, 2010. **3**: p. 4-20.
151. Tam, H.W. and J.G. Webster, *Minimizing electrode motion artifact by skin abrasion.* IEEE Trans Biomed Eng, 1977. **24**(2): p. 134-9.
152. Burbank, D.P. and J.G. Webster, *Reducing skin potential motion artefact by skin abrasion.* Med Biol Eng Comput, 1978. **16**(1): p. 31-8.
153. Yelderman, M., et al., *ECG enhancement by adaptive cancellation of electrosurgical interference.* IEEE Trans Biomed Eng, 1983. **30**(7): p. 392-8.
154. Ferrara, E.R. and B. Widrow, *Fetal electrocardiogram enhancement by time-sequenced adaptive filtering.* IEEE Trans Biomed Eng, 1982. **29**(6): p. 458-60.
155. Vullings, R., B. de Vries, and J.W. Bergmans, *An adaptive Kalman filter for ECG signal enhancement.* IEEE Trans Biomed Eng, 2011. **58**(4): p. 1094-103.
156. Widrow, B., et al., *Adaptive noise cancelling: Principles and applications.* Proceedings of the IEEE, 1975. **63**(12): p. 1692-1716.
157. Thakor, N.V. and Y.S. Zhu, *Applications of adaptive filtering to ECG analysis: noise cancellation and arrhythmia detection.* IEEE Trans Biomed Eng, 1991. **38**(8): p. 785-94.

158. Rahman, M.Z.U., R.A. Shaik, and D.V.R.K. Reddy. *Noise cancellation in ECG signals using normalized Sign-Sign LMS algorithm*. in *Signal Processing and Information Technology (ISSPIT), 2009 IEEE International Symposium on*. 2009.
159. Rahman, M.Z.U., R.A. Shaik, and D.V.R.K. Reddy, *Efficient and Simplified Adaptive Noise Cancelers for ECG Sensor Based Remote Health Monitoring.* Sensors Journal, IEEE, 2012. **12**(3): p. 566-573.
160. Elbuni, A., et al. *ECG Parameter Extraction Algorithm using (DWTAE) Algorithm.* in *Computer Technology and Development, 2009. ICCTD '09. International Conference on*. 2009.
161. Thanapatay, D., C. Suwansaroj, and C. Thanawattano. *ECG beat classification method for ECG printout with Principle Components Analysis and Support Vector Machines*. in *Electronics and Information Engineering (ICEIE), 2010 International Conference On*. 2010.
162. Akshay, N., et al. *ECG noise removal and QRS complex detection using UWT*. in *Electronics and Information Engineering (ICEIE), 2010 International Conference On*. 2010.
163. Wentao, S. and Z. Dan. *Noise reduction of ECG using spatial correlation filtering and stationary wavelet transform*. in *Computer Science and Education (ICCSE), 2010 5th International Conference on*. 2010.
164. Suyi, L. and L. Jun. *The Optimal De-noising Algorithm for ECG Using Stationary Wavelet Transform*. in *Computer Science and Information Engineering, 2009 WRI World Congress on*. 2009.
165. Liu, X., et al., *Multiple Functional ECG Signal is Processing for Wearable Applications of Long-Term Cardiac Monitoring.* Biomedical Engineering, IEEE Transactions on, 2011. **58**(2): p. 380-389.
166. Mithun, P., et al. *A wavelet based technique for suppression of EMG noise and motion artifact in ambulatory ECG*. in *Engineering in Medicine and Biology Society, EMBC, 2011 Annual International Conference of the IEEE*. 2011.
167. Pawar, T., S. Chaudhuri, and S.P. Duttagupta. *Analysis of Ambulatory ECG Signal*. in *Engineering in Medicine and Biology Society, 2006. EMBS '06. 28th Annual International Conference of the IEEE*. 2006.
168. Pawar, T., S. Chaudhuri, and S.P. Duttagupta, *Body Movement Activity Recognition for Ambulatory Cardiac Monitoring.* Biomedical Engineering, IEEE Transactions on, 2007. **54**(5): p. 874-882.
169. Pawar, T., et al., *Impact analysis of body movement in ambulatory ECG.* Conf Proc IEEE Eng Med Biol Soc, 2007. **2007**: p. 5453-6.
170. Barros, A.K., A. Mansour, and N. Ohnishi, *Removing artifacts from electrocardiographic signals using independent components analysis.* Neurocomputing, 1998. **22**(1–3): p. 173-186.
171. Milanesi, M., et al., *Independent component analysis applied to the removal of motion artifacts from electrocardiographic signals.* Med Biol Eng Comput, 2008. **46**(3): p. 251-61.
172. Chawla, M.P.S., *PCA and ICA processing methods for removal of artifacts and noise in electrocardiograms: A survey and comparison.* Applied Soft Computing, 2011. **11**(2): p. 2216-2226.
173. Lee, J., et al., *Automatic motion and noise artifact detection in Holter ECG data using empirical mode decomposition and statistical approaches.* IEEE Trans Biomed Eng, 2012. **59**(6): p. 1499-506.
174. Chang, K.M., *Arrhythmia ECG noise reduction by ensemble empirical mode decomposition.* Sensors (Basel), 2010. **10**(6): p. 6063-80.
175. Maji, U., M. Mitra, and S. Pal, *Automatic Detection of Atrial Fibrillation Using Empirical Mode Decomposition and Statistical Approach.* Procedia Technology, 2013. **10**: p. 45-52.
176. Petterson, M.T., V.L. Begnoche, and J.M. Graybeal, *The effect of motion on pulse oximetry and its clinical significance.* Anesth Analg, 2007. **105**(6 Suppl): p. S78-84.

177. Nakajima, K., T. Tamura, and H. Miike, *Monitoring of heart and respiratory rates by photoplethysmography using a digital filtering technique.* Medical Engineering & Physics, 1996. **18**(5): p. 365-372.
178. Sahni, R., et al., *Motion resistant pulse oximetry in neonates.* Arch Dis Child Fetal Neonatal Ed, 2003. **88**(6): p. F505-8.
179. Barker, S.J. and N.K. Shah, *The effects of motion on the performance of pulse oximeters in volunteers (revised publication).* Anesthesiology, 1997. **86**(1): p. 101-8.
180. Foo, J.Y. and S.J. Wilson, *A computational system to optimise noise rejection in photoplethysmography signals during motion or poor perfusion states.* Med Biol Eng Comput, 2006. **44**(1-2): p. 140-5.
181. Lee, H., *The periodic moving average filter for removing motion artifacts from PPG signals.* International Journal of Control Automation and System, 2007. **5**(6): p. 701-706.
182. Sweeney, K.T., T.E. Ward, and S.F. McLoone, *Artifact Removal in Physiological Signals—Practices and Possibilities.* Information Technology in Biomedicine, IEEE Transactions on, 2012. **16**(3): p. 488-500.
183. Tobin, R.M., J.A. Pologe, and P.B. Batchelder, *A characterization of motion affecting pulse oximetry in 350 patients.* Anesth Analg, 2002. **94**(1 Suppl): p. S54-61.
184. Trivedi, N.S., et al., *Effects of motion, ambient light, and hypoperfusion on pulse oximeter function.* J Clin Anesth, 1997. **9**(3): p. 179-83.
185. Patterson, J.A.C. and Y. Guang-Zhong, *Ratiometric Artifact Reduction in Low Power Reflective Photoplethysmography.* Biomedical Circuits and Systems, IEEE Transactions on, 2011. **5**(4): p. 330-338.
186. Li, K. and S. Warren, *A wireless reflectance pulse oximeter with digital baseline control for unfiltered photoplethysmograms.* IEEE Trans Biomed Circuits Syst, 2012. **6**(3): p. 269-78.
187. Ram, M.R., et al., *A Novel Approach for Motion Artifact Reduction in PPG Signals Based on AS-LMS Adaptive Filter.* Instrumentation and Measurement, IEEE Transactions on, 2012. **61**(5): p. 1445-1457.
188. Rusch, T.L., R. Sankar, and J.E. Scharf, *Signal processing methods for pulse oximetry.* Comput Biol Med, 1996. **26**(2): p. 143-59.
189. Hong Enriquez, R., et al., *Analysis of the photoplethysmographic signal by means of the decomposition in principal components.* Physiol Meas, 2002. **23**(3): p. N17-29.
190. Kim, B.S. and S.K. Yoo, *Motion artifact reduction in photoplethysmography using independent component analysis.* Biomedical Engineering, IEEE Transactions on, 2006. **53**(3): p. 566-568.
191. Ram, M.R., et al. *Use of spectral estimation methods for computation of SpO_2 from artifact reduced PPG signals*. in *Recent Advances in Intelligent Computational Systems (RAICS), 2011 IEEE*. 2011.
192. Krishnan, R., B. Natarajan, and S. Warren, *Two-Stage Approach for Detection and Reduction of Motion Artifacts in Photoplethysmographic Data.* Biomedical Engineering, IEEE Transactions on, 2010. **57**(8): p. 1867-1876.
193. Sukor, J.A., S.J. Redmond, and N.H. Lovell, *Signal quality measures for pulse oximetry through waveform morphology analysis.* Physiol Meas, 2011. **32**(3): p. 369-84.
194. Li, K., S. Warren, and B. Natarajan, *Onboard Tagging for Real-Time Quality Assessment of Photoplethysmograms Acquired by a Wireless Reflectance Pulse Oximeter.* Biomedical Circuits and Systems, IEEE Transactions on, 2012. **6**(1): p. 54-63.
195. Li, Q., R.G. Mark, and G.D. Clifford, *Robust heart rate estimation from multiple asynchronous noisy sources using signal quality indices and a Kalman filter.* Physiol Meas, 2008. **29**(1): p. 15-32.
196. Karlen, W., et al., *Photoplethysmogram signal quality estimation using repeated Gaussian filters and cross-correlation.* Physiol Meas, 2012. **33**(10): p. 1617-29.

197. Lee, B., et al., *Improved elimination of motion artifacts from a photoplethysmographic signal using a Kalman smoother with simultaneous accelerometry.* Physiol Meas, 2010. **31**(12): p. 1585-603.
198. Dash, S., et al., *Automatic real time detection of atrial fibrillation.* Ann Biomed Eng, 2009. **37**(9): p. 1701-9.
199. Yu, C., et al., *A method for automatic identification of reliable heart rates calculated from ECG and PPG waveforms.* J Am Med Inform Assoc, 2006. **13**(3): p. 309-20.
200. Mannacio, V., et al., *Coronary perfusion: Impact of flow dynamics and geometric design of 2 different aortic prostheses of similar size.* The Journal of thoracic and cardiovascular surgery, 2012. **143**(5): p. 1030-1035.
201. Naraharisetti, K.V.P., M. Bawa, and M. Tahernezhadi. *Comparison of different signal processing methods for reducing artifacts from photoplethysmograph signal*. in *Electro/Information Technology (EIT), 2011 IEEE International Conference on*. 2011.
202. Hsu, C.-W., C.-C. Chang, and C.-J. Lin, *A Practical Guide to Support Vector Classification*. 2003, Department of Computer Science, National Taiwan University.
203. Gil, E., J. María Vergara, and P. Laguna, *Detection of decreases in the amplitude fluctuation of pulse photoplethysmography signal as indication of obstructive sleep apnea syndrome in children.* Biomedical Signal Processing and Control, 2008. **3**(3): p. 267-277.
204. Selvaraj, N., et al. *Statistical approach for the detection of motion/noise artifacts in Photoplethysmogram*. in *Engineering in Medicine and Biology Society,EMBC, 2011 Annual International Conference of the IEEE*. 2011.
205. Chang, K.-M. and K.-M. Chang, *Pulse rate derivation and its correlation with heart rate.* Journal of Medical and Biological Engineering, 2009. **29**(3): p. 132-137.
206. Engelen, M., et al., *Effects of hypoxic hypoxia on O2 uptake and heart rate kinetics during heavy exercise.* Journal of applied physiology, 1996. **81**(6): p. 2500-2508.
207. Andersen, P. and B. Saltin, *Maximal perfusion of skeletal muscle in man.* The Journal of Physiology, 1985. **366**(1): p. 233-249.
208. Samorodov, A., *Application of a fuzzy integral for weak classifiers boosting.* Pattern Recognition and Image Analysis, 2011. **21**(2): p. 206-210.
209. Comtois, G., Y. Mendelson, and P. Ramuka. *A Comparative Evaluation of Adaptive Noise Cancellation Algorithms for Minimizing Motion Artifacts in a Forehead-Mounted Wearable Pulse Oximeter*. in *Engineering in Medicine and Biology Society, 2007. EMBS 2007. 29th Annual International Conference of the IEEE*. 2007.
210. Ganeshapillai, G. and J. Guttag, *Real time reconstruction of quasiperiodic multi parameter physiological signals.* EURASIP Journal on Advances in Signal Processing, 2012. **2012**(1): p. 1-15.
211. Arafat, M.A., T.B. Mahmud, and M.S. Billah. *Retrieving and smoothing fundamental waves from noise corrupted ECG beat using Gaussian functions*. in *Electrical & Computer Engineering (ICECE), 2012 7th International Conference on*. 2012. IEEE.
212. Mangia, M., R. Rovatti, and G. Setti, *Rakeness in the design of Analog-to-Information Conversion of Sparse and Localized Signals*. Circuits and Systems I: Regular Chapters, IEEE Transactions on, 2012. **59**(5): p. 1001-1014.
213. Hjorth, B., *EEG analysis based on time domain properties.* Electroencephalography and Clinical Neurophysiology, 1970. **29**(3): p. 306-310.
214. Hjorth, B., *The physical significance of time domain descriptors in EEG analysis.* Electroencephalography and Clinical Neurophysiology, 1973. **34**(3): p. 321-325.
215. Olfati-Saber, R. and J.S. Shamma. *Consensus filters for sensor networks and distributed sensor fusion*. in *Decision and Control, 2005 and 2005 European Control Conference. CDC-ECC'05. 44th IEEE Conference on*. 2005. IEEE.

216. Antonsen, L.P. and K.A. Kirkebøen, *Evaluation of Fluid Responsiveness: Is Photoplethysmography a Noninvasive Alternative?* Anesthesiology Research and Practice, 2012. **2012**: p. 10.
217. Salehizadeh, S.M., et al., *Photoplethysmograph Signal Reconstruction based on a Novel Motion Artifact Detection-Reduction Approach. Part II: Motion and Noise Artifact Removal.* Ann Biomed Eng, 2014.
218. Ram, M.R., et al. *Computation of SpO<inf>2</inf> using non-parametric spectral estimation methods from wavelet based motion artifact reduced PPG signals*. in *Signal Processing, Communication, Computing and Networking Technologies (ICSCCN), 2011 International Conference on*. 2011.
219. Krishnan, R., B. Natarajan, and S. Warren. *Analysis and detection of motion artifact in photoplethysmographic data using higher order statistics*. in *Acoustics, Speech and Signal Processing, 2008. ICASSP 2008. IEEE International Conference on*. 2008.
220. Chong, J.W., et al., *Photoplethysmograph Signal Reconstruction Based on a Novel Hybrid Motion Artifact Detection-Reduction Approach. Part I: Motion and Noise Artifact Detection.* Ann Biomed Eng, 2014.
221. Eckmann, J.P., S.O. Kamphorst, and D. Ruelle, *Recurrence Plots of Dynamical Systems.* EPL (Europhysics Letters), 1987. **4**(9): p. 973.
222. Takens, F., *Detecting strange attractors in turbulence*, in *Dynamical Systems and Turbulence, Warwick 1980*, D. Rand and L.-S. Young, Editors. 1981, Springer Berlin Heidelberg. p. 366-381.
223. *MIT/BIH Atrial Fibrillation Database*. Available from: http://www.physionet.org/physiobank/database/afdb/.
224. Pan, J. and W.J. Tompkins, *A Real-Time QRS Detection Algorithm.* Biomedical Engineering, IEEE Transactions on, 1985. **BME-32**(3): p. 230-236.

Chapter 4: RepMA – A Novel Motion and Noise Detection Algorithm

4.1. Introduction

In previous chapter, we propose a technique for motion and noise artifact detection using features of PPG signal in time-domain. One drawback of TDV technique since it is based on statistical properties of the signal shape, is when the frequency of the signal is changing fast or the amplitude of it is changing due to dehydration or blood loss, it would detect the data as corrupted. Statistical measures, such as skewness, kurtosis (K), and quadratic phase coupling, Shannon entropy (SE), and Renyi's entropy [204], have been shown to be helpful in determining the SQI. These statistical algorithms discriminate amplitude distributions between PPG segments with an assumption that clean and corrupt segments would form two separate groups. However, PPG morphology vary among patients, thus yielding multitude of amplitude distributions. Therefore, it would be difficult to obtain high accuracy from these algorithms in practice. On the other hand, TDV method is highly dependent on accuracy of the peak amplitude detection. Unlike the electrocardiogram (ECG), the PPG waveform does not have distinctive peaks which make accurate peak detection challenging. The dependency on a peak detection subroutine is another drawback of the TDV algorithm and inevitably affects its performance.

In this chapter, a new real-time algorithm based on recurrence quantification is presented that can distinguish between PPG signal with motion and noise artifacts and MA-free signals. The idea is to process the PPG signal in time-time domain by transforming the 1-D signal to a 2-D image and analyze the image for MA detection. The algorithm comprised of 5 distinct stages and it is called "RepMA": (1) Downsampling, (2) Transforming 1-D PPG vector to time-time **Re**currence 2-D **p**lots (3) Image processing, (4) **MA** detection. By taking the raw PPG signal, RepMA algorithm first resamples the signal to ¼ of original sampling rate. Next by calculating the recurrence matrix of downsampled PPG signal, time-time recurrence image would be obtained. Next the recurrence image should be analyzed and processed to investigate MA corrupted patterns in the PPG recurrence image. By comparing the images of each 4-sec

segment to its correspondence reference clean image MA corrupted segments can be discriminated from clean PPG segments. Thus the algorithm can detect if a PPG segment at each 4-sec window is corrupted by movement and noise or not. We will show in result section that the proposed RepMA algorithm is well performed in real-time detection and discrimination between, clean and MA-corrupted PPG recordings in different movement scenarios and experiments.

4.2. Materials and Experiments

The RepMA algorithm was evaluated on four different datasets. The datasets (1) and (2) were recorded in controlled condition from 10 subjects in Chon lab and the datasets (3) and (4) were provided by UMASS Hospital recorded from 10 patients.

(1) and (2) [Chon Lab Dataset]: For the laboratory controlled environment, both forehead and finger worn PO sensor data were collected from healthy subjects recruited from the student community of Worcester Polytechnic Institute (WPI). Laboratory data allows us to have more control over the duration of MNA generated to ensure that the detection phase of algorithm was tested on a wide range of MNA duration. In laboratory-controlled head and finger movement data, motion artifacts were induced by head and finger movements for specific time intervals in both horizontal and vertical directions. For head movement data, 11 healthy volunteers were asked to wear our PO on the forehead along with a reference Masimo Radical (Masimo SET®) finger type transmittance pulse oximeter. The subjects were all healthy with no past histories of cardiovascular diseases. After baseline recording for 5 minutes without any movement, subjects were instructed to introduce motion artifacts for specific time intervals varying from 10 to 50% within a 1 minute segment. For example, if a subject was instructed to perform left-right random movements for 6 seconds, a 1 min segment of data would contain 10% noise. The finger laboratory movement data were recorded in a similar setup as the head data using our custom-made PPG finger sensor.

(3) and (4) [UMASS Hospital Dataset]: The next data set was acquired from patients who were admitted to our partner hospital at the UMass Memorial Medical Center (UMMC). Data from patients provided most realistic information on the motion artifacts since the patients were allowed to move freely as long as the sensors were positioned properly. The patient PPG data were recorded from 10 subjects admitted to emergency rooms at UMMC. Similar to the laboratory-controlled dataset, each patient was fitted with our custom-made sensors (both forehead and finger) and the Masimo POs on the forehead and fingers, respectively. One subject had hypertension and 2 subjects suffered from hypercholesterolemia and hyperlipidemia; the remaining subjects were considered free from cardiovascular diseases. All recording were performed in the Emergency Department with a room temperature of 68oF. The patients were admitted due to pain related symptoms and were not restrained from making natural movements. Therefore, they are expected to generate many different but natural characteristics of MNA in the recorded PPG.

This study was approved by both WPI's and UMMC's IRBs and all subjects were given informed consents prior to data recordings. Chon Lab data used in this chapter were collected using our custom-made multi-channel pulse oximeters. The subjects in the lab were all healthy with no past histories of cardiovascular diseases. All lab recordings were performed in a quiet room with temperature of 70oF. There were two versions with different form factors to capture PPG at the user's forehead and finger. The forehead sensor is termed 6PD-forehead since it consisted of 6 photodetectors concentric around the center-paired LEDs with the peak wavelengths of 660nm (red) and 940nm (infrared). The finger sensor, due to space constrain, consisted of 3 photodetectors concentric around center paired LEDs with the same specification of the 6PD-forehead sensor. The PPGs were sampled at 80Hz. The scope of this study was to evaluate the efficacy of our proposed RepMA algorithm. Therefore, only one infrared PPG channel deemed to contain the best signal quality data was used for analysis.

All PPG data were pre-processed by a 6th order infinite impulse response (IIR) band pass filter with cut-off frequencies of 0.1 Hz and 10 Hz. Zero-phase forward and reverse filtering was applied to

account for the non-linear phase of the IIR filter. Further details of this study's database including demographic of subjects are given in Table (1).

Table 4.1. PPG Datasets and Experiments Settings

No. Recordings	Dataset	Electrode Type	Subject's Age/Sex	Ethnicity
11	1 (Chon Lab)	Forehead Pulse Oximeter	23-58 y (9 Male, 1 Female)	3 Asian 2 Hispanic 3 American 2 White
11	2 (Chon Lab)	Finger Pulse Oximeter	23-58 y (9 Male, 1 Female)	3 Asian 2 Hispanic 3 American 2 White
10	3 (UMass Hospital database)	Forehead Pulse Oximeter	18-38 y (5 Female, 5 Male)	3 African-American (3 female) 6 Caucasian (1 females/5 male) 1 Puerto Rican (female)
10	4 (UMass Hospital database)	Finger Pulse Oximeter	18-45y (4 Female, 6 Male)	1 African-American 1 Hispanic 7 Caucasian 1 Puerto Rican

4.2.1. Reference signal for MNA Detection

Many recent publications on MNA detection utilized human visual inspection from experts who were familiar with PPG and their decisions are regard it as the gold standard for marking MNA corrupted data [204, 219, 220]. In our work, we also use the human visual inspection to establish a MNA reference for our datasets. Three inspectors individually marked MNA corrupted portions of the PPG. Disagreements of the marked portions were resolved by majority votes. Cohen's κ was used to determine if there was agreement between three inspectors' judgement on whether PPG segments were declared to be clean or corrupted. For each dataset, the average Cohan's κ was reported in Table (2) over three runs computed from each distinct inspector pair. Overall, the Cohan's κ showed substantial agreement between the inspectors with 95% CI and $p < 0.0005$.

Table 4.5 Averaged Cohen's κ Coefficients representing the agreement between inspectors' decision on PPG labels

	Lab. Head	Lab. Finger	Umass Head	Umass Finger
Cohan's κ	0.823	0.935	0.732	0.791
# of subjects	11	11	10	10
Duration (min)	5	5	10	10

Due to the differences with operating window lengths between the comparing methods, detection results and reference labels were converted to every second. For example, a 1 minute PPG segment would have 60 detection values from each method and 60 reference labels. These results were then used to compute sensitivity, specificity, accuracy for each method.

4.3. Methodology

Noise depending on the level, can distort any existing structure in a recurrence plot [221]. It is desirable that the smallest distance threshold be chosen to increase the resolution of the time-time 2D RP image. However higher threshold can help to preserve the distortions that are made by movement and noise artifacts. The embedding dimension on the other hand has to be chosen so that the dynamics of the system will be well presented by its phase space trajectory. Movement during PPG recordings can increase the laminar states by introducing irregular sudden peaks in the recordings which produce more vertical (horizontal) patterns that might be observed in a clean PPG signal (see Fig4.(a) and (c)). Motion and noise artifact detection procedure of the RepMA algorithm is presented in Table (3).

Table 4.6. RepMA Algorithm Steps

Step 1. Down-sampling PPG signal

- In order to reduce the complexity and run-time the PPG segment at each window is resampled to ¼ of its original sampling frequency.

Step 2. Transferring from 1-D PPG vector to 2-D time-time recurrence image

- At this step recurrence matrix is calculated using the Eq.3 for original PPG for each 4 sec window segment.

Step 3. Recurrence Image Processing

- The recurrence image in this step is preprocessed to distinguish between image of a clean PPG versus MA corrupted one.

Step 4. Motion artifact detection

- Results from of step 3 are compared to a reference threshold values to specify if a PPG segment is clean or corrupted.

4.3.1. Transforming PPG 1-D signal to 2-D image using Recurrence Plot

Recurrence analysis is a graphical method designed to locate hidden recurring patterns, nonstationarity and structural changes in signals which is proposed by Eckmann (1987) [221]. Recurrence is a fundamental property of dynamical systems, which can be exploited to characterize the system's behavior in phase space. Recurrence occurs when a dynamical system returns or recurs to former states. Given a time series $x_k, k = 1,2, \dots, N$; a recurrence plot (RP) shows when the time series visits the same region of phase space, that is

$$X_i \cong X_j, \qquad i \neq j \; and \; i, j = 1,2, \dots, N \qquad (1)$$

Takens [222] theorem shows that we can recreate a topologically equivalent picture of the original multidimensional system behavior by using the time series of a single observable variable, by means of the method of time delays: for the scalar series $x(t)$ we construct the embedded vectors

$$x_k^m = \{x_k, x_{k+d}, x_{k+2d}, \dots, x_{k+(m-1)d})\}, \quad k = 1,2, \dots, N \qquad (2)$$

where N is the number of data points in the signal and m is the embedding dimension and d is the time delay. A phase space does not have a dimension which allows it to be pictured, and higher dimensional phase space can only be visualized by projection into the two or three dimensional sub-space. To this end a matrix of recurrence distances (e.g., Euclidean distances) can be constructed by computing distances between all pairs of embedded vectors;

$$\boldsymbol{R}^m_{\boldsymbol{dist}(i,j)} = \|\vec{x}_i - \vec{x}_j\|, \quad \vec{x}_i \in \mathbb{R}^m, \qquad i, j = 1,2, \dots, N \qquad (3)$$

Fig1.b shows a colored recurrence (distance) plot of a single frequency sinusoid signal. As it can be observed the recurrence plot relates each distance to a color. Thus, the recurrence plot is a solid rectangular plot consisting of pixels whose colors correspond to the magnitude of data values in a two-dimensional array and whose coordinates correspond to the locations of the data values in the array. The

RP provides information for reordering the indices of the phase space vectors so that the vectors are sorted by their norm. If the cumulative distribution of the lengths of the phase space vectors is known, the restored phase space trajectory will recover its amplitude by equating the sorted indices with that distribution.

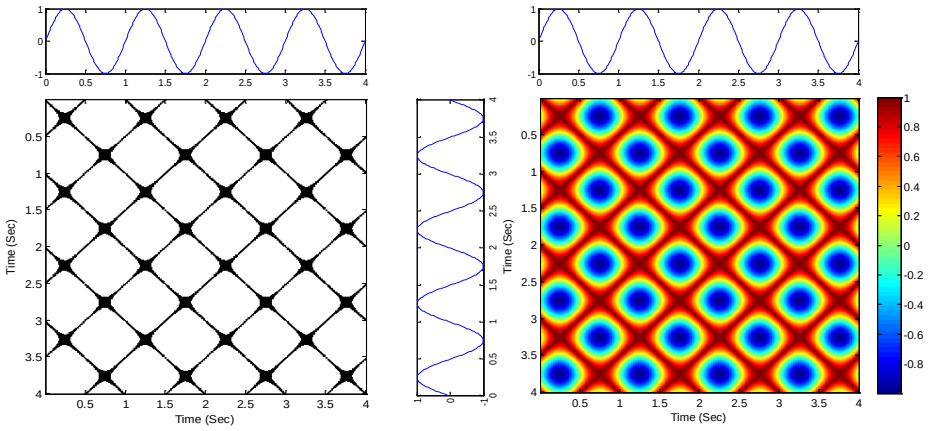

(a) (b)

Figure 4.1 – Recurrence time-time Plot of a single frequency sinusoid signal.
(a) Binary RP, (b) Colored distance RP

The common recurrence plot is usually defined according to a neighborhood criterion and a threshold distance $\mathcal{E}$, by which the paired distances smaller than the threshold assigned with 1 and the rest with 0. Such an RP can be mathematically expressed as

$$\boldsymbol{RP}_{i,j}^{m} = \Theta\left(\mathcal{E}_i - \left\|\vec{x}_i - \vec{x}_j\right\|\right), \qquad \vec{x}_i \in \mathbb{R}^m, \qquad i,j = 1,2,\dots,N \tag{4}$$

Where $\|.\|$ is a norm and $\Theta(.)$ The Heaviside function. Since $\boldsymbol{RP}_{i,j} = 1$ $(i = 1,\dots,N)$ by definition, the RP always has a black diagonal line. The neighborhood criterion determines the recurrence density, which mean with a given $\mathcal{E} = 0.15$, the local neighborhood covers 15% of all phase space vectors and thus the recurrence density is 0.15. In the original definition of the RPs, the neighborhood is a ball (i.e. $L_2 - norm$ is used) and its radius is chosen in such a way that it contains a fixed amount of states $\vec{x}_i$[221]. If the distance threshold $\mathcal{E}_i$ for each data point x_i is set to a constant value then it results to a symmetric binary RP where $\boldsymbol{RP}_{i,j} = \boldsymbol{RP}_{j,i}$.

Fig1.a illustrates the symmetric binary RP with a distance threshold $\varepsilon = 0.05$ corresponding to the sinusoid signal. Fig.2 presents the binary and distance RP of PPG recordings of subject#3 from dataset (1), with $\varepsilon = 0.2$.

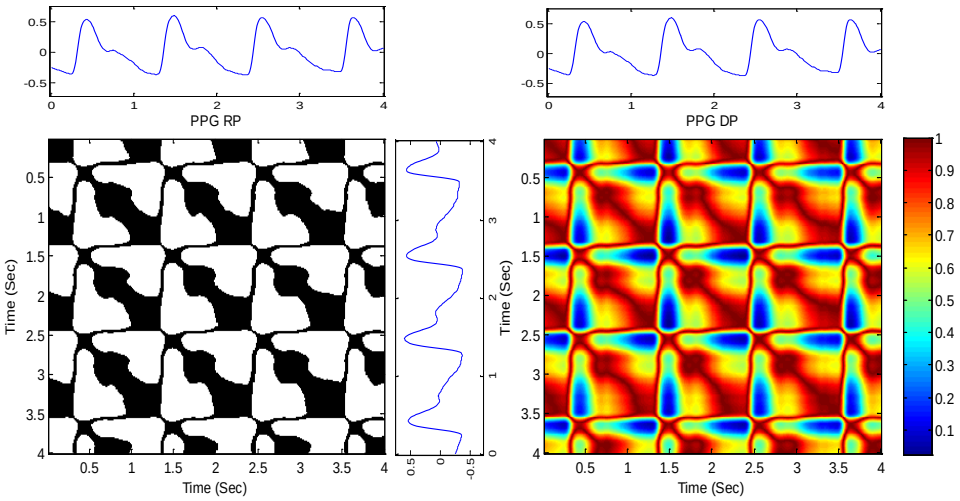

(a) (b)

Figure 4.2 – Recurrence time-time Plot of 4 sec PPG segment of recordings#3 from the first dataset. (a) Binary RP, (b) colored distance RP

Diagonal lines parallel to main diagonal in a RP indicates the time series is deterministic. It seems that the state is trapped for some time [221]. Fig.3b illustrates the reverse recurrence plot of the 4 sec PPG segment. In this chapter we call the reverse recurrence plot of PPG as its recurrence image.

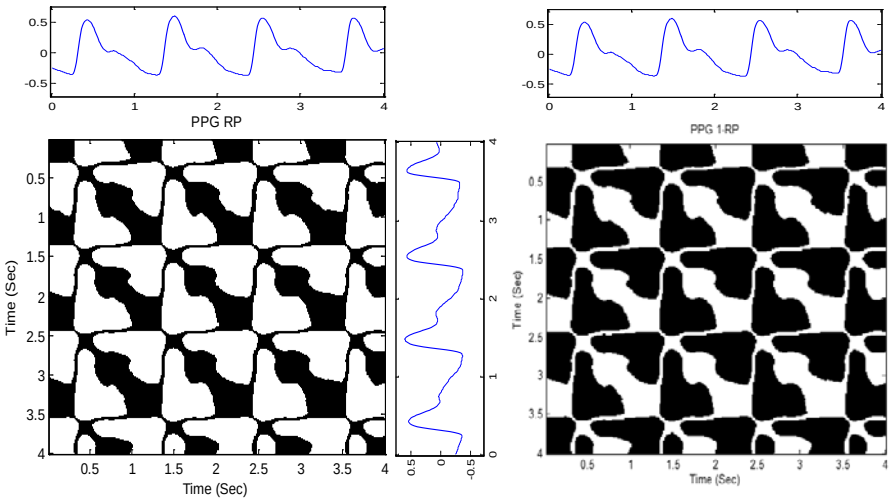

(a) **(b)**

Figure 4.3 – Recurrence time-time Plot of a 4 sec PPG signal. (a) Binary RP, (b) Recurrence Image (RI: 1- RP)

4.3.2. Recurrence Image Processing

Table (4) presents the step-by-step recurrence image processing procedure of RepMA algorithm. This procedure is also shown as flowchart in Fig. 4.

Fig. 4 (Right-Top) shows a 4 sec of a MA-corrupted PPG segment which the corresponding recurrence image is shown below the signal. In the following we analyze this typical corrupted PPG segment using the above RepMA procedure.

Table 4.7 Recurrence Image Processing Procedure in RepMA Algorithm

Stage 1. Calculating the recurrence image for each 4 sec PPG segment data

1.1. Save a reference clean image of PPG
1.2. Update clean reference when a new clean segment is detected

Stage 2. Removing objects attached to the sides of recurrence image

Stage 3. Extracting separate objects from the results of Step 2.

Stage 4. Objects alignment with reference by rescaling and rotation

Stage 5. Calculating the MA corruption criteria of objects from Step 4 using the image centroid equations

$$\mathrm{M}_{ij} = \sum_{x}\sum_{y} x^i \; y^i RI(x,y) \tag{5}$$

$$Centriod(x)_{Obj(k)} = \frac{\mathrm{M}_{10}}{\mathrm{M}_{00}}, \;\; Centriod(y)_{Obj(k)} = \frac{\mathrm{M}_{01}}{\mathrm{M}_{00}} \tag{6}$$

$$MAcr_{image(i)}(k) = \left|Centriod(x)_{Ref\_Object} - Centriod(x)_{Obj(k)}\right| \times \left|Centriod(x)_{Ref\_Object} - Centriod(x)_{Obj(k)}\right| \tag{7}$$

where $k = 1,2,\dots,K(\#objects\ in\ the\ image)$ and $i = 1,2,\dots,N$, is i^{th} PPG segment of 4 sec.

Step 6. Set the threshold for motion artifact detection as $Thd = 5\% \times Centriod(x)_{Ref\_Object} \times Centriod(y)_{Ref\_Object}$

By comparing the $MAcr(k)$ for each object (k) to the defined threshold, if $\max\left(MAcr_{image(i)}\right) > Thd$, then the object$(k)$ in the recurrence image of the corresponding 4-sec segment PPG is corrupted by motion and in total the segment labeled as corrupted. Otherwise if the criteria for all objects in the recurrence image fall below the threshold then the entire image belongs to a clean PPG segment.

As mentioned in section (i) recurrence matrix is symmetric. Thus in order process the recurrence image we concentrate on the left diagonal part of the image. Next step according to Table (4) is to remove the objects in the image that are attached to the edges. The idea here is in a 4 sec segment of PPG the beginning and ending of segment might not include a full cycle of PPG, thus by removing the objects attached to the edges of recurrence image, technically the objects that represent a full cycle of the signal remain in the image. Fig. 5 illustrate the results after removing the objects from the left diagonal recurrence image of both clean and corrupted segments. After removing edge objects, third step is to extract all of the separate objects remain in the image (see Fig.6).

Since the idea of RepMa is to compare the objects in a recurrence image with a reference clean object for MA corruption detection, for fair comparison the objects in each image should be rescaled and realigned with the reference object. Thus every objects that are extracted from previous step are rescale into a (100×100) image matrix. In order to align each object with reference object for fair comparison.

Eight rotation operator (rotate original object by 0o, 90o, 180o, 270o, and rotate the vertically flipped object by 0o, 90o, 180o, 270o). This way we should obtain 8 versions of each object then simply by calculating the error between reference object (100×100) matrix and those of the eight versions of an object, the object with the minimum error with reference is chosen to be the most aligned version of the object.

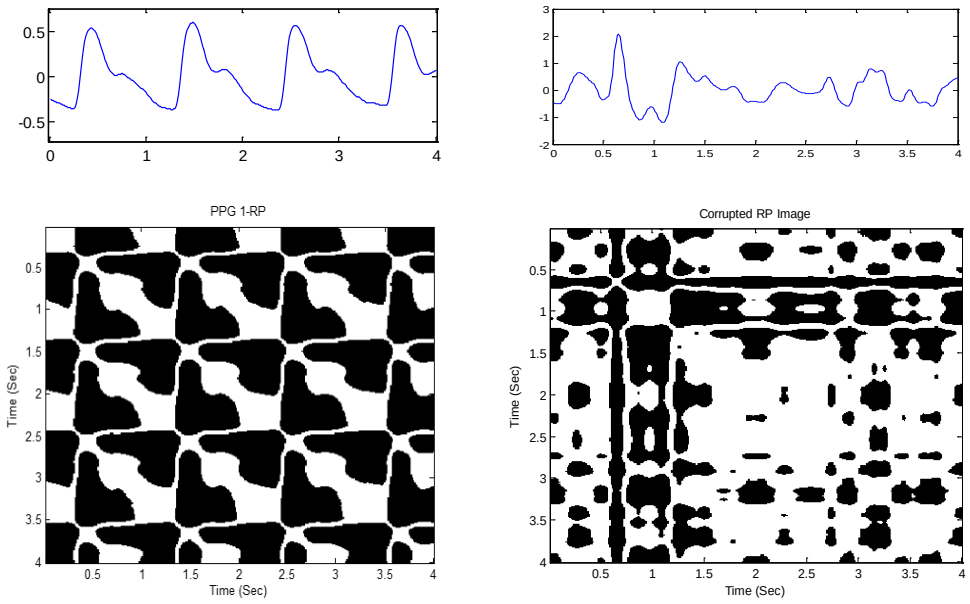

(a) (b)

Figure 4.4 – A typical Clean vs. Corrupted PPG segment from recording #3. (a-Top) Clean 4 sec PPG, (a-Bottom) Clean Recurrence Image (b-Top) MA Corrupted PPG, (b-Bottom) Corrupted Recurrence Image

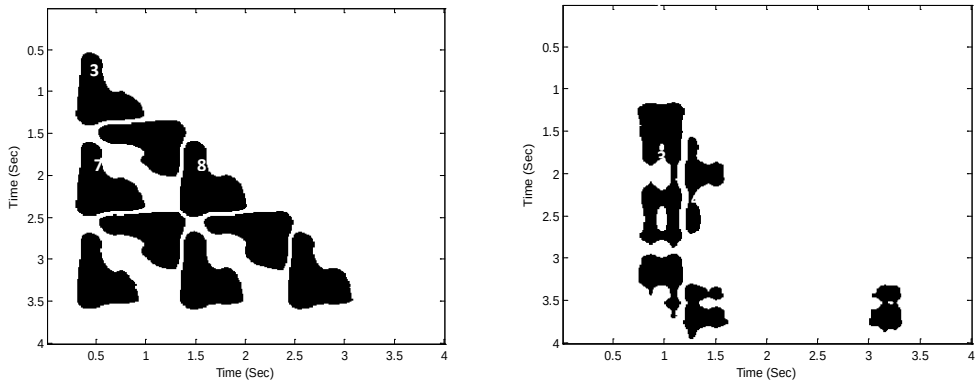

(a) (b)

Figure 4.5 – Removing edge objects from left-diagonal recurrence image. (a) Clean Image, (b) Corrupted Image

The following show the equation for choosing the optimal version of each object

$$V^* = \arg\min_{v} \left| Obj_{Ref} - Obj\{k\}_{image(i)}{}^{v} \right| \quad (8)$$

where $v = 1,2 \ldots ,8$ is version of object(k), $k = 1,2, \ldots , K$, is number of objects in each recurrence image(i), and $i = 1,2, \ldots , N$, is i^{th} PPG segment of 4 sec.

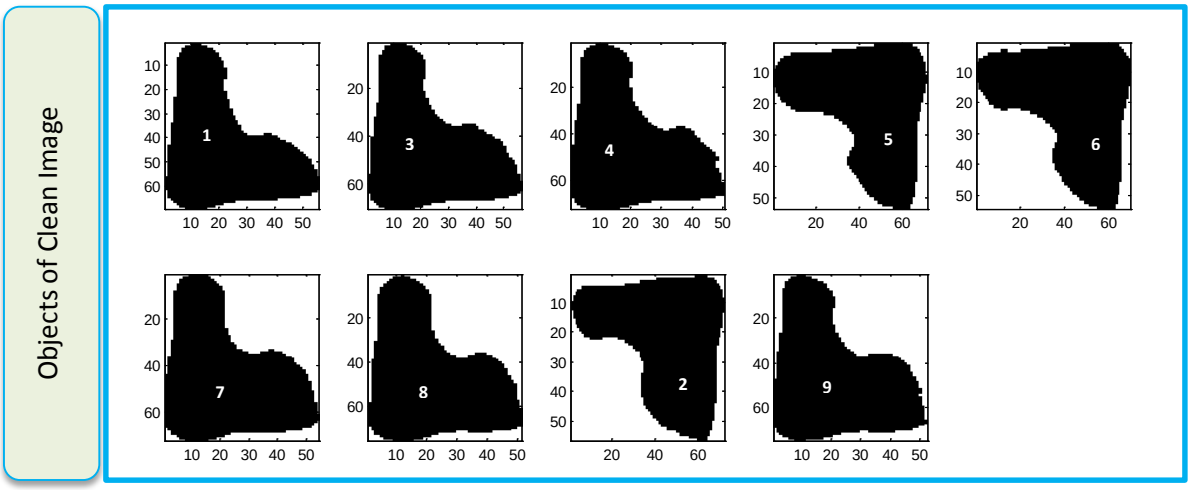

(a)

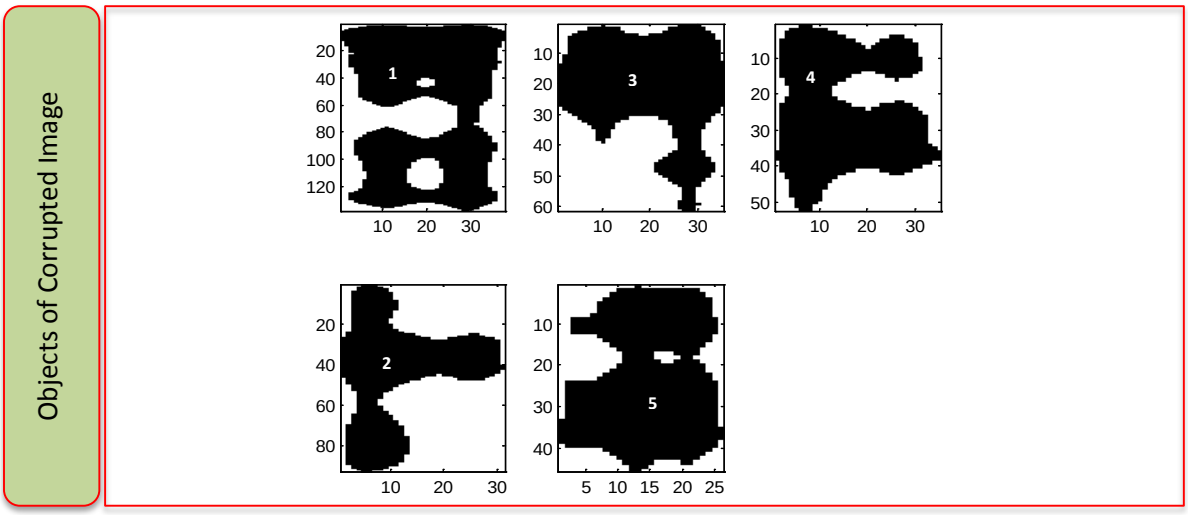

(b)

Figure 4.6 – Removing edge objects from left-diagonal recurrence image (a) Clean Image, (b) Corrupted Image

After alignment of each object with the reference now we can calculate the $MAcr$ of each object by using Eq (5-8) from Table (4). Fig.7 illustrates the objects of the typical clean and corrupted PPG segments from Fig.4, in comparison to the reference object with the $MAcr$ value of each object on top of it. It can be observed from this figure that the $MAcr$ values from corrupted segment are much larger than those of clean objects.

Finally by comparing to the threshold value $Thd = 5\% \times Centriod(x)_{Ref\_Object} \times Centriod(y)_{Ref\_Object}$ which in this case is 56.5, one can see that maximum of $MAcr$ corresponding to the clean PPG segment has value of 35 which is less than 56.5, while this value for corrupted PPG segment is 117 that is much higher than the threshold and indicates that the segment should be labeled as corrupted.

Fig. 8 represents the RepMA detection results when compared to reference MA detection index of the whole recordings #3. It can be seen that RepMA successfully detect the MA corrupted segments of PPG. In the next section, results of RepMA on all 4 datasets in comparison to three other MA detection are presented.

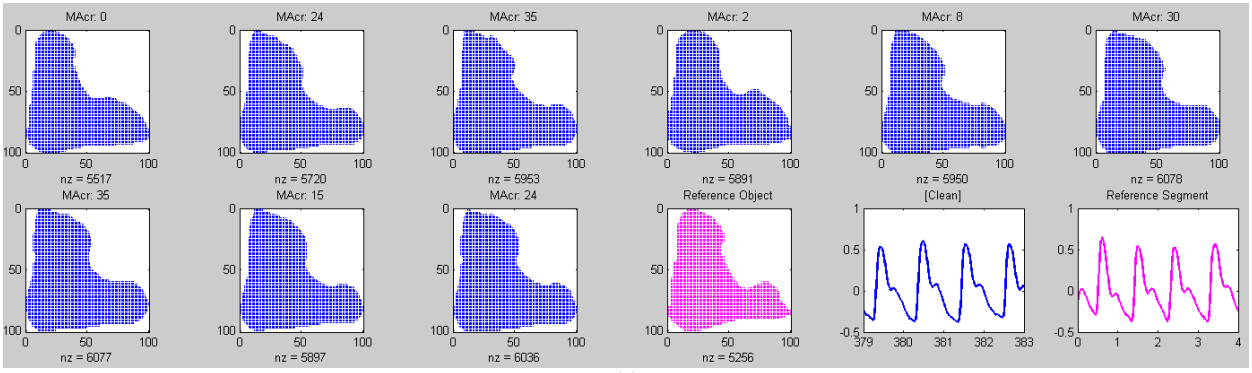

(a)

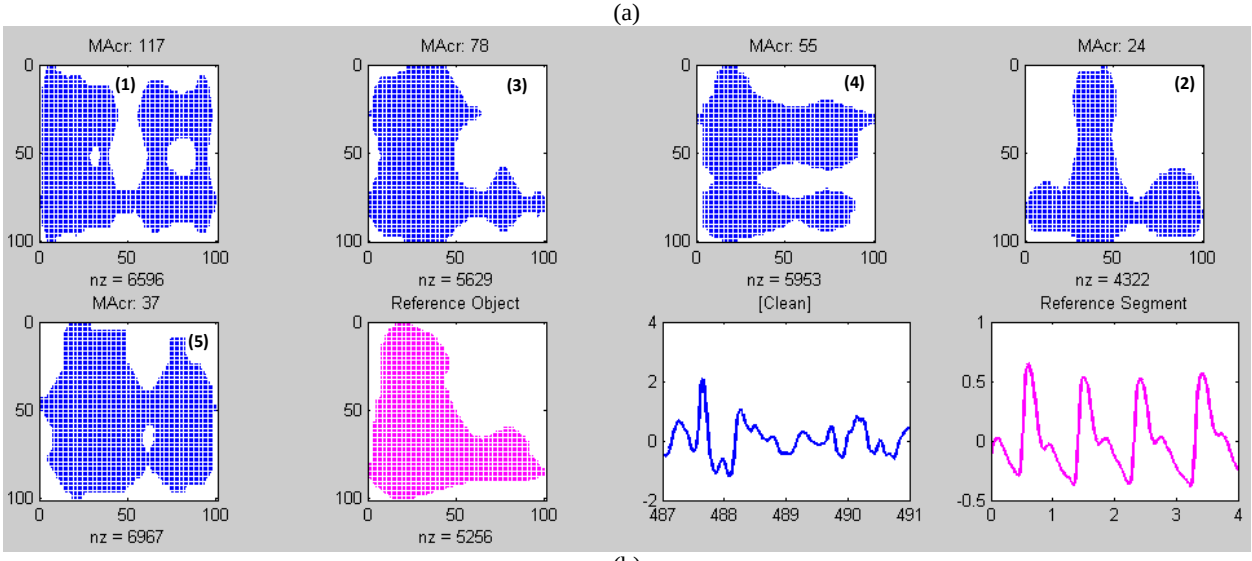

(b)

Figure 4.7 – Objects alignment and MA criteria calculations (a) Clean Image, (b) Corrupted Image

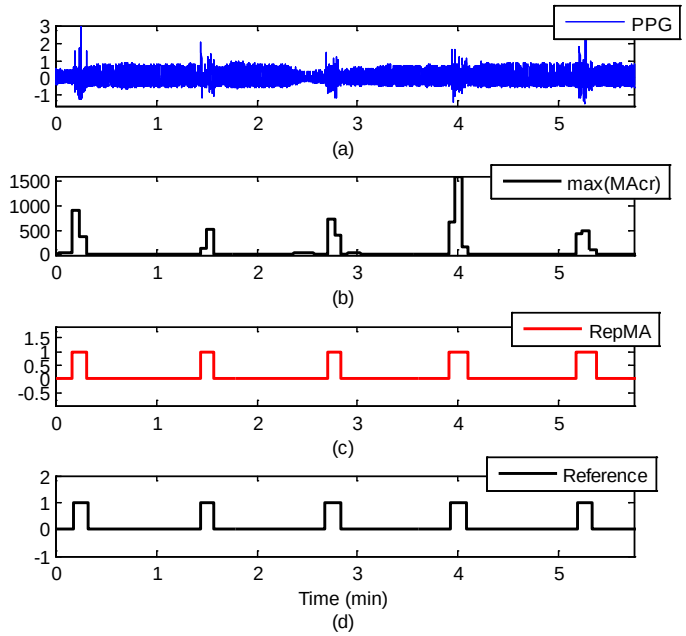

Figure 4.8 – Detection Results of Subject#3. (a) PPG signal. (b) RepMA detection signal, (c) max of MAcr signal, (d) Reference detection signal

4.4. Results

Tables (4-8) present the performance of REPMA algorithm on all of the recordings from four datasets. Detection performance was evaluated by comparing results of RepMA and the other three MA detection algorithms to the MNA reference (as determined visually by the experts) to obtain accuracy, sensitivity, and specificity. It can be observed from these tables that RepMA algorithm accuracy, sensitivity and specifity measurments of motion artifact corrupted PPG segments is higher than the other three methods on average over all recordings.

In addition to accurate MA detection, the other attractive feature of our proposed algorithm is that it has the potential to accurately locate the start and end points of MA occurrences. Accurate detection of the start and end time of the MAs is important for the subsequent reconstruction of the MA-corrupted data as we do not want to miss the MA portion of data for reconstruction or avoid having to reconstruct the noisy portion of the PPG when the segment is designated to be clean. To evaluate the algorithm's effectiveness

in pinpointing the start and end time of the MAs, we computed the time difference of start and end points between the visual reference and detection algorithms' results.

Table 4.8. MA Detection Performance on dataset #1: Lab Controlled Forehead PPG Recordings

Recording#	ACC%				SEN%				SPE%			
	Hjorth	KSE	TDV	**RepMA**	Hjorth	KSE	TDV	**RepMA**	Hjorth	KSE	TDV	**RepMA**
1	73.67	82.77	92.89	94.33	50.53	36.67	88.78	87.64	85.53	91.03	97.26	99.10
2	64.68	86.29	89.65	95.48	43.15	60.89	84.67	96.72	89.72	90.87	95.68	94.32
3	65.99	77.06	90.22	96.54	49.17	60.82	87.02	89.59	86.04	90.09	97.19	99.43
4	61.78	93.50	94.79	97.15	45.91	65.95	98.78	98.53	86.08	91.45	91.86	96.55
5	77.01	76.70	99.98	97.78	43.89	69.34	97.94	98.14	82.16	90.84	98.77	96.77
6	75.86	81.64	93.58	95.44	44.45	65.84	85.38	98.36	81.64	92.48	96.91	95.24
7	86.77	86.37	97.92	99.37	46.82	59.03	99.89	99.89	88.70	90.40	99.95	99.88
8	70.13	74.84	89.61	95.84	42.63	69.37	86.53	99.01	83.26	91.21	96.96	98.79
9	83.19	82.83	92.77	96.89	44.13	60.35	85.20	94.39	88.46	91.47	95.56	97.44
10	66.85	78.49	92.40	97.60	41.85	78.76	85.32	99.75	86.07	92.53	98.47	96.51
11	55.03	83.31	90.40	98.73	35.69	64.59	80.10	97.06	86.61	91.26	98.40	99.19
mean±std	72.5±10.74	83.1±7.31	93.4±3.50	**96.8±1.50**	47.2±28.8	56.6±17.88	88.8±7.90	**96.3±4.11**	84.4±4.63	91.5±1.14	96.7±3.00	**97.5±01.84**

Table 4.9. MA Detection Performance on dataset #2: Lab Controlled Finger PPG Recordings

Recording#	ACC%				SEN%				SPE%			
	Hjorth	KSE	TDV	**RepMA**	Hjorth	KSE	TDV	**RepMA**	Hjorth	KSE	TDV	**RepMA**
1	97.20	35.88	96.10	97.96	76.46	30.11	89.90	91.97	95.31	84.81	93.05	97.01
2	91.06	59.34	98.00	95.62	83.99	33.24	90.27	96.16	96.87	87.57	92.05	95.91
3	88.54	72.84	94.29	97.06	80.03	30.13	88.85	94.00	97.52	75.98	95.47	97.64
4	89.91	48.10	93.75	98.15	76.79	29.27	89.33	90.99	95.84	86.64	91.24	99.88
5	91.21	57.42	92.60	96.79	71.13	25.79	89.15	79.79	96.10	93.75	92.73	98.73
6	96.62	63.68	94.27	98.53	103.77	38.25	89.49	93.08	96.24	83.09	92.45	99.62
7	90.74	56.89	95.07	98.15	81.76	31.54	90.01	97.84	94.18	88.74	93.14	98.47
8	94.15	51.78	94.00	98.18	84.36	30.83	91.51	98.42	96.81	71.13	91.38	98.88
9	95.32	61.73	93.83	98.15	84.89	40.85	89.08	96.43	98.82	77.31	91.58	98.96
10	84.30	63.69	92.84	98.85	77.11	30.00	88.59	99.98	96.64	77.95	92.69	97.07
11	92.48	65.44	91.16	98.43	68.90	33.34	88.20	95.97	95.80	89.68	92.93	98.80
mean±std	91.1±3.78	58.5±9.91	94.4±1.81	**97.8±0.94**	83.5±9.23	34.6±4.23	89.48±0.91	**94.1±5.55**	96.2±3.02	86.3±15.65	92.6±1.16	**98.3±1.21**

Table 4.10. MA Detection Performance on dataset #3: UMASS Hospital Forehead PPG Recordings

Recording#	ACC%				SEN%				SPE%			
	Hjorth	KSE	TDV	**RepMA**	Hjorth	KSE	TDV	**RepMA**	Hjorth	KSE	TDV	**RepMA**
1	70.31	87.22	90.71	99.62	55.75	53.76	83.91	82.26	81.35	89.90	94.20	99.84
2	57.81	83.46	90.07	99.06	82.08	52.50	83.97	99.77	81.63	94.12	97.52	99.59
3	81.13	82.51	88.78	99.29	33.10	68.53	86.01	97.81	91.42	86.96	94.38	99.38
4	71.20	76.25	88.55	95.17	20.86	85.26	89.48	90.55	80.45	87.72	95.38	97.73
5	86.06	80.23	89.39	99.73	76.03	49.84	82.84	88.10	93.26	81.24	95.57	99.63
6	53.39	88.72	89.21	94.17	41.99	109.83	83.04	91.75	91.89	79.50	97.09	95.68
7	77.15	93.78	90.93	98.62	51.03	73.27	84.03	96.28	80.81	83.51	93.97	98.64
8	37.46	90.16	90.41	99.25	33.91	42.20	83.98	94.61	69.17	77.87	92.06	98.21
9	70.53	80.02	90.36	98.75	85.48	65.51	85.12	92.96	93.15	80.00	93.08	99.92
10	62.53	90.53	88.34	97.89	52.03	58.27	80.79	98.60	88.73	97.09	94.30	98.11
mean±std	69.5±21.83	85.1±8.34	89.8±1.45	**98.1±1.92**	53.8±26.05	68.7±17.72	84.6±2.89	**93.3±5.37**	84.5±8.83	86.4±7.82	94.3±3.95	**98.7±1.31**

The time difference is termed detection transition time, DTT, which reflects how accurately on average a MA algorithm detects the start and end time of the MAs. Table (5) provides average DTT comparison of RepMA and other detection algorithms on all four datasets and 42 PPG recordings.

Table 4.11. MA Detection Performance on dataset #4: UMASS Hospital Finger PPG Recordings

Recording#	ACC%				SEN%				SPE%			
	Hjorth	KSE	TDV	**RepMA**	Hjorth	KSE	TDV	**RepMA**	Hjorth	KSE	TDV	**RepMA**
1	46.34	86.11	88.54	99.30	47.30	71.40	85.96	88.01	98.74	89.94	92.27	99.19
2	54.72	88.00	91.00	97.54	54.84	76.91	82.94	85.10	90.79	90.37	92.50	99.04
3	65.70	87.07	89.65	95.58	31.74	70.81	92.93	84.63	79.65	90.82	93.58	96.49
4	46.90	85.81	89.00	98.47	24.85	83.07	88.10	98.13	87.39	92.93	92.19	97.69
5	69.65	87.79	91.36	96.44	42.08	74.24	85.52	74.01	76.78	91.63	90.79	99.33
6	80.44	86.87	90.16	94.77	29.80	84.59	77.42	76.83	99.94	90.94	91.73	97.07
7	69.02	84.69	88.78	94.99	99.95	66.39	87.91	91.90	92.16	90.49	92.04	94.27
8	55.29	93.15	87.91	95.09	74.56	76.76	86.45	93.52	93.22	91.47	91.23	95.25
9	64.06	85.22	87.29	97.02	82.59	61.92	85.14	82.15	81.18	92.40	92.18	98.34
10	77.94	88.03	85.03	96.73	15.43	71.03	78.45	90.68	88.04	89.44	92.36	95.86
mean±std	71.0±18.96	88.3±2.68	89.6±2.34	**95.6±1.53**	41.1±27.57	71.5±8.83	85.2±3.75	**86.5±7.50**	88.4±7.52	93.6±1.52	92.1±0.79	**97.2±1.76**

Table 4.12. Comparison of Detection Algorithms' Average DTT error from all recordings

DDT(start)				DDT(end)			
Hjorth	KSE	TDV	**RepMA**	Hjorth	KSE	TDV	**RepMA**
2.17±0.37	4.24±2.42	2.75±0.96	**0.56±0.24**	3.68±1.02	4.64±3.19	2.08±1.55	**0.61±0.33**

As shown in Table (5), our algorithm's detection error in pinpointing of the MAs is within almost 1 second whereas the second best algorithm, the TDV, is off by more than totally around 5 seconds and the least accurate method, the KSE, is off by more than 8 seconds.

4.5. Discussion

In this study, we propose a novel MA detection (RepMA) that is based on recurrence image processing. The idea is to transform the one dimensional PPG data into a 2 dimensional image using recurrence plot quantification. The main point is MA corrupted data is easier to be detected when we look into the recurrence features of PPG in its recurrence plot. We showed that RepMA can provide more accurate results on both lab-controlled and UMASS datasets when compared to three other MA detection method: (1) Hjorth [203], (2) KSE [22] and (3) TDV [220]. Concomitantly, the accuracy, sensitivity and

specificity values on average of our proposed method were significantly higher than other methods as indicated in Tables (4-8).

In conclusion, we proposed an accurate MA detection algorithm that utilizes time-time domain features to classify between clean and corrupted PPG data segments. Out algorithm also showed superiority with respect to detecting onset and offset of Mas with less than 1 sec error.

The proposed RepMA algorithm can be implemented in real time. We have found that the algorithm takes only 0.47 sec on PPG recordings of 60 sec. Therefore, given the high accuracy of the proposed approach in detection of motion artifacts, this method has the potential to be applicable for implementation on wearable devices such as smart watches and PPG-based fitness sensors.

ACKNOWLEDGEMENT

This work was supported in part by the US Army Medical Research and Materiel Command (USAMRMC) under Grant No. W81XWH-12-1-0541

References

1. Dash, S., et al., Automatic real time detection of atrial fibrillation. Ann Biomed Eng, 2009. 37(9): p. 1701-9.
2. Antonsen, L.P. and K.A. Kirkebøen, Evaluation of Fluid Responsiveness: Is Photoplethysmography a Noninvasive Alternative? Anesthesiology Research and Practice, 2012. 2012: p. 10.
3. Selvaraj, N., et al. Statistical approach for the detection of motion/noise artifacts in Photoplethysmogram. in Engineering in Medicine and Biology Society,EMBC, 2011 Annual International Conference of the IEEE. 2011.
4. Barker, S.J. and N.K. Shah, The effects of motion on the performance of pulse oximeters in volunteers (revised publication). Anesthesiology, 1997. 86(1): p. 101-8.
5. Sahni, R., et al., Motion resistant pulse oximetry in neonates. Arch Dis Child Fetal Neonatal Ed, 2003. 88(6): p. F505-8.
6. Salehizadeh, S.M., et al., Photoplethysmograph Signal Reconstruction based on a Novel Motion Artifact Detection-Reduction Approach. Part II: Motion and Noise Artifact Removal. Ann Biomed Eng, 2014.
7. Ram, M.R., et al., A Novel Approach for Motion Artifact Reduction in PPG Signals Based on AS-LMS Adaptive Filter. Instrumentation and Measurement, IEEE Transactions on, 2012. 61(5): p. 1445-1457.
8. Rusch, T.L., R. Sankar, and J.E. Scharf, Signal processing methods for pulse oximetry. Comput Biol Med, 1996. 26(2): p. 143-59.

9. Hong Enriquez, R., et al., Analysis of the photoplethysmographic signal by means of the decomposition in principal components. Physiol Meas, 2002. 23(3): p. N17-29.
10. Yan, Y.S., C.C. Poon, and Y.T. Zhang, Reduction of motion artifact in pulse oximetry by smoothed pseudo Wigner-Ville distribution. J Neuroeng Rehabil, 2005. 2(1): p. 3.
11. Lee, J., et al., Design of filter to reject motion artifact of pulse oximetry. Computer Standards & Interfaces, 2004. 26(3): p. 241-249.
12. Naraharisetti, K.V.P., M. Bawa, and M. Tahernezhadi. Comparison of different signal processing methods for reducing artifacts from photoplethysmograph signal. in Electro/Information Technology (EIT), 2011 IEEE International Conference on. 2011.
13. Ram, M.R., et al. Computation of SpO<inf>2</inf> using non-parametric spectral estimation methods from wavelet based motion artifact reduced PPG signals. in Signal Processing, Communication, Computing and Networking Technologies (ICSCCN), 2011 International Conference on. 2011.
14. Krishnan, R., B. Natarajan, and S. Warren, Two-Stage Approach for Detection and Reduction of Motion Artifacts in Photoplethysmographic Data. Biomedical Engineering, IEEE Transactions on, 2010. 57(8): p. 1867-1876.
15. Sukor, J.A., S.J. Redmond, and N.H. Lovell, Signal quality measures for pulse oximetry through waveform morphology analysis. Physiol Meas, 2011. 32(3): p. 369-84.
16. Li, K., S. Warren, and B. Natarajan, Onboard Tagging for Real-Time Quality Assessment of Photoplethysmograms Acquired by a Wireless Reflectance Pulse Oximeter. Biomedical Circuits and Systems, IEEE Transactions on, 2012. 6(1): p. 54-63.
17. Li, Q., R.G. Mark, and G.D. Clifford, Robust heart rate estimation from multiple asynchronous noisy sources using signal quality indices and a Kalman filter. Physiol Meas, 2008. 29(1): p. 15-32.
18. Nakajima, K., T. Tamura, and H. Miike, Monitoring of heart and respiratory rates by photoplethysmography using a digital filtering technique. Medical Engineering & Physics, 1996. 18(5): p. 365-372.
19. Karlen, W., et al., Photoplethysmogram signal quality estimation using repeated Gaussian filters and cross-correlation. Physiol Meas, 2012. 33(10): p. 1617-29.
20. Lee, B., et al., Improved elimination of motion artifacts from a photoplethysmographic signal using a Kalman smoother with simultaneous accelerometry. Physiol Meas, 2010. 31(12): p. 1585-603.
21. Foo, J.Y. and S.J. Wilson, A computational system to optimise noise rejection in photoplethysmography signals during motion or poor perfusion states. Med Biol Eng Comput, 2006. 44(1-2): p. 140-5.
22. Krishnan, R., B. Natarajan, and S. Warren. Analysis and detection of motion artifact in photoplethysmographic data using higher order statistics. in Acoustics, Speech and Signal Processing, 2008. ICASSP 2008. IEEE International Conference on. 2008.
23. Hjorth, B., The physical significance of time domain descriptors in EEG analysis. Electroencephalography and Clinical Neurophysiology, 1973. 34(3): p. 321-325.
24. Hjorth, B., EEG analysis based on time domain properties. Electroencephalography and Clinical Neurophysiology, 1970. 29(3): p. 306-310.
25. Gil, E., J. María Vergara, and P. Laguna, Detection of decreases in the amplitude fluctuation of pulse photoplethysmography signal as indication of obstructive sleep apnea syndrome in children. Biomedical Signal Processing and Control, 2008. 3(3): p. 267-277.
26. Chong, J.W., et al., Photoplethysmograph Signal Reconstruction Based on a Novel Hybrid Motion Artifact Detection-Reduction Approach. Part I: Motion and Noise Artifact Detection. Ann Biomed Eng, 2014.
27. Eckmann, J.P., S.O. Kamphorst, and D. Ruelle, Recurrence Plots of Dynamical Systems. EPL (Europhysics Letters), 1987. 4(9): p. 973.
28. Takens, F., Detecting strange attractors in turbulence, in Dynamical Systems and Turbulence, Warwick 1980, D. Rand and L.-S. Young, Editors. 1981, Springer Berlin Heidelberg. p. 366-381.

Chapter 5: RAFMA – A Novel Motion and Noise Artifact Detection and Atrial Fibrillation Detection Algorithm

5.1. Introduction

Atrial fibrillation (AF) is the most common diagnosed dysrhythmia affecting approximately 3 millions of Americans. AF is the most common arrhythmia among the elderly, with the median age of those affected to be around 75 years of age. Prevalence of AF increases with age and reaches 8% of people in the United States over the age of 80 years [1]. Atrial fibrillation is an independent risk factor for death (relative risk in men 1.5 and in women 1.9) [2] and a major cause of ischemic stroke whose impact increases with age, reaching 23.5% in patients older than 80 years [3]. Although the 12-lead electrocardiogram remains the gold-standard diagnostic test for AF, a major challenge in the diagnosis of this arrhythmia is its paroxysmal nature, particularly in its early stages [4].

Diagnostic testing is one method of detection and is usually the result of symptomatic patients. Some of these tests include long-term Holter monitoring, electrocardiogram interpretation and blood tests. Use of ECG monitors (e.g., Holter monitors) is common in the diagnosis and management of patients with, or at risk for, AF, given the paroxysmal, short-lived, and frequently asymptomatic nature of this serious arrhythmia. Biological imaging is a method that involves the analysis of images obtained from echocardiograms and chest x-rays. The prevalence of asymptomatic AF found incidentally on clinical examination is 20%, [4, 5] even higher with Holter or event recorders [6, 7]. Given these difficulties, a recent National Health Heart Lung & Blood Institute Expert panel has emphasized the pressing need to develop new methods for accurate AF detection and monitoring [8]. One study of patients with implantable pacemakers for AF detection found an incidence of 50% of asymptomatic AF [9]. Given the significant risk of mortality and morbidity and the fact that asymptomatic AF is not detected unless specifically looked for, there is a strong impetus for ambulatory monitoring. With the greater need for ambulatory monitoring, accurate and automated detection of asymptomatic AF becomes an important task. If atrial fibrillation can

be easily and automatically detected early in their pathology, the risk of complications that are consequential due to late detection can be drastically reduced. Early detection could also potentially save billions of dollars spent on health care costs and research directly related to the heart conditions. A method to automatically detect atrial fibrillation and atrial flutter will save lives, improve quality of life of millions of people at-risk, and reduce the economic burden placed by AF.

Several algorithms have been developed to detect AF which either rely on the absence of P-waves [10-18] or are based on RR variability [7, 18-25]. Since there is no uniform depolarization of the atria during AF and consequently no discernible P-waves in the ECG, their absence has been utilized in the detection of AF. However, locating the P-wave fiducial point is very difficult because the low amplitude of the P-wave makes it susceptible to corruption by noise. The methods in the second category are based on RR interval dynamics and do not require identification of the P-wave. By using these intervals, we can first detect whether or not there is a normal sinus rhythm associated with the heart activity. Due to the irregularity of AF, the arrhythmias could be detected based on these irregularities. However, few algorithms in this category show high predictive value for clinical application [19, 23, 24, 26]. Notable exceptions include Duverney et al., [7] Sarkar et al. [26] and Tateno and Glass [23, 24]. Duverney et al. used wavelet transform of the RR time series while the latter used the Kolmogorov–Smirnov test to compare the density histogram of the test RR (and DRR) segment with previously compiled standard density histograms of RR (and DRR) segments during AF. Sarkar et al. used the Lorenz distribution of a time series of RR intervals for AF and tachycardia detection for its use in a chronic implantable monitor. Tateno and Glass reported a sensitivity of 94.4% and specificity of 97.2% for the MIT BIH Atrial Fibrillation database [23, 24]. Although the accuracy of the study by Duverney et al. was high, their results were based on a small database. The main drawback of these algorithms is that they are dependent on the robustness of the training data. For example, if the characteristics of AF are different from those learned in the training data, the accuracy of AF detection is compromised. In [22] Dash et al. used a combination of three different statistical methods: Root Mean Square of Successive RR Differences to quantify variability (RMSSD), the Turning Points Ratio to test for

randomness of the time series (TPR) and Shannon entropy to characterize its complexity (SE), to be able to detect the presence of randomness in the ECG signal.

Noise and motion artifact is another important factor to take into account when analyzing the ECG data; noise that occurs due to patient activities, small movements, or other types of motion artifacts and environmental interference will severely affect standard deviation and variance. Clinicians have cited MNA artifacts in ambulatory monitoring devices as the most common cause of false alarms, loss of signal, and inaccurate readings [27, 28]. Previous computational efforts have largely relied on MNA removal, and some of the popular methods include linear filtering [29], adaptive filtering [30, 31], wavelet denoising [32-34], and Bayesian filtering methods [35]. One main disadvantage of the adaptive filtering methods is that they require a reference signal, which is presumed to be correlated in some way with the MN artifacts. For mitigating this limitation, use of accelerometers to obtain a reference signal has resulted in some success [36, 37]; however, this approach has not been applied to Holter monitors. The wavelet denoising approach attempts to separate clean and noisy wavelet coefficients, but it can be difficult to use since it requires identification of the location of each ECG morphology including the P and T waves [32-34]. Bayesian filtering requires estimation of optimal parameters using any variant of Kalman filtering methods: extended Kalman filter, extended Kalman smoother, or unscented Kalman filter [35]. The main disadvantage of the Bayesian filtering approach is the improper assumption that noise has an additive Gaussian probability density function. Further, the method requires R-peak locations for each cycle of ECG data. The most recent effort in detection of motion artifacts in Holter ECG data for AF detection application was proposed by Lee et al. [38] based on two stages approach using empirical mode decomposition (EMD) and three statistical measures to detect MNA and then using an AF detection algorithm [22] on the MNA free episode of data. One potential issue with MNA detection algorithm in [38] is that segment disconnectivity can occur when an identified corrupted segment is not used for subsequent AF detection. Another limitation is that the segments with saturated ECG values can often be detected as noise free.

While the aforementioned signal processing approaches have been applied, they cannot address the MNA/AF detection problem, and consequently MNA artifacts remain a key obstacle to the accurate detection of AF. A novel real-time method to separate clean ECG portions from segments with MNA artifacts in real time is urgently needed for more accurate diagnosis and treatment of clinically important atrial arrhythmias. In this chapter, a new real-time algorithm based on recurrence quantification is presented that can distinguish between ECG signal with motion and noise artifacts and ECG recordings from Arterial Fibrillation patients. The idea is to process the ECG signal in time-time domain by transforming the 1-D signal to a 2-D image and analyze the image for MNA detection and AF diagnosis. The algorithm is called RAFMA and is based on Recurrence quantification analysis to detect Atrial Fibrillation from ECG recordings with Motion and noise Artifacts. RAFMA is comprised of 4 distinct stages and it: (1) Resampling and taking Derivative of ECG, (2) Transforming the ECG and its derivative to time-time recurrence plots (4) Motion Artifact detection, (5) AF detection. By taking the raw ECG signal, RAFMA first resamples the signal to ¼ of original sampling rate. After downsampling the distance between R peaks and its previous data sample is larger and taking the derivative of it would result in sharper peaks. Next by calculating the recurrence matrix of downsampled ECG signal and its derivative, two time-time recurrence plots would be obtained. By comparing the images of ECG and its derivative the ECG components can be discriminated from MNA's components. Thus the algorithm can detect if an ECG segment at each window is corrupted by movement and noise or not. Next after verifying that the segment is clean the recurrence plot of ECG's derivative is further processed. Irregular distances between vertical patterns in recurrence plot indicates AF otherwise the recordings are labeled as non-AF. We show in result section that the proposed RAFMA algorithm is well performed in real-time detection and discrimination between, clean/healthy and MA-corrupted/AF ECG recordings. In this chapter we provide a comparison study between our proposed RAFMA algorithm and the algorithm that was presented in [38] and we call it EMDAF for simplicity.

5.2. Materials and Experiments

The RAFMA algorithm was evaluated on two different datasets (see Table (1)). The first datasets were provided by MIT from 23 patients and are publically available [39] and the second one is recorded in Chon lab from 10 subjects.

(1) MIT BIH Atrial Fibrillation database: This database includes 23 ten-hour ECG recordings of human subjects with atrial fibrillation (mostly paroxysmal). The individual recordings are each 10 hours in duration, and contain two ECG signals each sampled at 250 samples per second with 12-bit resolution over a range of ±10 millivolts. The original analog recordings were made at Boston's Beth Israel Deaconess Medical Center using ambulatory ECG recorders with a typical recording bandwidth of approximately 0.1 Hz to 40 Hz. This database include 319 episodes of AF with total 230 hours of recordings [25].

(2) Chon Lab Dataset: RAFMA algorithm was evaluated on one dataset. An experiment with a challenging protocol that includes 17-min ECG recordings from 10 healthy subjects was designed, in which each subject were asked to wear a ECG wrist wearable with a tight suit as shown in Table (2). The wearable system was built in Chon Lab and it consists of two wrist modules which are designed to fabricate a 1-channel ECG signal (Lead I) on the top of right and left wrists. This device was designed and developed for ECG measurement based on two leads with virtual right-leg driven circuit and provides a frequency band at -3 dB from 0.05 to 150 Hz with second-order high-pass and low-pass filters to cover the full ECG range. A wire was connected between both modules to produce an ECG signal and is attached to a tight suit for minimizing motion artifact caused by wire moving. ECG signal was sampled at 360 samples per second with 12-bit resolution over a range between 0 and 3.3 volts. Electrodes for ECG measurement are carbon black (CB) based film electrode (Flexcon, MA, USA). The electrode has sticky surface, so it makes it possible to collect stable ECG signal without hydrogel and there was no complain about skin irritation from subjects as well. Each subject were asked to perform different types of physical activities (see Table (2)) during the experiment to investigate the performance of algorithm in variety types of daily activities and movements. The reference ECG signals for evaluation of RAFMA were recorded from chest using Holter monitor.

Table 5.1. ECG Datasets and Experiments Settings

No. Subjects	Dataset	Sampling Rate	Device	Subject's Age/Sex
23	1 (MIT BIH Atrial Fibrillation database [223])	250 Hz	Holter Monitor	43-89 y (12 Male/11 Female)
10	2 (Chon Lab)	360 Hz	ECG Suit (Built in Chon Lab)	23-58 y (9 Male, 1 Female)

Table 5.2. Chon Lab Experiment Settings

Setup	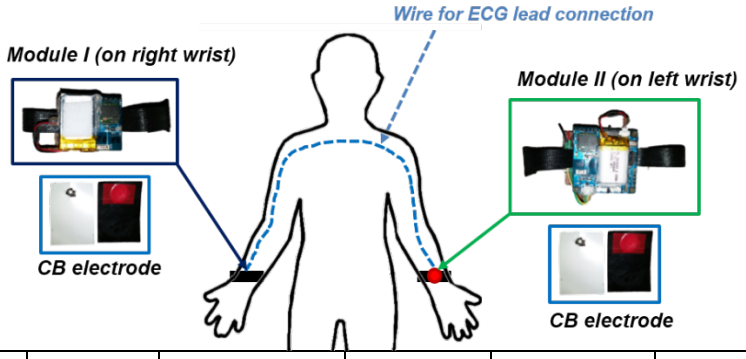								
Activity Type	Rest (Supine Position)	Walking (2 mph)/Jogging (4 mph)/ Running (6 mph)	Rest (Standing)	Standing/Sitting on a chair	Arm Movements (Up/Down) and (Left/Right)	Wrist Rotation/Shaking	Body Rotation/Shaking	Weight Lifting and Box Moving	Deep breathing
Duration (min)	5	1.5	0.5	0.5	3	3	1.5	3	0.5

5.3. Methodology

AF is characterized by uncoordinated atrial activation due to disrupted electrical pathways and structural changes in the heart [40]. While these changes can cause specific symptoms, AF is difficult to diagnosis due to the many cases that do not present symptoms. A normal ECG has three distinct waveforms. There is the P-wave, which represents atrial depolarization (the atria contract); the QRS complex, which represents ventricular depolarization (the ventricles contract while the atria begin to relax); and the T-wave, which denotes ventricular repolarization (the ventricles relax) [41].

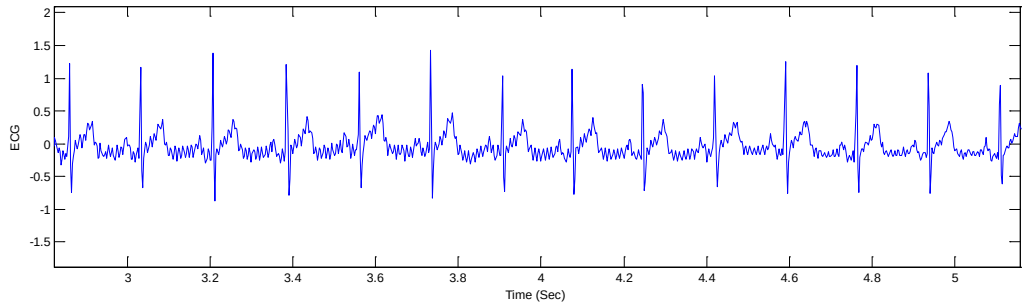

(a)

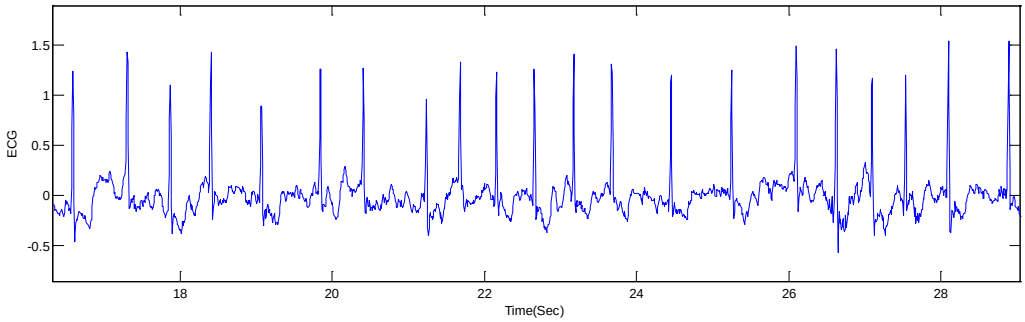

(b)

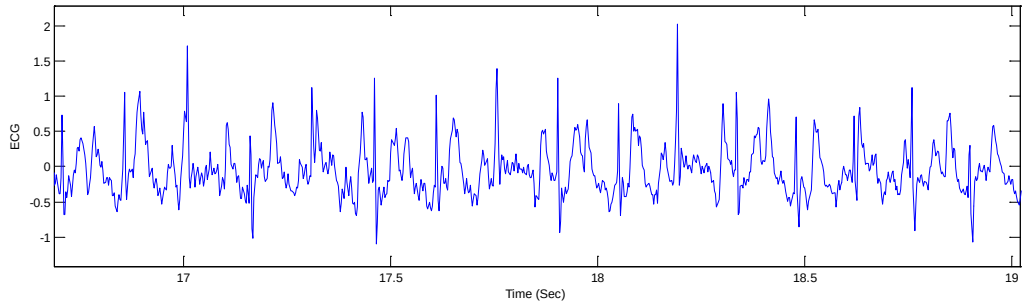

(c)

Figure 5.1 – ECG recordings (a) clean signal form healthy subject with prominent-waves and regular, consistent RR-interval, (b) clean signal from a patient with AF which shows irregular RR-intervals as well as indistinguishable P-waves, (c) MA corrupted signal from healthy subject which shows irregular pattern with indistinguishable P-waves and RR-interval

Atrial fibrillation is a cardiac arrhythmia associated with uncoordinated electrical impulses that disrupt the steady atrial activation in the heart [42]. This disruption will usually show an absence of P-waves on the ECG and an irregularity among the RR-intervals. However, non-distinguishable P-waves can be a result of motion and noise artifact in the recordings, which makes it difficult to discriminate between a healthy clean ECG, AF clean/corrupted ECG and MA corrupted ECG recordings as shown in Fig.1. So the challenge is first to detect if the ECG signal is clean of MA or not and then if it is clean one can examine the signal for AF. In this section a 2-phase algorithm is introduced to address the MA/AF detection problem.

5.3.1. R-peak Detection in ECG signal using Recurrence Plot

Recurrence analysis is a graphical method designed to locate hidden recurring patterns, nonstationarity and structural changes in signals which is proposed by Eckmann (1987) [221]. Recurrence is a fundamental property of dynamical systems, which can be exploited to characterize the system's behavior in phase space. Recurrence occurs when a dynamical system returns or recurs to former states. Given a time series$x_k, k = 1,2, \dots, N$, a recurrence plot (RP) shows when the time series visits the same region of phase space, that is

$$X_i \cong X_j, \qquad i \neq j \; and \; i,j = 1,2, \dots, N \qquad (1)$$

Takens [222] theorem shows that we can recreate a topologically equivalent picture of the original multidimensional system behavior from the time series of a single observable variable, by means of the method of time delays: for the scalar series x_k, the embedded vectors can be constructed as follows:

$$x_k^m = \{x_k, x_{k+d}, x_{k+2d}, \dots, x_{k+(m-1)d})\}, \quad k = 1,2, \dots, N \qquad (2)$$

where m is the embedding dimension and d is the time delay. A phase space does not have a dimension which allows it to be pictured, and higher dimensional phase space can only be visualized by projection into the two or three dimensional sub-space. To a matrix of recurrence distances (e.g., Euclidean distances) can be constructed by computing distances between all pairs of embedded vectors;

$$\boldsymbol{R}^m_{\boldsymbol{dist}(\boldsymbol{i},\boldsymbol{j})} = \|\vec{x}_i - \vec{x}_j\|, \quad \vec{x}_i \in \mathbb{R}^m, \quad i,j = 1,2, \dots, N \qquad (3)$$

Fig1.a shows a colored recurrence (distance) plot of a single frequency sinusoid signal. As it can be observed the recurrence plot relates each distance to a color. Thus, the recurrence plot is a solid rectangular plot consisting of pixels whose colors correspond to the magnitude of data values in a two-dimensional array and whose coordinates correspond to the locations of the data values in the array. The RP provides information of the vicinity among indices based on the distance of each indices' phase space vectors so that the vectors are sorted by their norm. If the cumulative distribution of the lengths of the phase

space vectors is known, the restored phase space trajectory will recover its amplitude by equating the sorted indices with that distribution.

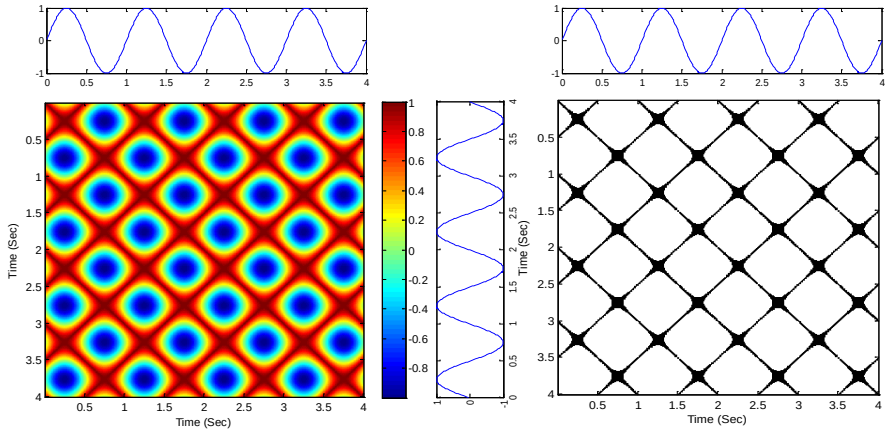

(a) (b)

Figure 5.2 – Recurrence time-time Plot of a single frequency sinusoid signal. (a) Colored distance RP, (b) Binary RP

The common recurrence plot is usually defined according to a neighborhood criterion and a threshold distance $\mathcal{E}$, by which the paired distances smaller than the threshold assigned with 1 and the rest with 0. Such an RP can be mathematically expressed as

$$\boldsymbol{RP}_{\boldsymbol{i,j}}^{m} = \Theta\left(\mathcal{E}_i - \left\|\vec{x}_i - \vec{x}_j\right\|\right), \qquad \vec{x}_i \in \mathbb{R}^m, \qquad i,j = 1,2,\dots,N \tag{4}$$

Where $\|.\|$ is a norm and $\Theta(.)$ is the Heaviside function. Since $\boldsymbol{RP}_{\boldsymbol{i,i}} = 1\ (i = 1,\dots,N)$ by definition, the RP always has a black diagonal line. The neighborhood criterion determines the recurrence density, which mean for example with a given $\mathcal{E} = 0.15$, the local neighborhood covers 15% of all phase space vectors and thus the recurrence density is 0.15. In the original definition of the RPs, the neighborhood is a ball (i.e. $L_2 - norm$ is used) and its radius is chosen in such a way that it contains a fixed amount of states $\vec{x}_i$ [26]. If the distance threshold $\mathcal{E}_i$ for each data point x_i is set to a constant value then it results to a symmetric binary RP where $\boldsymbol{RP}_{\boldsymbol{i,j}} = \boldsymbol{RP}_{\boldsymbol{j,i}}$.

Fig1.b illustrates the symmetric binary RP with a distance threshold $\varepsilon = 0.05$ corresponding to the sinusoid signal. Fig.3 presents the binary and distance RP of a typical ECG signal with $\varepsilon = 0.1$. It can be observed that white vertical (horizontal) patterns in the binary RP is due to the R-peaks in the original ECG segment.

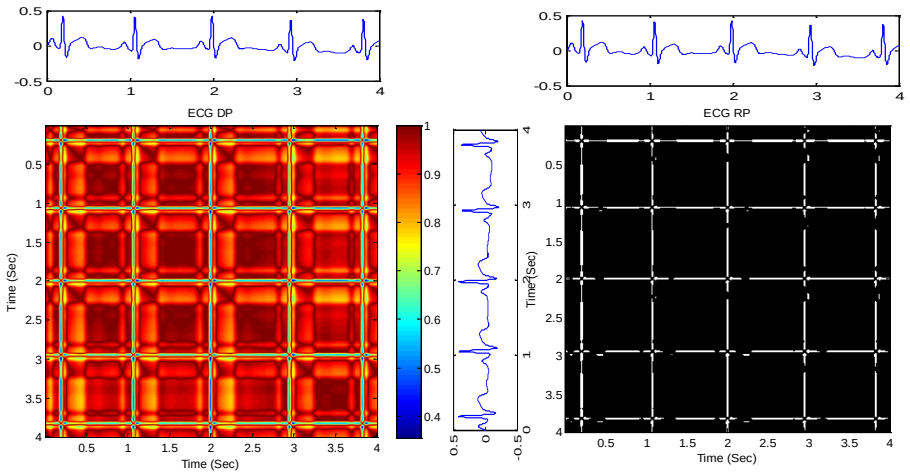

Figure 5.3 – Recurrence time-time Plot of a 4 sec ECG signal. (a) Colored distance RP, (b) Binary RP

Vertical lines in a RP marks a time interval during which a state does not change and it changes abruptly from a previous state. It seems that the state is trapped for some time. This is a typical behavior of short laminar states (intermittency) [221]. Hence, by taking the 1-RP recurrence matrix of an ECG signal, columns with 1's represent the R-peaks in the signal. That is RP has a potential to be used as peak detection technique, where each vertical line in ECG recurrence plot corresponds to an R-peak in ECG signal (see Fig.4).

5.3.2. Motion and Noise Artifact Detection in ECG Using RP

Noise depending on the level, can distort any existing structure in a recurrence plot [221]. It is desirable that the smallest distance threshold be chosen to increase the resolution of the time-time 2D RP image. However, higher threshold can help preserving the distortions that are made by movement and noise artifacts. The embedding dimension on the other hand has to be chosen so that the dynamics of the system will be well presented by its phase space trajectory. Movement during ECG recordings can increase the

laminar states by introducing irregular sudden peaks in the recordings which produce more vertical (horizontal) patterns that might be observed in a clean ECG signal (see Fig4.(a) and (c)).

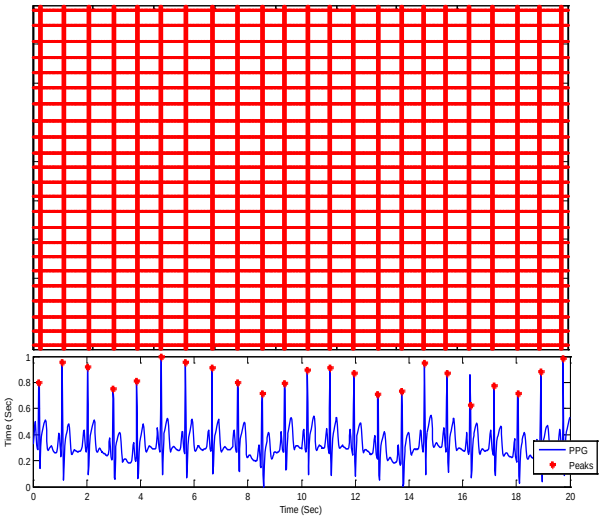

Figure 5.4 – Recurrence Plot as a tool for peak detection in 20 sec ECG data

Motion and noise artifact detection procedure of the RAFMA algorithm comprised of the following steps:

1. Down-sampling ECG signal: In order to make the R-peaks more prominent in the signal and especially in the derivative of the ECG, the ECG segment at each window is resampled to ¼ of its original sampling frequency. Then we take the derivative of each segment of the resampled ECG: taking derivative of a signal would help suppress the low variations in the signal and strengthen the higher variations like R-peaks in the ECG signal. This step was inspired from ECG peak detection algorithm proposed by Pan and Tompkins [224].

2. Transferring from 1-D ECG vector to 2-D time-time recurrence plot: At this stage recurrence matrix is calculated using Eq. (3) for both original ECG and its derivative for each 3 sec window segment (Fig.5 (a-d)). It can be observed from Fig.5 (a) and (b) that when the ECG segment is clean, the vertical (horizontal) lines in RP of original ECG remain the same as the RP of derivative of ECG which this is not

the case when it comes to MNA corrupted ECG segment, by taking the derivative of ECG one can observe that the corruption reduced in the RP.

3. Motion and Noise Artifact Detection: Now to discriminate between the MNA-corrupted ECG and clean ECG, the algorithm removes the vertical (or horizontal) lines in the RP obtained from the original ECG according to its derivative's RP, what remains represents the noise and corruption introduced mainly on P and T-wave of each cycle of ECG. The remaining RP is called MNA_{RP}. Fig.5 (e) illustrates the MNA_{RP} after removing the lines in ECG according to their arrangements in the RP of ECG's derivative. One can observe that the RP is clean, which indicates that the ECG segment is clean. On the other hand, from Fig.5 (f) the MNA_{RP} seems to have scattered dots and patterns, which shows that motion and noise artifacts exist in that segment of ECG.

In order to automatically discriminate between MNA corrupted and clean ECG segments, number of dots (1's) in the MNA-RP is computed as follows and the criterion is then compared to a threshold value (50%).

$$MNAcr\% = \frac{100}{2L}\sum_{i=1}^{L}\sum_{j=1}^{L} MNA_{RP}(i,j) \qquad (5)$$

$MNAcr$ values higher than 50% signifies that the segment is corrupted.

5.3.3. Atrial Fibrillation Detection Using RP of ECG signal

From the previous step, if the data segment is clean then by calculating the distance between vertical lines in ECG's derivative RP we can determine if the R-R intervals in the signal are consistent or inconsistent. Inconsistent distance between vertical patterns in RP indicates AF. Fig. 6(a) illustrate 3-sec segment of ECG after resampling to ¼ of its original sampling frequency (400 Hz). By taking the derivative of the data and calculating the recurrence matrices of ECG and its derivative we can now calculate the MNA_{RP} to investigate if the segment is clean of MNA or corrupted. Since the RP shown in Fig.6(c) is clean the ECG segment is clean.

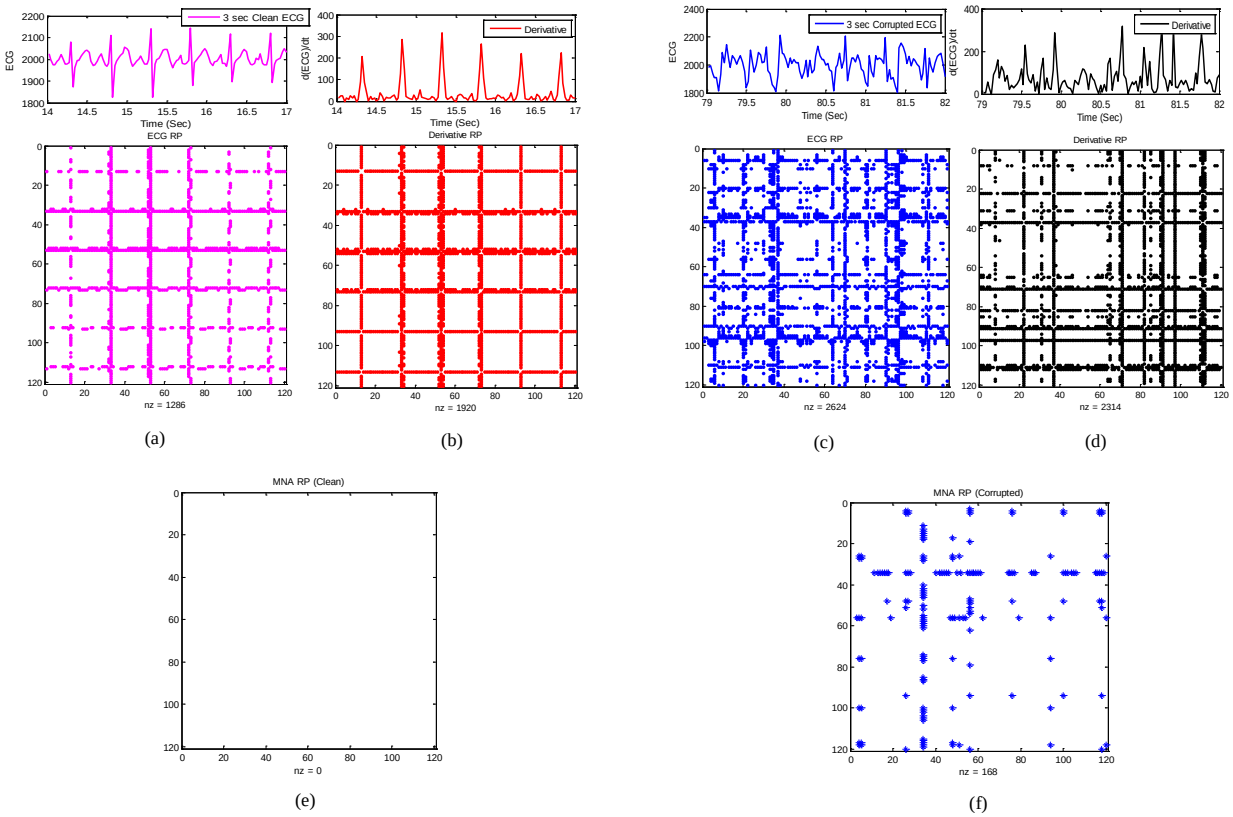

Figure 5.5 – Motion Artifact Detection using Recurrence Plot of 3 sec ECG segment: (a) recurrence plot of a clean ECG segment, (b) recurrence plot of derivative of (a); (c) recurrence plot of a corrupted ECG segment, (d) recurrence plot of derivative of (b), (e) $\boldsymbol{MNA_{RP}}$of clean ECG, (d) $\boldsymbol{MNA_{RP}}$ of a corrupted ECG

By computing the distance between vertical lines of ECG derivative's RP and calculating the standard deviation of the distance values, if the deviation from average is more than a threshold of 3.5, then it indicates AF. For the below example the standard deviation of intervals is 5.9 which verifies that the ECG recordings are from a patient with AF.

The flowchart of the RAFMA algorithm is presented in Fig.7.

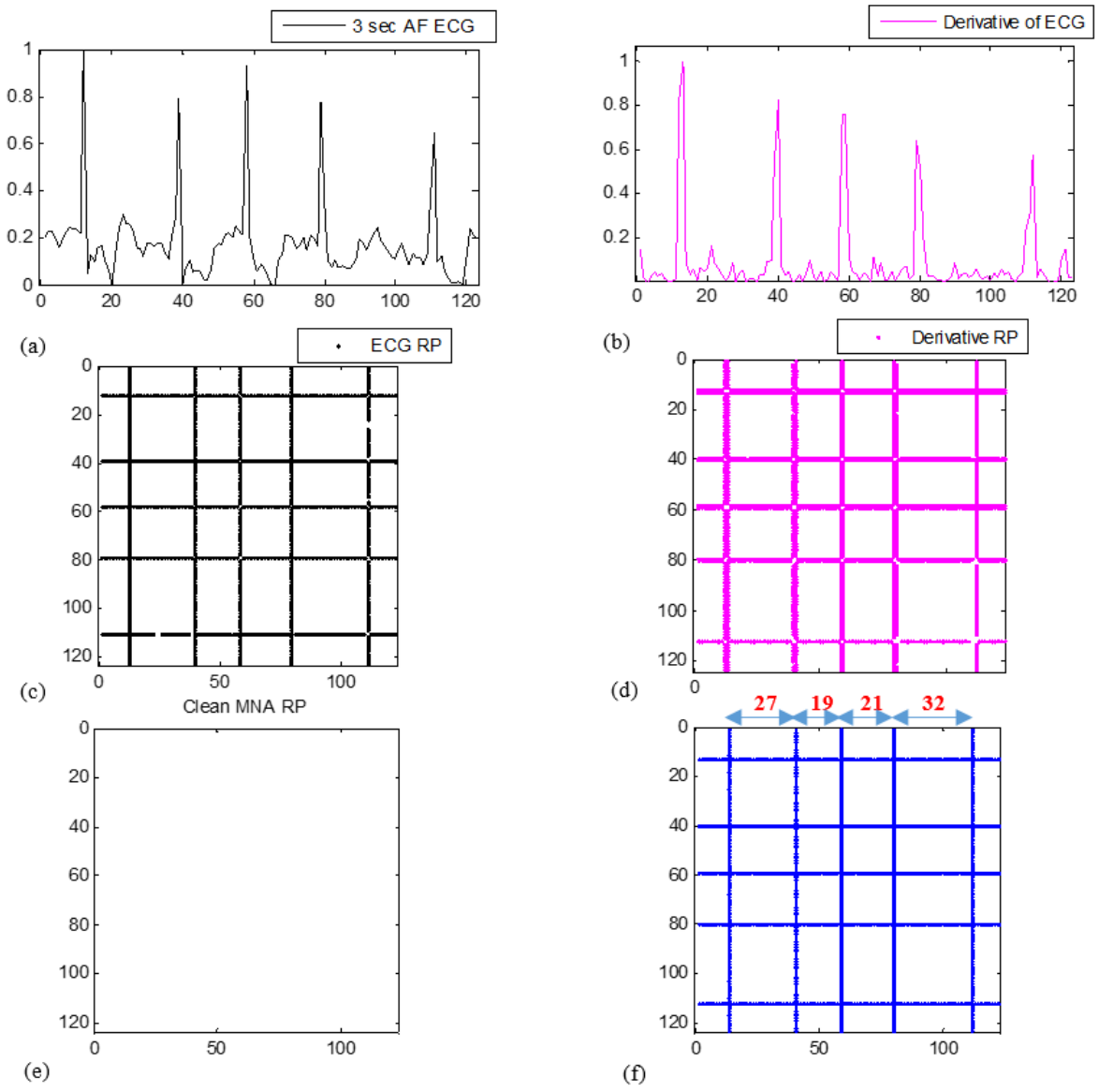

Figure 5.6 – Atrial Fibrillation Detection using Recurrence Plot of 3 sec ECG segment: (a) 3 sec of down-sampled ECG recordings from a patient with AF; (b) derivative of the down-sampled ECG segment; (c) Recurrence plot corresponding to (a); (d) recurrence plot corresponding to (b); (e) resultant $\boldsymbol{MNA_{RP}}$from motion and noise artifact detection procedure; (f) the equivalent $\boldsymbol{AFIB_{RP}}$which the numbers on top show samples interval between vertical lines

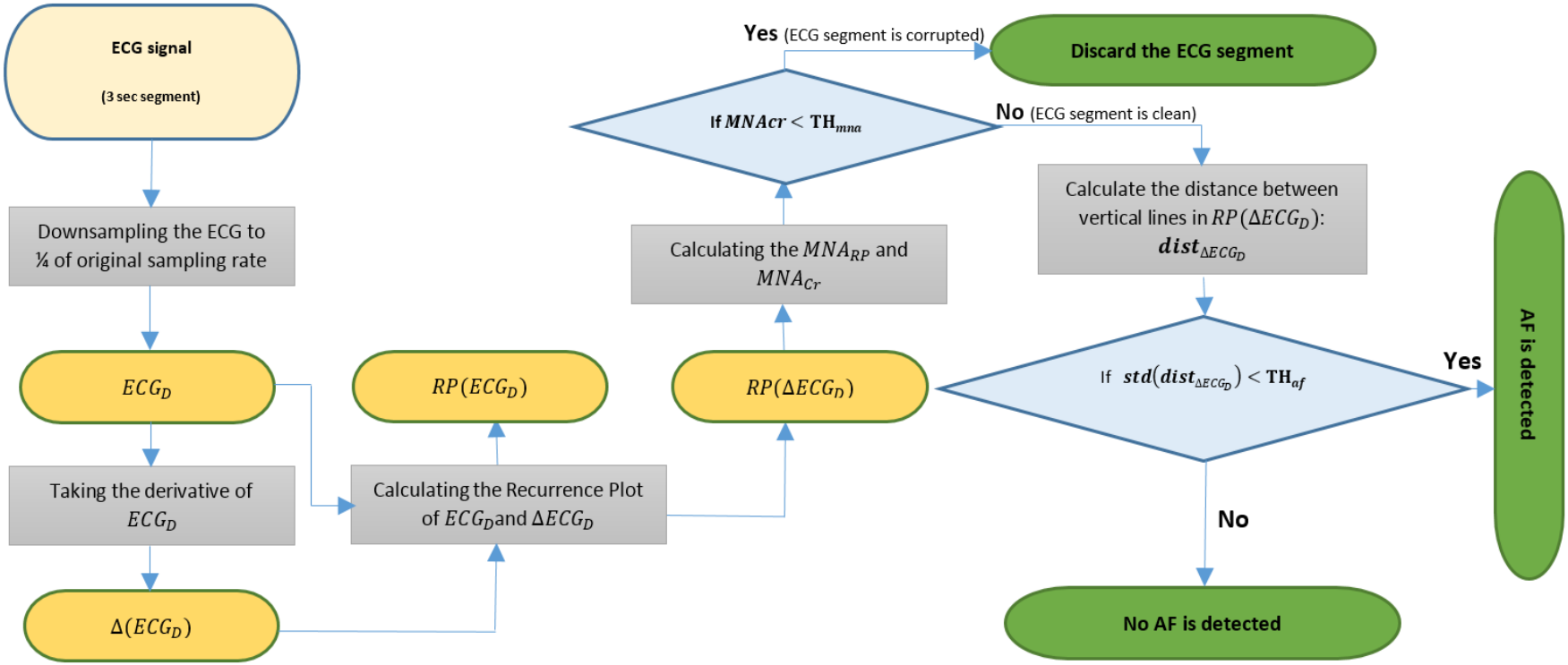

Figure 5.7 – Flowchart of RAFMA Algorithm

5.4. Results

In order to measure the performance of RAFMA algorithm on MNA detection, since the data will be processed for AF diagnosis afterwards, we derive the reference for MNA corrupted data according to HR estimation from the ECG recordings. The HR is estimated according to R-R peaks intervals. Fig. 8 illustrates the results of MNA detection on subject#4. The reference MNA detection signal is derived according to the corrupted inaccurate HR readings from the blue ECG signal.

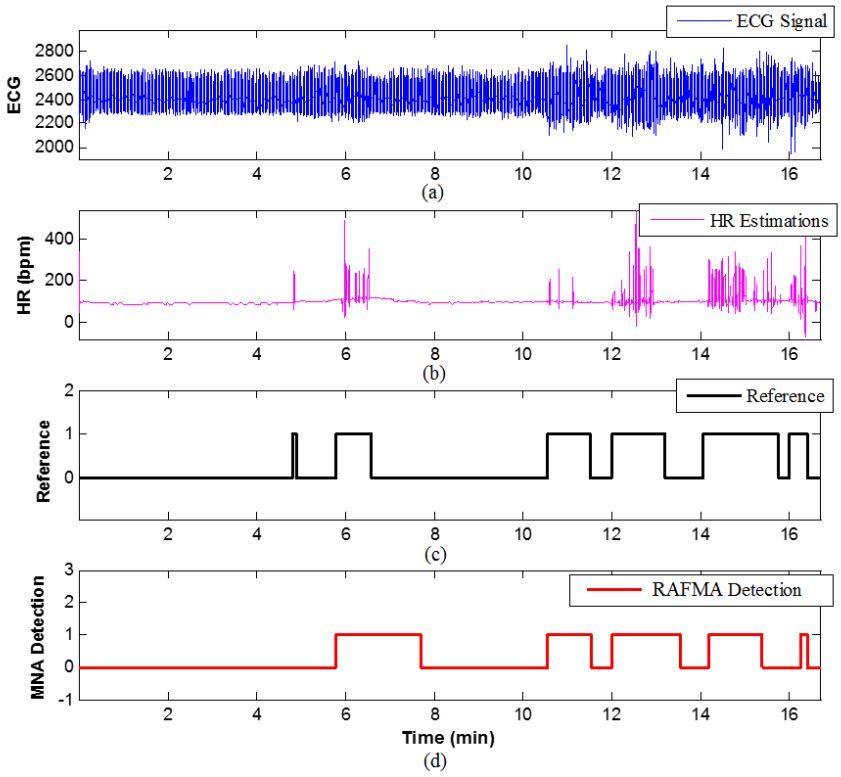

Figure 5.8 – RAFMA MNA Detection Results for Subject 9 (Chon Lab Dataset). (a) ECG signal. (b) Estimated HR from ECG recordings, (c) reference detection signal (d) RAFMA detection signal

Table (3) presents the accuracy, sensitivity and specifity of the detection algorithm comparing to EMD algorithm on Chon Lab datasets and all of the 10 recordings. It can be observed from Table (3) that RAFMA algorithm outperform EMD algorithm in terms of better accuracy, specifity and specifity. The performance of the RAFMA in AF diagnosis comparing to EMDAF [173] algorithm is reflected in Table

(4). The RAFMA algorithms is able to discriminate between healthy and AF ECG recordings with accuracy around 97%.

Table 5.3. MNA Detection Performance Comparison

Subjects	Database	Accuracy		Sensitivity		Specifity	
		RAFMA	EMDAF	RAFMA	EMDAF	RAFMA	EMDAF
1	**Chon Lab**	0.84	0.79	0.92	0.73	0.88	0.70
2		0.90	0.76	0.96	0.86	0.87	0.73
3		0.85	0.81	0.86	0.80	0.84	0.82
4		0.92	0.90	0.97	0.87	0.93	0.86
5		0.91	0.80	0.85	0.86	0.93	0.84
6		0.90	0.73	0.96	0.78	0.87	0.71
7		0.88	0.77	0.87	0.79	0.89	0.80
8		0.88	0.86	0.87	0.78	0.84	0.82
9		0.85	0.85	0.84	0.73	0.83	0.88
10		0.88	0.72	0.89	0.79	0.92	0.76
mean $\pm$ std		**0.88$\pm$0.02**	0.80$\pm$0.06	**0.90$\pm$0.05**	0.80$\pm$0.05	**0.88$\pm$0.03**	0.79$\pm$0.06

Table 5.4. AF Detection Performance Comparison on all 33 (23 with AF and 10 healthy) subjects

	Accuracy		**Sensitivity**		**Specifity**	
	RAFMA	EMDAF	RAFMA	EMDAF	RAFMA	EMDAF
AF Diagnosis	**0.97**	0.89	**1.00**	0.87	**0.90**	0.83

5.5. Discussion

In this study, a new approach (RAFMA) based on time-time recurrence analysis of the ECG signal is introduced to address Atrial Fibrillation detection in the presence motion and noise artifacts. Fig. 9 shows noise-contaminated ECG segments from a non-AF subject (top) and an AF subject (bottom), where the segments are captured from the HolterCare program supported by Scottcare Corporation.

As shown in above figure, all three channels show that the ECG segments are corrupted by MN artifacts to such an extent that the correct RR interval cannot be obtained. Especially for the segment from a non-AF subject, the RR intervals are highly irregular and hence they could be mistaken as AF. Thus, it is reasonable to exclude the noise-contaminated segment in order to accurately detect fibrillation.

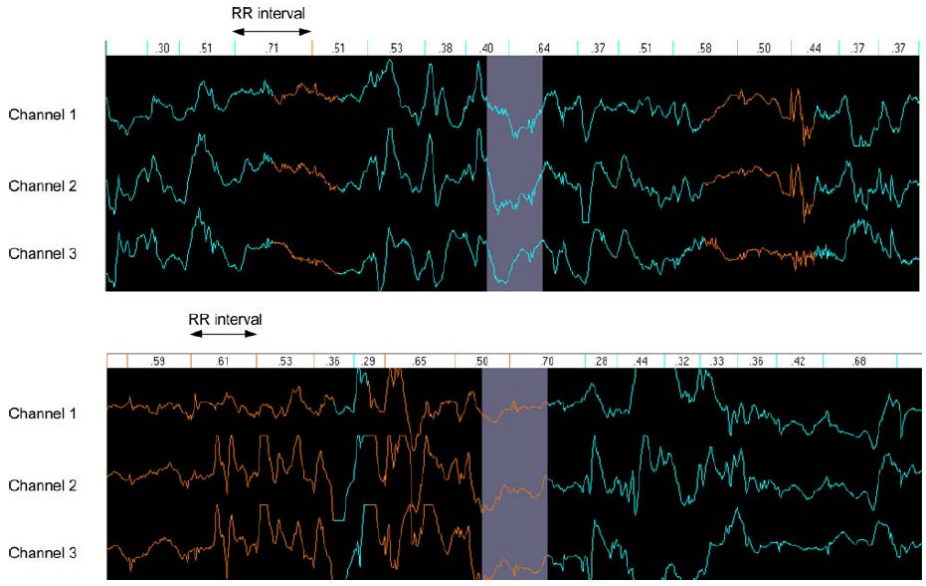

Figure 5.9 – Noise-contaminated ECG segments from a non-AF subject (top) and an AF subject (bottom) [38].

The idea behind the RAFMA algorithm is to transform the time domain signal into a time-time domain matrix using recurrence quantification. We showed in time-time domain the AF episodes of MNA free and MNA corrupted ECG signals are easier to be distinguished. Two datasets has been used to verify the algorithm performance. The second dataset reflects different types of activities and movements. In all of the recordings of dataset (2), the reference HR was calculated from an ECG signal that was collected simultaneously with the ECG signal. It has been shown in the results section that the proposed RAFMA algorithm can be used for MNA detection in ECG recordings with performance around 90% from 10 healthy subjects and detection of AF episodes in the signal with accuracy of 97% from 33 subjects.

We can use our RAFMA approach for many applications in need of discrimination between clean and noise-contaminated ECG segments. It may be possible that RAFMA can be applied to respiratory rate estimation [46-49] and autonomic nervous function assessment [50] as well. The respiratory sinus arrhythmia is associated with RR intervals or heart rate variability [46-49] and the sympathetic and parasympathetic nervous systems were assessed from RR intervals [50]. Thus, incorrect RR interval detection due to MNA can lead inaccurate respiratory rate and autonomic nervous function assessments.

The proposed RAFMA algorithm can also be implemented in real time. We have found that the algorithm takes 0.2s to process 60 sec of ECG data for both MNA and AF detection in MATLAB R2014a on a 3.4 GHz Intel Core-i7 processor. While the run-time with EMDAF algorithm is 12 times slower around 2.4 for 60 sec of data. Therefore, given the high accuracy of the proposed approach in detection of motion artifacts and AF this method has the potential to be applicable for implementation on wearable devices such as smart watches and ECG-based fitness sensors. We believe our real-time realizable methods will significantly improve automated AF detection using continuous ECG data, perhaps ushering in a new era of automated arrhythmia monitoring.

ACKNOWLEDGEMENT

This work was supported in part by the US Army Medical Research and Materiel Command (USAMRMC) under Grant No. W81XWH-12-1-0541

References

1. Heeringa, J., et al., Prevalence, incidence and lifetime risk of atrial fibrillation: the Rotterdam study. European Heart Journal, 2006. 27(8): p. 949-953.
2. Benjamin, E.J., et al., Impact of atrial fibrillation on the risk of death: the Framingham Heart Study. Circulation, 1998. 98(10): p. 946-52.
3. Wolf, P.A., R.D. Abbott, and W.B. Kannel, Atrial fibrillation as an independent risk factor for stroke: the Framingham Study. Stroke, 1991. 22(8): p. 983-8.
4. Humphries, K.H., et al., New-onset atrial fibrillation: sex differences in presentation, treatment, and outcome. Circulation, 2001. 103(19): p. 2365-70.
5. Kerr, C., et al., Follow-up of atrial fibrillation: The initial experience of the Canadian Registry of Atrial Fibrillation. Eur Heart J, 1996. 17 Suppl C: p. 48-51.
6. Kinlay, S., et al., Cardiac event recorders yield more diagnoses and are more cost-effective than 48-hour Holter monitoring in patients with palpitations. A controlled clinical trial. Ann Intern Med, 1996. 124(1 Pt 1): p. 16-20.
7. Roche, F., et al., Frequent and prolonged asymptomatic episodes of paroxysmal atrial fibrillation revealed by automatic long-term event recorders in patients with a negative 24-hour Holter. Pacing Clin Electrophysiol, 2002. 25(11): p. 1587-93.
8. Benjamin, E.J., et al., Prevention of atrial fibrillation: report from a national heart, lung, and blood institute workshop. Circulation, 2009. 119(4): p. 606-18.
9. Defaye, P., F. Dournaux, and E. Mouton, Prevalence of supraventricular arrhythmias from the automated analysis of data stored in the DDD pacemakers of 617 patients: the AIDA study. The AIDA Multicenter Study Group. Automatic Interpretation for Diagnosis Assistance. Pacing Clin Electrophysiol, 1998. 21(1 Pt 2): p. 250-5.
10. Aytemir, K., et al., Prediction of atrial fibrillation recurrence after cardioversion by P wave signal-averaged electrocardiography. Int J Cardiol, 1999. 70(1): p. 15-21.

11. Clavier, L., et al., Automatic P-wave analysis of patients prone to atrial fibrillation. Med Biol Eng Comput, 2002. 40(1): p. 63-71.
12. Dotsinsky, I., Atrial wave detection algorithm for discovery of some rhythm abnormalities. Physiol Meas, 2007. 28(5): p. 595-610.
13. Ehrlich, J.R., et al., Prediction of early recurrence of atrial fibrillation after external cardioversion by means of P wave signal-averaged electrocardiogram. Z Kardiol, 2003. 92(7): p. 540-6.
14. Fukunami, M., et al., Detection of patients at risk for paroxysmal atrial fibrillation during sinus rhythm by P wave-triggered signal-averaged electrocardiogram. Circulation, 1991. 83(1): p. 162-9.
15. Michalkiewicz, D., et al., [Detection of patients at risk for paroxysmal atrial fibrillation (PAF) by signal averaged P wave, standard ECG and echocardiography]. Pol Merkur Lekarski, 2006. 20(115): p. 69-72.
16. Opolski, G., et al., Detection of patients at risk for recurrence of atrial fibrillation after successful electrical cardioversion by signal-averaged P-wave ECG. Int J Cardiol, 1997. 60(2): p. 181-5.
17. Portet, F., P wave detector with PP rhythm tracking: evaluation in different arrhythmia contexts. Physiol Meas, 2008. 29(1): p. 141-55.
18. Reddy, S., et al., Review of methods to predict and detect atrial fibrillation in post-cardiac surgery patients. J Electrocardiol, 1999. 32 Suppl: p. 23-8.
19. Murgatroyd, F.D., et al., Identification of atrial fibrillation episodes in ambulatory electrocardiographic recordings: validation of a method for obtaining labeled R-R interval files. Pacing Clin Electrophysiol, 1995. 18(6): p. 1315-20.
20. Page, R.L., et al., Asymptomatic arrhythmias in patients with symptomatic paroxysmal atrial fibrillation and paroxysmal supraventricular tachycardia. Circulation, 1994. 89(1): p. 224-7.
21. Rawles, J.M. and E. Rowland, Is the pulse in atrial fibrillation irregularly irregular? Br Heart J, 1986. 56(1): p. 4-11.
22. Dash, S., et al., Automatic real time detection of atrial fibrillation. Ann Biomed Eng, 2009. 37(9): p. 1701-9.
23. Tateno, K. and L. Glass. A method for detection of atrial fibrillation using RR intervals. in Computers in Cardiology 2000. 2000.
24. Tateno, K. and L. Glass, Automatic detection of atrial fibrillation using the coefficient of variation and density histograms of RR and ΔRR intervals. Medical and Biological Engineering and Computing, 2001. 39(6): p. 664-671.
25. Lian, J., L. Wang, and D. Muessig, A simple method to detect atrial fibrillation using RR intervals. Am J Cardiol, 2011. 107(10): p. 1494-7.
26. Sarkar, S., D. Ritscher, and R. Mehra, A detector for a chronic implantable atrial tachyarrhythmia monitor. IEEE Trans Biomed Eng, 2008. 55(3): p. 1219-24.
27. Lawless, S.T., Crying wolf: false alarms in a pediatric intensive care unit. Crit Care Med, 1994. 22(6): p. 981-5.
28. Muhlsteff, J., et al., Wearable approach for continuous ECG--and activity patient-monitoring. Conf Proc IEEE Eng Med Biol Soc, 2004. 3: p. 2184-7.
29. Paul, J.S., M.R. Reddy, and V.J. Kumar, A transform domain SVD filter for suppression of muscle noise artefacts in exercise ECG's. IEEE Trans Biomed Eng, 2000. 47(5): p. 654-63.
30. Thakor, N.V. and Y.S. Zhu, Applications of adaptive filtering to ECG analysis: noise cancellation and arrhythmia detection. IEEE Trans Biomed Eng, 1991. 38(8): p. 785-94.
31. Lu, G., et al., Removing ECG noise from surface EMG signals using adaptive filtering. Neurosci Lett, 2009. 462(1): p. 14-9.
32. Donoho, D.L., De-noising by soft-thresholding. Information Theory, IEEE Transactions on, 1995. 41(3): p. 613-627.
33. Sayadi, O. and M.B. Shamsollahi. ECG Denoising with Adaptive Bionic Wavelet Transform. in Engineering in Medicine and Biology Society, 2006. EMBS '06. 28th Annual International Conference of the IEEE. 2006.

34. Ayat, M., et al., ECG denoising using modulus maxima of wavelet transform. Conf Proc IEEE Eng Med Biol Soc, 2009. 2009: p. 416-9.
35. Sameni, R., et al., A Nonlinear Bayesian Filtering Framework for ECG Denoising. Biomedical Engineering, IEEE Transactions on, 2007. 54(12): p. 2172-2185.
36. Kishimoto, Y., Y. Kutsuna, and K. Oguri. Detecting Motion Artifact ECG Noise During Sleeping by Means of a Tri-axis Accelerometer. in Engineering in Medicine and Biology Society, 2007. EMBS 2007. 29th Annual International Conference of the IEEE. 2007.
37. Yoon, S., et al., Adaptive Motion Artifacts Reduction Using 3-axis Accelerometer in E-textile ECG Measurement System. Journal of Medical Systems, 2008. 32(2): p. 101-106.
38. Lee, J., et al., Automatic motion and noise artifact detection in Holter ECG data using empirical mode decomposition and statistical approaches. IEEE Trans Biomed Eng, 2012. 59(6): p. 1499-506.
39. MIT/BIH Atrial Fibrillation Database. Available from: http://www.physionet.org/physiobank/database/afdb/.
40. Cynthia A. Sanoski, Clinical, Economic, and Quality of Life Impact of Atrial Fibrillation FCCP, BCPS. Manag Care Pharm., 2009. 15(6-b): p. 4-9.
41. Sherwood, L., Human Physiology: From Cells to Systems. 2008: Cengage Learning.
42. Ashley, E.A. and J. Niebauer, Cardiology Explained. 2004: Remedica.
43. Eckmann, J.P., S.O. Kamphorst, and D. Ruelle, Recurrence Plots of Dynamical Systems. EPL (Europhysics Letters), 1987. 4(9): p. 973.
44. Takens, F., Detecting strange attractors in turbulence, in Dynamical Systems and Turbulence, Warwick 1980, D. Rand and L.-S. Young, Editors. 1981, Springer Berlin Heidelberg. p. 366-381.
45. Pan, J. and W.J. Tompkins, A Real-Time QRS Detection Algorithm. Biomedical Engineering, IEEE Transactions on, 1985. BME-32(3): p. 230-236.
46. Boyle, J., et al., Automatic detection of respiration rate from ambulatory single-lead ECG. IEEE Trans Inf Technol Biomed, 2009. 13(6): p. 890-6.
47. Babaeizadeh, S., et al., Electrocardiogram-derived respiration in screening of sleep-disordered breathing. J Electrocardiol, 2011. 44(6): p. 700-6.
48. Stein, P.K., et al., A simple method to identify sleep apnea using Holter recordings. J Cardiovasc Electrophysiol, 2003. 14(5): p. 467-73.
49. Chan, C.T., et al., Impact of nocturnal hemodialysis on the variability of heart rate and duration of hypoxemia during sleep. Kidney Int, 2004. 65(2): p. 661-5.
50. Bai, Y., et al., Impairment of the autonomic nervous function during decompression sickness in swine. J Appl Physiol (1985), 2009. 106(3): p. 1004-9.

Chapter 6: IMAR – A Time-Domain Motion and Noise Artifact Reduction Algorithm

6.1. Introduction

In previous chapters we introduced three different motion and noise artifact detection techniques. In this chapter we present a motion and noise artifact reduction and vital sign reconstruction method using a blind source separation (BSS) technique. There are many MNA reduction techniques based on the concept of blind source separation. BSS is attractive and has garnered significant interest since this approach does not require a reference signal. The aim of the BSS is to estimate a set of uncorrupted signals from a set of mixed signals which is assumed to contain both the clean and MNA sources [23]. Some of the popular BSS techniques are independent component analysis (ICA) [3], canonical correlation analysis (CCA) 28, principle component analysis (PCA) [12], and singular spectrum analysis (SSA) [5].

In ICA, the recorded signals are decomposed into their independent components or sources [3]. CCA uses the second order statistics (SOS) to generate components derived from their uncorrelated nature [7]. PCA is another noise reduction technique which aims to separate the clean signal dynamics from the MNA data. A multi-scale PCA has been also proposed to account for time-varying dynamics of the signal and motion artifacts from PPG recordings [20].

A promising approach that can be applied to signal reconstruction is the singular spectrum analysis (SSA). The SSA is a model-free BSS technique, which decomposes the data into a number of components which may include trends, oscillatory components, and noise (see historical reviews in [9]). The main advantage of SSA over ICA is that SSA does not require user input to choose the appropriate components for reconstruction and MNA removal. Comparing PCA to SSA, SSA can be applied in cases where the number of signal components is more than the rank of the PCA covariance matrix. Applications of the SSA

include extraction of the amplitude and low frequency artifacts from single channel EEG recordings [26], and removing heart sound dynamics from respiratory signals [8].

In this chapter, we introduce a novel approach to reconstruct a PPG signal from those portions of data that have been identified to be corrupted using the algorithm detailed in Part I of the companion chapter. The fidelity of the reconstructed signal was determined by comparing the estimated SpO2 and heart rate (HR) to reference values. In addition, we compare the reconstructed SpO2 and HR values obtained via the ICA to our method. We have chosen to compare our method to ICA since the latter has recently been shown to provide accurate reconstruction of corrupted PPG signals [17].

6.1. Materials and Method

6.1.1. Experimental Protocol and Preprocessing

Three sets of data were collected from healthy subjects recruited from the student community of Worcester Polytechnic Institute (WPI). This study was approved by WPI's institutional review board and all the subjects gave informed consent before data recording.

In the first experiment, 11 healthy volunteers were asked to wear a forehead reflectance pulse oximeter developed in our lab along with a reference Masimo Radical (Masimo SET®) finger transmittance pulse oximeter. PPG signals from the forehead sensor and reference (HR) derived from a finger pulse oximeter were acquired simultaneously. The HR and SpO2 signals were acquired at 80Hz and 1Hz, respectively. After baseline recording for 5 minutes without any movement (i.e. clean data), motion artifacts were induced in the PPG data by the spontaneous movements in both horizontal and vertical directions of the subject's head while the right middle finger was kept stationary. Subjects were directed to introduce the motions for specific time intervals that determined the percentage of noise within each 1 minute segment, varying from 10 to 50%. For example, if a subject was instructed to make left-right movements for 6 seconds, a 1 minute segment of data would contain 10% noise.

The second dataset consisted of finger-PPG signals from the same 9 healthy volunteers in an upright sitting posture using an infrared reflection type PPG transducer (TSD200). An MP1000 pulse oximeter (BIOPAC Systems Inc., CA, USA) was also used to acquire finger PPG signals at 100Hz. One pulse oximeter of each model was placed on the same hand's index finger (one model) and middle finger (the other model) simultaneously. After baseline recording for 5 minutes without any movement (i.e. clean data), motion artifacts were induced in the PPG data by the left-right movements of the index finger while the middle finger was kept stationary to provide a reference. Similar to the first dataset, motion was induced at specific time intervals corresponding to 10 to 50% corruption duration in 1 minute segments, i.e. the controlled movement was carried out five times per subject.

The third dataset consisted of data measurements from 9 subjects with the PPG signal recorded from the subjects' forehead using our custom sensor simultaneously with the reference ECG, HR and SpO2 from a Holter Monitor at 180Hz and Masimo (Rad-57) pulse oximeter at 0.5Hz respectively. The reference pulse oximeter provided HR and SpO2 measured from the subject's right index finger, which was held steadily to their chest. The signals were recorded while the subjects were going through sets of walking and climbing up and down flights of stairs for approximately 45 min.

Once data were acquired, PPG signals from all three experiments outlined above were preprocessed offline using Matlab (MathWorks, R2012a). The PPG signals were filtered using a zero-phase forward-reverse 4th order IIR band-pass filter with cutoff frequency 0.5-12Hz.

6.1.2. Motion Artifact Reduction

To reconstruct the artifact-corrupted portion of the PPG signal that has been detected using the support vector machine approach provided in the accompanying chapter, we propose a novel hybrid procedure using Iterative Singular Spectrum Analysis (ISSA) and a frequency matching algorithm. Henceforth, we will call these combined procedures the iterative motion artifact removal (IMAR) algorithm.

Singular Spectrum Analysis

The SSA is composed of two stages: singular decomposition and spectral reconstruction. The former is the spectral decomposition or eigen-decomposition of the data matrix whereas the latter is the reconstruction of the signal based on using only the significant eigenvectors and associated eigenvalues. The assumption is that given a relatively high signal-to-noise ratio of data, significant eigenvectors and associated eigenvalues represent the signal dynamics and less significant values represent the MNA components.

The calculation of the singular stage of the SSA consists of two steps: embedding followed by singular value decomposition (SVD). In essence, these procedures decompose the data into signal dynamics consisting of trends, oscillatory components, and MNA. The spectral stage of the SSA algorithm also consists of two steps: grouping and diagonal averaging. These two procedures are used to reconstruct the signal dynamics but without the MNA components. In the following section, we detail all four steps in the SSA algorithm.

1) Singular Decomposition

- Embedding

Assume we have a nonzero real-value time series of length N samples, i.e., $X = \{x_1, x_2, \dots, x_N\}$. In the embedding step, window length $f_s/f_l < L < N/2$ is chosen to embed the initial time series, where f_s is the sampling frequency and f_l is the lowest frequency in the signal. We map the time series X into the L lagged vectors, $X = \{x_i, x_{i+1}, \dots, x_{i+L-1}\}$ for $i = 1,2, \dots, K$, where $K = N - L + 1$ [9]. The result is the trajectory data matrix T_x or vector X_i that is each row of T_x for $i = 1,2, \dots, K$.

$$T_x = \begin{bmatrix} X_1 \\ X_2 \\ \vdots \\ X_K \end{bmatrix} = \begin{bmatrix} x_1 & x_2 & \cdots & x_L \\ x_2 & x_3 & \cdots & x_{L+1} \\ \vdots & \vdots & \ddots & \vdots \\ x_K & x_{K+1} & \cdots & x_N \end{bmatrix} \quad (1)$$

From Eq. 1, it is evident that the trajectory matrix, T_x, is a Hankel matrix.

- Singular Value Decomposition

The next step is to apply the SVD to the trajectory matrix $T_x$which results in eigenvalues and eigenvectors of the matrix $T_x{T_x}^T$ where T_i for $i = 1, \dots, L$can be defined as $T = USV^T$ [9]. U_i for $1 < i < L$ is a $K \times L$ orthonormal matrix. Si for $1 < i < L$ is a diagonal matrix and V_i for $1 < i < L$ is an $L \times L$ square orthonormal matrix, which is considered the principle component. In this step, T_x has L many singular values which are $\sqrt{\lambda_1} > \sqrt{\lambda_2} >, \dots, \sqrt{\lambda_L}$. By removing components with eigenvalues equal to zero, then the i^{th} eigentriple of T_i can be written as $U_i \times \sqrt{\lambda_i} \times {V_i}^T$ for $i = 1,2, \dots, d$, in which $d = \max(i: \sqrt{\lambda_i} > 0)$ is the number of nonzero singular values of T_x. Normally every harmonic component with a different frequency produces two eigentriples with similar singular values. So the trajectory matrix T_x can be denoted as [9]

$$T_x = T_1 + T_2 + \cdots + T_d = U_1\sqrt{\lambda_1}{V_1}^T + \cdots + U_d\sqrt{\lambda_d}{V_d}^T = \sum_{i=1}^{d} U_i\sqrt{\lambda_i}{V_i}^T \qquad (2)$$

Projecting the time series onto the direction of each eigenvector yields the corresponding temporal principal component (PC) [6].

2) Spectral Reconstruction:

The reconstruction stage has two steps: grouping and diagonal averaging. First the subgroups of the decomposed trajectory matrices are grouped and then a diagonal averaging step is needed so that a new time series can be formed [5].

- Grouping

The grouping step of the reconstruction stage decomposes the $L \times K$matrix $T_i (i = 1,2, \dots, d)$ into subgroups according to the trend, oscillatory components, and MNA dynamics. The grouping step divides

the set of indices $1,2,\ldots,d$ into a collection of m disjoint subsets of $I=\{I_1,\ldots,I_m\}$ [11]. Thus, T_I corresponds to the group I. $T_{I_i}$is a sum of T_j, where $j \in I_i$. So $T_x$can be expanded as

$$T_x = \overbrace{T_1+\ldots+T_L}^{SVD} = \overbrace{T_{I_1}+\ldots+T_{I_m}}^{Grouping} \quad (3)$$

- Diagonal averaging

In the final step of analysis, each resultant matrix, T_{I_i}, in Eq. (3) is transformed into a time series of length N. We obtain the new Hankel matrices $\tilde{X}^{(i)}$ by averaging the diagonal elements of the matrix T_{I_i} [6]. Let H be denoted as the Hankel operator. So that we obtain the Hankel matrix $\tilde{X}^{(i)} = HT_{I_i}$ for $i = 1,\ldots,m$ [11]. Under the assumption of weak separability and applying the Hankel procedure to all matrix components of Eq. (3), we obtain the following expansion

$$X = \tilde{X}^{(1)} + \tilde{X}^{(2)} + \ldots + \tilde{X}^{(M)} \quad (4)$$

We can assert that $\tilde{X}^{(1)}$ is related to the trend of the signal; however, harmonic and noisy components do not necessarily follow the order of $\sqrt{\lambda_1} > \sqrt{\lambda_2} >, \ldots, \sqrt{\lambda_M}$.

Iterative Motion Artifact Reduction based on SSA

In order to reconstruct the MNA corrupted segment of the signal, an iterative motion artifact removal approach based on SSA was explained in the last section. The ultimate goodness of the reconstructed signal is determined by the accuracy of the estimated SpO_2 and HR values. The top and bottom panels of Fig.1 show clean and MNA corrupted signals, respectively.

Fig. 2(a) and (b) shows the first 12 eigenvectors of the clean and MNA corrupted data as shown in Fig. 1, respectively. The most important part of the SSA is to choose the proper eigenvector components for reconstruction of the signal. Under the assumption of high SNR, the normal practice is to select only the largest eigenvalues and associated eigenvectors for signal reconstruction.

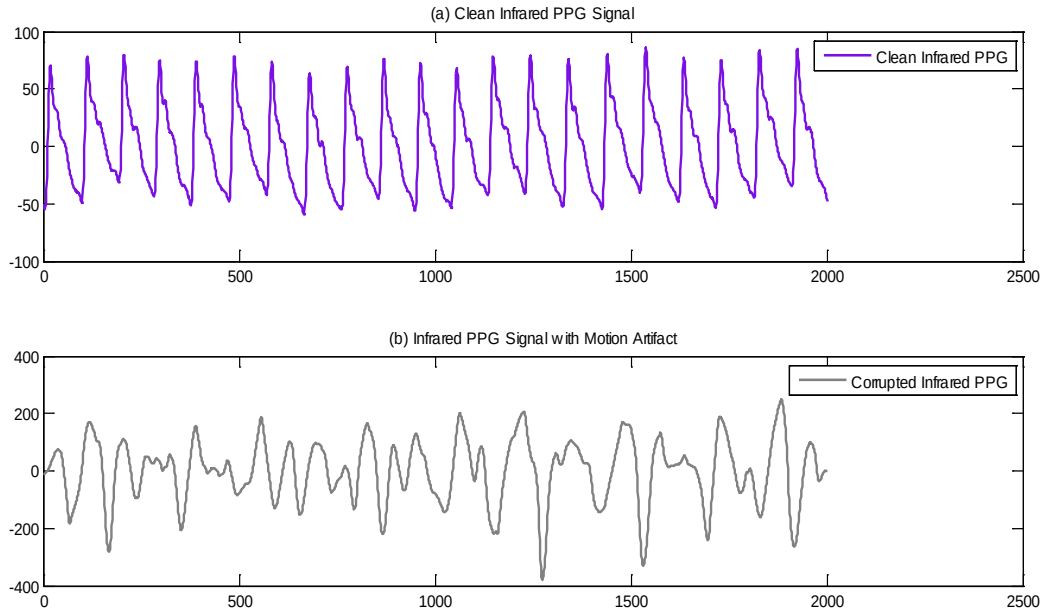

Figure 6.1 - Typical infrared PPG signal; (a) clean, (b) corrupted with motion artifacts.

However, most often it is difficult to determine the demarcation of the significant from non-significant eigenvalues. Further, the MNA dynamics can overlap with the signal dynamics, hence, choosing the largest eigenvalues does not necessarily result in an MNA-free signal.

To overcome the above limitations, we have modified the SSA approach. The first step of our modified SSA involves computing singular value decomposition on both a corrupted data segment and its most prior adjacent clean data segment. Under the assumption of a high SNR of the data, the second step is to retain only the top 5% of the eigenvalues and their associated eigenvectors. The third step is to replace the corrupted segment's top 5% eigenvalues with the clean segment's eigenvalues. The fourth step is to further limit the number of eigenvectors by choosing only those eigenvectors that have heart rates between $0.66Hz < f_s < 3Hz$ for both the clean and noise corrupted data segments. The two extreme heart rates are chosen so that they account for possible scenarios that one may encounter with low and high heart rates.

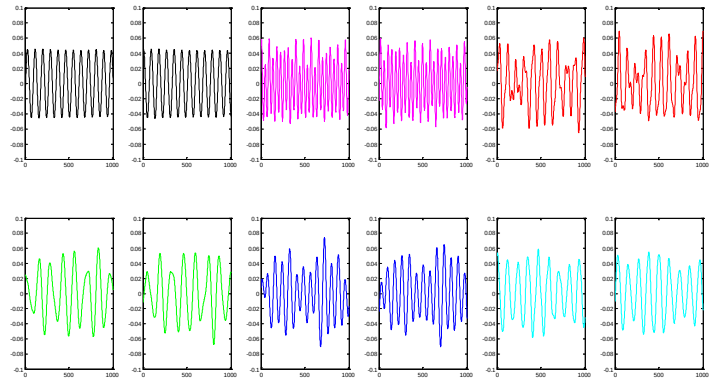

(a)

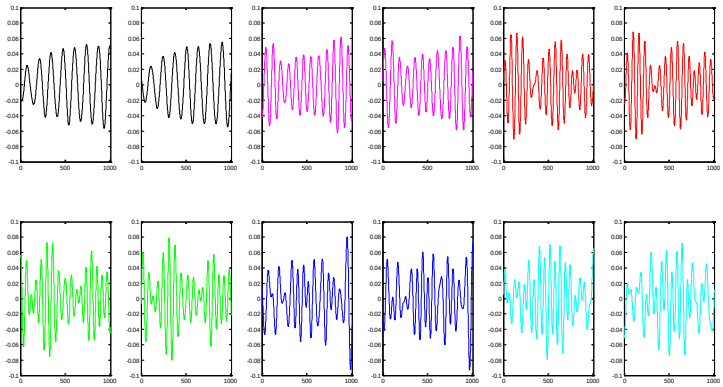

(b)

Figure 6.2 - The first 12 eigenvector components of the PPG signal for: (a) Clean Infrared PPG, (b) Corrupted Infrared PPG.

With the remaining candidate eigenvectors resulting from step four, we further prune non-significant eigenvectors by performing frequency matching of the noise corrupted eigenvectors to those of the clean data segment's eigenvectors, in the fifth step. Only those eigenvectors' frequencies that match to those of the clean eigenvectors are retained from the pool of eigenvectors remaining from step four. For the remaining eigenvector candidates, we perform iterative SSA to further reduce MNA and match the dynamics of the clean data segments' eigenvectors for the final step. For each iteration we perform the standard SSA algorithm. It is our experience that this convergence is achieved within 4 iterations. Fig. 3

shows an example of the iterative SSA procedure applied to candidate eigenvectors that have resulted from step four of the procedure for the modified SSA algorithm.

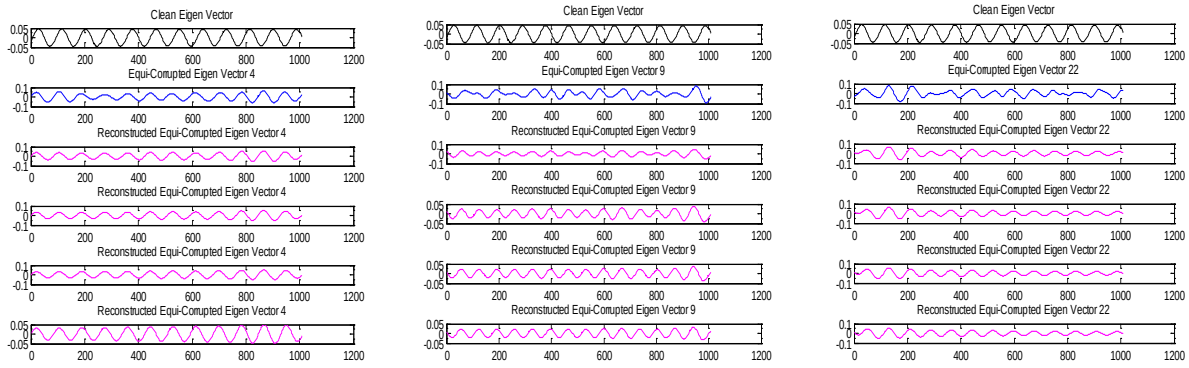

(a) (c) (b)

Figure 6.3 - Iterative reconstruction of a corrupted eigenvector with frequency of 0.967 Hz. Black font signals (top panels) represent the clean component with frequency of 0.967 Hz; Blue font signals (2nd rows) indicate the corrupted component with the same frequency; Pink font signals are related to iterative evolution of corrupted component to a clean oscillatory signal. (a) Reconstruction of 4th corrupted eigenvector compared to the corresponding clean component. The final pattern after 4 iterations resembles the black font clean component in the top panel. This component is chosen among the components with the same frequency, since it shows the most similarity to the black font clean component. (b) Reconstruction of 9th corrupted eigenvector compared to the corresponding clean component. (c) Reconstruction of 22nd corrupted eigenvector compared to the corresponding clean component.

Note that there may be several eigenvectors remaining after the fifth step, hence, this example shows an iterative SSA procedure performed on a particular set of candidate eigenvectors that may match most closely to an eigenvector of a clean data segment. The top row of panels of Fig. 3 represents one of the eigenvectors of the clean signal and the second row of panels represents the MNA corrupted signal's candidate eigenvectors which have the same frequency as that of the clean signal's eigenvector. The remaining lower panels of Fig. 3 represent the candidate eigenvectors after they have gone through four successive iterations of the SSA algorithm. For this portion of the SSA algorithm, we perform SVD on the trajectory matrix of Eq. (1) created from the candidate eigenvector and then reconstruct the eigenvectors

based on SSA using only the first 3 largest eigenvalues obtained from the SVD. This process repeats iteratively until the shape of the reconstructed eigenvector closely resembles one of the clean eigenvectors with the same frequency. It can be seen from Fig. 3 that after 4 iterations the result shown in the (a) panel corresponds most closely to the clean signal's eigenvector, hence, this eigenvector is selected rather than the eigenvectors shown in panels b-c. We calculate the discarding metric (DM) at each iteration and compare this value to the DM value of the corresponding clean component. The DM is calculated according to:

$$DM = {\Sigma|u|}/{L(u)} \qquad (5)$$

where u is the signal component, and $|.|$, $L(.)$ are absolute operator and component length, respectively. The entire procedure for the modified SSA algorithm is summarized in Table (1).

6.2. Results

6.2.1. Noise Sensitivity Analysis

To validate the proposed IMAR procedure, we added different SNR levels of Gaussian white noise (GWN) and colored noise to an experimentally collected clean segment of PPG signal. The purpose of the simulation was to quantitatively determine the level of noise that can be tolerated by the algorithm. Seven different SNR levels ranging from 10 dB to -25 dB were considered. For each SNR level, 50 independent realizations of GWN and colored noise were added separately to a clean PPG signal. The Euler-Maruyama method was used to generate colored noise [16].

Fig. 4 shows the results of these simulations with additive GWN. The left panels show pre- and post-reconstruction HR in comparison to the reference HR; the right panels show the corresponding comparison for SpO2. Tables (2) and (3) show the mean and standard deviation values of the pre- (2nd column) and post-reconstruction (4th column), and the reference (3rd column) HR and SpO2 values, respectively for all SNR.

Table 6.1. Iterative Motion Artifact Reduction (IMAR) Procedure

Assumption –Heart rate and SpO_2 do not change abruptly and are stationary within the short data segment.

Application – Offline Motion Artifact Removal

Objective – Reconstruction of corrupted PPG segment for the purpose of estimating heart rates and SpO_2.

Routine

Step 1. First, compute SVD on both corrupted data segments and their most prior adjacent clean data segments

Step 2. Next, keep the top 5% of the clean and corrupted components, based on the eigenvalues being sorted from largest to smallest.

Step 3. Replace the corrupted eigenvalues with corresponding clean eigenvalues.

Step 4. Among the clean and corrupted components, only choose those with frequency within the heart rate frequency range of $0.66 < F_S < 3$Hz.

Step 5. Apply frequency matching to discard those corrupted components (from Step 4) with different frequencies compared to clean components' frequencies.

Step 6. Remove corruption from each component obtained from Step 5 by applying the basic SSA algorithm iteratively.

6.a. Calculate the discarding metric for components achieved from SSA iterations and their counterpart clean components from Eq. 5.

6.b. Select those processed components with the closest DM and frequency value to the corresponding clean component's DM and frequency value.

Step 7. Finally, reconstruct the corrupted PPG segment based on the components achieved from Step 6.

The last columns of Tables (2) and (3) also show the estimated HR and SpO2 values obtained by the ICA method [17]. As shown in Fig. 4 and Tables (2) and (3), the reconstructed HR and SpO2 values using our IMAR approach were found to be not statistically different when compared to the reference values for all SNR except for -20 and -25 dB. However, the ICA method fails and we obtain significantly different values to those of the reference HR and SpO2 values when the SNR is lower than -10 dB.

Fig. 5 and Tables (4) and (5) show corresponding results to that of Fig. 4 and Tables (2) and (3) but with additive colored noise. Similar to the GWN case, the reconstructed HR and SpO2 values using the proposed IMAR approach are found to be not significantly different than the reference values for all SNR except for -20 and -25 dB. Moreover, the ICA compares poorly compared to our IMAR as the HR and

SpO2 values from the former method are found to be significantly different to the reference values for all SNR.

Table 6.2. Comparison & Statistical Analysis of HR Estimations from IMAR-reconstructed PPG for Different Levels of Additive White Noise. * represents p<0.05.

SNR (dB)	Head HR (mean ± std)	Finger HR (Reference) (mean ± std)	IMAR Reconstructed HR (mean ± std)	ICA Reconstructed HR (mean ± std)
10	54.80 ± 2.08	54.81 ± 1.81	55.05 ± 0.15	52.86 ± 0.44*
0	54.80 ± 2.72	54.81 ± 1.81	55.05 ± 0.14	50.58 ± 0.62*
-5	56.37 ± 8.18	54.81 ± 1.81	55.05 ± 0.15	48.64 ± 0.51*
-10	46.02 ± 22.93	54.81 ± 1.81	55.09 ± 0.15	46.85 ± 0.45*
-15	121.62 ± 69.33	54.81 ± 1.81	54.73 ± 0.62	45.17 ± 0.28*
-20	80.08 ± 37.69	54.81 ± 1.81	56.49 ± 2.69	43.08 ± 0.32*
-25	103.62 ± 52.49	54.81 ± 1.81	76.45 ± 7.52*	41.11 ± 0.30*

Table 6.3. Comparison & Statistical Analysis of Estimations from IMAR-reconstructed PPG for Different Levels of Additive White Noise. * represents p<0.05.

SNR (dB)	Head SpO_2 (mean ± std)	Finger SpO_2 (Reference) (mean ± std)	IMAR Reconstructed SpO_2 (mean ± std)	ICA Reconstructed SpO_2 (mean ± std)
10	106.88 ± 0.51	94.23 ± 0.80	94.83 ± 0.38	90.92 ± 0.38*
0	108.98 ± 0.14	94.23 ± 0.80	94.81 ± 0.42	86.88 ± 0.16*
-5	109.42 ± 0.06	94.23 ± 0.80	94.77 ± 0.26	82.86 ± 0.27*
-10	109.69 ± 0.04	94.23 ± 0.80	94.68 ± 0.30	78.81 ± 0.29*
-15	109.82 ± 0.02	94.23 ± 0.80	94.90 ± 0.41	74.88 ± 0.23*
-20	109.89 ± 0.01	94.23 ± 0.80	107.38 ± 1.06*	70.87 ± 0.22*
-25	109.94 ± 0.00	94.23 ± 0.80	97.38 ± 7.39*	66.91 ± 0.26*

Table 6.4. Comparison & Statistical Analysis of HR Estimations from IMAR-reconstructed PPG for Different Levels of Additive Colored Noise. * represents p<0.05.

SNR (dB)	Head HR (mean ± std)	Finger HR (Reference) (mean ± std)	IMAR Reconstructed HR (mean ± std)	ICA Reconstructed HR (mean ± std)
10	54.75 ± 1.73	54.81 ± 1.81	55.05 ± 0.26	53.36 ± 0.79
0	55.64 ± 2.72	54.81 ± 1.81	55.06 ± 0.27	50.83 ± 0.54*
-5	55.67 ± 2.88	54.81 ± 1.81	55.06 ± 0.15	48.90 ± 0.32*
-10	51.05 ± 8.24	54.81 ± 1.81	55.07 ± 0.13	46.79 ± 0.30*
-15	61.65 ± 32.08	54.81 ± 1.81	55.17 ± 0.08	45.15 ± 0.30*
-20	73.41 ± 47.73	54.81 ± 1.81	45.96 ± 5.59*	42.96 ± 0.41*
-25	66.37 ± 40.80	54.81 ± 1.81	61.86 ± 2.12*	41.04 ± 0.37*

Table 6.5. Comparison & Statistical Analysis of SpO2 Estimations from IMAR-reconstructed PPG for Different Levels of Additive Colored Noise. * represents p<0.05.

SNR (dB)	Head SpO2 (mean ± std)	Finger SpO2 (Reference) (mean ± std)	IMAR Reconstructed SpO2 (mean ± std)	ICA Reconstructed SpO2 (mean ± std)
10	94.14 ± 0.99	94.23 ± 0.80	94.85 ± 0.41	90.95 ± 0.18*
0	94.71 ± 1.20	94.23 ± 0.80	94.85 ± 0.53	86.84 ± 0.24*
-5	96.19 ± 1.41	94.23 ± 0.80	93.92 ± 0.83	82.86 ± 0.34*
-10	99.27 ± 1.46	94.23 ± 0.80	94.88 ± 0.96	78.89 ± 0.18*
-15	103.00 ± 0.88	94.23 ± 0.80	94.42 ± 1.71	74.87 ± 0.25*
-20	107.63 ± 0.26	94.23 ± 0.80	74.74 ± 7.92*	70.89 ± 0.17*
-25	105.91 ± 0.49	94.23 ± 0.80	70.75 ± 15.08*	66.89 ± 0.26*

6.2.2. Heart Rate and SpO2 Estimation from Forehead sensor

As described in section 2, we collected PPG data under three different experimental settings so that our proposed approach could be more thoroughly tested and validated. For all three experimental settings, the efficacy of our IMAR approach for the reconstruction of the MNA-affected portion of the signal will be compared with the reference HR and SpO2 values for all experimental datasets.

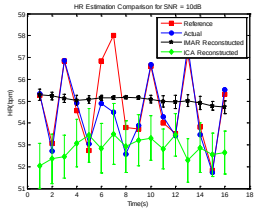

(1)

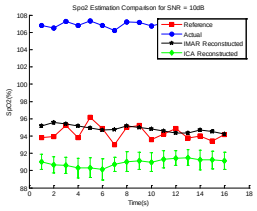

(2)

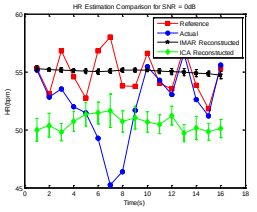

(3)

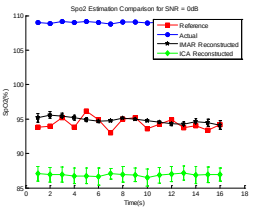

(4)

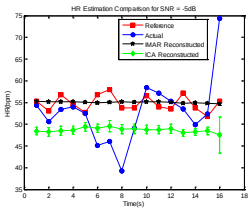

(5)

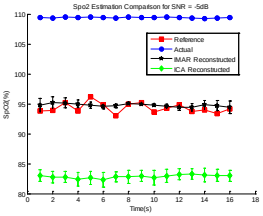

(6)

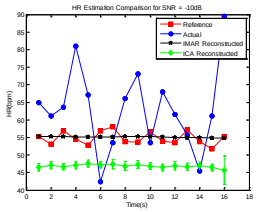

(7)

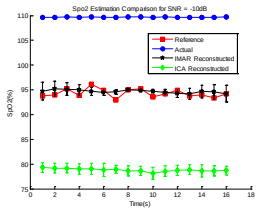

(8)

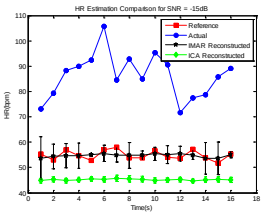

(10)

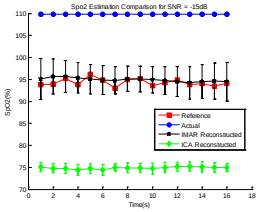

(11)

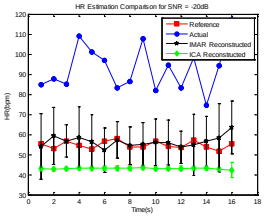

(12)

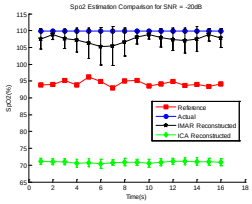

(13)

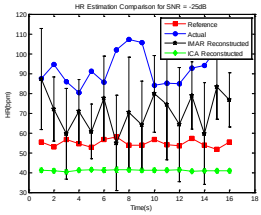

(14)

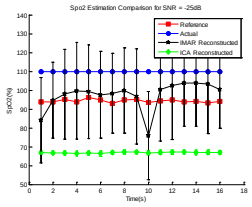

(15)

Figure 6.4 - (Odd#) HR estimated from reconstructed PPG for different additive white noise levels; (Even#) SpO2 estimated from reconstructed PPG for different levels of additive white noise.

For the error-free SpO2 estimation, Red and IR PPG signals with clearly separable DC and AC components are required. The pulsatile components of the Red and IR PPG signals are denoted as AC_{Red} and DC_{Red}, respectively, and the "ratio-of-ratio" R is estimated [21,22] as

$$R = \frac{AC_{Red}/DC_{Red}}{AC_{IR}/DC_{IR}} \qquad (6)$$

Accordingly, SpO2 is computed by substituting the R value in an empirical linear approximate relation given by

$$SpO2(\%) = (110 - 25R)(\%) \qquad (7)$$

After applying the proposed IMAR procedure to the identified MNA segment of the PPG signal, we estimate the SpO2 (using Eqs. 6-7) and HR, and compare it to the corresponding reference and MNA contaminated segment values. As was the case with the noise sensitivity analysis section, we compare the performance of the IMAR algorithm to the ICA method. The top and bottom panels of Fig. 6 represent a representative HR and SpO2 comparison result, respectively.

We can see from these figures that the estimated values for both HR (left panels) and SpO2 (right panels) from the IMAR (black font) track closely to the reference values recorded by the Masimo transmittance type finger pulse oximeter (red square line), while the estimated HR and SpO2 obtained from the ICA method (green font) deviate significantly from the reference signal. Tables (6) and (7) show comparison of the IMAR and the ICA reconstructed HR and SpO2 values, respectively, for all 10 subjects. As shown in Table (6), there was no significant difference between the finger reference HR and the IMAR reconstructed HR in 6 out of 10 subjects.

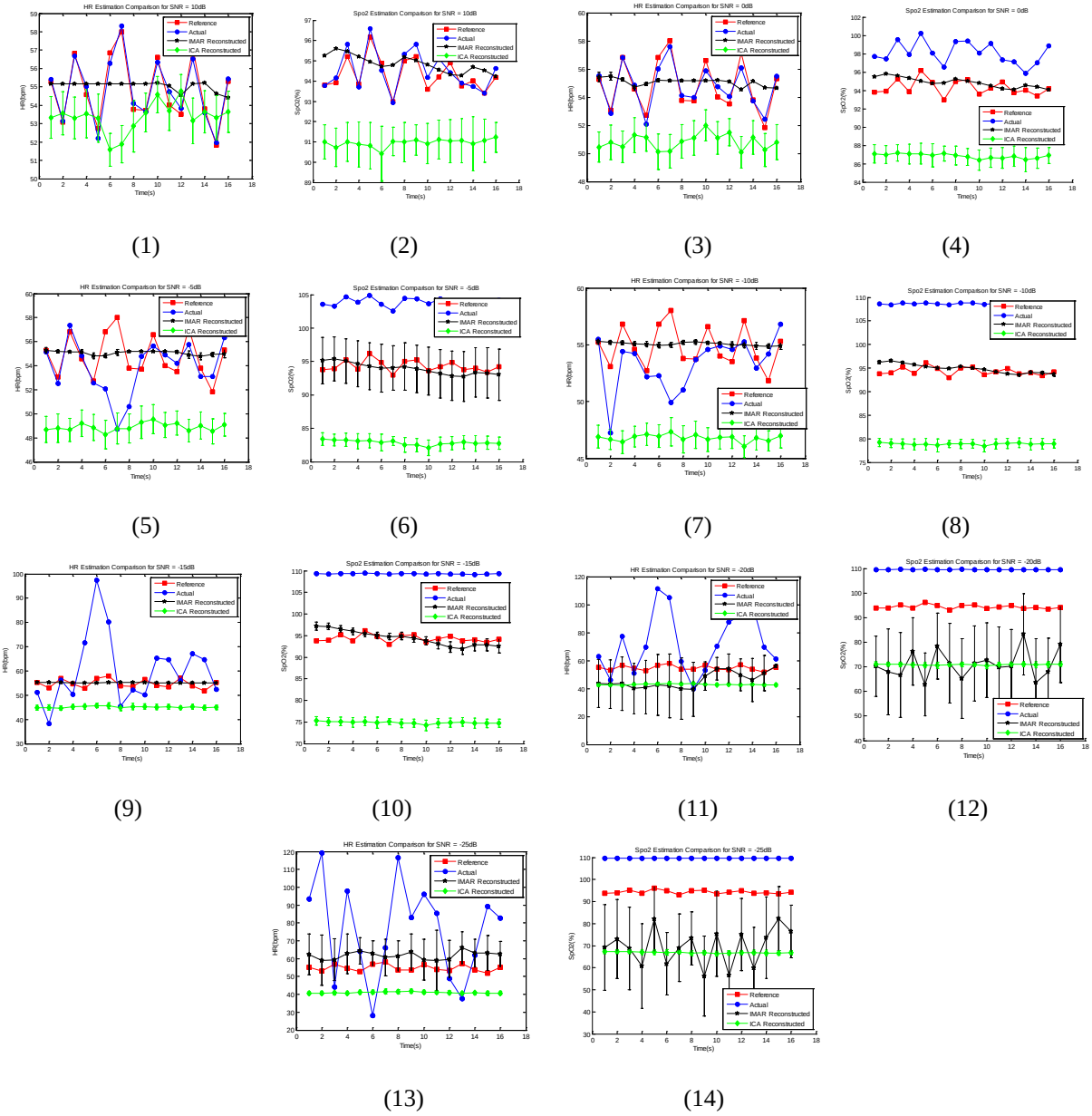

Figure 6.5 - (Odd#) HR estimated from reconstructed PPG for different additive colored noise levels; (Even#) SpO2 estimated from reconstructed PPG for different levels of additive colored

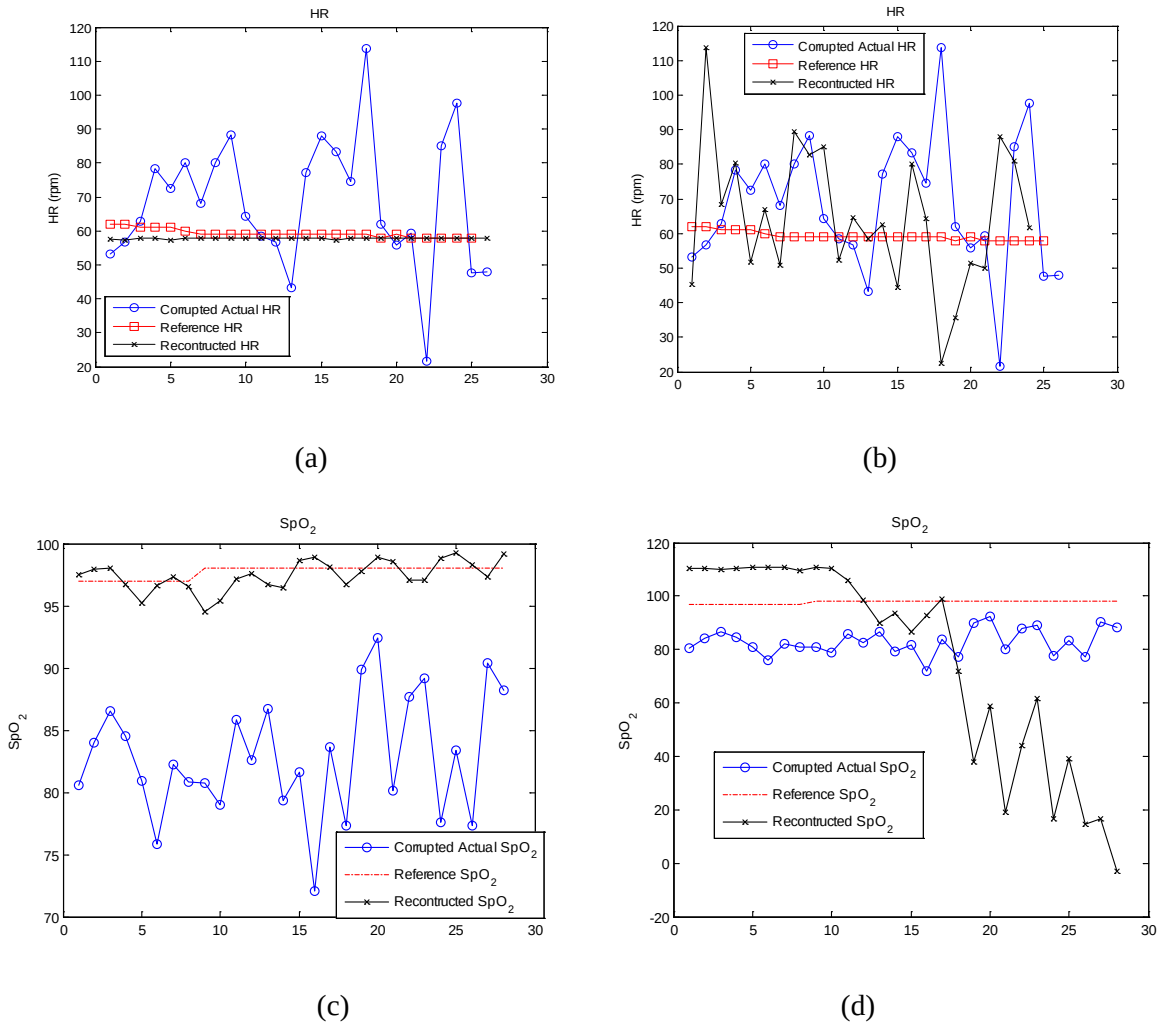

Figure 6.6 - (a) HR estimated from IMAR-reconstructed PPG compared to reference and corrupted PPG; (b) HR estimated from ICA-reconstructed PPG compared to reference and corrupted PPG; (c) SpO2 estimated from IMAR-reconstructed PPG compared to reference and corrupted PPG; (d) SpO2 estimated from ICA-reconstructed PPG compared to reference and corrupted PPG noise.

However, there was significant difference between the finger reference HR and the ICA reconstructed HR in all 10 subjects. Similarly, the reconstructed SpO2 values from the IMAR were found to be not significantly different than the finger reference values in 6 out of 10 subjects, but the ICA method was found to be significantly different for all 10 subjects.

Table 6.6. Comparison & Statistical Analysis of HR Estimations from IMAR-reconstructed PPG for 10 Different Subjects (Head Experiment). * represents p<0.05.

Subject	Head HR (mean ± std)	Finger HR (Reference) (mean ± std)	IMAR Reconstructed HR (mean ± std)	ICA Reconstructed HR (mean ± std)
1	68.31±19.25	59.23±1.49	59.76±0.22*	65.68±20.98*
2	85.39±34.53	71.55±3.037	73.72±0.31*	91.02±35.48*
3	76.19±8.88	77.39±1.360	78.705±0.33	68.06±14.14*
4	94.47±39.05	70.55±3.686	73.66±0.38*	75.32±13.42*
5	72.33±29.82	67.88±4.643	66.83±0.39	69.97±20.20*
6	45.09±10.06	51.44±1.481	49.00±0.09*	59.43±22.97*
7	44.82±24.47	59.82±1.486	57.56±0.21	64.49±35.63*
8	63.46±13.35	62.08±0.865	62.23±0.25	60.68±10.70*
9	59.37±30.85	49.05±1.555	49.19±0.20	60.27±13.24*
10	46.89±32.25	79.35±1.323	78.93±0.45	64.80±25.60*

Table 6.7. Comparison & Statistical Analysis of SpO2 Estimations from IMAR-reconstructed PPG for 10 Different Subjects (Head Experiment). * represents p<0.05.

Subject	Head SpO_2 (mean± std)	Finger SpO_2 (Reference) (mean± std)	IMAR Reconstructed SpO_2 (mean± std)	ICA Reconstructed SpO_2
1	82.86±4.86	97.70±0.46	97.94±0.93	76.721±38.132*
2	80.33±2.82	97.67±0.47	97.972±4.048*	111.097±1.496*
3	87.20±4.54	95.41±0.49	98.53±0.727*	74.081±21.678*
4	87.36±2.64	97±0	97,13±0.23	81.391±11.81*
5	84.25±3.76	98±0	96.82±5.25*	77.593±22.16*
6	92.38±2.64	98±0	97.47±0.97	84.069±14.84*
7	85.18±3.06	98.41±0.49	96.68±0.38	75.632±17.24*

8	90.94 ± 2.38	99.82 ± 0.06	97.99 ± 0.38	89.322 ± 17.77*
9	83.93 ± 4.54	98 ± 0	99.61 ± 3.87*	100.15 ± 16.96*
10	84.94 ± 4.24	95.97 ± 0.67	96.53 ± 4.62	86.731 ± 19.305*

6.2.3. PPG Signal Reconstruction Performance in Finger Experiment

The performance of the signal reconstruction of the proposed IMAR approach is compared to ICA for the PPG data with an index finger moving left-to-right patterns. The pulse oximeter on the middle finger of the right hand, which was stationary, was used as the reference signal. Since the subjects were directed to produce the motions for 30 seconds within each 1-minute segment, corresponding to 50% corruption by duration, the window length of both clean and corrupted segments were both set as half length of the signal.

Table 6.8. Comparison & Statistical Analysis of HR Estimations from IMAR-reconstructed PPG for 10 Different Subjects (Finger Experiment). * represents p<0.05.

Subject	Head HR (mean ± std)	Finger HR (Reference) (mean ± std)	IMAR Reconstructed HR (mean ± std)	ICA Reconstructed HR (mean ± std)
1	77.43 ± 1.91	70.61 ± 0.73	70.42 ± 0.42	77.32 ± 8.34*
2	63.60 ± 2.42	78.80 ± 0.41	78.36 ± 0.35	79.57 ± 9.68
3	70.82 ± 15.01	66.18 ± 0.76	67.21 ± 0.26	62.96 ± 22.53*
4	87.70 ± 20.53	72.59 ± 0.26	70.85 ± 0.34	73.58 ± 11.34*
5	84.34 ± 4.86	74.43 ± 0.29	73.51 ± 0.29*	77.62 ± 18.55*
6	81.75 ± 6.34	67.78 ± 0.36	69.07 ± 0.26*	67.75 ± 18.01
7	63.75 ± 3.05	57.57 ± 0.54	58.32 ± 2.49	52.51 ± 24.06*
8	66.75 ± 5.03	58.27 ± 0.75	60.34 ± 0.44*	61.64 ± 28.83*
9	97.27 ± 22.74	74.39 ± 0.46	74.25 ± 0.68	63.60 ± 14.96*
10	73.76 ± 2.85	61.58 ± 0.50	61.40 ± 0.35	50.80 ± 13.72*

Table (8) compares the HR reconstruction results between the IMAR and ICA methods for all 10

subjects. As shown in Table (8), the IMAR reconstructed HR values are not significantly different from the reference HR in 7 out of 10 subjects. However, the ICA's reconstructed HR is significantly different from the reference HR in 8 out of 10 subjects indicating poor reconstruction fidelity.

6.2.4. PPG Signal Reconstruction Performance for the Walking and Stair Climbing Experimental Data

The signal reconstruction of the MNA identified data segments of the walking and stair climbing experiments using our proposed IMAR and its comparison to ICA are provided in this section. Detection of the MNA data segments was performed using the algorithm described in Part I of the companion chapter. The reconstructed HR and SpO2 values using our proposed algorithm and ICA are provided in Tables (9) and (10), respectively. For both HR and SpO2 reconstruction, the measurements were carried out using PPG data recorded from the head pulse oximeter. The right hand index finger's PPG data was used as HR and SpO2 references.

Table 6.9. Comparison & Statistical Analysis of HR Estimations from IMAR-reconstructed PPG for 9 Different Subjects (Walking & Stair Climbing Experiment). * represents $p<0.05$.

Subject	Head HR (mean ± std)	Finger HR (Reference) (mean ± std)	IMAR Reconstructed HR (mean ± std)	ICA Reconstructed HR (mean ± std)
1	62.16 ± 18.96	70.73 ± 5.80	70.55 ± 0.56	77.39 ± 11.90*
2	94.30 ± 20.37	94.40 ± 1.69	95.54 ± 0.86	92.94 ± 9.99*
3	105.53 ± 17.23	120.64 ± 2.98	122.00 ± 1.05	95.67 ± 13.10*
4	95.48 ± 8.37	101.61 ± 3.06	99.89 ± 0.44*	90.89 ± 8.28*
5	82.20 ± 13.07	86.99 ± 3.71	87.71 ± 1.07	82.84 ± 17.96*
6	77.40 ± 12.69	82.48 ± 1.68	81.93 ± 0.48	86.81 ± 12.54*
7	121.02 ± 19.26	107.58 ± 1.51	109.15 ± 0.07	138.62 ± 6.18*
8	86.57 ± 9.85	91.95 ± 6.07	91.73 ± 0.57	80.44 ± 4.61*
9	87.09 ± 6.56	82.55 ± 5.24	84.22 ± 1.93*	104.30 ± 21.43*

For the reconstructed SpO2 values, our algorithm again significantly outperforms ICA. All but one subject are not significantly different than the SpO2 reference values for ICA. For our IMAR algorithm, only 4 out of 9 subjects do not show significant difference from the reference values. Note the zero standard deviation reference SpO2 values from Massimo's pulse oximeter in 7 out of 9 subjects. This is because Massimo uses a proprietary averaging scheme based on several past values. Hence, it is possible that the significant difference seen with our algorithm in some of the subjects would turn out to be not significant if the averaging scheme were not used. While some of the SpO2 values from our algorithm are significantly different from the reference, the actual deviations are minimal and they are far less than with ICA.

Table 6.10. Comparison & Statistical Analysis of SpO2 Estimations from IMAR-reconstructed PPG for 9 Different Subjects (Walking & Stair Climbing Experiment)

Subject	Head SpO_2 (mean ± std)	Finger SpO_2 (Reference) (mean ± std)	IMAR Reconstructed SpO_2 (mean ± std)	ICA Reconstructed SpO_2
1	95.70 ± 7.62	99.00 ± 0	97.64 ± 2.50	84.21 ± 1.34*
2	94.55 ± 5.51	95.37 ± 0	96.37 ± 0.99	95.53 ± 1.59
3	91.00 ± 15.58	96.75 ± 0	94.51 ± 0.42*	84.64 ± 4.63*
4	89.61 ± 3.36	99.62 ± 0	102.25 ± 0.65*	87.33 ± 2.67*
5	94.27 ± 8.12	98.00 ± 0.50	97.34 ± 1.45	76.50 ± 1.53*
6	88.50 ± 13.95	96.00 ± 0.31	94.97 ± 4.07*	82.94 ± 1.05*
7	94.92 ± 16.77	98.00 ± 0	100.37 ± 3.15	90.69 ± 8.11*
8	96.11 ± 6.60	97.00 ± 0	98.70 ± 4.16*	96.11 ± 0.39
9	93.78 ± 6.60	98.62 ± 0	95.99 ± 2.39*	89.11 ± 5.03*

6.3. Discussion

In this study, a novel IMAR method is introduced to reconstruct MNA contaminated segments of PPG data. Detection of MNA using a support vector machine algorithm was introduced in the companion chapter. The aim of the current chapter is to reconstruct the MNA corrupted segments as closely as possible to the

non-corrupted data so that accurate heart rates and SpO_2 values can be derived. The question is how to reconstruct the MNA data segments when there is no reference signal. To address this question, we use the most adjacent prior clean data segment and use its dynamics to derive the MNA contaminated segment's heart rates and oxygen saturation values. Hence, the key assumption with our IMAR technique is that signal's dynamics do not change abruptly between the MNA contaminated segment and its most adjacent prior clean portion of data. Clearly, if this assumption is violated, the IMAR's ability to reconstruct the dynamics of the signal will be compromised. We are currently working on a time-varying IMAR algorithm to address this issue.

There are hosts of algorithms available for MNA elimination and signal reconstruction. Various adaptive filter approaches to remove MNA have been proposed with good results but the test data to fully evaluate the algorithms are either limited or confined to laboratory controlled MNA involving simple finger or arm movements [10,18,24,25]. Moreover, these adaptive filter methods work best when a reference signal is available.

For those methods that do not require a reference signal to remove MNA, there have been many algorithms developed based on variants of the ICA [15,17,19,25]. Most of the ICA-based methods produced reasonably good signal reconstructions of the MNA contaminated data. However, most of these methods were validated on data that were collected using laboratory controlled MNA involving pre-defined simple side-to-side or up-and-down finger and arm movements [15,17,19,25].

Given that ICA-based methods produced good signal reconstructions of the MNA contaminated data, we have compared our proposed approach to an ICA method as described by Krishnan et al. [17] using simulated data, laboratory controlled data as well as daily activity data involving both walking and stair climbing movements. Comparison of the performance of our method to ICA was based on reconstruction of HR and SpO_2 values since these measures are currently used by clinicians.

Comparing HR and SpO_2 estimations of the reconstructed signal to the reference measurements using both simulation and experimental data have shown that the proposed IMAR method is a promising tool as the reconstructed values were found to be accurate. The simulation results from noise sensitivity

analysis showed that SNR level down to -20dB and -15dB from additive white and colored noise, respectively, can be tolerated well by the application of the proposed IMAR procedure, compared to the SNR values of -10dB and -15dB for the ICA method. Application of the proposed IMAR approach and the ICA to three different sets of experimental data have also shown significantly better signal reconstruction performance with our IMAR algorithm.

The use of singular spectrum analysis (SSA) to a single channel EEG recordings to extract high amplitude and low frequency MNA has been previously performed [26]. The main aim of the work by Teixeira et al. was to remove the artifacts in EEG signals, hence, an iterative approach to reconstruct the main dynamics of the signal was not implemented. The novelty of our approach is based on the use of SSA combined with an iterative approach to reconstruct the portion of the MNA contaminated data with the most likely true dynamics (i.e., non-MNA contaminated data) of the pulse oximeter signal. We are not aware of any previous applications of SSA-based algorithms for MNA reconstruction of pulse oximeter data. In conclusion, a scenario where a reference signal is not available to remove the MNA, the proposed IMAR algorithm is a promising new approach to accurately reconstruct HR and SpO_2 values from MNA contaminated data segments.

References

1 Bishop, G. Welch and G., An introduction to the Kalman filter. (Tech. Rep, 2006).

2 Chon, K. H., S. Dash and K. Ju. Estimation of respiratory rate from photoplethysmogram data using time-frequency spectral estimation. IEEE transactions on bio-medical engineering, 56:2054-2063, 2009.

3 Comon, Pierre. Independent component analysis, a new concept? Signal Process, 36:287-314, 1994.

4 Diniz, P., Adaptive filtering: algorithms and practical implementation. (. Springer Science, Business Media L.L.C., , 2008).

5 Elsner, J.B. and A.A. Tsonis, Singular Spectrum Analysis: A New Tool in Time Series Analysis. (Springer, 1996).

6 Feleppa, J. Mamou and E. J. Singular spectrum analysis applied to ultrasonic detection and imaging of brachytherapy seeds. Acoust Soc Amer, 21, :1790–1801, 2007.

7 Gao, Junfeng; Zheng, Chongxun; Wang, Pei. Online Removal of Muscle Artifact from Electroencephalogram Signals Based on Canonical Correlation Analysis. Clinical EEG and Neuroscience, EEG and Clinical Neuroscience Society ECNS, 2010.

8 Ghaderi, F., H. R. Mohseni and S. Sanei. Localizing Heart Sounds in Respiratory Signals Using Singular Spectrum Analysis. Biomedical Engineering, IEEE Transactions on, 58:3360-3367, 2011.

9 Golyandina, N., V. Nekrutkin and A.A. Zhigljavsky, Analysis of Time Series Structure: SSA and Related Techniques. (Taylor & Francis, 2001).

10 Hamilton, P. S., M. G. Curley, R. M. Aimi et al., "Comparison of methods for adaptive removal of motion artifact," in Computers in Cardiology 2000, 2000, pp. 383-386.

11 Hassani, H. Singular Spectrum Analysis: Methodology and Comparison. Journal of Data Science 5:239-257, 2007.

12 Jolliffe, I.T., Principal component analysis. (Springer-Verlang, 1986).

13 Jubran, Amal, in Applied Physiology in Intensive Care Medicine, edited by Hedenstierna, Göran, Jordi Mancebo, Laurent Brochard et al. (Springer Berlin Heidelberg, 2009), pp. 45-48.

14 Kalman, R. E. A New Approach to Linear Filtering and Prediction Problems Transactions of the ASME – Journal of Basic Engineering, Series D:1960.

15 Kim, B. S. and S. K. Yoo. Motion artifact reduction in photoplethysmography using independent component analysis. Biomedical Engineering, IEEE Transactions on, 53:566-568, 2006.

16 Kloeden, P.E., & Platen, E. , Numerical Solution of Stochastic Differential Equations. (Springer, 1992).

17 Krishnan, R., B. Natarajan and S. Warren. Two-Stage Approach for Detection and Reduction of Motion Artifacts in Photoplethysmographic Data. Biomedical Engineering, IEEE Transactions on, 57:1867-1876, 2010.

18 Morbidi, F., A. Garulli, D. Prattichizzo et al. Application of Kalman Filter to Remove TMS-Induced Artifacts from EEG Recordings. Control Systems Technology, IEEE Transactions on, 16:1360-1366, 2008.

19 Ram, M. R., K. V. Madhav, E. H. Krishna et al. ICA-Based Improved DTCWT Technique for MA Reduction in PPG Signals With Restored Respiratory Information. Instrumentation and Measurement, IEEE Transactions on, 62:2639-2651, 2013.

20 Ram, M. R., K. V. Madhav, E. H. Krishna et al., "Use of Multi-Scale Principal Component Analysis for motion artifact reduction of PPG signals," in Recent Advances in Intelligent Computational Systems (RAICS), 2011 IEEE, 2011, pp. 425-430.

21 Reddy, K. A., B. George, N. Madhu Mohan et al., "A Novel Method of Measurement of Oxygen Saturation in Arterial Blood," in Instrumentation and Measurement Technology Conference Proceedings, 2008 IMTC 2008 IEEE, 2008, pp. 1627-1630.

22 Reddy, K. A., B. George, N. M. Mohan et al. A Novel Calibration-Free Method of Measurement of Oxygen Saturation in Arterial Blood. Instrumentation and Measurement, IEEE Transactions on, 58:1699-1705, 2009.

23 S. Choi, A. Cichocki, H. Min Park, and S. Young Lee. Blind source separation and independent component analysis: A review. Neural Information Processing, Letters and Reviews, 6:1–57, , 2004.

24 Seyedtabaii, S. Seyedtabaii and L. Kalman filter based adaptive reduction of motion artifact from photoplethysmographic signal. World Academy of Science, Engineering and Technology, 37:2008.

25 Sweeney, K. T., T. E. Ward and S. F. Mcloone. Artifact Removal in Physiological Signals—Practices and Possibilities. Information Technology in Biomedicine, IEEE Transactions on, 16:488-500, 2012.

26 Teixeira, A. R., A. M. Tomé, E. W. Lang et al. Automatic removal of high-amplitude artefacts from single-channel electroencephalograms. Computer Methods and Programs in Biomedicine, 83:125-138, 2006.

27 Thakor, N. V. and Zhu Yi-Sheng. Applications of adaptive filtering to ECG analysis: noise cancellation and arrhythmia detection. Biomedical Engineering, IEEE Transactions on, 38:785-794, 1991.

28 Thompson, B., Canonical Correlation Analysis: Uses and Interpretation. (SAGE Publications, 1984).

Chapter 7: DyParam – A Time-Domain Motion and Noise Artifact Reduction Algorithm

7.1. Introduction

In Chapter 6, we introduce a blind source separation technique for PPG signal reconstruction and HR and SpO2 accurate estimations during motion and noise artifact. One issue with the propsed IMAR method is it cannot be implemented in real-time due to high computational complexity. In this chapter we propose a time-series modeling and prediction technique for PPG signal reconstruction during movement and physical activities.

A viable approach that has not yet been applied to PPG signal reconstruction is via the parametric time-varying modeling. We call this type of signal reconstruction technique as DyParam. This approach uses a parametric time-varying regression model to capture the dynamics of a short segment of a clean portion of the PPG signal and then the adjacent noise corrupted segment is replaced with the dynamics of the uncorrupted segment. This approach is feasible only if the adjacent clean and corrupted segments' dynamics do not change abruptly which is a reasonable assumption especially for short duration data. To this end, we introduce two different time-varying regression models based on sinusoidal and autoregressive basis functions. The first approach is called the time-varying sinusoidal function (TVSF) model which uses the sines and cosines as basis functions to capture frequency changes in the clean portion of the signal. We believe using the sinusoids as the basis for capturing the dynamics of the PPG signal is appropriate since it exhibits cyclical sinusoidal-like waveforms. The adjacent noise corrupted segment is then reconstructed using the model determined from the clean segment.

The second approach we use is the time varying autoregressive (TVAR) model to capture dynamics of the PPG signal. The TVAR model parameters are projected onto both Legendre and Walsh functions to

capture both slow and fast transients. This approach has been shown to provide good modeling of both linear and nonlinear characteristics of signals such as blood pressure and PPG signals [29] .

In order to verify the performance of the proposed two regression models, the normalized mean square error (NMSE) values between the reconstructed to the reference clean signals are calculated. Moreover, heart rate (HR) and SpO2 values of the reconstructed signal are estimated and compared to the reference signal's values to evaluate the accuracy of the reconstructed signal. Finally, we compare the performance of our method to AR-MDL and AR-DEKF methods using the NMSE, SpO2 and HR values.

7.2. Materials and Method

7.2.1. Experimental Protocol and Preprocessing

This study was approved by WPI's IRB and all subjects were given informed consent prior to data recording. Total of three data sets were used to evaluate our proposed methods. Two sets of data were collected from healthy subjects recruited from the student community of Worcester Polytechnic Institute; students were instructed to move in random manner their PPG sensor worn at either a finger or the head location. The third data set was acquired from patients who were admitted to our partner hospital, University of Massachusetts Medical Center (UMMC). This study was approved by WPI and UMMC's institutional review boards and all subjects were given informed consent prior to data recording.

In laboratory-controlled head movement data, motion artifacts were induced by head movements for specific time intervals in both horizontal and vertical directions. 11 healthy volunteers were asked to wear a forehead reflectance pulse oximeter along with a reference Masimo Radical (Masimo SET®) finger type transmittance pulse oximeter. After baseline recording for 5 minutes without any movement, subjects were instructed to introduce motion artifacts for specific time intervals varying from 10 to 50% within a 1 minute segment. For example, if a subject was instructed to perform left-right movements for 6 seconds, a 1 min segment of data would contain 10% noise. In laboratory-controlled finger movement data, motion artifacts were induced by left-right movements of the index finger. Eleven healthy volunteers were asked

to sit and wear two PPG pulse oximeters (TSD200, reflection type) on their index and middle fingers, respectively. After baseline recording for 5 minutes without any movement to acquire clean PPG data, motion artifacts were induced by left-right movements of the index finger while the middle finger was kept stationary as a reference. The motion artifact was induced 10-50% during an 1 minute recording. Such controlled movement was repeated five times per subject. The pulse oximeters were connected to a biopotential amplifier (PPG100) having a gain of 100 and cut-off frequencies of 0.05-10Hz. The MP1000 (BIOPAC Systems Inc., CA, USA) was used to acquire finger PPG signals at 100 Hz.

For the third data set, patient PPG were recorded at UMMC. Each patient was equipped with our custom-made sensors: a reflectance PO and a transmittance PO mounted on the patient's forehead and finger, respectively. The patients were admitted due to pain related symptoms and were not restrained to make movement. Therefore, they are expected to generate various degrees of MNAs in the recorded PPG.

All the PPG data were pre-processed by a 6th order infinite impulse response (IIR) band pass filter with cut-off frequencies of 0.5 Hz and 12Hz. Zero-phase forward and reverse filtering were applied to account for the non-linear phase of the IIR filter.

7.2.2. DYNAMIC PARAMETRIC MODELING

Given time series data points $(1, y(1)), (2, y(2)), \dots, (N, y(N))$ where $y \in \mathbb{R}$ is observations and N is the length of the time series, the task of regression is to fit a real valued function g: $\mathbb{R} \mapsto \mathbb{R}$ to these data points. The easiest way to address this problem is to look for g in a finite dimensional space of functions spanned by some given basis. That is, we specify a set of basis functions $\phi_1, \phi_2, \dots, \phi_s$ from $\mathbb{R}$ to $\mathbb{R}$ and fit the model g in the form of a linear combination as

$$g(x,n) = \sum_{i=1}^{s} \theta_i \phi_i(x,n) \qquad (1)$$

$$y(n) = g(x,n) + e(n), \quad n = 1,2,\dots,N \qquad (2)$$

where $e(n)$ is considered as noise source at each data point n. Hence, performing the regression then reduces to estimating the unknown parameters $\theta_1, \theta_2, \dots, \theta_s$ which minimizes the error term e.

Let P and Q be two different type of basis functions, then equations Eq.(1) and (2) can be rewritten as:

$$y(n) = \sum_{m=1}^{M} a_m P_m(n) + \sum_{l=1}^{L} b_l Q_l(n) + e(n) \quad (3)$$

where $a_1, a_2, \dots, a_M$ and $b_1, b_2, \dots, b_L$ are unknown time-invariant coefficients corresponding to the P and Q basis functions, respectively. The time-varying version of the above regression model can be obtained by

$$y(n) = \sum_{m=1}^{M} a_{m,n} P_m(n) + \sum_{l=1}^{L} b_{l,n} Q_l(n) + e(n) \quad (4)$$

In order to solve the time-varying regression problem, we first need to determine the number of basis functions (M and L) and then find a time-varying parameter $a_{m,n}$ and $b_{l,n}$,($m: 1,2, \dots, M$ and $l: 1,2, \dots, L$). In this chapter, we introduce two distinct models based on the equation Eq. (4), TVAR and TVSF models to address the PPG time series modeling and prediction problem. For the TVAR model by taking basis function $P_m = y(n-m)$ as the past observations, equation Eq. (4) can be rewritten as

$$y(n) = \sum_{m=1}^{M} a_{m,n}\, y(n-m) \; + e(n) \quad (5)$$

where in this case M represents the maximum AR model order. However, if we consider Cosine and Sine functions as P and Q basis functions in equation Eq. (4), we have the TVSF model as follows:

$$y(n) = \sum_{m=1}^{M} a_{m,n}\, Cos(\omega_m n) + \sum_{l=1}^{L} b_{l,n}\, Sin(\omega_m n) + e(n) \quad (6)$$

where M and L here represent the number of distinct frequencies required to track the time-varying frequency in the signal. In subsections III.C and III.D, we will show how these two models are applied in reconstructing MNA-free PPG signals from MNA-corrupted PPG signals.

Next, we will introduce a combined algorithm for order determination and parameter estimation called optimal parameter search (OPS) to obtain only the significant terms, in order to obtain TVAR and TVSF models for training and predicting a typical time series.

7.2.3. PPG Signal Modeling: Time-Varying Regression Model

Least-mean-square (LMS) and recursive least-squares (RLS), which track TV coefficients using adaptive filters, are the most popular two approaches to identify a TV system. These methods work reasonably well when time variations are slow. However, if TV coefficients change quickly, these adaptive approaches are not able to track time-varying properties of the system, because the convergence speed of algorithms is not fast enough. Another approach of tracking a slow TV system is employing an ensemble averaging technique. Consistent data recording from either the same or different preparations over prolonged time is often impractical in practice, thus, these conditions preclude this from being a widely utilized approach. In this study, we improve the technique introduced in 37 which is based on expansion of time-varying parameters over basis functions. By expanding each time-varying coefficient onto a finite set of basis functions, Zou et al. 37 showed that the model order selection criterion of TV systems becomes equivalent to determining model order for time-invariant model. Consider the time varying linear regressive model from Eq. (4). To track TV dynamics of the system, we project the TV parameters onto multiple sets of basis functions. From 37, we choose Walsh and Legendre functions to perform the parameters expansion. Legendre polynomials perform well if the coefficients are smoothly changing with time, e.g., sinusoids. Walsh functions on the other hand, behave well with piecewise stationary TV coefficients (i.e. fast changes of parameters) and should be used when the dynamics are expected to exhibit fast transients burst-like dynamics. Most physiological signals inevitably exhibit both fast and slowly

varying dynamics at different stages of a signal, therefore, it is appropriate to utilize multiple sets of basis function, i.e., combinations of both Legendre and Walsh basis functions.

Then, the general time-varying regressive model can be rewritten as

$$y(n) = \sum_{m=1}^{M} \sum_{k=0}^{V} \alpha_{m,k} \pi_k(n)\, P_m(n) + \beta_{m,k} \pi_k(n) Q_m(n) + e(n) \qquad (7)$$

where $\pi_k(n)$ is the expanding basis functions (Walsh/Legendre) and V is the number of expanding basis functions.

1. Time-varying autoregressive (TVAR) model

By setting AR terms as the basis functions of the model (6), we can obtain the AR model as

$$y(n) = \sum_{m=1}^{M} \sum_{k=0}^{V} \alpha_{m,k} \pi_k(n)\, y(n-m) \;\; + e(n) \qquad (8)$$

Now let

$$y_k(n-m) = \pi_k(n)\mathrm{y(n-m)} \qquad (9)$$

Substituting Eq. (9) into Eq. (8) we have

$$y(n) = \sum_{m=1}^{M} \sum_{k=0}^{V} \alpha_{m,k}\, y_k(n-m) \;\; + e(n) \qquad (10)$$

Eq. (10) shows that the original TV-AR model (5) can now be treated like a TIV-AR model, since $\alpha_{m,k}$ are no longer changing by time. Thus, any time-invariant parameter estimation algorithm can now be applied for estimating the $\alpha_{m,k}$ coefficients of the AR model equation (10). In this chapter we use AR model equation (10) as one of the tools to model and predict the PPG time series. Two different

techniques have been utilized to determine the AR model order and estimate the parameters. We use POPS algorithm as a combined technique for model order determination and parameters estimation.

2. Time-varying sinusoidal frequency (TVSF) model

Most physiological signals exhibit cyclical and sinusoidal characteristics (e.g., blood pressure and PPG). Thus, modeling PPG via the TVSF approach is a natural choice. We can obtain the equivalence sinusoidal frequency model by choosing Cosine and Sine functions as the P and Q basis functions, which can be described as:

$$y(n) = \sum_{m=1}^{M} \sum_{k=0}^{V} \alpha_{m,k} \pi_k(n)\, Cos(\omega_m n) + \beta_{m,k} \pi_k(n) Sin(\omega_m n) + e(n) \qquad (11)$$

We can denote a new set of TV sinusoidal functions as

$$Cos_k(\omega_m n) = \pi_k(n) Cos(\omega_m n)$$

$$Sin_k(\omega_m n) = \pi_k(n) Sin(\omega_m n) \qquad (12)$$

Substituting Eq. (12) into Eq. (11) we obtain the transformed time-invariant sinusoidal frequency model as follows

$$y(n) = \sum_{m=1}^{M} \sum_{k=0}^{V} \alpha_{m,k}\, Cos_{.k}(\omega_m n) + \beta_{m,k} Sin_k(\omega_m n) \; + e(n) \qquad (13)$$

We can use any time-invariant parameter estimation algorithm to estimate the $\alpha_{m,k}$ and $\beta_{m,k}$ coefficients, ($m = 1, \dots, M$ and $k = 0, \dots, V$). The next step is to determine the optimal model order M & V in Eq. (13). The proceeding section discusses in detail how to select the optimal model order.

7.2.4. Model Order Determination and Parameter Estimation: Optimal Parameter Search (OPS) Algorithm

The predictive optimal parameter search (OPS) 29 algorithm procedure is succinctly presented in Table 1. The OPS algorithm is originally designed for parameter estimation and it has been shown to provide only the significant model terms among the initially chosen pool of candidate terms. That is, unlike the Akaike Information criterion or the minimum description length, the OPS only provides model terms that contribute the most to the overall dynamics of the system29. For example, while AIC and MDL provide only the maximum model order, inconsequential model terms are also estimated which reduces the accuracy of the true model terms since all terms are estimated. However, the OPS, by design, provides only the significant terms, hence there can be many missing terms since they are deemed to be insignificant. The benefit of this strategy has been shown to provide more accurate parameter estimation than the least-squares using either AIC or MDL. For reconstructing MNA corrupted PPG segment, where we are interested in capturing most of the PPG dynamics including dicrotic notch, we use more model terms as.

Table 7.1. Predictive Optimal Parameter Search Algorithm

Step 1: Selecting only the linearly independent vectors from the pool of candidate vectors

$$\begin{bmatrix} \mathbf{P_1(1)} & \mathbf{Q_1(1)} & \mathbf{P_2(1)} & \mathbf{Q_2(1)} & \cdots & \mathbf{P_M(1)} & \mathbf{Q_L(1)} \\ \mathbf{P_1(2)} & \mathbf{Q_1(2)} & \mathbf{P_2(2)} & \mathbf{Q_2(2)} & & \mathbf{P_M(2)} & \mathbf{Q_L(2)} \\ & \vdots & & & \ddots & \vdots & \\ \mathbf{P_1(N)} & \mathbf{Q_1(N)} & \mathbf{P_2(N)} & \mathbf{Q_2(N)} & \cdots & \mathbf{P_M(N)} & \mathbf{Q_L(N)} \end{bmatrix}$$

The first step toward achieving linear independence among candidate vectors is to select $\boldsymbol{P_1(n)}$ as the first candidate and $\boldsymbol{Q_1(n)}$ as the next and check the linear independence between them by applying least square and calculate the error between $\boldsymbol{Q_1(n)}$ and $\widehat{\boldsymbol{Q}}_{\boldsymbol{1}}\boldsymbol{(n)}$:

$$\widehat{\boldsymbol{Q}}_{\boldsymbol{1}}\boldsymbol{(n)} = \boldsymbol{cP_1(n)}$$
$$\boldsymbol{E} = [\boldsymbol{Q_1(n)} - \widehat{\boldsymbol{Q}}_{\boldsymbol{1}}\boldsymbol{(n)}]^{\boldsymbol{2}}\,, \boldsymbol{n} = \boldsymbol{1, 2, \ldots,\ N}$$

If the error is larger than $\boldsymbol{E}$ (threshold value=0.001) then $\boldsymbol{Q_1(n)}$ and $\boldsymbol{P_1(n)}$ are linearly independent. Once it is determined that $\boldsymbol{Q_1(n)}$is a linear independent vector the vectors $\boldsymbol{P_1(n)}$ and $\boldsymbol{Q_1(n)}$ are used to determine the linear independency of $\boldsymbol{P_2(n)}$.

$$\widehat{\boldsymbol{Q}}_{\boldsymbol{2}}\boldsymbol{(n)} = \boldsymbol{c_1P_1(n)} + \boldsymbol{c_2Q_1(n)}$$

This procedure is continued until all the linearly independent vectors are selected.

Step 2: Let $\boldsymbol{W} = \{\boldsymbol{w_1, w_2, \ldots, w_S}\}$. be the number of selected independent vectors. With the new matrix of linearly independent vectors, least-squares analysis is performed

$$\boldsymbol{y(n)} = \boldsymbol{\theta^T W} + \boldsymbol{e(n)}$$

Where $\boldsymbol{\theta} = [\boldsymbol{\theta_1, \theta_2, \ldots, \theta_S}]$ are parameters estimate of the model. The objective is to minimize the error $\boldsymbol{e(n)}$

$$J = \sum_{n=1}^{N} [y(n) - \theta^T W]^2$$

Applying least square we have

$$\hat{\theta} = [WW^T]^{-1} Wy$$

Step 3: Finding only significant model terms among the pool of selected vectors W by calculating the projection distance

$$Dist_m = \frac{1}{N} \sum_{n=1}^{N} \hat{\theta}^2 w_m(n)^2$$

Where $m = 1, 2, \dots, S$

Step 4: Using the terms with larger projection distance (In this study we sort the model terms from largest projection distance to smallest and choose the first 15% of total model terms as the significant model terms).

In this study, the above OPS algorithm has been utilized as the main parameter estimation algorithm for AR and SF models, since we use the algorithm for prediction purposes we use predictive OPS later on in the chapter and refer to the methods as SF-POPS and AR-POPS.

7.3. Results

We evaluated the performance of our reconstruction algorithm with various types of (simulated, laboratory-controlled, and daily activities) of MNA. We compared proposed methods with AR-MDL and DEKF. As performance metrics, we considered NMSE of the reconstructed signal, HR and SpO2.

7.3.1. Noise Sensitivity Analysis

To compare the noise sensitivity of the above modeling approaches, we added different SNR levels of Gaussian white noise (GWN) and colored noise to a simulated time-varying frequency sinusoidal signal:

$$y(n) = \begin{cases} 10\cos\left(2\pi\frac{n}{Fs}\right) + \cos\left(2\pi\frac{0.4n}{Fs}\right) + noise, & if \;\; 1 < n < 600 \\ 10\cos\left(2\pi\frac{3n}{Fs}\right) + \cos\left(2\pi\frac{0.3n}{Fs}\right) + noise, & if \; 601 < n < 1200 \end{cases} \quad (15)$$

The purpose of the simulation was to compare the performance of the PPG modeling methods in capturing time-varying frequencies of the signal and to quantitatively determine the level of noise that can be tolerated by each of the algorithms and models.

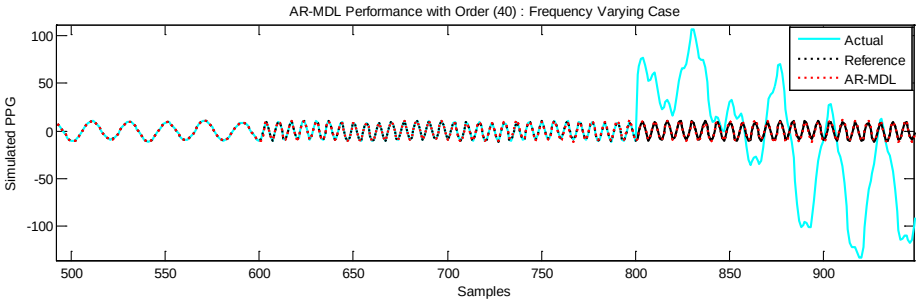

(a)

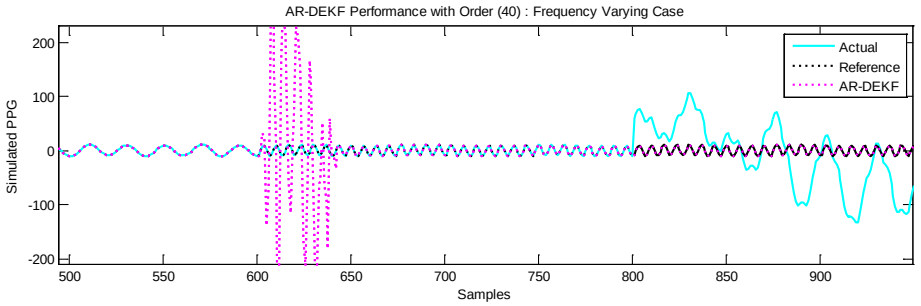

(b)

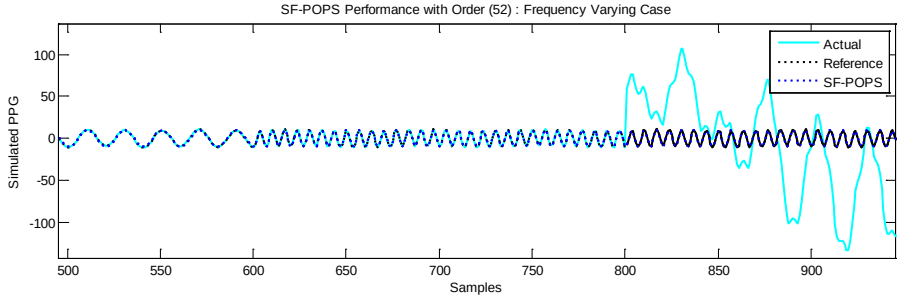

(c)

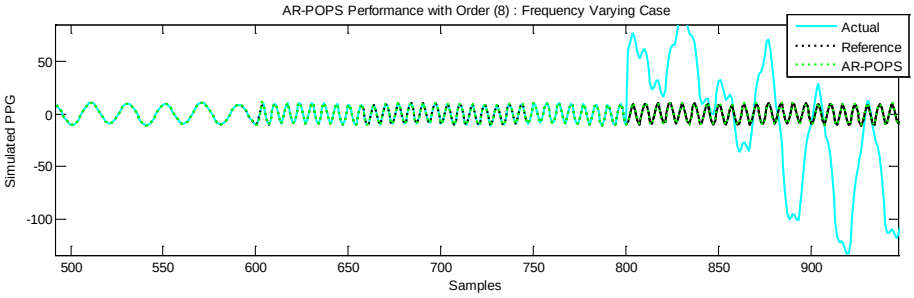

(d)

Figure 7.1 - Training and Prediction results obtained by using 4 different models on the simulated signal with -20dB additive color noise, (a) AR-MDL model, (b) DEKF model, (c) SF-POPS model and (d) AR-POPS model for the signal presented by equation (15)

Seven different SNR levels ranging from 10 dB to -20 dB were considered. For each SNR level, 50 independent realizations of GWN and colored noise were added separately to a clean PPG signal.

The Euler-Maruyama method was used to generate colored noise [32]. Figure 1 shows the performance of the PPG modeling methods on the simulated clean signal (y). We took 800 data points as the training set and the rest 400 samples for the prediction. It can be seen that all of the four models are capable of capturing the frequency changes in the signal when the noise is minor as shown in Table (2). Figure 1 illustrates the performance of the four methods on the noisy PPG signal in which color noise is added to the last 400 hundred samples. Since all methods introduced in this chapter perform signal reconstruction by predicting the corrupted segment based only on the information and pattern of the clean (training) segment, all the reconstruction outputs are similar irrespective of SNR as in Fig.1.

Tables (2) and (3) show the noise sensitivity analysis results. We can say that SF-POPS is more robust against additive white noise in the range above -5 dB. SF model inherently can capture the reference clean signal better until the signal is not severely distorted. However, if the additive noise starting to increase and the shape of the signal gets distorted, then the modeling and prediction performance of the SF model decreases accordingly. For the color noise case study, SF-POPS and AR-POPS methods are more robust against noise for the noise level up to -5 dB as shown in Tables (3). For lower SNR levels (-10 to -20 dB), however, none of the models can produce reasonable results since they cannot tolerate that level of noise in the signal.

Table 7.2. Frequency Varying Scenario. NMSE Comparison Results (additive white noise)

SNR Level (dB)	SF-POPS	DEKF	AR-MDL	AR-POPS
40	0.010 ± 0.00	0.012 ± 0.00	0.138 ± 0.00	0.012 ± 0.00
10	0.029 ± 0.01	$0.560\pm0.46^{*}$	0.282 ± 0.31	0.215 ± 0.12
5	0.079 ± 0.02	$0.882\pm0.69^{*}$	$0.804\pm0.26^{*}$	$0.791\pm0.06^{*}$
0	0.193 ± 0.05	$1.67\pm2.84^{*}$	$0.944\pm0.28^{*}$	$0.925\pm0.03^{*}$
-5	$0.642\pm0.17^{*}$	$7.09\pm12.52^{*}$	$0.922\pm0.19^{*}$	$0.917\pm0.02^{*}$
-10	$1.975\pm0.50^{*}$	$17.08\pm19.26^{*}$	$1.012\pm0.28^{*}$	$0.998\pm0.01^{*}$
-15	$6.609\pm2.17^{*}$	$21.51\pm22.03^{*}$	$1.078\pm0.16^{*}$	$1.009\pm0.01^{*}$
-20	$16.123\pm6.05^{*}$	$38.40\pm37.08^{*}$	$1.288\pm0.18^{*}$	$1.027\pm0.03^{*}$
*P<0.05				

Table 7.3. Frequency Varying Scenario. NMSE Comparison Results (additive color noise)

SNR Level (dB)	SF-POPS	DEKF	AR-MDL	AR-POPS
Clean	0.010±0.00	0.02±0.00	0.089±0.00	0.015±0.00
10	0.021±0.00	0.189±0.61	0.046±0.00	0.016±0.00
5	0.046±0.00	0.199±2.11*	0.067±0.01	0.033±0.00
0	0.102±0.02	0.475±6.56*	0.192±0.03	0.041±0.00
-5	0.340±0.09	0.217±7.24*	0.390±0.02	0.065±0.01
-10	1.159±0.32*	0.813±15.8*	0.626±0.11*	0.207±0.06
-15	3.433±1.03*	11.384±27.6*	2.809±1.12*	0.696±0.24*
-20	9.677±2.78*	32.723±32.1*	9.176±2.92*	2.451±0.88*
***P<0.05**				

7.3.2. Application of the Regression Models in Real Experiments

Finger Experiment

We first tested PPG modeling and prediction methods on the finer PPG data. The procedure in running the 4 models (SF-POPS, DEKF, AR-MDL and AR-POPS) for the data collected from this experiment is as follows. PPG segments of 1000 samples from 11 subjects, in each of which the first 600 samples are clean and the rest are MNA-corrupted data, have been considered. The first 600 clean samples are considered as the training set and we kept the rest 400 samples for test (or prediction). Fig.2 illustrates the training and prediction performance of each model on the PPG segment measured from subject #2 in Finger experiment. Comparing to the reference PPG, POPS based model is shown to give the best prediction results. For this data, DEKF completely failed in predicting the signal. Table (4) and (5) presents the RMSE comparison results calculated for the four algorithms. The SF model with POPS parameter estimation provides the best performance in terms of RMSE and NMSE.

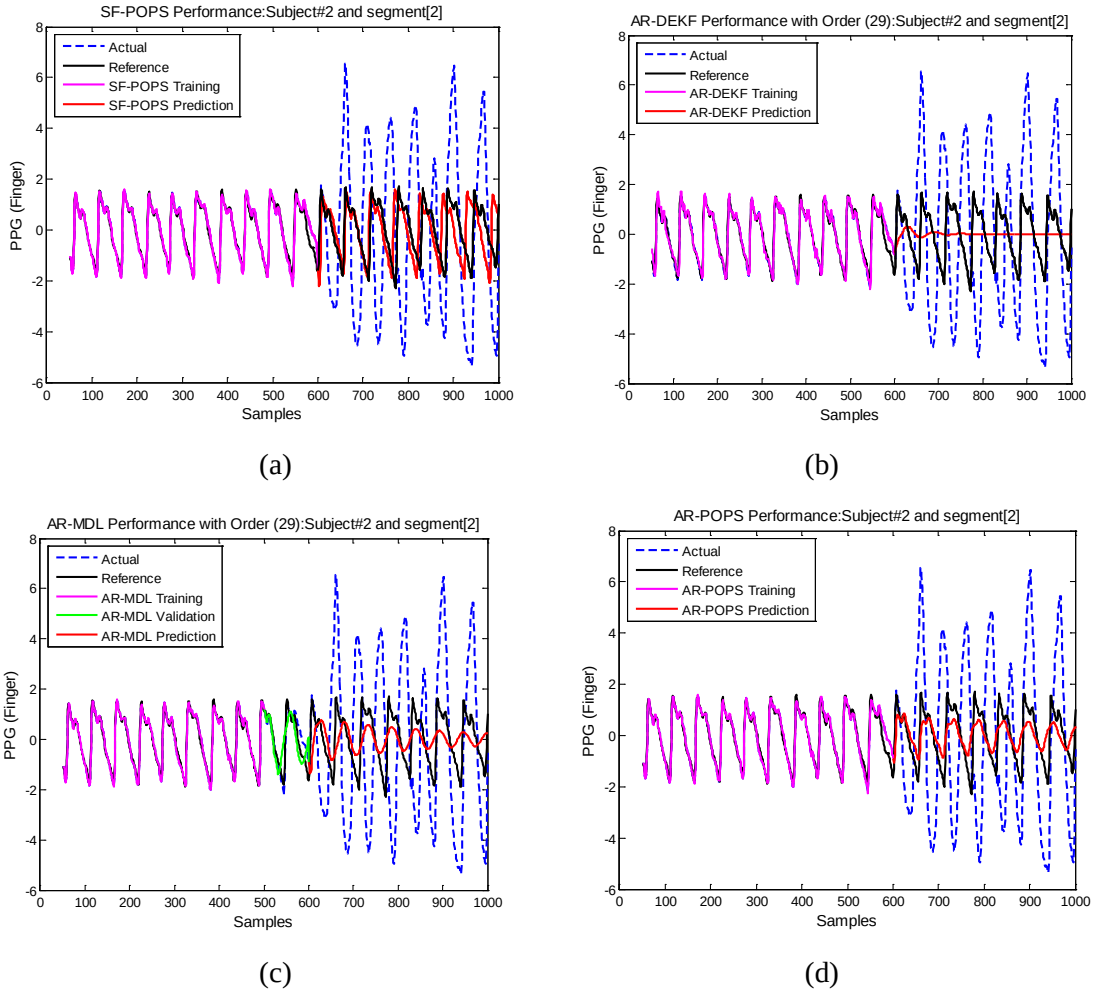

Figure 7.2 - Training and prediction performance of the 4 models on subject#2, (a) SF-POPS, (b) DEKF, (c) AR-MDL and (d) AR-POPS. Reference: Black, Actual PPG: dashed blue, Training Output: pink, Validation output: green, and Test output: red.

SF-POPS and AR-POPS algorithms show better HR estimation than the other two as shown in Table (9). SF-POPS, in general, gives us the estimated HR values very close to those of reference HR values. Fig.3 shows the estimated HR from all four methods applying on the PPG segment of Fig.2 with the reference HR. Estimated HR from the output of the POPS based methods are very close to that of reference.

Table 7.4. Real Experiment (1). NMSE Comparison Results

Subject	SF-POPS	DEKF	AR-MDL	AR-POPS
1	0.70±0.20	1.08±0.67*	0.74±0.44	0.64±0.28
2	0.69±0.15	1.12±1.4	1.03±0.03*	0.88±0.20
3	0.52±0.49	0.72±0.39*	0.54±0.21	0.57±0.02
4	0.71±0.63	1.12±0.40*	1.36±0.30*	1.31±0.14*
5	0.45±0.44	11.12±14.1*	1.13±0.13*	0.99±0.61*
6	0.79±0.18	1.08±1.12*	1.07±0.54*	1.06±0.35*
7	0.87±0.28	33.15±44.87*	1.71±0.20*	1.68±0.17*
8	0.24±0.25	3.59±4.95*	0.48±0.27	0.32±0.05
9	0.60±0.46	9.43±12.55*	0.87±0.97*	0.88±1.08*
10	1.25±0.12*	34.04±28.5*	2.31±0.31*	2.64±0.55*
11	0.76±0.29	1.37±1.02*	0.51±0.36	0.82±0.53*
***P<0.05**				

Table 7.5. Real Experiment (1). Estimated Heart Rate Comparison Results

Subject	Corrupted HR	Reference HR	AR-MDL	DEKF	SF-POPS	AR-POPS
1	107.55±49.9	58.28±1.2	66.13±0.6*	142.02±35.6*	59.27±1.7	59.33±0.7
2	81.32±22.3	68.49±1.3	65.77±2.1*	49.69±12.5*	67.43±3.0	64.98±33.6*
3	89.37±20.9	80.24±6.5	82.19±1.7*	140.84±45.6*	82.39±12.3*	81.59±7.0
4	87.08±30.5	73.73±22.4	76.65±1.8*	67.94±21.2*	73.21±5.1	74.61±14.6*
5	87.33±13.6	84.42±3.0	87.85±1.2*	97.04±12.6*	89.91±7.6*	87.54±15.7*
6	74.45±11.9	73.68±3.5	77.84±0.8*	169.68±75.4*	73.22±3.4	71.91±1.3*
7	79.67±33.7	58.33±2.2	60.92±0.7*	100.50±33.7*	57.55±3.5	56.37±3.0*
8	90.74±10.7	90.13±3.1	90.64±1.4	96.34±6.6*	90.47±5.9	88.99±9.0*
9	79.89±15.8	79.75±4.6	83.80±4.0*	104.31±20.5*	81.18±2.2*	80.52±6.0
10	81.32±23.8	83.17±1.1	85.40±2.2*	61.05±21.4*	81.28±2.3*	85.70±1.8*
11	80.76±28.1	66.38±5.5	72.83±1.1*	69.74±12.5*	68.00±6.9*	66.88±0.8
***P<0.05**						

From the above table we can clearly see that SF-POPS and AR-POPS algorithms are better than the other two algorithms in term of estimated HR and in general SF-POPS can gives us the estimated HR values very close to those of reference HR values. Fig.3 shows the estimated HR from all four methods applying on segment#2 of data recorded from subject#2 in comparison to the reference HR. From this figure we can see that estimated HR from the output of the POPS based methods are very close to that of reference.

The second real experiment considered in this study is the Head experiment. The procedure in running the 4 models (SF-POPS, DEKF, AR-MDL and AR-POPS) for the data collected from this experiment is as follows. The data, which was recorded from 11 subjects and has 7 corrupted segments, are required to be reconstructed. We have the reference HR and SpO2 values which has been recorded by Masimo.

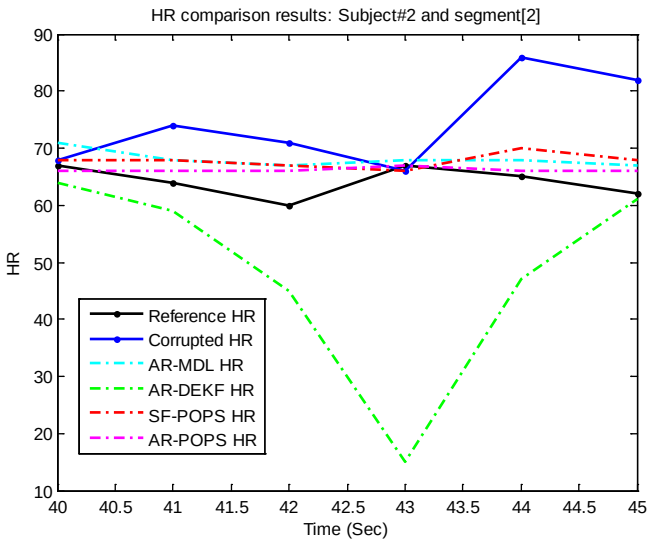

Figure 7.3 - HR estimations from the output of the 4 models on a typical segment from subjects #2, Actual value: blue, Reference: black, AR-MDL: light blue, AR-POPS: pink, SF-POPS: red and DEKF: light green.

Head Experiment

Fig.4 compare the performance of the 4 algorithms by testing them on typical PPG segments of the subject #10. We can see that POPS based algorithms give better results and its ability in capturing the shape of the PPG and hence reconstructing the PPG in corrupted areas very efficiently. Fig.5, Tables 8 and 9 show the superiority of the SF-POPS model over the other three algorithms in estimating HR and SpO2.

UMASS Experiment

The last data was recorded from real patients of UMMC. The procedure in running the 4 models (SF-POPS, DEKF, AR-MDL and AR-POPS) for this data is as follows. The data, which was collected from 8 subjects and have multiple non-equal corrupted segments, is required to be reconstructed. This data again has been recorded by the same sensors as the Head experiment and we have the reference HR and SpO2 values which has been recorded by Masimo.

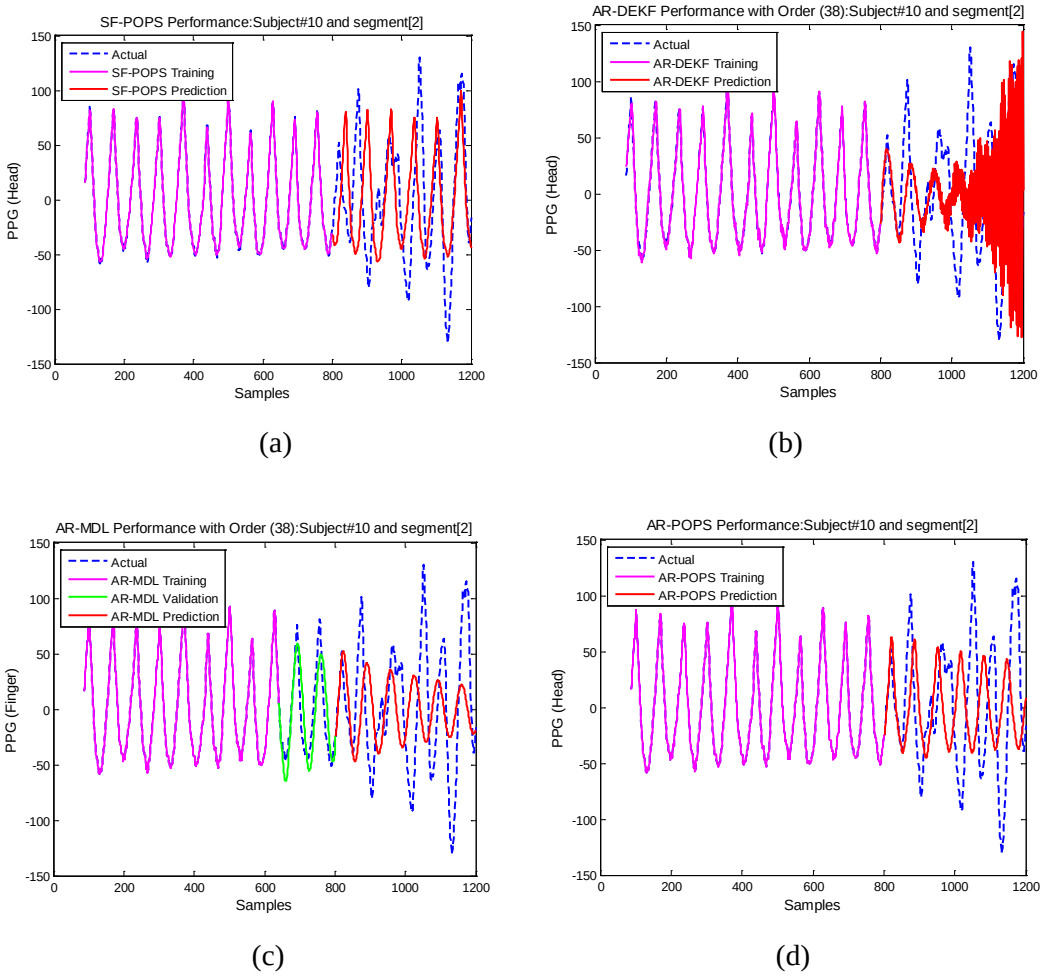

Figure 7.4 - Training and prediction performance of the 4 models on a typical IR segment from subject #10, (a) SF-POPS, (b) DEKF, (c) AR-MDL and (d) AR-POPS. Actual PPG: dashed blue, Training Output: pink, Validation output: green, and Test output: red.

Table 7.6. Real Experiment (2). Estimated Heart Rate Comparison Results

Subject	Corrupted HR	Reference HR	AR-MDL	DEKF	SF-POPS	AR-POPS
1	72.74±15.1	61.38±0.6	61.27±0.5	143.40±32.6*	61.65±2.6	60.37±1.0*
2	110.81±36.9	68.38±0.8	66.57±0.8*	126.41±16.8*	66.06±1.3	67.69±2.3
3	89.58±26.9	75.00±0.4	76.75±1.8*	79.36±35.7*	77.22±4.2*	75.28±4.8
4	73.88±19.4	65.58±0.2	66.63±0.6*	108.53±24.1*	65.08±2.1	66.19±0.6*
5	69.45±12.8	64.46±0.5	64.53±1.0	142.44±15.6*	64.40±2.1	64.15±0.8
6	77.53±32.4	51.35±0.5	55.95±0.4*	154.12±42.1*	50.36±4.4	48.79±1.1*
7	75.62±20.2	58.75±0.3	59.86±0.4*	56.04±12.5*	57.52±3.8	60.05±1.2*
8	85.78±18.3	64.25±0.9	62.73±4.3*	147.97±16.2*	62.46±4.0*	62.74±6.7*
9	73.14±19.4	48.71±0.9	52.53±0.5*	105.28±23.6*	50.24±3.6*	48.63±1.3
10	78.87±15.8	75.46±1.5	75.19±0.7	107.01±34.4*	74.78±2.6	75.34±0.7
11	86.24±32.3	77.92±1.9	79.15±1.8*	80.23±23.6*	79.40±2.5*	76.00±1.5*
mean±std	81.24±22.7	64.66±0.8	65.56±1.2	113.71±36.7	64.29±3.5	64.11±2.0
***P<0.05**						

Table 7.7. Real Experiment (2). Estimated SpO2 Comparison Results

Subject	Corrupted SpO2	Reference SpO2	AR-MDL	DEKF	SF-POPS	AR-POPS
1	100.92±3.1	96.69±0.1	108.55±4.0*	102.25±0.0*	98.93±0.7*	100.29±1.5*
2	130.63±24.4	97.00±0.0	124.53±1.4*	262.00±112*	97.15±1.5	100.63±2.0*
3	73.85±8.0	96.00±0.0	82.41±1.1*	374.87±447*	95.20±2.5	97.03±2.0
4	167.50±5.6	96.75±0.0	100.08±1.8*	104.98±0.0*	96.34±2.9	90.44±3.0*
5	85.21±12.5	98.00±0.0	107.70±3.4*	98.69±5.7	99.84±3.8*	98.08±5.4
6	119.16±25.5	98.75±0.0	121.40±4.4*	223.56±283*	97.95±3.8	97.00±4.4*
7	97.18±9.3	98.31±0.3	105.53±2.8*	113.62±0.0*	100.60±0.7*	109.35±4.4*
8	69.40±42.7	99.75±0.0	100.84±1.2	126.00±219*	98.42±2.5	94.22±2.6*
9	69.82±11.5	97.50±0.0	74.23±8.6*	218.10±119*	100.89±4.4*	93.02±6.0*
10	81.04±12.1	96.00±0.0	101.06±5.7*	104.90±0.1*	96.62±5.1	99.48±4.4*
11	139.54±10.3	98.88±0.1	105.57±5.7*	54.94±38*	98.87±0.8	94.50±8.3*
mean±std	103.11±15.0	97.60±0.0	76.28±3.6	167.45±266	98.26±2.6	98.55±4.0
***P<0.05**						

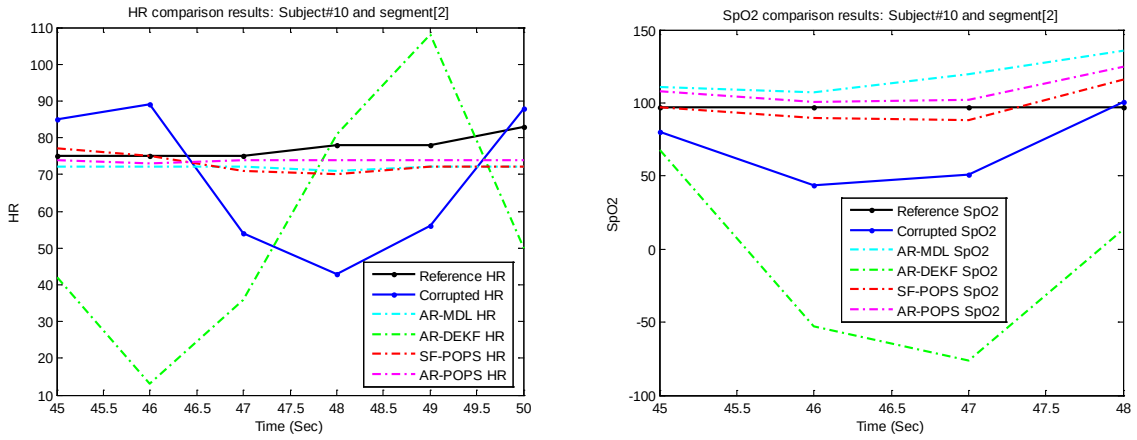

(a) (b)

Figure 7.5 - HR and SpO2 estimations from the output of the 4 models on a typical PPG segment from subject #10, **(a) HR. (b) SpO2: Actual value: blue, Reference: black, AR-MDL: light blue, AR-POPS: pink, SF-POPS: red and DEKF: light green.**

Fig.6 and 7 illustrate the performance of the 4 algorithms after applying them on a typical PPG segment of the patient #2. SF-POPS method outperform the other methods in both capturing the shape of the PPG and estimated HR and SpO2 (See Fig.7, Tables (8) and (9)).

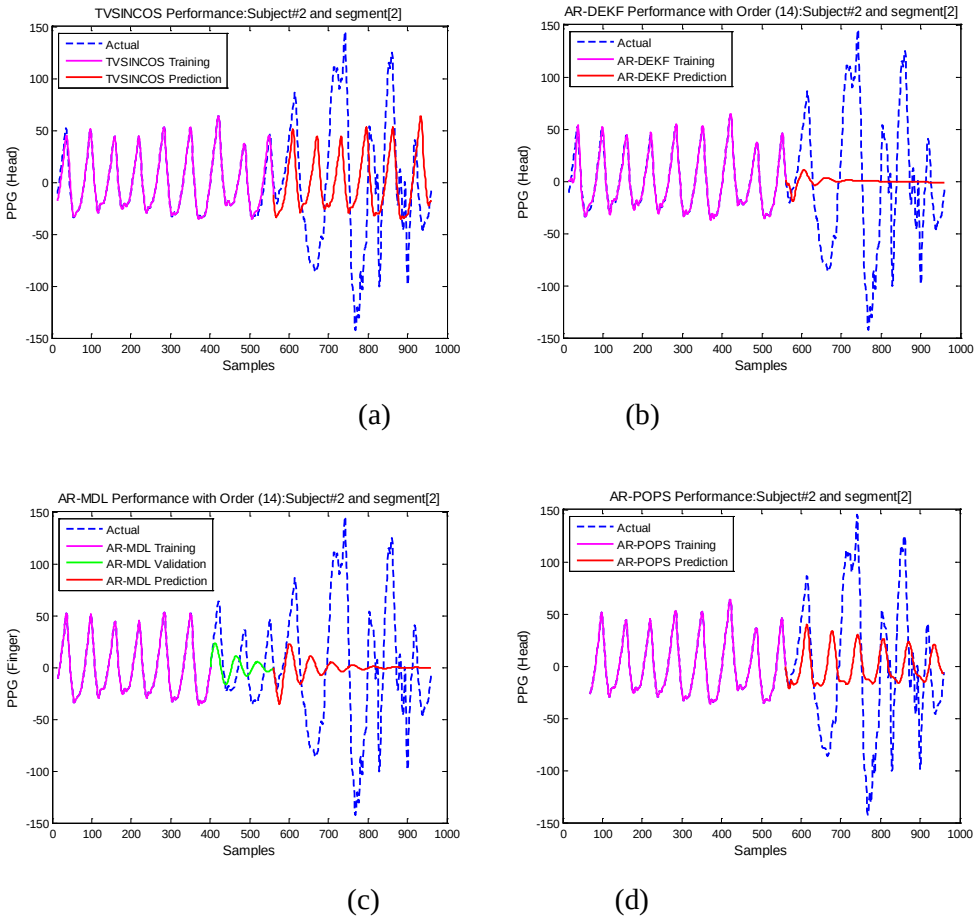

Figure 7.6 - Training and prediction performance of the 4 models on a typical IR segment from patient #2, (a) SF-POPS, (b) DEKF, (c) AR-MDL and (d) AR-POPS. Actual PPG: dashed blue, Training Output: pink, Validation output: green, and Test output: red.

Table 7.8. Real Experiment (3). Estimated Heart Rate Comparison Results

Subject	Corrupted HR	Reference HR	AR-MDL	DEKF	SF-POPS	AR-POPS
1	96.12±21.7	93.77±2.5	104.61±15.0*	101.17±15.9*	93.45±6.7	90.50±1.9*
2	81.60±30.8	73.37±3.0	74.97±1.3	67.17±23.3*	74.87±8.7*	68.11±2.5*
3	73.60±22.1	69.40±1.4	69.15±1.2	70.87±12.8*	69.03±3.9	65.56±2.0*
4	79.68±22.5	73.77±2.6	71.75±1.3*	71.32±12.6*	74.67±6.3	73.03±4.8
5	75.87±18.6	62.08±4.2	83.54±3.3*	76.06±19.7*	69.52±4.6	66.80±1.2*
6	102.92±22.6	100.11±6.2	97.72±3.1*	85.44±18.7*	102.53±7.8*	99.97±2.3
7	91.01±29.7	74.97±3.1	72.11±3.3*	82.83±12.5*	73.18±7.3*	71.77±2.2*
8	129.07±28.2	98.51±0.6	100.65±9.5*	134.11±30.8*	97.04±5.2	94.90±10.0*
mean±std	91.23±24.5	80.74±2.95	84.31±4.75	86.12±18.28	81.78±6.3	78.45±3.36
***P<0.05**						

Table 7.9. Real Experiment (3). Estimated SpO2 Comparison Results

Subject	Corrupted SpO2	Reference SpO2	AR-MDL	DEKF	SF-POPS	AR-POPS
1	87.21±1.5	99.21±0.0	112.19±3.2*	113.51±16.7*	99.01±1.3	85.70±30.2*
2	95.56±1.6	97.92±0.0	90.21±17.7*	61.29±49.9*	96.98±0.7	79.36±3.2*
3	91.19±3.6	98.00±0.0	80.95±15.1*	385.59±43.54*	94.34±1.1*	111.18±4.8*
4	93.23±2.2	97.80±0.0	48.29±66.2*	111.49±108.7*	93.38±1.8*	93.85±7.0*
5	108.49±0.5	100.05±0.0	106.63±3.61*	107.52±2.76*	108.74±0.2*	98.96±4.4*
6	94.77±1.3	98.66±0.0	82.65±24.25*	219.14±120.6*	95.79±0.8*	60.35±15.7*
7	103.63±0.6	96.59±0.0	86.52±29.01*	273.13±215.0*	97.65±0.6	98.31±3.8*
8	98.82±1.5	93.98±0.0	78.34±28.32*	196.81±199.9*	98.96±0.7*	126.83±59.8*
mean±std	95.61±1.6	98.02±0.0	85.72±23.42	183.56±94.63	98.98±0.9	94.31±16.11
***P<0.05**						

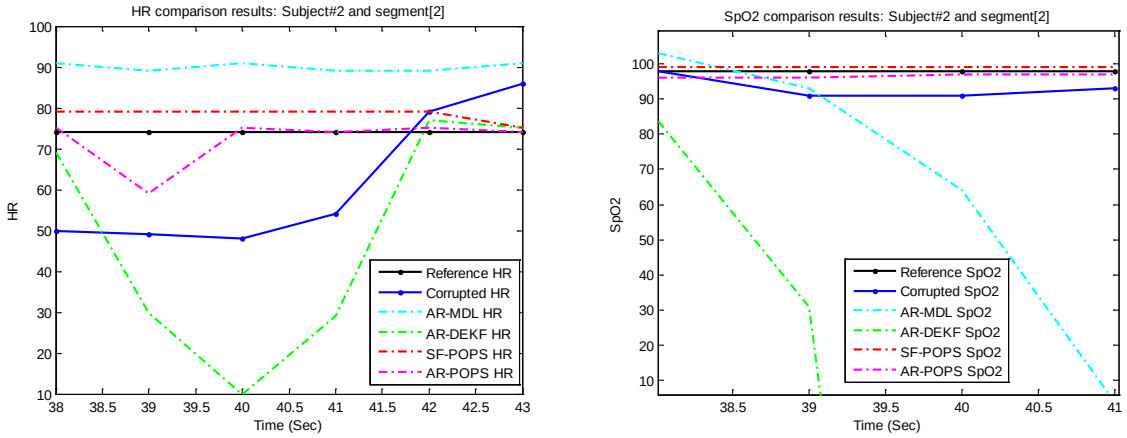

(a) (b)

Figure 7.7 - HR and SpO2 estimations from the output of the 4 models on a typical segment from patient #2. (a) HR. (b) SpO2, Actual value: blue, Reference: black, AR-MDL: light blue, AR-POPS: pink, SF-POPS: red and DEKF: light green.

7.4. Discussion

In this study, we have proposed two methods (SF-POPS and AR-POPS) to address the modeling and prediction of the PPG signals. The whole study has been done to solve the motion and noise artifact (MNA) removal for MNA-corrupted PPG signal to reconstruct PPG signal in the scenario where the dynamics of the PPG in corrupted segments does not change abruptly from the adjunct clean signal. Based on this assumption, we introduced two regression models, one with sinusoidal basis functions (SF model) and the other with autoregressive components (AR model), where SF model is designed for particular cases

where only predicting the PPG segment is done by using the frequency changing in the adjunct clean PPG segment, and AR model has been developed to deal with those cases where one is seeking to predict the trend in both amplitude and frequency from the adjunct clean PPG segment. Due to sinusoidal characteristics of PPG signal, a sinusoidal frequency (SF) model combined with predictive optimal parameter search algorithm has been proposed and we studied the performance of the Autoregressive models as well using the fact that the PPG signal dynamics do not change abruptly. . In this chapter, the main objective is to model PPG signal by extracting the dynamics and behaviors of the clean signal and to utilize the model to predict (reconstruct) the segments of the MNA-corrupted PPG signal. The whole study underlies an assumption that the signal may experience changes in frequency at least 3 seconds before it gets corrupted so that the real PPG signal dynamics in the corrupted segment would be preserved compared to the adjunct clean segment.

We took two other conventional methods (DEKF, AR-MDL) besides SF-POPS and AR-POPS approaches to do a comparison study using simulated and real experiment data. In simulation section, we indicated that all four methods perform well for estimating frequency changes since they can track the changes in frequency fairly well. Next, we have added white and color noise to the simulated signal and showed that SF-POPS and AR-POPS is less sensitive to these noises compared to DEKF and AR-MDL. We have observed that four methods cannot tolerate noise levels lower than -5dB. We have evaluated the performance of the algorithms in a scenario which a part of signal is corrupted by severe color noise. We have observed that that all of the four algorithms are independent of the corruption level in corrupted segments since they reconstruct the noise corrupted segment by doing a prediction via a model that is trained by the adjunct clean samples. .

We have further explored the ability of the proposed algorithms (SF-POPS and AR-POPS) by applying the methods on three real experiment data sets (two controlled and one spontaneous experiments) and comparing the predicted output (reconstructed signal) to the other two methods (DEKF and AR-MDL) in terms of NMSE and HR estimations. The comparison study with real data verifies that the SF-POPS

algorithm is doing better than the others in terms of accurate (close to the reference) PPG signal shape (NMSE) and accurate estimated HR and SpO2. The interesting aspect of this research is that how come AR based algorithm was not as successful as the SF based model. The answer to this question lies in the fact that AR-MDL or AR-POPS algorithms did the prediction task by selecting its model order in its way which does not guarantee optimal prediction. MDL uses residual variance for estimating the prediction error from the pool of AR models and choose the one that has trade-off between minimum residual variance and minimum number of model parameters. However, experimental results show that the AR model itself determines the relationship between the prediction error and the residual variance so there is no guarantee that the AR order obtained by MDL would give us the optimal order for prediction. Furthermore, model order selection in POPS algorithm is very dependent on the threshold value which we set for the projection distance of the AR terms that is choosing different threshold values yield different model orders. The way how we define the threshold for projection distance seems to be efficient with SF model but may not be always optimal when it comes to AR model, although AR model might be more general solution to the PPG signal modeling and prediction. We are currently working on a new technique based on particle filtering to estimating the AR model order for prediction tasks to get as close as possible to the optimal model order and consequently an optimal AR model.

References

[1] Akaike, Hirotugu. Power spectrum estimation through autoregressive model fitting. Ann Inst Stat Math, 21:407-419, 1969.

[2] Bagarinao, Epifanio and Shunsuke Sato. Algorithm for Vector Autoregressive Model Parameter Estimation Using an Orthogonalization Procedure. Annals of Biomedical Engineering, 30:260-271, 2002.

[3] Bishop, G. Welch and G., *An introduction to the Kalman filter*. (Tech. Rep, 2006).

[4] Chon, K. H., S. Dash and Ju Kihwan. Estimation of Respiratory Rate From Photoplethysmogram Data Using Time–Frequency Spectral Estimation. Biomedical Engineering, IEEE Transactions on, 56:2054-2063, 2009.

[5] Comon, Pierre. Independent component analysis, a new concept? Signal Process, 36:287-314, 1994.

[6] Comtois, G., Y. Mendelson and P. Ramuka, "A Comparative Evaluation of Adaptive Noise Cancellation Algorithms for Minimizing Motion Artifacts in a Forehead-Mounted Wearable Pulse Oximeter," in *Engineering in Medicine and Biology Society, 2007 EMBS 2007 29th Annual International Conference of the IEEE*, 2007, pp. 1528-1531.

[7] Diniz, P., *Adaptive filtering: algorithms and practical implementation*. (. Springer Science, Business Media L.L.C., , 2008).

[8] Forster, Malcolm R. Key Concepts in Model Selection: Performance and Generalizability. Journal of Mathematical Psychology, 44:205-231, 2000.

[9] Gao, Junfeng; Zheng, Chongxun; Wang, Pei. Online Removal of Muscle Artifact from Electroencephalogram Signals Based on Canonical Correlation Analysis. Clinical EEG and Neuroscience, EEG and Clinical Neuroscience Society ECNS, 2010.

[10] Gil, Eduardo, José María Vergara and Pablo Laguna. Detection of decreases in the amplitude fluctuation of pulse photoplethysmography signal as indication of obstructive sleep apnea syndrome in children. Biomedical Signal Processing and Control, 3:267-277, 2008.

[11] Golyandina, N., V. Nekrutkin and A.A. Zhigljavsky, *Analysis of Time Series Structure: SSA and Related Techniques*. (Taylor & Francis, 2001).

[12] Hamilton, P. S., M. G. Curley, R. M. Aimi et al., "Comparison of methods for adaptive removal of motion artifact," in *Computers in Cardiology 2000*, 2000, pp. 383-386.

[13] Hjorth, Bo. EEG analysis based on time domain properties. Electroencephalography and Clinical Neurophysiology, 29:306-310, 1970.

[14] Hjorth, Bo. The physical significance of time domain descriptors in EEG analysis. Electroencephalography and Clinical Neurophysiology, 34:321-325, 1973.

[15] Jolliffe, I.T., *Principal component analysis*. (Springer-Verlang, 1986).

[16] Jubran, Amal, in *Applied Physiology in Intensive Care Medicine*, edited by Hedenstierna, Göran, Jordi Mancebo, Laurent Brochard et al. (Springer Berlin Heidelberg, 2009), pp. 45-48.

[17] Kalman, R. E. A New Approach to Linear Filtering and Prediction Problems Transactions of the ASME – Journal of Basic Engineering, Series D:1960.

[18] Kim, B. S. and S. K. Yoo. Motion artifact reduction in photoplethysmography using independent component analysis. Biomedical Engineering, IEEE Transactions on, 53:566-568, 2006.

[19] Kim, H S, T S Kim, Y H Choi et al., *The prediction of EEG signals using a feedback-structured adaptive rational function filter*. (2000), pp.131-138.

[20] Korenberg, Michaelj, in *Advanced Methods of Physiological System Modeling*, edited by Marmarelis, Vasilisz (Springer US, 1989), pp. 165-177.

[21] Krishnan, R., B. Natarajan and S. Warren. Two-Stage Approach for Detection and Reduction of Motion Artifacts in Photoplethysmographic Data. Biomedical Engineering, IEEE Transactions on, 57:1867-1876, 2010.

[22] Morbidi, F., A. Garulli, D. Prattichizzo et al. Application of Kalman Filter to Remove TMS-Induced Artifacts from EEG Recordings. Control Systems Technology, IEEE Transactions on, 16:1360-1366, 2008.

[23] Ram, M. R., K. V. Madhav, E. H. Krishna et al. ICA-Based Improved DTCWT Technique for MA Reduction in PPG Signals With Restored Respiratory Information. Instrumentation and Measurement, IEEE Transactions on, 62:2639-2651, 2013.

[24] Rissanen, J. A Universal Prior for Integers and Estimation by Minimum Description Length. The Annals of Statistics, 11:416-431, 1983.

[25] S. Choi, A. Cichocki, H. Min Park, and S. Young Lee. Blind source separation and independent component analysis: A review. Neural Information Processing, Letters and Reviews, 6:1–57, , 2004.

[26] Salehizadeh, S. M. A., Duyk Dao, Jowoon Chong et al. Photoplethysmograph Signal Reconstruction based on a Novel Motion Artifact Detection-Reduction Approach. Part II: Motion and Noise Artifact Removal. Annals of Biomedical Engineering, 1-13, 2014.

[27] Selvaraj, N., Y. Mendelson, K. H. Shelley et al., "Statistical approach for the detection of motion/noise artifacts in Photoplethysmogram," in *Engineering in Medicine and Biology Society,EMBC, 2011 Annual International Conference of the IEEE*, 2011, pp. 4972-4975.

[28] Seyedtabaii, S. Seyedtabaii and L. Kalman filter based adaptive reduction of motion artifact from photoplethysmographic signal. World Academy of Science, Engineering and Technology, 37:2008.

[29] Sheng, Lu, Ju Ki Hwan and K. H. Chon. A new algorithm for linear and nonlinear ARMA model parameter estimation using affine geometry [and application to blood flow/pressure data]. Biomedical Engineering, IEEE Transactions on, 48:1116-1124, 2001.

[30] Teixeira, A. R., A. M. Tomé, E. W. Lang et al. Automatic removal of high-amplitude artefacts from single-channel electroencephalograms. Computer Methods and Programs in Biomedicine, 83:125-138, 2006.

[31] Thakor, N. V. and Zhu Yi-Sheng. Applications of adaptive filtering to ECG analysis: noise cancellation and arrhythmia detection. Biomedical Engineering, IEEE Transactions on, 38:785-794, 1991.

[32] Thompson, B., *Canonical Correlation Analysis: Uses and Interpretation*. (SAGE Publications, 1984).

[33] Wan, Eric A. and Alex T. Nelson, in *Kalman Filtering and Neural Networks* (John Wiley & Sons, Inc., 2002), pp. 123-173.

[34] Wiggins, Ralph A. and Enders A. Robinson. Recursive solution to the multichannel filtering problem. Journal of Geophysical Research, 70:1885-1891, 1965.

[35] Yang, Bufan and Kih Chon. A Novel Approach to Monitor Nonstationary Dynamics in Physiological Signals: Application to Blood Pressure, Pulse Oximeter, and Respiratory Data. Annals of Biomedical Engineering, 38:3478-3488, 2010.

[36] Yu, C., Z. Liu, T. Mckenna et al. A method for automatic identification of reliable heart rates calculated from ECG and PPG waveforms. J Am Med Inform Assoc, 13:309-320, 2006.

[37] Zou, Rui, Hengliang Wang and Kih Chon. A Robust Time-Varying Identification Algorithm Using Basis Functions. Annals of Biomedical Engineering, 31:840-853, 2003.

Chapter 8: TifMA – A Novel Algorithm for Motion and Noise Artifact Corrupted Data Usability Index Measurement

8.1. Introduction

In chapters 3-5 we presented three different motion and noise artifact algorithm. In this chapter, a new motion and noise artifact technique is presented which is not only can be used for motion artifact detection but also it can be utilized for investigating the motion corrupted signal usability for HR estimations. Although there are techniques which have been proposed to alleviate the effects of MNAs, solution to this problem still remains unsatisfactory in practice. Time-frequency (TF) techniques such as Smoothed Pseudo Wigner-Ville, Short Time Fourier Transform, Continuous Wavelet Transform, Hilbert-Huang Transform, and Variable Frequency Complex Demodulation (VFCDM) received considerable attention as means to analysis the signal of interest in both temporal and spectral domains [28]–[30]. Yan et al. used smoothed pseudo Wigner-Ville TF technique for MNA reduction albeit with limited success [10]. In this chapter, we introduced a novel algorithm for MNA detection utilizing TF representation produced by VFCDM. It is hypothesized in the design of our proposed MNA detection algorithm that TF information would provide meaningful dynamic features for improved differentiation of MNAs.

In this chapter, we present a new MNA detection algorithm "TifMA" which not only has the potential to detect MNA corrupted PPG segment but also is able to discriminate between usable versus non-usable PPG segments. TifMA algorithm was developed based on the features from Time-frequency spectrum of PPG signal. Variable frequency demodulation technique was used to derive the time-frequency spectrum of PPG. The proposed algorithm includes two phases: (1) MNA detection, (2) Usability of the MNA corrupted data segment detection. The algorithm performance was evaluated at each phase using different PPG recordings. We show that features from time-frequency spectrum of PPG have a great potential in discriminating between MNA corrupted and clean PPG data while on the other hand it can provide a new ability to determine if the corrupted data are usable or not for estimating HR. Typically

features that are extracted from VFCDM TF were used as inputs for the machine-learning classifier algorithm which utilized the Support Vector Machine (SVM). The results of MNA detection phase of TifMA were compared to three other existing MNA detection algorithms: the Hjorth [26], kurtosis-Shannon Entropy [23] and time-domain variability-SVM approach, an approach recently developed in our lab [27]. The output of usability detection stage of the algorithm obtained according to a fixed threshold value and were evaluated by comparing the reference HR to the estimated HR from VFCDM time-frequency spectrum.

8.2. Material and Methods

8.2.1. Experimental Protocol and Preprocessing

To develop, analyze and evaluate the proposed TifMA algorithm we used 5 different datasets. The datasets (2) and (3) were recorded in controlled condition from 10 subjects in Chon lab and the datasets (4) and (5) were provided by UMASS Hospital recorded from 10 patients. Dataset (5) was also recorded in Chon Lab during a treadmill experiment. The details of experiments and data collection protocols are as follow

(1) and (2) [Chon Lab Dataset]: For the laboratory controlled environment, both forehead and finger worn PO sensor data were collected from healthy subjects recruited from the student community of Worcester Polytechnic Institute (WPI). Laboratory data allows us to have more control over the duration of MNA generated to ensure that the detection phase of algorithm was tested on a wide range of MNA duration. In laboratory-controlled head and finger movement data, motion artifacts were induced by head and finger movements for specific time intervals in both horizontal and vertical directions. For head movement data, 11 healthy volunteers were asked to wear our PO on the forehead along with a reference Masimo Radical (Masimo SET®) finger type transmittance pulse oximeter. The subjects were all healthy with no past histories of cardiovascular diseases. After baseline recording for 5 minutes without any movement, subjects were instructed to introduce motion artifacts for specific time intervals varying from

10 to 50% within a 1 minute segment. For example, if a subject was instructed to perform left-right random movements for 6 seconds, a 1 min segment of data would contain 10% noise. The finger laboratory movement data were recorded in a similar setup as the head data using our custom-made PPG finger sensor.

(3) and (4) [UMASS Hospital Dataset]: The next data set was acquired from patients who were admitted to our partner hospital at the UMass Memorial Medical Center (UMMC). Data from patients provided most realistic information on the motion artifacts since the patients were allowed to move freely as long as the sensors were positioned properly. The patient PPG data were recorded from 10 subjects admitted to emergency rooms at UMMC. Similar to the laboratory-controlled dataset, each patient was fitted with our custom-made sensors (both forehead and finger) and the Masimo POs on the forehead and fingers, respectively. One subject had hypertension and 2 subjects suffered from hypercholesterolemia and hyperlipidemia; the remaining subjects were considered free from cardiovascular diseases. All recording were performed in the Emergency Department with a room temperature of 68^{o}F. The patients were admitted due to pain related symptoms and were not restrained from making natural movements. Therefore, they are expected to generate many different but natural characteristics of MNA in the recorded PPG.

(5) Chon Lab Dataset: This dataset was also recorded in the Chon Lab from 10 healthy subjects (9 male/1 female), with ages ranging from 26 to 55. For each subject, the PPG signal was recorded from their forehead using a PO. The ECG signal was recorded as a reference from the chest using ECG sensors, sampled at 400Hz. During data recording, subjects walked, jogged and ran on a treadmill with speeds of 3, 5 and 7 mph, respectively, for 9 min. At the end, all experimental subjects were asked to perform random arbitrary movements for 1 min. Activities involved are 1 min rest, 1 min walking (3 mph), 1 min rest, 2 min jogging (5 mph), 1 min rest, 2 min running (7 mph), 1 min rest, 1 min arbitrary movement. The ECG-based reference HR was recorded in order to assess the performance of the second phase of TifMA algorithm.

This study was approved by both WPI's and UMMC's IRBs and all subjects were given informed consents prior to data recordings. Chon Lab data used in this chapter were collected using our custom-

made multi-channel pulse oximeters. The subjects in the lab were all healthy with no past histories of cardiovascular diseases. All lab recordings were performed in a quiet room with temperature of 70 oF. There were two versions with different form factors to capture PPG at the user's forehead and finger. The forehead sensor is termed 6PD-forehead since it consisted of 6 photodetectors concentric around the center-paired LEDs with the peak wavelengths of 660nm (red) and 940nm (infrared). The finger sensor, due to space constrain, consisted of 3 photodetectors concentric around center paired LEDs with the same specification of the 6PD-forehead sensor. The PPGs were sampled at 80Hz. The scope of this study was to evaluate the efficacy of our proposed TifMA algorithm. Therefore, only one infrared PPG channel deemed to contain the best signal quality data was used for analysis.

All PPG data were pre-processed by a 6th order infinite impulse response (IIR) band pass filter with cut-off frequencies of 0.1 Hz and 10 Hz. Zero-phase forward and reverse filtering was applied to account for the non-linear phase of the IIR filter. Further details of this study's database including demographic of subjects are given in Table (1).

Table 8.1. PPG Datasets and Experiments Settings

No. Recordings	**Dataset**	**Electrode Type**	**Subject's Age/Sex**	**Ethnicity**
11	1 (Chon Lab)	Forehead Pulse Oximeter	23-58 y (9 Male, 1 Female)	3 Asian 2 Hispanic 3 American 2 White
11	2 (Chon Lab)	Finger Pulse Oximeter	23-58 y (9 Male, 1 Female)	3 Asian 2 Hispanic 3 American 2 White
10	3 (UMass Hospital database)	Forehead Pulse Oximeter	18-38 y (5 Female, 5 Male)	3 African-American (3 female) 6 Caucasian (1 females/5 male) 1 Puerto Rican (female)
10	4 (UMass Hospital database)	Finger Pulse Oximeter	18-45 y (4 Female, 6 Male)	1 African-American 1 Hispanic 7 Caucasian 1 Puerto Rican
10	5 (Chon Lab)	Forehead Pulse Oximeter	23-58 y (9 Male, 1 Female)	3 Asian 2 Hispanic 3 American 2 White

8.2.2. Reference signal for MNA Detection

Many recent publications on MNA detection utilized human visual inspection from experts who were familiar with PPG and their decisions are regard it as the gold standard for marking MNA corrupted data [22], [23], [27]. In our work, we also use the human visual inspection to establish a MNA reference for our datasets. Three inspectors individually marked MNA corrupted portions of the PPG. Disagreements of the marked portions were resolved by majority votes. Cohen's κ was used to determine if there was agreement between three inspectors' judgement on whether PPG segments were declared to be clean or corrupted. For each dataset, the average Cohan's κ was reported in Table (2) over three runs computed from each distinct inspector pair. Overall, the Cohan's κ showed substantial agreement between the inspectors with 95% CI and $p < 0.0005$.

Table 8.2. Averaged Cohen's κ coefficients representing the agreement between inspectors' decision on PPG labels.

	Lab. Head	Lab. Finger	Umass. Head	Umass. Finger
Cohan's κ	0.823	0.935	0.732	0.791
# of subjects	11	11	10	10
Duration (min)	5	5	10	10

Due to the differences with operating window lengths between the comparing methods, detection results and reference labels were converted to every second. For example, a 1 minute PPG segment would have 60 detection values from each method and 60 reference labels. These results were then used to compute sensitivity, specificity, accuracy for each method.

8.2.3. Reference signal for Data Usability Detection

A usability index was calculated to measure the usability of MNA corrupted segments of PPG recordings. In order to verify the performance of the index, it was compared to the reference usability measurements. The reference was determined according to the deviation of reference HR from chest, and the estimated HR obtained from phase 2 of TifMA algorithm.

8.2.4. TifMA

As mentioned above TifMA algorithm consists of two major phases: (1) MNA detection, (2) Usability detection. Both phases of algorithm were developed based on a time-frequency technique named VFCDM. VFCDM is a method for estimating time-frequency spectrum (TFS) of a time-varying signal. This method was shown to provide concomitant high time and frequency resolution as well as preservation of the amplitude distribution of the signal [31]. VFCDM has two steps: (1) constructing an initial TFS (iTFS) using a method developed in our laboratory, termed fixed frequency complex demodulation (FFCDM); (2) the center frequencies of the iTFS are used for further complex demodulation (CDM) to obtain even more accurate TFS and amplitude of the TFS. The VFCDM methodology is presented in Table (3).

Table 8.3. VFCDM Algorithm Procedure

Consider a sinusoidal signal $\boldsymbol{x(t)}$ to be a narrow band oscillation with a time-varying center frequency $\boldsymbol{f(\tau)}$, instantaneous amplitude $\boldsymbol{A(t)}$, phase $\boldsymbol{\phi(t)}$, and the direct current component $\boldsymbol{dc(t)}$:

$$\boldsymbol{x(t) = dc(t) + A(t)\cos\left(\int_0^t 2\pi f(\tau)d\tau + \phi(t)\right)} \quad (1)$$

Step (1) For a given center frequency, we can extract the instantaneous amplitude information $\boldsymbol{A(t)}$ and phase information $\boldsymbol{\phi(t)}$ by multiplying (1) by $\boldsymbol{e^{-j\int_0^t 2\pi f(\tau)d\tau}}$ which results in the following:

$$\boldsymbol{z(t) = x(t)e^{-j\int_0^t 2\pi f(\tau)d\tau} = dc(t)e^{-j\int_0^t 2\pi f(\tau)d\tau} + \frac{A(t)}{2}e^{j\phi(t)} + \frac{A(t)}{2}e^{-j\left(\int_0^t 4\pi f(\tau)d\tau + \phi(t)\right)}} \quad (2)$$

Step (2) From (2), if $\boldsymbol{z(t)}$ is filtered with an ideal low-pass filter (LPF) with a cutoff frequency $\boldsymbol{f_c < f_0}$, where $\boldsymbol{f_0}$ is the center frequency of interest. Then the filtered signal $\boldsymbol{z_{lp}(t)}$ will contain only the component of interest:

$$\boldsymbol{z_{lp}(t) = \frac{A(t)}{2}e^{j\phi(t)}} \quad (3)$$

Step (3) By changing the center frequency followed by using the variable frequency approach as well as the LPF, the signal, $\boldsymbol{x(t)}$, will be decomposed into the sinusoid modulations, $\boldsymbol{d_i}$, by the CDM technique as follows:

$$\boldsymbol{x(t) = \sum_i d_i = dc(t) + \sum_i A_i(t)\cos\left(\int_0^t 2\pi f_i(\tau)d\tau + \phi_i(t)\right)} \quad (4)$$

Step (4) The instantaneous frequency and amplitude of $\mathbf{d_i}$ can be calculated using the Hilbert transform

$$\boldsymbol{A(t) = 2\left|z_{lp}(t)\right| = [X^2(t) + Y^2(t)]^{1/2}} \quad (5A)$$

$$\boldsymbol{X(t) = real(z_{lp}(t))}$$

$$\boldsymbol{Y(t) = imag\left(z_{lp}(t)\right) = H[X(t)] = \frac{1}{\pi}\int \frac{X(t')}{t - t'}dt'}$$

$$\boldsymbol{\phi(t) = \arctan\left(\frac{imag\left(z_{lp}(t)\right)}{real\left(z_{lp}(t)\right)}\right) = \arctan\left(\frac{Y(t)}{X(t)}\right)} \quad (5B)$$

$$\boldsymbol{f(t) = f_0 + \frac{1}{2\pi}\frac{d\phi(t)}{dt}} \quad (5C)$$

FFCDM operates by performing CDM on fixed frequency f_0 within confined bandwidth and repeat it over entire frequency band. In order to obtain even higher resolution TFS, center frequencies in iTFS obtained from FFCDM were used for subsequent CDM with finer bandwidth.

TifMA Phase (1): MNA Detection

The first phase of algorithm time-frequency spectrum (TFS) of PPG is utilized to extract features that contribute in discriminating between MNA corrupted PPG data and clean data segments. Fig. 1 (A) and (B) illustrates an example of VFCDM-TFS of 4 sec segment of clean and MNA corrupted PPG data. It can be observed from this figure that TFS of a corrupted PPG segment has different characteristics comparing to TFS of the clean segment. The heart rate trace and its harmonics are distinguishable in the clean TFS while motion and noise artifacts distort the HR and its harmonics' traces in TFS of MNA corrupted PPG. In this chapter FM_1, FM_2 and FM_3 terms are referred to the HR trace and two of its harmonic traces, while to refer the corresponding spectral power, the terms AM_1, AM_2 and AM_3 are used. FM, and AM stands for frequency modulation and amplitude modulation respectively. Since respiratory induced fluctuation in PPG is highly dynamic and not trivial to characterize in a TFS, regions associated with respiratory frequencies are removed from the TFS by setting their powers to zero. The respiratory frequencies are defined to be between 0 – 0.5Hz. Our algorithm first determines the dominant frequency in the PPG segment termed f_1 as predicated that PPG is dominantly driven by cardiac cycles. To determine instantaneous f_1, total powers within narrow band spectral window $W_k = [f_k - BW, f_k + BW]$ are computed: where $BW = 0.2\ Hz$ is the bandwidth of the band; f_k is the center frequency of the window ranging from 0.6Hz – 2.4Hz with increment of 0.1Hz. BW was determined based on an assumption that within a short time HR does not fluctuate more than 12 beat per minute. f_1 is estimated as the f_k at which W_k is maximum.

The TFS of the segment is normalized by the total power in the f_1 band. It then extracts FM_1 *and* AM_1 within $[f_1 - BW, f_1 + BW]$. Note that each point in the TFS has three instantaneous

values: time, frequency, and spectral power. The maximal power in each time instance is taken to form $AM_1 = AM_1(t): t = 1, \dots, N-2$ where N is a number of data-points in the PPG segment. Its corresponding FM_1 is also extracted. Once located, AM_1 is removed from the TFS by setting its power to zero. Similarly, $\{AM_2, \mathrm{FM}_2\} \in [2\mathrm{f}_1 - \mathrm{BW}, 2\mathrm{f}_1 + \mathrm{BW}]$ and $\{AM_3, FM_3\} \in [3f_1 - BW, 3f_1 + BW]$ are found and removed. Note that, the proposed algorithm assumes that corrupted PPG would exhibit irregularity in the time series waveform. Thus, the TFS of a corrupted segment would have broadband dynamics. In this case, the proposed fundamental frequency estimation method would probably yield inaccurate result. However, an arbitrary estimation of HR (fundamental frequency and its harmonics) in such cases would remove only a portion of the noise power within the defined bands, but would retain the rest.

From the extracted TFS and $\{FM_i, AM_i: i = 1,2,3\}$, three time-frequency (TF) features were derived to quantify the noise level between clean versus corrupted PPG segments. Residual noise power (P_{noise})

After extracting the first three dominant traces, remaining power in the TFS is considered the residual noise power P_{noise} and is denoted as:

$$P_{noise} = P_{TFS} - \sum_{i=1}^{3} \sum_t AM_{i,t} \qquad (6)$$

where P_{noise} is the total power in the TFS. In a clean PPG segment as illustrated in Fig. 1B, the first three harmonics would be located within the predetermined narrow band. Thus extracting their power would effectively remove most of the spectral power from the TFS. The remaining noise power would be negligibly small. On the other hand, artifacts in the corrupted PPG segment produce spectral power at various frequency locations which are often not associated with the harmonics' frequency bands as illustrated in Fig. 1D. Some of these spectral power are outside of the bands and/or there are multiple powers within a band. Therefore, these powers would not be extracted which in turn yields high P_{noise} level.

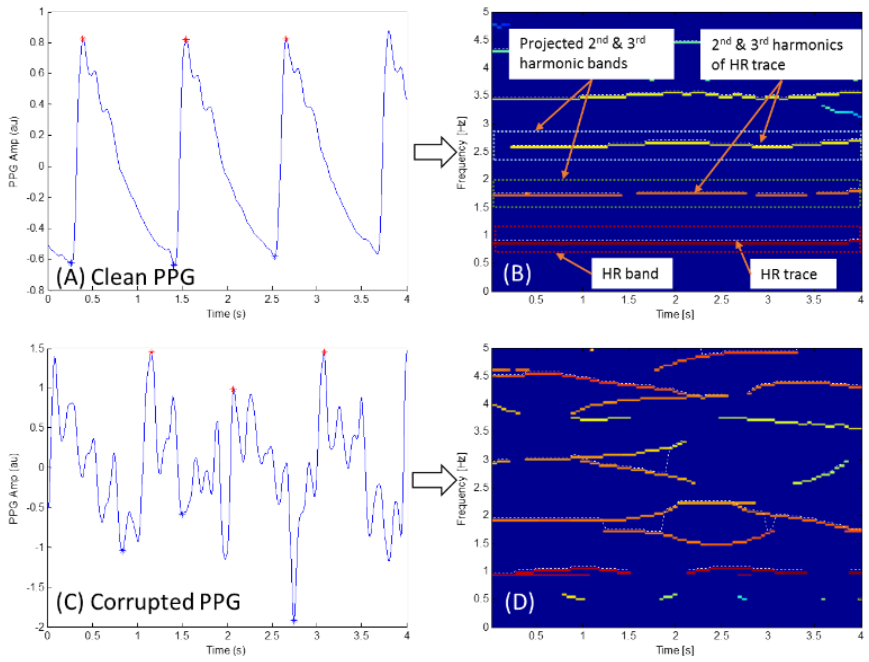

Figure 8.1 - Time-Frequency Spectrum produced by VFCDM in 8sec PPG window (L = 4s). The rectangular boxes are fundamental band and its 2nd and 3rd projected harmonic bands. The white dotted lines inside their corresponding bands are extracted fundamental and harmonic traces of the PPG segment. (A) Clean PPG. (B) TFS of clean PPG. (C) Corrupted PPG. (D) TFS of corrupted PPG.

a) Projected frequency modulation difference ($\boldsymbol{df_{FM}}$)

Projected difference is defined as the difference in frequency between the fundamental HR trace and its harmonic traces and is computed as:

$$df_{FM} = \sum_{i=2}^{3} \sum_{t} \left| FM_{i,t} - i \times FM_{1,t} \right| \qquad (7)$$

Similar to the previous assumption, frequency location of the harmonic traces are expected to be proportional to that of the fundamental trace, which would result in a low df_{FM} for a clean segment. For artifact corrupted segment, the proportionality in the frequency of the harmonics would no longer hold, thus driving df_{FM} value to be high.

b) Heart rate frequency difference ($\boldsymbol{df_{HR}}$)

Heart rate frequency difference is defined as the difference between the fundamental frequency modulation FM_1 and HR computed from time-domain peak calculation. This feature measures the agreement between the fundamental frequencies detected from the TFS and from the time domain signal. It is assumed that the frequencies would be in agreement in a clean PPG segment. But there would be potentially large difference in corrupted segment. df_{HR} is computed as:

$$df_{HR} = \sum_t \left| FM_{1,\mathrm{t}} - \mathrm{median}\left(\frac{1}{PP}\right) \right| \qquad (8)$$

where PP (sec) are the peak-to-peak intervals in a PPG segment. As mentioned above the results of MNA detection phase of TifMA were compared to three other existing MNA detection algorithms: the Hjorth [26], kurtosis-Shannon Entropy [23] and time-domain variability-SVM approach, an approach recently developed in our lab [27]. Table (4) present the features these methods extract from PPG data.

Feature extraction from PPG was done on a sliding window segment of length L_1 = 8 seconds with 50% overlap. Each segment was transformed using VFCDM into TFR, of which only the middle portion of length $L_2 = 4$ seconds was considered for further processing. This is because as shown in the Results section, the middle 4 second data length from the initial L_1 = 8 seconds for the subsequent VFCDM analysis provided the best accuracy in detection of MNAs.

To accurate pinpoint the time occurrence of MNAs, we implemented a trace-back strategy, which is triggered when the P_{noise} value changes its state as illustrated in Fig 2. When P_{noise} goes from lower than a threshold value of 0.15 to greater than 0.15, the trace-back algorithm update new TF features three times with shifting backward a second at each time instant. For example in Fig. 2A, P_{noise} changes to a value that is greater than 0.15 at time duration 4-8 seconds. The trace-back scheme would call the VFCDM routine to compute new TF features for the back-shifted segments at time durations starting at 3-7 seconds,

2-6 seconds, and ending at 1-5 seconds. As detailed above, our VFCDM algorithm is designed to indicate that a segment is corrupted even if only 1 second of the 4 second duration data contain MNAs.

Table 8.4. Frequently used MNA Detection Methods in Literature

- Kurtosis and Shannon Entropy detector (KSE)

KSE algorithms utilized two statistical measures, Kurtosis and Shannon Entropy, that quantify distributions of PPG segment [23]. Kurtosis (K) describes the distribution of observed data around the mean. K is defined as:

$$K = \frac{E(x-\mu)^4}{\sigma^4} \quad (10)$$

where μ the mean of is x, σ is the standard deviation of x, and $E(t)$ represents the expected value of the quantity t. Shannon Entropy (SE) quantifies how much the probability density function of the signal is different from a uniform distribution. SE is

- Hjorth detector

Gil et al.used Hjorth parameters with an assumption that when the signal differs largely from an oscillatory signal, it is very likely an artifact [26]. Hjorth parameters are defined from the i^{th}-ordered spectral moment $\overline{w_i}$:

$$\overline{w_i}(n) = \int_{-\pi}^{\pi} w^i S_x(e^{J\omega}) d\omega$$

$$H_1 = \sqrt{\frac{\overline{w_2}(n)}{\overline{w_0}(n)}} \; and \; H_2 = \sqrt{\frac{\overline{w_4}(n)}{\overline{w_2}(n)}} \quad (12)$$

where $S_x(e^{J\omega})$ is the power spectrum of a PPG segment $x(n)$. $H_1 and \; H_2$ represent the

- Time-domain variability and support vector machine (TDV)

TDV algorithm utilized four time-domain features to describe the variability in clean versus MNA corrupted PPG segments [27]. The features are:

- Variance in HRs (TDV_{HR})
- Variance in pulse amplitudes (TDV_{AMP})
- Variance in systolic-diastolic ratios (TDV_{SD})

Hence, since the 3-7 second segment is determined to be corrupted, it allows us to deduce that the 8th second time point is corrupted. The same logic applies to the 2-6 and 1-5 second segments. An example of the track-back strategy on an actual PPG signal is illustrated in Fig. 2 where: (A) shows TF features are

updated at a possible starting point of a MNA-corrupted segment; and (B) shows TF features are updated at a possible ending point of a MNA-corrupted segment.

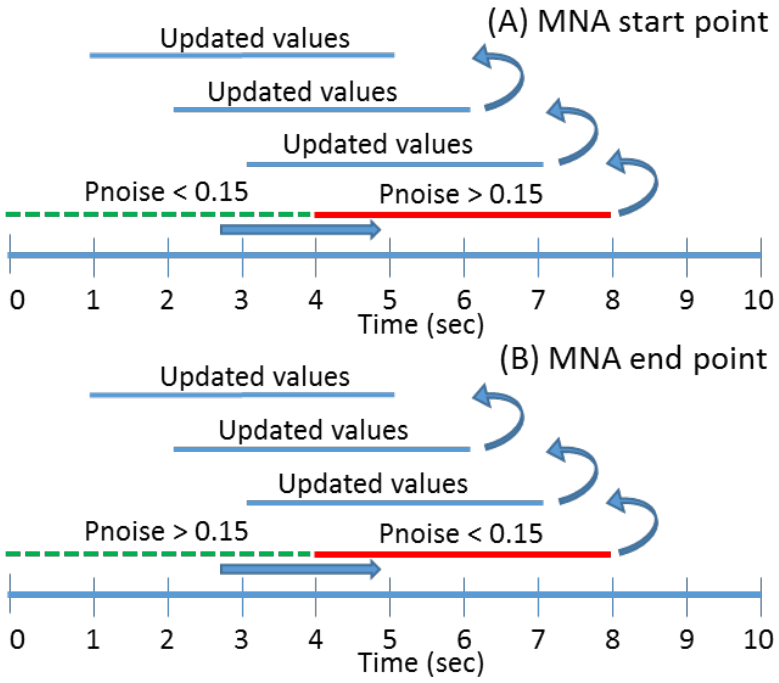

Figure 8.2 - Trace-back strategy to find the start (A) and end (B) points of MNA.

Support Vector Machine (SVM) was applied to build a decision boundary to detection MNA corrupted PPG segments from clean data. SVM is widely used for classification and regression analysis due to its accuracy and robustness to noise [12], [32].

Fig.3 shows a representative illustration of the performance of our proposed approach. Fig.3A displays a pre-processed PPG containing both clean and MNA-corrupted periods. Fig.3B-D depict the corresponding TF features explained in Section B.2. As shown, the TF features have low values for the clean portion of the data whereas it is high where MNAs occur. The TF features are used for the SVM classifier to determine whether the given segment is clean or corrupted. Fig.3F shows the classification results.

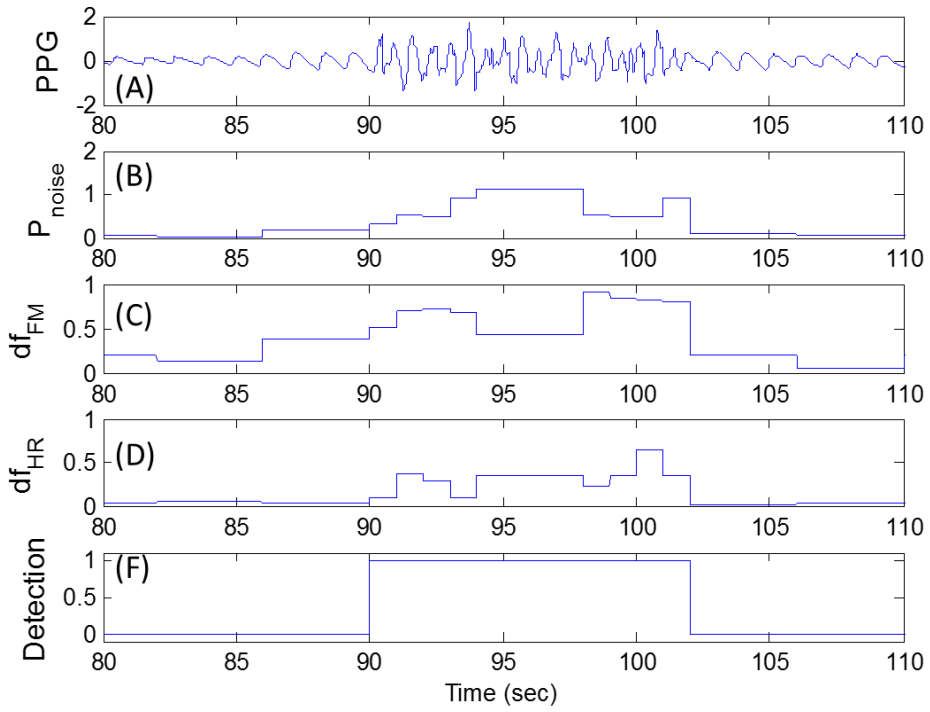

Figure 8.3 - An example of MNA detection using VFCDM. (A) PPG signal corrupted with MNA. (B) noiseQI derived from VFCDM. (C) Detection decision of VFCDM (blue) and reference MNA (red).

A representative example of the MNA detection comparing all of the aforementioned methods is illustrated in Fig. 4.

TifMA Phase (2): Usability Detection

From the previous section we show that when the PPG signal is corrupted, the HR trace and its harmonics in TFS also exhibit distortion but the amount of distortion is not uniform. Thus, a proper way to determine if a corrupted signal is usable for accurate HR estimation or not is to extract the tracing of HR values from TFS and analyze the tracing time series for missing values and abrupt changes in HR estimations. In order to fully investigate and evaluate the above described idea, a more challenging dataset with slow and rapidly changing HR scenarios was adopted in this phase of the study. The data were recorded from subjects while walking, jogging and running on a treadmill.

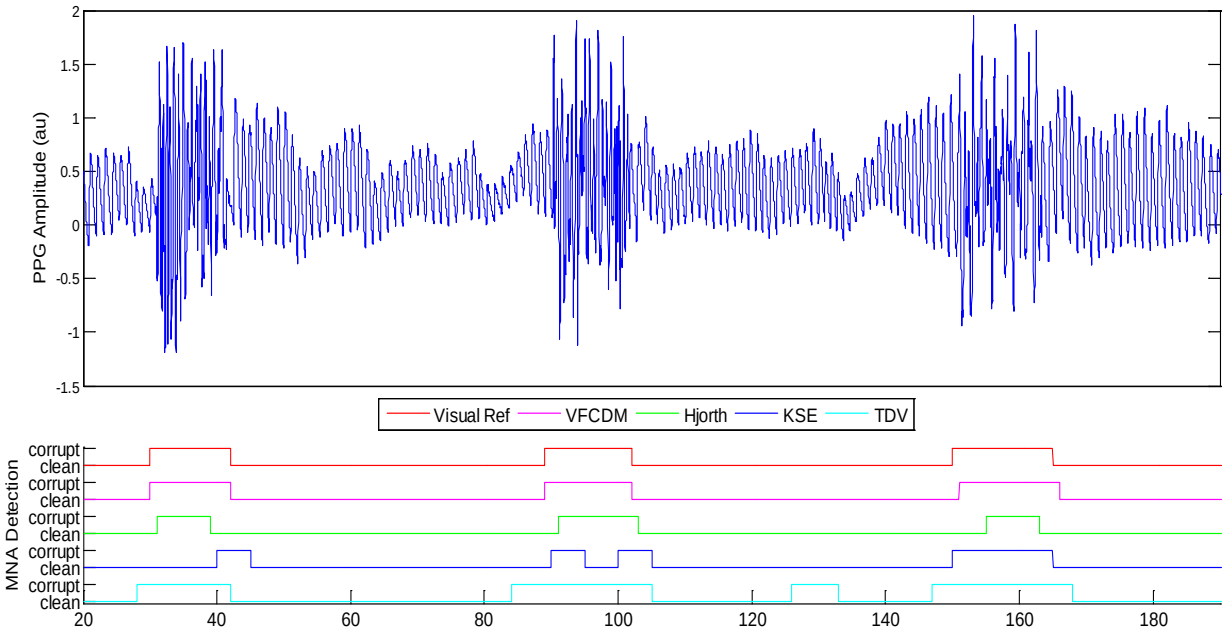

Figure 8.4 - An example of MNA detection using our VFCDM method versus other methods: Hjorth, Time-domain and Kurtosis-Shannon Entropy. The pulse-like traces are the MNA reference and detection results from the feature sets. High value indicates detected MNA, otherwise clean PPG signal

Fig.5 illustrates a 7.5 min (0.5min rest, 2 min walking (3mph), 1 min rest, 2 min jogging (5 mph), 1 min rest, 1 min running (7 mph)) segment of the 9 min recordings from subject 1. It can be observed from the reference HR (Fig.5D) estimated from a five-lead Holter monitor with hydrogel ECG electrodes (Fig.5A) that the HR is changing during this episode of experiment in a range of 80-160 bpm. Fig.6 represents the VFCDM-TFS of the corresponding PPG data in Fig.5B. One can identify the tracing of HR in TFS which begins to show distortion during the timestamps of 260-340 sec and 440-500 sec. By applying the MNA detection procedure of TifMA one can see that motion related segments truly marked as MA corrupted segments. Now we would like to investigate if any part of this MNA corrupted segments is still usable for accurate HR estimation.

The following describes the second phase of TifMA algorithm, which is detection of non-usable and usable parts of the identified corrupted data segments.

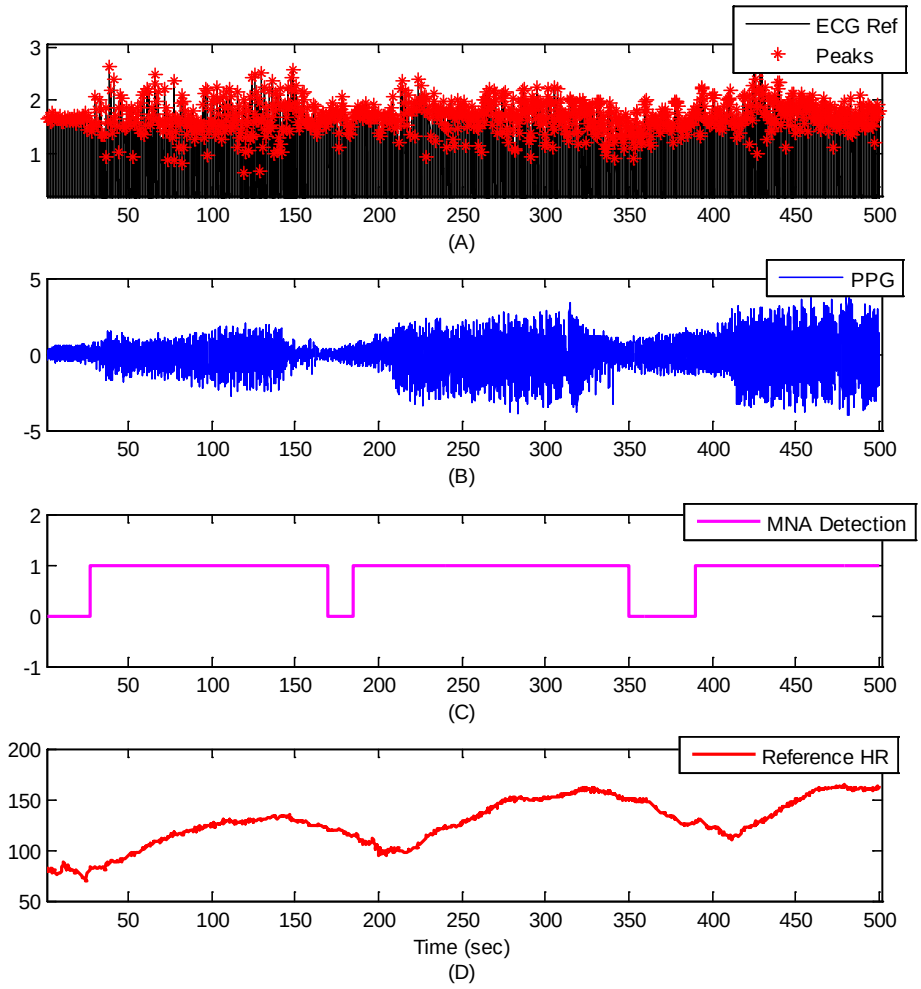

Figure 8.5 - Subject # 7 from dataset (3): (A) reference ECG, (B) PPG recordings, (C) TifMA detection, (D) Estimated reference HR from reference ECG

The usability detection stage is comprised of three steps: (1) TFS filtering, (2) HR tracking and extraction (3) Usability index measurement. In TFS filtering step, the TFS spectrum is reduced to a two component TF. Fig.7 is the plot of three typical columns of PPG TFS matrix in Fig.6. In the Fig.7A and B, the true HR frequency is close to the first and second peak respectively, while in the Fig.7C the true HR

frequency is far from the dominant peaks in the spectrum. Thus, the first two those type of data that is usable for HR estimation but the third one is not usable at all.

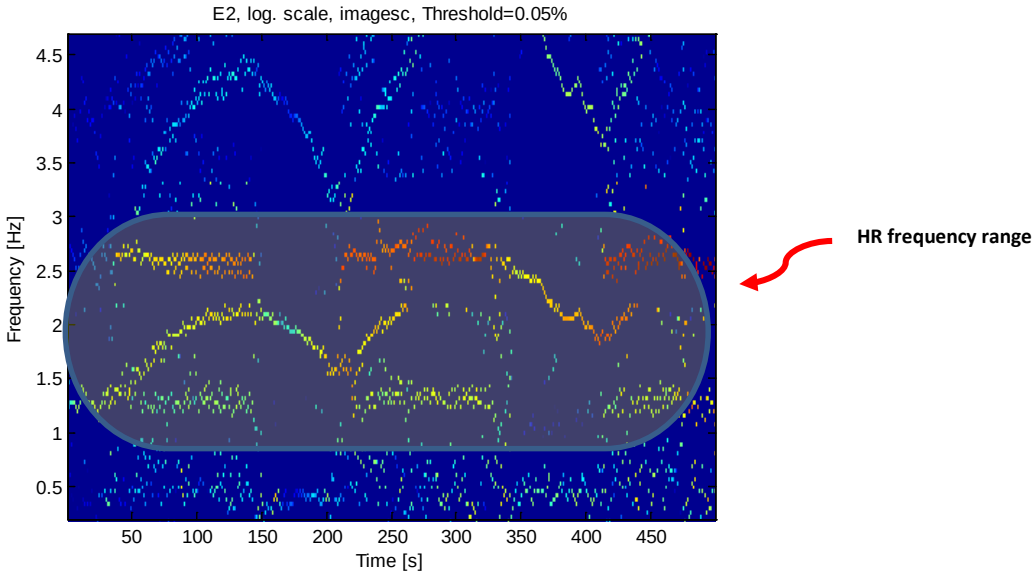

Figure 8.6 - VFCDM Time-Frequency Spectrum of Subject #7 from dataset (3)

We can assume that as long as the PPG data is clean the HR frequency belong to the frequency component with highest power (peak) in the each column of TFS matrix. On the other hand when the data get corrupted by MNA, it might shift the HR frequency to the next highest peak in the spectrum or might lose HR frequency. Here we proposed to design a TFS filtering step to look into the first two highest peaks power and frequencies in each column of TFS. Hence, the original TFS (Fig.6) can be filtered to keep only the prominent components of spectrum (see Fig.8A).

The next step after filtering the TFS is extracting HR from it. The HR tracking procedure is straightforward as follow: Assuming that we have the knowledge of the initial HR, the HR at each window is extracted by comparing the peaks to the previous HR value, if either of the peaks are in 0.8 Hz (5 bpm) range from the most recent value of HR it is chosen as usable if the value deviates more than (10 bpm) it is considered as non-usable. Fig.9A represents the estimated moving averaged HR from TFS comparing to

the reference HR from ECG. The reference of usability detection procedure is set according to the deviation of TifMA estimated HR and the true reference HR (see Fig.9B). Fig.9C shows the results of MNA detection, the first phase of the algorithm. It can be observed from this figure that segments of PPG recordings during movement (walking/jogging/running) has been mostly detected as noisy.

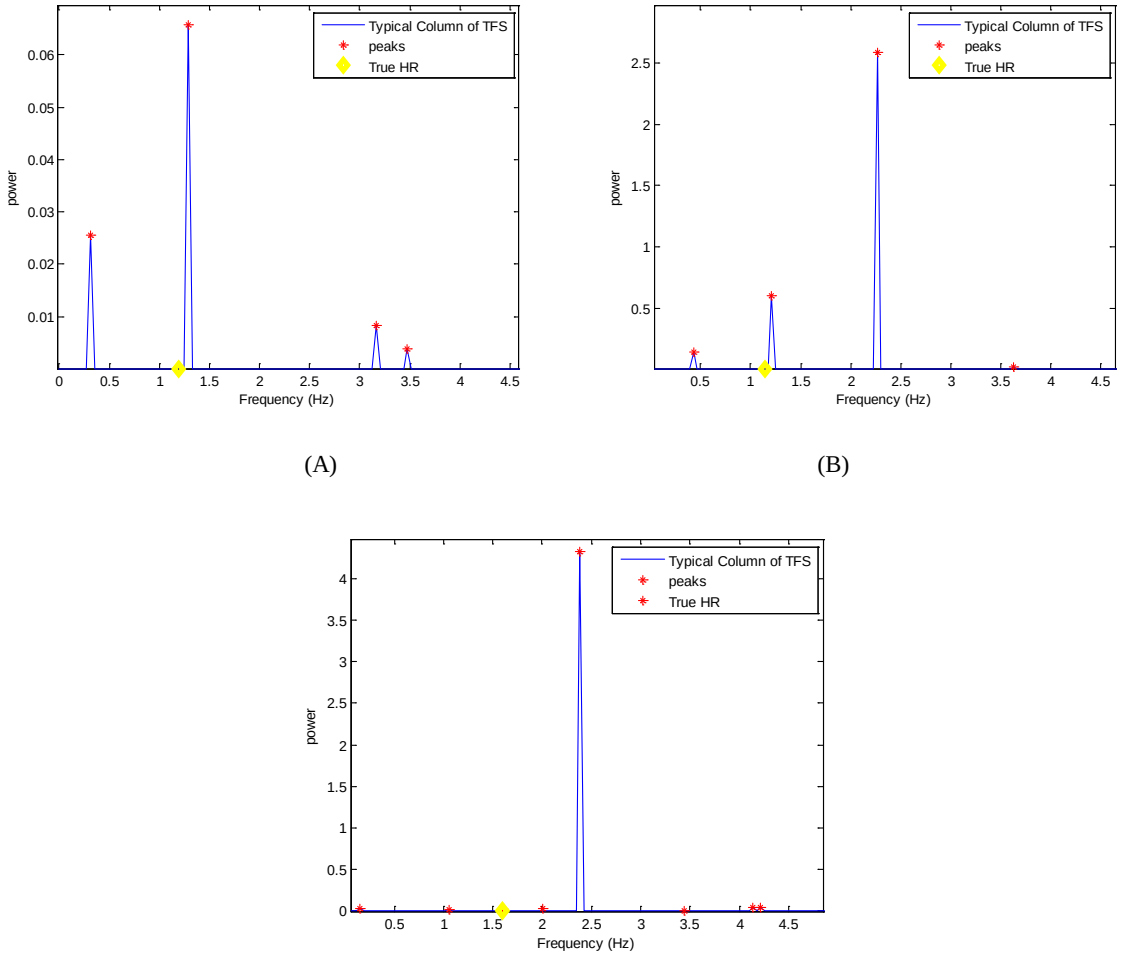

Figure 8.7 - Example of usable and non-usable PPG data: (A) Usable: True HR frequency is close to the first highest peak of spectrum, (B) Usable: True HR frequency is close to the second highest peak, (C) Non-usable: True HR is not close to any of prominent peaks in the spectrum

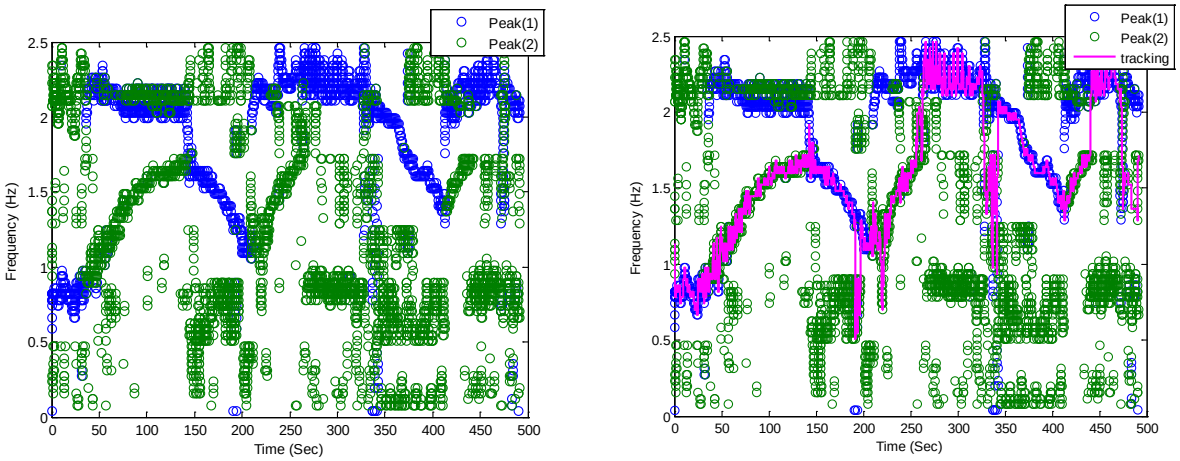

(A) (B)

Figure 8.8 - Filtered TFS: (A) First and second prominent components of TFS shown in Fig.5, (B) HR Extraction from filtered TFS

Fig.9D shows the usability index derived by second phase of TifMA. One can observe by comaring the reference UI and TifMA's UI, that TifMA is detecting the usable/nonusable portions of data for HR estimations very well. The accuracy, specificity and sensitivity of the proposed algorithm on all of the 10 recordings from dataset#5 is presented in the following section.

The overall TifMA algorithm flowchart is depicted in Fig.10.

8.3. Results

We evaluated the performance of the TifMA algorithm on 5 datasets. The first 4 datasets (laboratory controlled, and hospital patients with motion-corrupted PPGs) were used to measure the performance of the first phase of the algorithm (MNA detection) and the fifth (treadmill experiment) dataset was used to evaluate the second phase of algorithm (usability detection).

8.3.1. MNA Detection Results

Leave-one-out cross validation was adopted to evaluate the performance of MNA detection phase [33]. Specifically, for a dataset of N subjects, data from N-1 subjects were used for training and the remaining subject data were used for testing. The train-test cycle was repeated N times, each time with a different test subject. We optimized the regularization parameter value $C = 10$ for the linear kernel SVM by minimizing the training error.

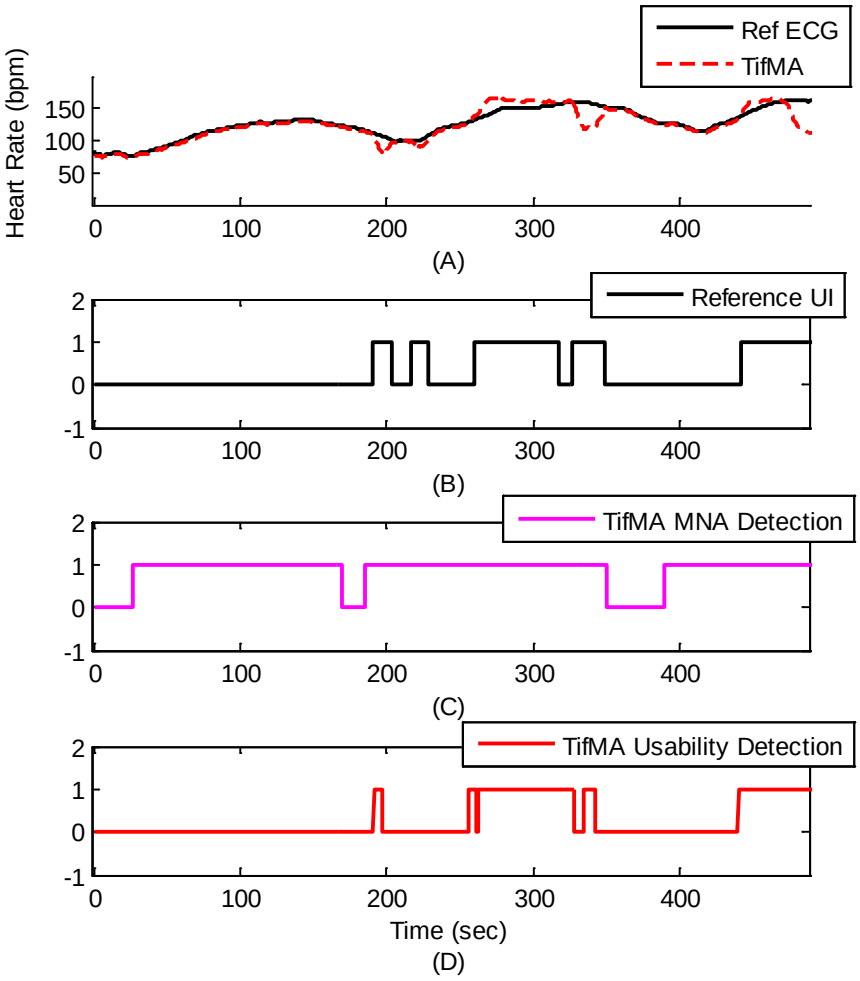

Figure 8.9 - Reference usability index. (A) Comparison of TifMA estimated HR to reference HR from ECG, (B) Reference Usability Index (UI) as an indicator of HR estimability from TFS during motion, (C) TifMA MNA Detection Result, (D) TifMA Usability Detection

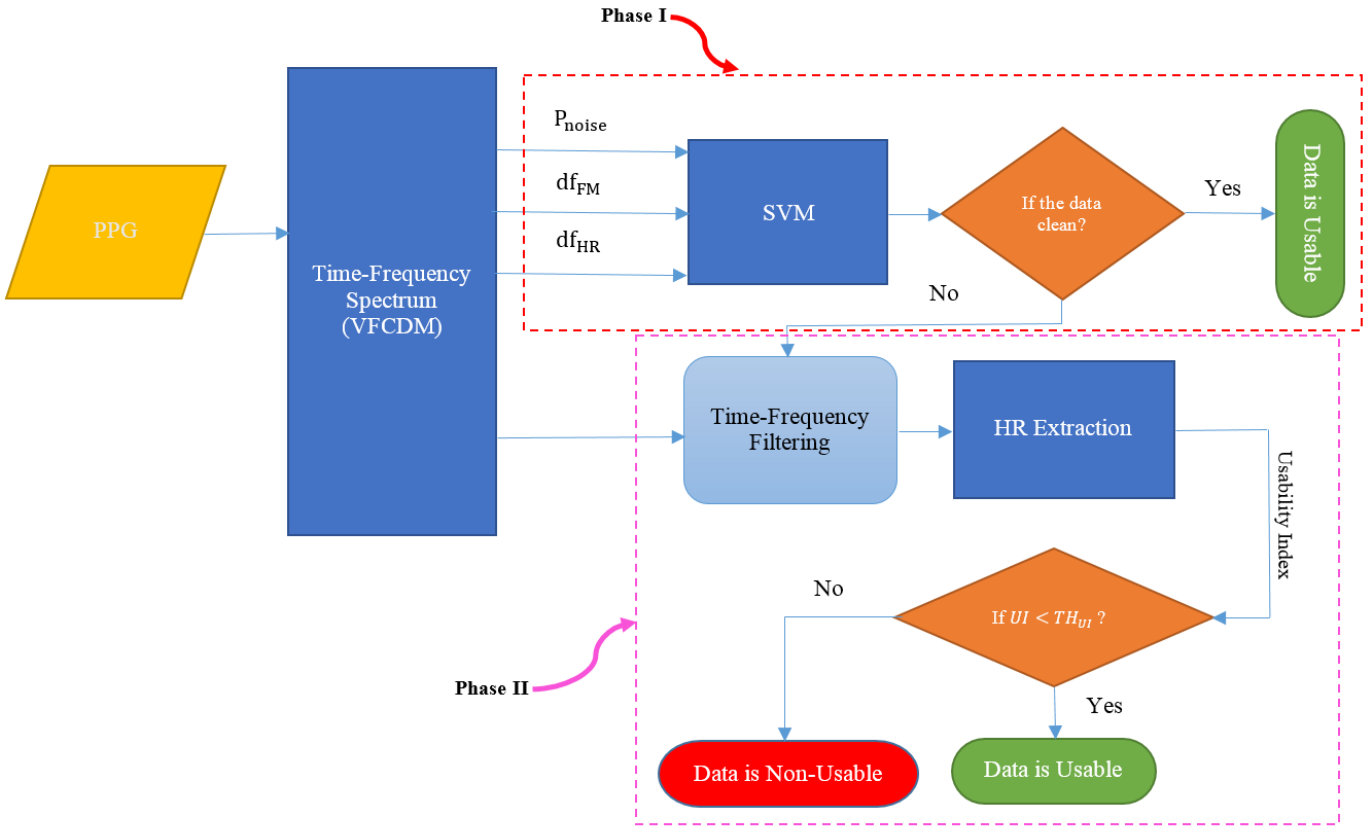

Figure 8.10 - TifMA Algorithm Flowchart

The optimal window length was determined by varying L_2 from 3 to 6 sec while keeping L_1 constant at 8 sec, as described in phase one of the TifMA. Detection performance was evaluated by comparing our classification results to the MNA reference (as determined visually by the experts) to yield accuracy, sensitivity, and specificity.

Table (5) shows performance statistics in terms of accuracy (Acc), sensitivity (Sen), and specificity (Spe) of our MNA detection algorithm at various window lengths (L_2) for the laboratory collected dataset (1). The window length of 4 sec ($L_2 = 4$ second) yielded the best performance in term of accuracy among the various window lengths.

Table 8.5. Mean ± Std. Deviation of Performance Metrics of Our Proposed TifMA Using Various Window Length.

L		3s	4s	5s	6s
Lab. Head	Acc	86.8 ± 5.52	95.7 ± 0.82	86.9 ± 4.27	85.5 ± 6.96
	Sen	82.0 ± 9.59	93.0 ± 5.75	81.5 ± 8.47	79.8 ± 9.58
	Spe	89.1 ± 5.86	96.6 ± 1.48	81.5 ± 3.19	90.0 ± 5.97

We compared the proposed algorithm with three other published MNA detection algorithms: 1) Hjorth features (Hjorth); 2) time-domain variability SVM (TDV) approach; 3) Kurtosis-Shannon Entropy (KSE) features [22], [23], [26], [27]. Table (6) represents the performance results of each method in term of means and standard variations of the accuracy, sensitivity, and specificity results from the cross-validation. Kruskal-Wallis H tests were done to determine if there was a statistical difference in accuracy, sensitivity, and specificity among different detection methods. If there was a statistical difference, Mann-Whitney post-hoc test was performed between our proposed TifMA method and each of the compared methods.

In order to measure and compare the detection powers, receiver operative characteristic (ROC) curves were generated for all the features used in TifMA and other detection algorithms. Area under these curves (AUCs) represent the strength of these features. In Fig. 11, ROC curves of the three TF features as well as the AUCs of all features used for MNA detection are shown.

In addition to accurate MNA detection, the other attractive feature of our proposed algorithm is that it is able to accurately locate the start and end points of MNA occurrences. Accurate detection of the start and end time of the MNAs is important for the subsequent reconstruction of the MNA-corrupted data as we do not want to miss the MNA portion of data for reconstruction or avoid having to reconstruct the noisy portion of the PPG when the segment is designated to be clean.

Table 8.6. Mean ± Std. Deviation of Performance Metrics of Our Proposed TifMA, Other Methods. (*) Indicate Statistical Significance (p<0.05) BETWEEN Our Method vs. the Others.

		TifMA	Hjorth	TDV	KSE
Lab. Head	Acc	95.7 ± 0.82	72.5 ± 10.74 *	93.4 ± 3.50 *	83.1 ± 7.31 *
	Sen	93.0 ± 5.75	47.2 ± 28.80 *	88.8 ± 7.90 *	56.6 ± 17.88 *
	Spe	96.6 ± 1.48	84.4 ± 4.63 *	96.7 ± 3.00	91.5 ± 1.14 *
Umass. Head	Acc	95.3 ± 1.34	69.5 ± 21.83 *	89.8 ± 1.45 *	85.1 ± 8.34 *
	Sen	90.8 ± 2.83	53.8 ± 26.05 *	84.6 ± 2.89 *	68.7 ± 17.72 *
	Spe	98.7 ± 1.07	84.5 ± 8.83 *	94.3 ± 3.95 *	86.4 ± 7.82 *
Lab. Finger	Acc	97.5 ± 1.50	91.1 ± 6.87 *	94.4 ± 3.30 *	58.5 ± 20.67 *
	Sen	96.4 ± 2.34	83.5 ± 21.04 *	94.7 ± 3.40	34.6 ± 12.23 *
	Spe	98.1 ± 1.43	96.2 ± 3.02	94.7 ± 3.00 *	86.3 ± 15.65 *
Umass. Finger	Acc	94.3 ± 1.64	71.0 ± 18.96 *	89.6 ± 2.34 *	88.3 ± 2.68 *
	Sen	88.5 ± 2.23	41.1 ± 27.57 *	85.2 ± 3.75 *	71.5 ± 8.83 *
	Spe	96.9 ± 1.86	88.4 ± 7.52 *	95.1 ± 0.79	93.6 ± 1.52 *

To evaluate the algorithm's effectiveness in pinpointing the start and end time of the MNAs, we computed the time difference of start and end points between the visual reference and detection algorithms' results. The time difference is termed detection transition time, DTT, which reflects how accurately on average a MNA algorithm detects the start and end time of the MNAs. Table (7) provides DTT comparison of TifMA algorithm and other detection algorithms. As shown in Table (7), our algorithm's detection accuracy of the duration of the MNAs is significantly better than three other methods we compared. Our algorithm's DTT is less than one second whereas the second best algorithm, the Hjorth, is off by more than two seconds and the least accurate method, the KSE, is off by more than four seconds.

Table 8.7. Mean ± Std. Detection of Transition Time (DTT) of TifMA and Other Methods.

Algorithm	DTT (sec)
TifMA	0.91 ± 0.59
Hjorth	2.17 ± 0.37
KSE	4.24 ± 2.42
TDV	2.75 ± 0.96

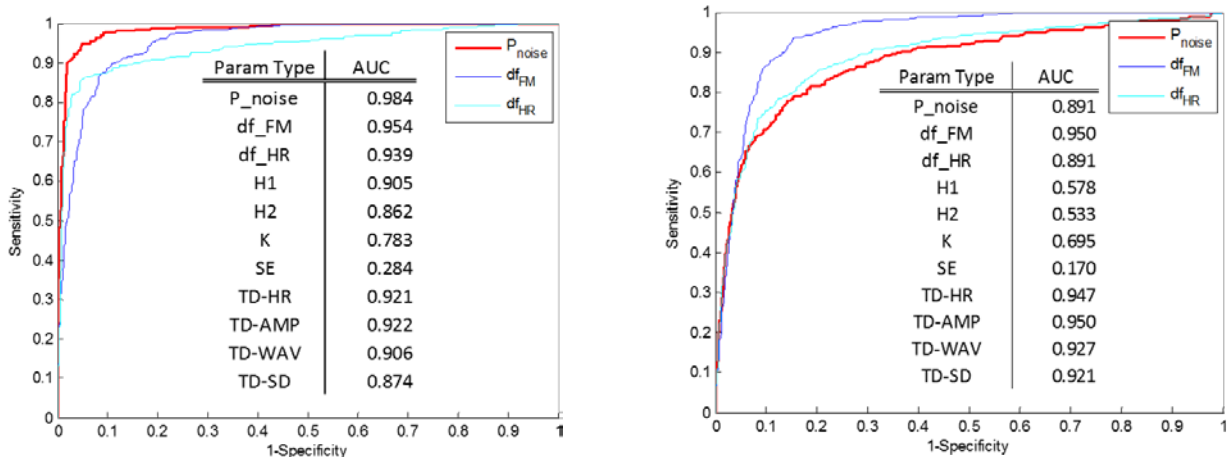

(A) (B)

Figure 8.11 - Receiver-operative-curves (ROCs) of all the features used in MNA detection algorithms: Our proposed VFCDM (P_noise,df_HR,df_FM); Hjorth parameters (H1,H2); Statistical features (K,SE), Time-domain features (TD-HR, TD-AMP,TD-WAV,TD-SD). (A) Lab. Finger data; (B) Lab. Head data.

8.3.2. Usability Detection Results

By applying the first phase of TifMA algorithm we showed that the algorithm is able to determine if a PPG data segment is clean from MNA or is corrupted. However being corrupted by movement does not necessarily indicate that the whole noisy data is non-usable especially for HR monitoring applications. It was shown that HR frequency changes can be tracked using VFCDM time-frequency plot as long as the signal is usable and the level of corruption is not too high. This non-usable scenario can be occurred during any PPG recordings due to abrupt and fast movements that makes tracking of frequency harder in time-frequency domain. To this end the second phase of algorithm was tested on PPG recordings from 10 subjects who performed 9 min (walk/jog/run) experiment. The data initially was fed into the MNA detection phase and when a corrupted data segment is obtained, the second phase of algorithm perform usability measurement of data, that is whether the corrupted signal is usable for HR estimations or not. Table (8)

presents the accuracy, sensitivity, and specificity of usability detection comparing to the reference usability index.

Table 8.8. TifMA Usability Detection Performance.

Subjects	Dataset (5)	Acc	Sen	Spe	Non-usable period (min)
1		0.89	0.94	0.92	1.80
2		0.93	0.90	0.88	1.31
3		0.95	0.92	0.90	1.58
4		0.93	0.91	0.96	0.12
5		0.91	0.93	0.84	0.35
6		0.91	0.90	0.90	0.48
7		0.93	0.92	0.91	2.23
8		0.95	0.94	0.92	0.33
9		0.94	0.96	0.94	0.62
10		0.90	0.97	0.90	1.05
mean±std		0.92±0.02	0.93±0.02	0.90±0.03	0.98±0.71

It can be seen from the above table that on average almost 10% of PPG recordings during a treadmill experiment were non-usable and should be discarded.

8.5. Discussion

We propose a novel MNA and usability detection method "TifMA" that uses dynamic characteristics of the corrupted PPG derived via the VFCDM. The algorithm comes in two phases: (1) MNA detection, (2) Usability detection. The efficacy of the detection phase was validated using contrived motion data from healthy subjects and unconstrained MNA data from participants recruited from a hospital-setting. The second phase of the algorithm was tested on HR varying scenario where subjects were asked to walk/jog/run for 9 min on a treadmill. For MNA detection several key features associated with MNAs derived from the VFCDM-based time-frequency spectrum. By transforming the PPG time series into the time-frequency domain, we were able to better capture time-varying characteristics of the MNAs. Specifically, we recognized that PPG's clean signal dynamics are largely concentrated at the heart rate and its harmonic frequency bands. Hence, we surmised that the presence of large amplitudes in the other frequency bands must be associated with MNAs. This is clearly seen in Fig. 1B as VFCDM results from a clean PPG yields distinct peaks across all times at the HR frequencies and its two successive harmonic frequencies. Therefore, we divided the TFS into three narrow band spectra and tracked down these

frequency traces accordingly. In a clean PPG segment (shown in Fig. 1A-B) most of the spectral power is concentrated in the $FM_1, FM_2, \text{and } FM_3$ traces since the signal is sinusoidal-like and periodic in nature. In a MNA corrupted PPG segment shown in Fig. 1C-D, however, the signal is disturbed by inconsistent changes in the signal amplitude due to motion. These changes are typically irregular thus creating various spectral contents in the resulting TFS and eventually yielding high values of TF features.

The detection accuracy on both lab-controlled and UMMC datasets using TifMA outperformed the other three detection methods: Hjorth, TDV, and KSE. We compared each method's performance based on their own unique feature selection by evaluating the area under the ROC curve. The AUCs showed that our TF features provided the highest values AUCs > 0.89 for both finger data and forehead recorded PPG, as shown in Fig. 5. Concomitantly, the accuracy, sensitivity and specificity values of our proposed method were significantly higher than other methods as indicated in Table III.

Since TifMA uses the features in frequency domain, not all noise dynamics in time domain are reflected in the frequency domain. Thus, time-domain motion noise artifact detection techniques [20, 21, 27] (e.g. accelerometer based MNA detection) are not always accurate when it comes to heart rate or respiratory rate monitoring applications. Fig. 12 illustrates an example of MNA analysis of PPG recordings from a subject during walking. Fig.12D shows the HR estimations from PPG and reference HR estimated from clean reference ECG. Fig.12C represents the accelerometer intensity of raw tri-axial accelerometer recordings. Movement intensity from three axial accelerometer signals is calculated by taking moving average of squared derivative of accelerometer raw data [21]. It can be observed from this figure that accelerometer is very sensitive to movement and as soon as the subject start to move (walk) it shows a level of increase in the accelerometer signal intensity. However by looking into Fig.12D, the HR from PPG can be accurately estimated is some section of movement period. By applying TifMA algorithm on this segment of PPG, the algorithm is able to discriminate between the usable and non-usable segments of PPG for HR estimations (see Fig.12B).

It can be seen from the above example that accelerometers' high intensity values do not always lead to gross inaccurate HR estimation. For instance during the time window 95 to 115 sec of recordings, the HRs estimated from PPG significantly deviate from the reference ECG HR, as expected since the accelerometers intensity during this segment is quite high especially for the X-axis accelerometer. However, for a time segment from 130 to 160 sec, the HR estimation from PPG is very close to that of reference ECG even though the accelerometers' intensity is as high as the time window segment between 95-115 seconds. Therefore, just relying on accelerometers can lead to incorrect detection of MNA in the time segment between 130-160 seconds in Fig.12. Note however, with our proposed TifMA algorithm, it can pinpoint and the start and end points of usable and non-usable segments of data that is it can correctly labeled the data segment between 130-160 seconds as usable data for HR accurate estimations.

The eventual aim of our proposed algorithm is to detect MNAs in real time. The algorithm only takes 33.3ms to compute TF features for a 4s PPG window length using Matlab running on a PC with the Intel Xeon processor operating at 3.6GHz. Therefore, it would be straightforward to optimize the algorithm for real time detection of MNAs in PPGs.

In conclusion, we proposed an accurate MNA detection algorithm that utilizes both time and spectral features to classify between clean and corrupted PPG data segments. Moreover, it has the ability to go beyond MNA detection and can detect if the corrupted signal is still usable for accurate HR estimations or not. Comparison using four datasets showed our algorithm out-performed other contemporary MNA detection algorithms. Out algorithm also showed superiority with respect to detecting onset and offset of MNAs. Finally, TifMA is real-time realizable and it is applicable to either transmission (finger) or reflectance (forehead) recorded PPGs.

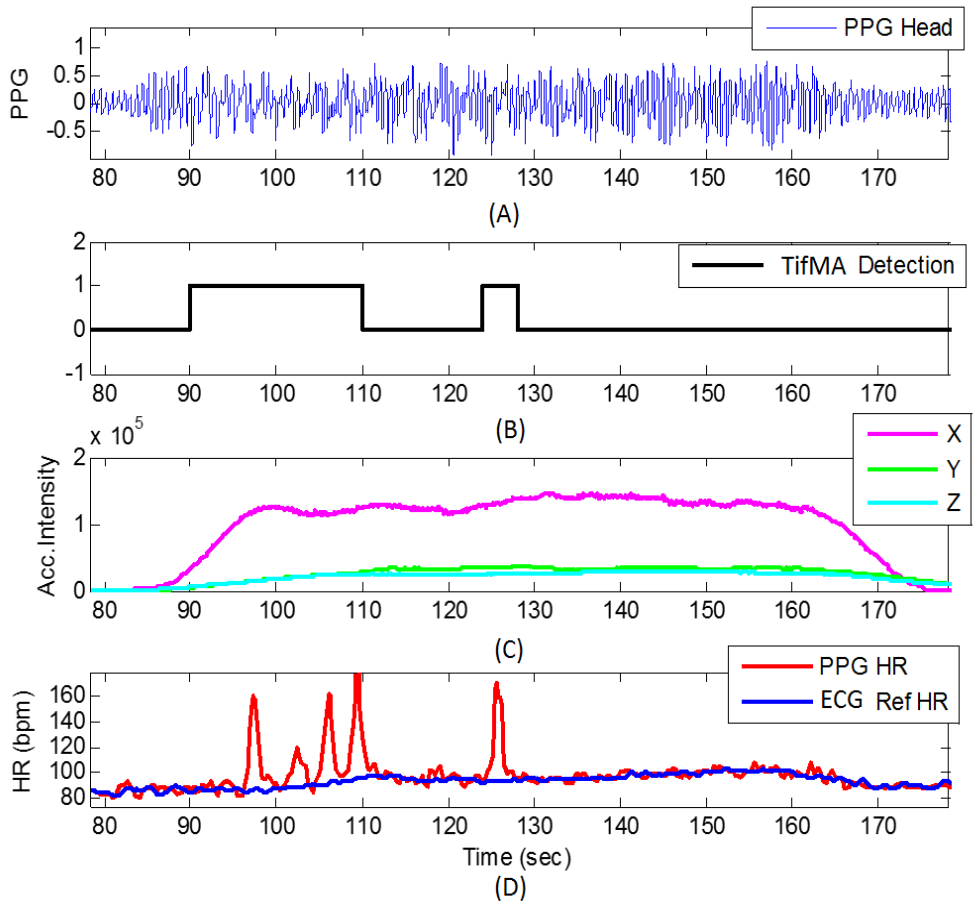

Figure 8.12 - An example showing Accelerometer vs. TifMA based methods performance on a typical PPG signal recorded from a subject during walking.

References

[1] S. Dash, K. H. Chon, S. Lu, and E. A. Raeder, "Automatic real time detection of atrial fibrillation," *Ann. Biomed. Eng.*, vol. 37, no. 9, pp. 1701–1709, Sep. 2009.

[2] L. P. Antonsen and K. A. Kirkebøen, "Evaluation of fluid responsiveness: is photoplethysmography a noninvasive alternative?," *Anesthesiol. Res. Pract.*, vol. 2012, p. 617380, 2012.

[3] F. Camacho, "Statistical Analysis of Central Aortic Blood Pressure Parameters Derived From the Peripheral Pulse," PhD Thesis, The University of New South Wales, Sydney, 2005.

[4] M. T. Petterson, V. L. Begnoche, and J. M. Graybeal, "The effect of motion on pulse oximetry and its clinical significance," *Anesth. Analg.*, vol. 105, no. 6 Suppl, pp. S78–84, Dec. 2007.

[5] R. Sahni, A. Gupta, K. Ohira-Kist, and T. Rosen, "Motion resistant pulse oximetry in neonates," *Arch. Dis. Child. Fetal Neonatal Ed.*, vol. 88, no. 6, pp. F505–F508, Nov. 2003.

[6] M. R. Ram, K. V. Madhav, E. H. Krishna, N. R. Komalla, and K. A. Reddy, "A Novel Approach for Motion Artifact Reduction in PPG Signals Based on AS-LMS Adaptive Filter," *IEEE Trans. Instrum. Meas.*, vol. 61, no. 5, pp. 1445–1457, May 2012.

[7] T. L. Rusch, R. Sankar, and J. E. Scharf, “Signal processing methods for pulse oximetry,” *Comput. Biol. Med.*, vol. 26, no. 2, pp. 143–159, Mar. 1996.

[8] R. Hong Enríquez, M. Sautié Castellanos, J. Falcón Rodríguez, and J. L. Hernández Cáceres, “Analysis of the photoplethysmographic signal by means of the decomposition in principal components,” *Physiol.*

Meas., vol. 23, no. 3, pp. N17–29, Aug. 2002.

[9] S. M. A. Salehizadeh, Duy K. Dao, Jo Woon Chong, David McManus, Chad Darling, Yitzhak Mendelson, Ki H. Chon, “Photoplethysmograph signal reconstruction based on a novel hybrid motion artifact detection-reduction approach. Part II: Motion and noise artifact detection,” Ann. Biomed. Eng., vol. 42, no. 11, pp. 2238–2250, Nov. 2014.

[10] Y. Yan, C. C. Poon, and Y. Zhang, “Reduction of motion artifact in pulse oximetry by smoothed pseudo Wigner-Ville distribution,” *J. NeuroEngineering Rehabil.*, vol. 2, p. 3, Mar. 2005.

[11] J. Lee, W. Jung, I. Kang, Y. Kim, and G. Lee, “Design of filter to reject motion artifact of pulse oximetry,” *Comput. Stand. Interfaces*, vol. 26, no. 3, pp. 241–249, May 2004.

[12] K. V. P. Naraharisetti, M. Bawa, and M. Tahernezhadi, “Comparison of different signal processing methods for reducing artifacts from photoplethysmograph signal,” in *2011 IEEE International Conference on Electro/Information Technology (EIT)*, 2011, pp. 1–8.

[13] M. R. Ram, K. V. Madhav, E. H. Krishna, K. N. Reddy, and K. A. Reddy, “Computation of SpO2 using non-parametric spectral estimation methods from wavelet based motion artifact reduced PPG signals,” in *2011 International Conference on Signal Processing, Communication, Computing and Networking Technologies (ICSCCN)*, 2011, pp. 776–780.

[14] R. Krishnan, B. Natarajan, and S. Warren, “Two-Stage Approach for Detection and Reduction of Motion Artifacts in Photoplethysmographic Data,” *IEEE Trans. Biomed. Eng.*, vol. 57, no. 8, pp. 1867–1876, Aug. 2010.

[15] J. A. Sukor, S. J. Redmond, and N. H. Lovell, “Signal quality measures for pulse oximetry through waveform morphology analysis,” *Physiol. Meas.*, vol. 32, no. 3, pp. 369–384, Mar. 2011.

[16] K. Li, S. Warren, and B. Natarajan, “Onboard Tagging for Real-Time Quality Assessment of Photoplethysmograms Acquired by a Wireless Reflectance Pulse Oximeter,” *IEEE Trans. Biomed. Circuits Syst.*, vol. 6, no. 1, pp. 54–63, Feb. 2012.

[17] Q. Li, R. G. Mark, and G. D. Clifford, “Robust heart rate estimation from multiple asynchronous noisy sources using signal quality indices and a Kalman filter,” *Physiol. Meas.*, vol. 29, no. 1, pp. 15–32, Jan. 2008.

[18] K. Nakajima, T. Tamura, and H. Miike, “Monitoring of heart and respiratory rates by photoplethysmography using a digital filtering technique,” *Med. Eng. Phys.*, vol. 18, no. 5, pp. 365–372, Jul. 1996.

[19] W. Karlen, K. Kobayashi, J. M. Ansermino, and G. A. Dumont, “Photoplethysmogram signal quality estimation using repeated Gaussian filters and cross-correlation,” *Physiol. Meas.*, vol. 33, no. 10, pp. 1617–1629, Oct. 2012.

[20] B. Lee, J. Han, H. J. Baek, J. H. Shin, K. S. Park, and W. J. Yi, “Improved elimination of motion artifacts from a photoplethysmographic signal using a Kalman smoother with simultaneous accelerometry,” *Physiol. Meas.*, vol. 31, no. 12, p. 1585, Dec. 2010.

[21] J. Y. A. Foo and S. J. Wilson, “A computational system to optimise noise rejection in photoplethysmography signals during motion or poor perfusion states,” *Med. Biol. Eng. Comput.*, vol. 44, no. 1–2, pp. 140–145, Mar. 2006.

[22] R. Krishnan, B. Natarajan, and S. Warren, “Analysis and detection of motion artifact in photoplethysmographic data using higher order statistics,” in *IEEE International Conference on Acoustics, Speech and Signal Processing, 2008. ICASSP 2008*, 2008, pp. 613–616.

[23] N. Selvaraj, Y. Mendelson, K. H. Shelley, D. G. Silverman, and K. H. Chon, “Statistical approach for the detection of motion/noise artifacts in Photoplethysmogram,” *Conf. Proc. Annu. Int. Conf. IEEE Eng. Med. Biol. Soc. IEEE Eng. Med. Biol. Soc. Annu. Conf.*, vol. 2011, pp. 4972–4975, 2011.

[24] B. Hjorth, “The physical significance of time domain descriptors in EEG analysis,” *Electroencephalogr. Clin. Neurophysiol.*, vol. 34, no. 3, pp. 321–325, Mar. 1973.

[25] B. Hjorth, “EEG analysis based on time domain properties,” *Electroencephalogr. Clin. Neurophysiol.*, vol. 29, no. 3, pp. 306–310, Sep. 1970.

[26] E. Gil, J. María Vergara, and P. Laguna, “Detection of decreases in the amplitude fluctuation of pulse photoplethysmography signal as indication of obstructive sleep apnea syndrome in children,” *Biomed. Signal Process. Control*, vol. 3, no. 3, pp. 267–277, Jul. 2008.

[27] J. W. Chong, D. K. Dao, S. M. A. Salehizadeh, D. D. McManus, C. E. Darling, K. H. Chon, and Y. Mendelson, “Photoplethysmograph signal reconstruction based on a novel hybrid motion artifact detection-reduction approach. Part I: Motion and noise artifact detection,” *Ann. Biomed. Eng.*, vol. 42, no. 11, pp. 2238–2250, Nov. 2014.

[28] C. G. Scully, N. Selvaraj, F. W. Romberg, R. Wardhan, J. Ryan, J. P. Florian, D. G. Silverman, K. H. Shelley, and K. H. Chon, “Using time-frequency analysis of the photoplethysmographic waveform to detect the withdrawal of 900 mL of blood,” *Anesth. Analg.*, vol. 115, no. 1, pp. 74–81, Jul. 2012.

[29] N. Selvaraj, J. Lee, and K. H. Chon, “Time-varying methods for characterizing nonstationary dynamics of physiological systems,” *Methods Inf. Med.*, vol. 49, no. 5, pp. 435–442, 2010.

[30] N. Selvaraj, K. H. Shelley, D. G. Silverman, N. Stachenfeld, N. Galante, J. P. Florian, Y. Mendelson, and K. Chon, “A novel approach using time-frequency analysis of pulse-oximeter data to detect progressive hypovolemia in spontaneously breathing healthy subjects,” *IEEE Trans. Biomed. Eng.*, vol. 58, no. 8, Aug. 2011.

[31] H. Wang, K. Siu, K. Ju, and K. H. Chon, “A high resolution approach to estimating time-frequency spectra and their amplitudes,” *Ann. Biomed. Eng.*, vol. 34, no. 2, pp. 326–338, Feb. 2006.

[32] C. . Hsu and C. Chang, “A Practical Guide to Support Vector Classification.” Department of Computer Science, National Taiwan University, 2003.

[33] M. Kearns and D. Ron, “Algorithmic stability and sanity-check bounds for leave-one-out cross-validation,” *Neural Comput.*, vol. 11, no. 6, pp. 1427–1453, Aug. 1999.

Chapter 9: OxiMA: A Novel Motion and Noise Artifact Reduction for the purpose of SpO2 and HR reconstruction

9.1. Introduction

In chapters 6 and 7 we introduced two motion and noise corrupted vital signal reconstruction techniques. We discussed the limitations of blind source separation and time-series modeling/prediction methods. The next three chapter will be about three signal reconstruction techniques that were developed in time-frequency domain. We will show that using the time-freuqnecy based technqie we were able to achieve better performance and accuracy in HR/SpO2 estimations from a PPG/ECG signal that is corrupted by motion and noise artifact. Two noteworthy time-frequency based algorithms recently published for HR estimations during motion and physical activities are TROIKA, JOSS [20, 21] in which time-frequency spectrum estimation, and spectral peak tracking and verification, are used to estimate and monitor HR during intensive physical activity, respectively. Both approaches make use of PPG and accelerometer information to obtain an accurate estimation of HR during running on a treadmill. Neither time-domain PPG signal reconstruction nor SpO2 estimations can be done using JOSS or TROIKA.

In this chapter, a new PPG signal reconstruction and SpO2/HR monitoring approach is presented using time-varying spectral analysis. The algorithm is called OxiMA and it has its foundation from TifMA algorithm. OxiMA is comprised of six distinct stages: (1) Time-frequency spectral analysis, (2) signal decomposition (3) spectral filtering, (4) HR extraction and tracking, (5) signal reconstruction, and (6) SpO2 estimation. The first and second step are accomplished by employing a variable frequency complex demodulation (VFCDM) technique to derive the time-frequency spectrum (TFS) and components of the PPG. VFCDM is a method for estimating time-frequency spectrum of a time-varying signal. This method was shown to provide concomitant high time and frequency resolution as well as preservation of the amplitude distribution of the signal [22]. Next, we limit the spectrum to the 0.5 Hz – 3 Hz HR frequency range and take the frequency and power information of the first two peaks in the PSD at each window and

signal segment. We are assuming that the HR component in a typical clean (motion free) PPG signal is always the dominant frequency component in the time-varying power spectrum, hence, the highest peak of the spectrum corresponds to the HR frequency. Thus, when movement happens the dominant component can be shifted to the second peak in the spectrum. After reducing the time-frequency spectrum to the first two peaks, HR is extracted from the TFS. By calculating the HR, we choose the two components among all PPG components with a closer frequency to the HR frequency and reconstruct the signal using the two components. That is, we reconstruct the time-domain signals from the time-frequency domain. We show in the Results section that the new OxiMA method provides HR reconstruction with accurate SpO2 estimation even during movement.

9.2. Experiments and Materials

The OxiMA algorithm was evaluated on a lab controlled dataset that was recorded during voluntary induced hypoxia. In an IRB approved study which recruited 10 subjects, one set of data was collected from each subject for a duration of 22 min. Reference arterial SpO2 and HR were collected from the FDA approved Masimo SET Radical RDS-1 pulse oximeter (mounted on the left hand), while a Nellcor OxiMax sensor (mounted on the right hand) was used to collect analog PPG signals, simultaneously.

Each subject sat in a chair and was asked to breathe into a 1-gallon bag four times for approximately two minutes each time. During the first and third time the subject breathed into the bag, subjects were asked to remain still. During the second and fourth time the subject breathed into the bag, subjects were asked to introduce noise into the measurement by shaking their right hand. Each subject wore a disposable nose clip whenever breathing into the bag to prevent accidental breathing of room air. The Masimo reference sensor remained motionless for the entire duration of the study. Subjects had at least two minutes of rest between successive bag-breathing maneuvers, with more time if requested. The protocol for this experiment is presented in Table 2. This sequence of data recording allowed us to test the efficacy of the OxiMA algorithm while a subject experienced different levels of hypoxia during motion artifacts.

Table 9.1. PPG Datasets and Experiments Settings

Subject	Dataset	Scenario	Sensor Type	Subject's Age/Sex	Ethnicity
1 2 3 4 5 6 7 8 9 10	Lab Controlled	Oxygen Saturation Variations 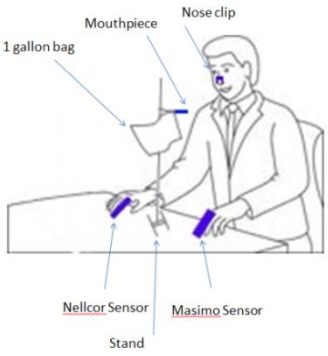	• [Actual PPG] Finger Pulse Oximeter Nellcor  • [Ref SpO_2] Finger Pulse Oximeter  • [Ref HR] SilverRest ECG Electrode 	23-58 yr (10 Males)	3 Asian 2 Hispanic 3 American 2 White

This experiment was considered safe since subjects experienced only temporary hypoxia for brief (less than 1 minute) periods of time. For reference, clinical studies showed SpO2 levels in patients suffering from mild to moderate sleep apnea can drop to about 80% for short periods of time until the patient is awakened without irreversible physiological effects [23].

Table 9.2. Experiment Protocol

End Time (min)	**2**	**4**	**5**	**7**	**9**	**10**	**12**
Event	Rest (baseline)	Bag breathing (no motion)	Rest (oxygen recovery)	Rest	Bag breathing (motion)	Rest (oxygen recovery)	Rest
End Time (min)	14	15	17	19	20	22	
Event	Bag breathing (no motion)	Rest (oxygen recovery)	Rest	Bag breathing (motion)	Rest (oxygen recovery)	Rest	

9.4. Methodology

The procedure for the OxiMA algorithm is presented in Table (3). Details of each stage will be described in subsections *i* to *vi*.

Table 9.3. The proposed OxiMA algorithm: HR and SpO2 Reconstruction

Stage 1. VFCDM Time-Frequency Spectrum

1.1. Downsample the PPG signal to ¼ of the original sampling frequency
1.2. Compute the VFCDM based time-frequency spectrum (TFS)

Stage 2. Signal Decomposition

2.1. Decompose the PPG signal into its frequency components according to frequency bands in the TFS

Stage 3. Spectral Filtering

3.1. Assume HR to be in the frequency range of [0.5Hz – 3Hz], to account for both low and high HR values.
3.2. The first highest two peaks and their corresponding frequencies in the PPG filtered spectrum are assumed to have HR information.

Stage 4. Heart Rate Tracking and Extraction from PPG Spectrum

Case (1): From 3.1- if the spectrum is corrupted by movement and only the first largest peak is corrupted, then the HR frequency should be the frequency of the second peak in the spectrum.
Case (2): Due to the sensor-skin interface interruption, which could be a result of a gap between the pulse oximeter and a subject's skin or slight sensor alignment variations relative to skin, the HR frequency cannot be extracted from the spectrum and in this case the previous HR frequency is used or for offline implementation a cubic spline interpolation can be applied to fill in the missing HR information.

Stage 5. PPG Signal Reconstruction

5.1. The PPG signal is reconstructed by using the summation of VFCDM components with frequency closest to the HR frequency at each window.

Stage 6. Oxygen Saturation Estimation

6.1. Calculate the SpO_2 estimations from reconstructed infrared and red PPG signals using the following equation [2]

$$\boldsymbol{SpO_2}(\%) = (\mathbf{110} - \mathbf{25}\boldsymbol{R})$$

where,

$$\boldsymbol{R} = \frac{\boldsymbol{AC_{Red}}/\boldsymbol{DC_{Red}}}{\boldsymbol{AC_{IR}}/\boldsymbol{DC_{IR}}}$$

9.4.1. Time-Varying Spectral Analysis of PPG

In this study in order to compute the time-frequency spectrum, a variable frequency complex demodulation technique was adopted. Table (4) present the VFCDM procedure.

We produce a time-varying spectrum by taking a T-sec window of the PPG signal and computing the VFCDM time-frequency of the segment and then sliding the window through the whole dataset. The sliding process is simple and there is no overlapping between the time windows. The window segment length T was set to 8 seconds and was shifted by 8 seconds. The assumption of 8 second data length largely stems from the fact that SpO2 and heart rates do not change instantaneously, hence, an 8 second duration is a reasonable choice. As a representative example, the resultant VFCDM time-frequency spectrum of recordings from subject #5 is shown in Fig.1.

Table 9.4. VFCDM Algorithm Procedure

Consider a sinusoidal signal $\boldsymbol{x(t)}$ to be a narrow band oscillation with a time-varying center frequency $\boldsymbol{f(\tau)}$, instantaneous amplitude $\boldsymbol{A(t)}$, phase $\boldsymbol{\phi(t)}$, and the direct current component $\boldsymbol{dc(t)}$:

$$\boldsymbol{x(t) = dc(t) + A(t)\cos\left(\int_0^t 2\pi f(\tau)d\tau + \phi(t)\right)}$$

Step (1) For a given center frequency, we can extract the instantaneous amplitude information $\boldsymbol{A(t)}$ and phase information $\boldsymbol{\phi(t)}$ by multiplying **(1)** by $\boldsymbol{e^{-j\int_0^t 2\pi f(\tau)d\tau}}$ which results in the following:

$$\boldsymbol{z(t) = x(t)e^{-j\int_0^t 2\pi f(\tau)d\tau} = dc(t)e^{-j\int_0^t 2\pi f(\tau)d\tau} + \frac{A(t)}{2}e^{j\phi(t)} + \frac{A(t)}{2}e^{-j\left(\int_0^t 4\pi f(\tau)d\tau + \phi(t)\right)}}$$

Step (2) From **(2)**, if $\boldsymbol{z(t)}$ is filtered with an ideal low-pass filter (LPF) with a cutoff frequency $\boldsymbol{f_c < f_0}$, where $\boldsymbol{f_0}$ is the center frequency of interest. Then the filtered signal $\boldsymbol{z_{lp}(t)}$ will contain only the component of interest $\boldsymbol{z_{lp}(t) = \frac{A(t)}{2}e^{j\phi(t)}}$.

Step (3) By changing the center frequency followed by using the variable frequency approach as well as the LPF, the signal, $\boldsymbol{x(t)}$, will be decomposed into the sinusoid modulations, $\boldsymbol{d_i}$, by the CDM technique as follows:

$$\boldsymbol{x(t) = \sum_i d_i = dc(t) + \sum_i A_i(t)\cos\left(\int_0^t 2\pi f_i(\tau)d\tau + \phi_i(t)\right)}$$

Step (4) The instantaneous frequency and amplitude of $\mathbf{d_i}$ can be calculated using the Hilbert transform

$$\boldsymbol{A(t) = 2\left|z_{lp}(t)\right| = [X^2(t) + Y^2(t)]^{1/2}}$$

$$\boldsymbol{X(t) = real(z_{lp}(t))}$$

$$\boldsymbol{Y(t) = imag\left(z_{lp}(t)\right) = H[X(t)] = \frac{1}{\pi}\int \frac{X(t')}{t - t'}dt'}$$

$$\boldsymbol{\phi(t) = \arctan\left(\frac{imag\left(z_{lp}(t)\right)}{real\left(z_{lp}(t)\right)}\right) = \arctan\left(\frac{Y(t)}{X(t)}\right) f(t) = f_0 + \frac{1}{2\pi}\frac{d\phi(t)}{dt}}$$

The panels in Fig. 1a and 1b show infrared and red PPG time series data, respectively. Fig. 1c represents the time-frequency plot of the infrared PPG signal. The next section details how the PPG data is decomposed into its frequency components using VFCDM.

9.4.2. Signal Decomposition

We can decompose the original PPG signal into sinusoidal modulations using VFCDM (see Table 4).

$$x(t) = \sum_{i=1}^{N} Component\{i\} = \sum_{i=1}^{N} dc_i(t) + A_i(t)cos\left(2\pi f_i(t) + \phi_i(t)\right) \quad (1)$$

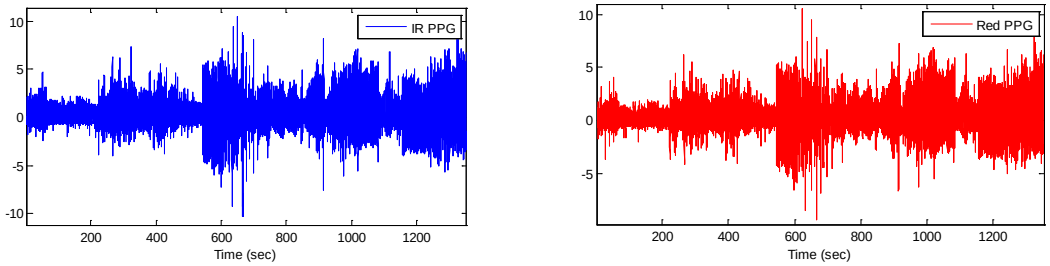

(a) (b)

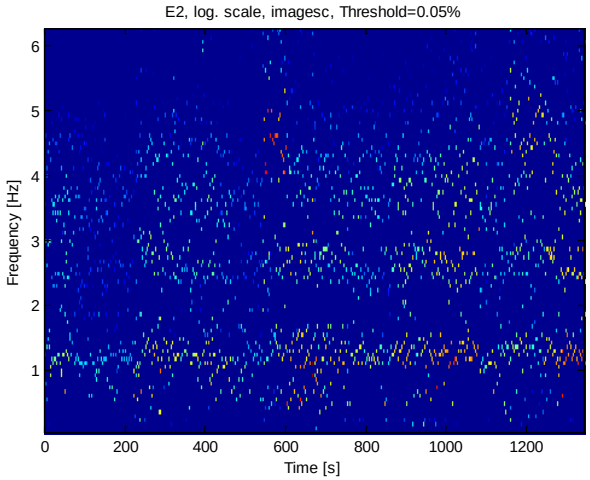

(c)

Figure 9.1 - Time-Frequency spectra of recording #5: (a) PPG infrared signal, (b) simultaneous PPG red signal, (c) VFCDM TF spectrum of the PPG.

By assuming $\boldsymbol{N} = 12$ fixed frequency bands each with a distinct central frequency, we can decompose PPG signals using the VFCDM procedure, which yields 12 components. Fig.2 shows the twelve components corresponding to the IR and Red signal of subject number (5).

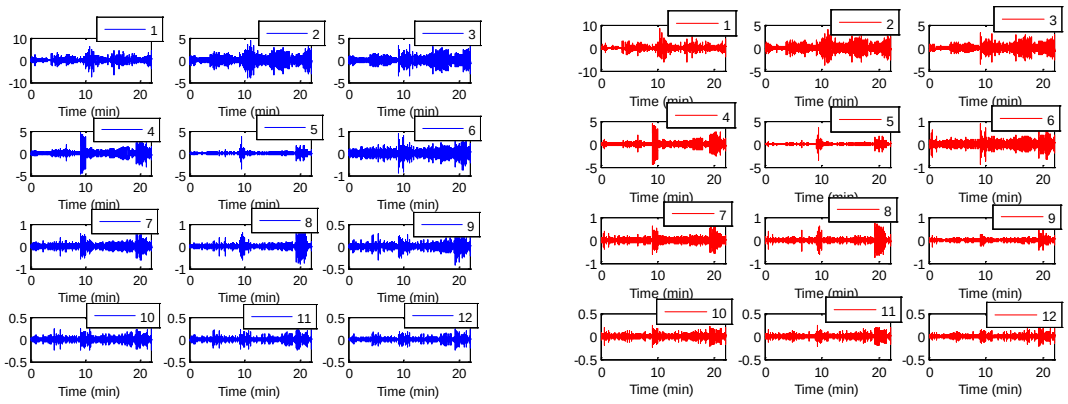

(a) (b)

Figure 9.2 - VFCDM Signal Decomposition on subject 5's data: (a) 12 components obtained from VFCDM procedure (Table 5) corresponding to the PPG infrared signal, (b) 12 components obtained from VFCDM procedure corresponding to the PPG red signal

Among the twelve frequency bands, bands 1 to 5 corresponds to frequency range of [0.5 Hz to 3 Hz], which is typically the HR frequency range. Now the problem is which components out of these 5 components should be chosen to reconstruct the signal that preserves the HR and is less corrupted by the motion artifacts?

In order to address the above problem, we first need to estimate an accurate HR and next select the components with closest frequency to the actual HR frequency in order to reconstruct a less noisy signal than the original data. In this study a new approach to extract HR from the time-frequency spectrum is presented and we show its robustness against MA by comparing the new approach to the common peak detection based HR estimation method.

9.4.3. Spectral Filtering

After obtaining the power spectral density at each window, HR frequency is assumed to be confined in the range [0.5 Hz – 3 Hz], which takes into account both at rest and high HR values due to either

tachycardia or exercise scenarios. Next, for HR estimation, only frequencies that correspond to the first and second peak at each column of time-frequency matrix are retained.

In general, HR frequency in the VFCDM based power spectral density of the PPG at each window can have three different scenarios: (1) PPG is devoid of MA and there is no sensor-skin interface problems like a spatial gap between the sensor and the subject's skin during recording, (2) PPG is corrupted by MA and there is no spatial gap between the sensor and the subject's skin during recording and (3) There is a spatial gap between the sensor and the subject's skin during recording. For the ideal case (1), HR can be extracted and it is most likely represented as the highest peak in the PPG spectrum. For case (2), MA dynamics can result in the dominant peak and HR frequency peak's magnitude become smaller than the MA frequency peak in the spectrum. The only scenario that makes it difficult to extract HR from the spectrum is scenario (3) when there is a spatial gap between the PPG sensor and the subject's skin during recording. In this scenario, assuming that the motion artifacts are brief in duration, the missing HR values can be interpolated using the cubic spline approach. Fig. 3 is the plot of the above three scenarios. In Fig. 3a and b, the true HR frequency is close to the first and second peak respectively, while in Fig. 7c, the true HR frequency is far from the dominant peaks in the spectrum. We can assume that as long as the PPG data is clean the HR frequency belongs to the frequency component with the highest power (peak) at each column of the TFS matrix. On the other hand, when the data is corrupted by MA, the second highest peak may contain the heart rate frequency or the HR frequency may have negligible power and be lost. Here we designed a TFS filter to assess the two highest power peaks and frequencies in each column of the TFS. Hence, the original TFS (Fig. 1c) can be filtered to keep only the prominent components of the spectrum (see Fig. 4).

Fig. 4a shows a representative filtered time-frequency spectral plot of PPG recording #5. This step in the OxiMA process involves retaining only the two largest frequency peaks at each time point within the defined HR range (30-180 bpm) and they are represented as blue and green traces, respectively. It is our

opinion that retaining only the two largest frequency peaks at each time point is reasonable for the first two scenarios as outlined above.

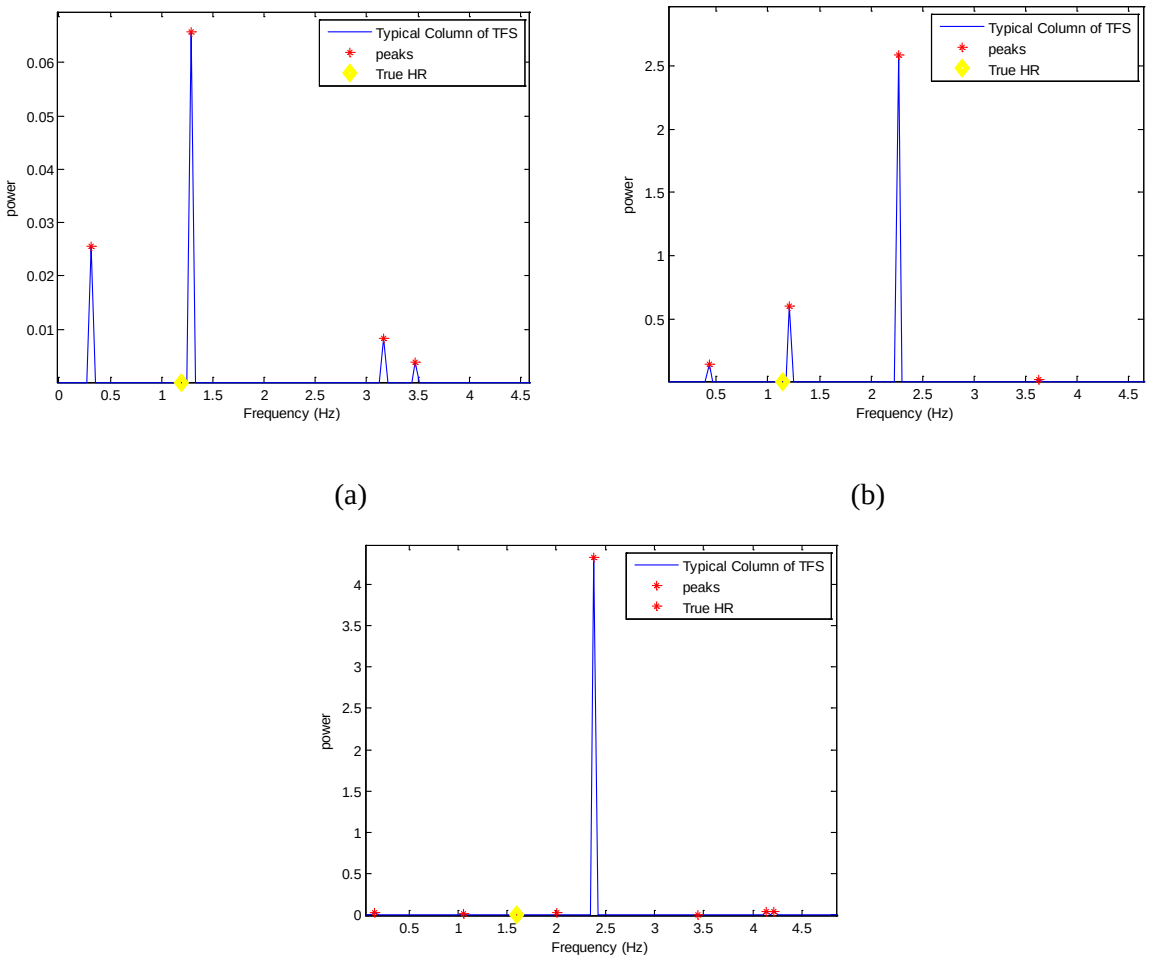

Figure 9.3 - Three scenarios of HR frequency estimation: (a) True HR frequency is close to the first highest peak of spectrum, (b) True HR frequency is close to the second highest peak, (c) True HR is not close to any of the prominent peaks in the spectrum.

9.4.4. Heart Rate Tracking and Extraction

Heart rate extraction is performed after TFS filtering. The HR tracking procedure is as follows: Assuming that we have the knowledge of the initial HR, the HR at each window is extracted by comparing

the peaks to the previous HR value., If either of the peaks are within the 0.03 Hz (2 bpm) range from the most recent value of HR it is chosen, but if the value deviates by more than 2 bpm, the HR from the previous window is preserved. Fig.4b illustrates the tracking of HR from the filtered TFS. Fig. 4c and Fig. 4d represents the estimated 8 second moving averaged HR from the TFS and the original HR from the time-domain PPG signal compared to the reference HR from the Masimo, respectively. In order to calculate the performance of the OxiMA algorithm for HR reconstruction, the error value in each time window was calculated from the estimated HR to the reference Masimo-derived HR. Two measurement indices of absolute error similar to the indices in [22] were used.

$$Error(1) = \frac{1}{W}\sum_{k=1}^{w}\left|HR_{OxiMA}(k) - HR_{ref}(k)\right| \quad (2)$$

$$Error(2) = \frac{1}{W}\sum_{k=1}^{w}\frac{\left|HR_{OxiMA}(k) - HR_{ref}(k)\right|}{HR_{OxiMA}(k)} \times 100\% \quad (3)$$

where, W is the total number of windows. It can be observed that the accuracy of HR estimation after reconstruction was improved by almost 100%. PPG signal reconstruction

Now that accurate HR values at each time window are estimated from the time-frequency spectrum, in the signal reconstruction phase of OxiMA, the algorithm compares the frequency of the decomposed VFCDM components from stage (II) of the algorithm and chooses those with the closest frequency to the true HR frequency. The assumption here is that the signal components corresponding to the HR frequency are more robust against motion and thus a less corrupted signal can be reconstructed using the summation of these components (see Fig. 5a and b).

9.4.5. Oxygen Saturation Estimation

In order to calculate SpO2 from PPG signals, red and infrared PPG signals with clearly separable DC and AC components are required. Let the pulsatile components of the red and infrared PPG signals be denoted as AC_{Red} and AC_{IR}, respectively, then the "ratio-of-ratio" R is estimated [24, 25] as

$$R = \frac{AC_{Red}/DC_{Red}}{AC_{IR}/DC_{IR}} \qquad (4)$$

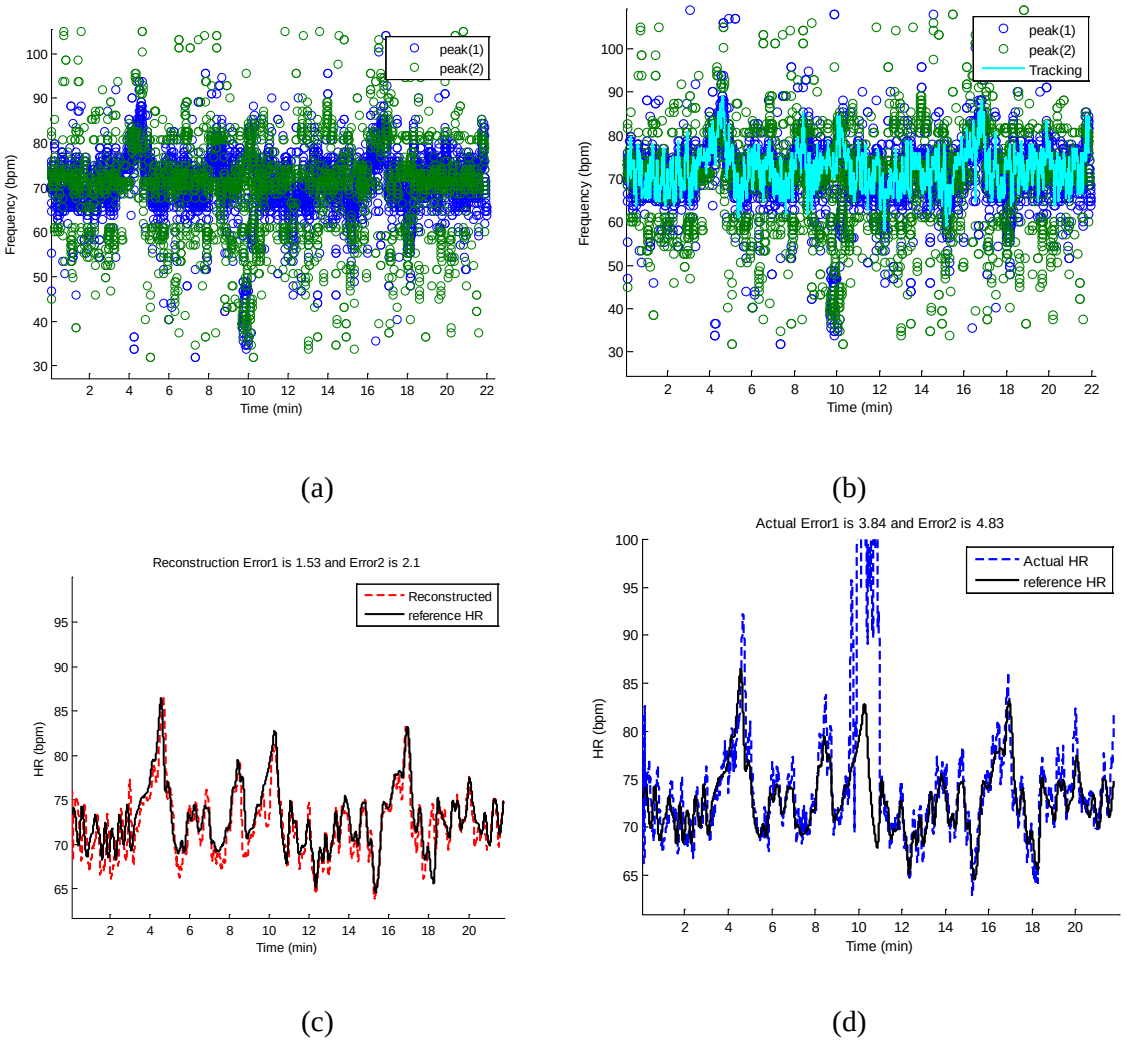

Figure 9.4 - Filtered TFS and HR Extraction: (a) First and second prominent components of TFS shown in Fig.1c, (b) HR Extraction from filtered TFS, (c) Comparison of moving averaged reconstructed estimate of HR vs. reference HR. (d) Comparison of moving averaged before-reconstruction HR vs. reference HR.

Accordingly, SpO2 is computed by substituting the R value in an empirical linear approximated relation given by $SpO_2(\%) = (110 - 25R)$

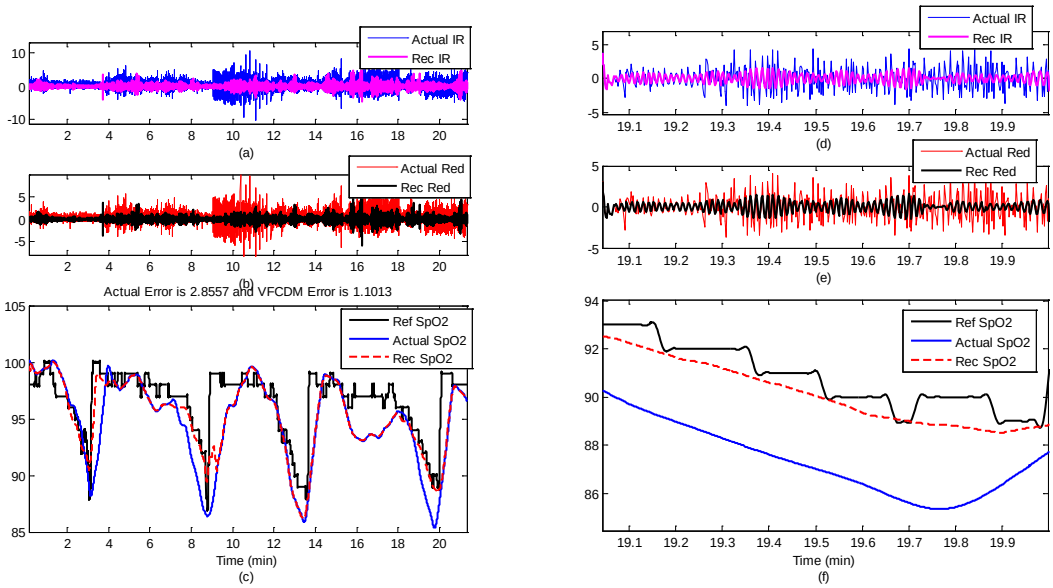

Figure 9.5 - PPG signal reconstruction and SpO2 estimation: (a) Actual (blue) and reconstructed (magenta) infrared PPG signal, (b) Actual (red) and reconstructed (black) red PPG signal, (c) Comparison of reconstructed estimated SpO2 vs. actual and reference SpO2. (d) zoom-in version of (a). (e) zoom-in version of (b). (f) zoom-in version of (c)

9.5. Results

Table (6) represents the average absolute error (E1) and the average absolute error percentage (E2) of HR and SpO2 estimations of the proposed OxiMA algorithm on the varying hypoxia level dataset. Our OxiMA algorithm is compared to the HR and SpO2 estimations before the reconstruction algorithms, where both before and after reconstruction estimations are compared to the reference HR and reference SpO2 from the Masimo commercial pulse oximeter. The results presented in Table (7) show that OxiMA on average improves the HR and SpO2 estimations by 100% and 105% respectively compared to those estimations before reconstruction. Improvement rates were calculated as follows:

$$ImRate1(\%) = \frac{1}{W}\sum_{k=1}^{W}\frac{|Error1_{OxiMA}(k) - Error1_{Act}(k)|}{Error1_{OxiMA}(k)} \times 100\% \qquad (5)$$

$$ImRate2(\%) = \frac{1}{W}\sum_{k=1}^{w}\frac{|Error2_{OxiMA}(k) - Error2_{Act}(k)|}{Error2_{OxiMA}(k)} \times 100\% \qquad (6)$$

Fig.6 shows the reconstructed HR and SpO2 in comparison to the reference HR from ECG recordings for subject#5. The largest error among the recordings came from this recording. The larger error could be due to rapid movements or skin-sensor gap during the recordings. We can see that the E1 (HR) for this particular subject is as low as 4.05 bpm while the E1 (SpO2) is as low as 3.25%. It can be seen from Table (7) that HR and SpO2 both improved by 160% and 119%, respectively, after reconstruction even if the corruption caused by movement was quite severe.

Table 9.5. OxiMA Algorithm Performance Comparison

Subject	Actual HR estimation error		OxiMA HR estimation error		Actual SpO_2 estimation error		OxiMA SpO_2 estimation error	
	E1	E2%	E1	E2%	E1	E2%	E1	E2%
1	3.84	4.83	**1.53**	**2.10**	2.51	2.63	**0.86**	**0.90**
2	6.84	9.57	**2.72**	**3.97**	7.14	9.63	**2.45**	**3.10**
3	8.15	9.59	**1.69**	**2.29**	6.21	6.59	**1.61**	**1.67**
4	4.55	5.39	**2.61**	**3.18**	1.89	2.46	**0.95**	**1.16**
5	10.53	11.96	**4.04**	**4.60**	7.13	7.80	**3.25**	**3.47**
6	4.46	5.52	**2.04**	**2.66**	2.85	2.99	**1.10**	**1.14**
7	12.41	19.65	**2.81**	**4.37**	5.83	9.09	**2.57**	**4.52**
8	3.84	4.35	**2.10**	**2.46**	3.51	4.63	**1.73**	**2.22**
9	3.80	4.13	**2.57**	**2.83**	1.81	2.10	**1.50**	**1.61**
10	3.65	4.20	**1.85**	**2.41**	4.85	5.91	**1.93**	**2.07**
mean±std	6.20±3.2	7.91±5.0	2.40±0.73	3.09±0.90	4.37±2.1	5.38±2.8	1.79±0.8	2.19±1.2

9.6. Discussion

In this study, a new approach (OxiMA) based on VFCDM analysis of the PPG signal is introduced to address SpO2 and HR monitoring during motion artifacts. The idea behind the proposed OxiMA approach was to extract the accurate HR from MA corrupted PPG signals and then use the VFCDM components with closes frequency to the estimated HR to reconstruct the red and infrared PPG signals.

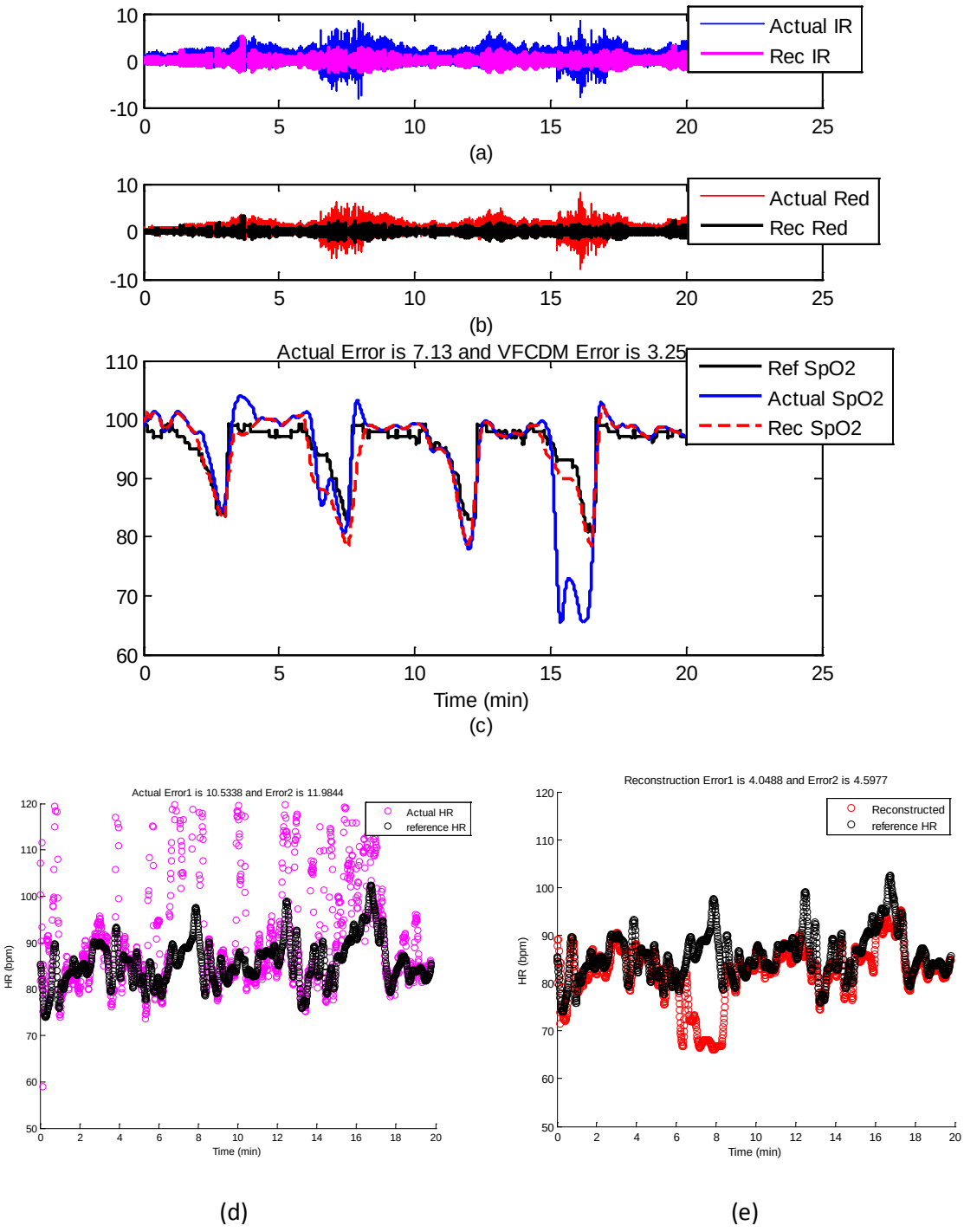

Figure 9.6 - Subject 5. (a-b) Reconstructed infrared and red PPG vs. actual PPG recordings. (c) Reconstructed SpO2 vs. reference and actual SpO2. (d) Reconstructed HR vs. reference HR. (e) Actual HR vs. reference HR.

Table 9.6. OxiMA Algorithm Improvement Rate

Subject	HR Improvement Rate		SpO_2 Improvement Rate	
	ImRate1%	ImRate2%	ImRate1%	ImRate2%
1	150.90	130.00	191.86	192.22
2	151.47	141.05	191.43	210.64
3	323.08	318.78	285.71	294.61
4	74.33	69.50	98.95	112.07
5	160.17	160.66	119.38	124.78
6	118.63	107.52	159.09	162.28
7	377.22	372.54	126.85	101.10
8	82.86	76.83	102.89	108.55
9	47.86	45.94	20.67	30.43
10	97.30	74.27	151.30	185.5
mean±std	158.38±108.2	149.71±109.9	144.81±70.5	152.2±73.2

Finally the reconstructed red and infrared we applied to estimate accurate MA free SpO2 signals. The dataset used to verify the algorithms performance was collected from 10 subjects during a hypoxic experiment. In all of the experiments, the reference HR and reference SpO2 readings from the Masimo finger pulse oximeter and the estimated HR and SpO2 values were calculated from reconstructed spectrum of the PPG signals in 8 second time windows.

It has been shown in the results section that the proposed OxiMA algorithm can be used for tracking HR and SpO2 changes during severe motion artifacts with an average error of around 2.4 bpm and 1.8% compared to that of the reference ECG. These results are superior to those estimations before OxiMA reconstruction.

We made several observations while analyzing the data. The tracking ability of the OxiMA algorithm decreased as the frequency changes during recordings increased. This is mostly likely because OxiMA tracks a dominant frequency through an 8-second window. Since each subjects' motion varied throughout each hypoxic maneuver, the dominant frequency can change within the observed window. The strength of the PPG's LED is one of the most important factors determining the performance. A reduction in the strength of the PPG signal can be caused by ambient light leaking into the gap between a PPG sensor

and the skin surface [21]. This is because the power of the signal is dependent on the depth and reflection of the light from the pulse oximeter sensor to the subject's skin. This gap between skin and sensors may be the result of movement during physical activities or the shape of tissue that the sensors touch. In the datasets that have been analyzed, recordings #5 and #7 are examples of the above two scenarios.

Additionally, the perfusion of the monitored region affects the signal-to-noise ratio of the PPG signal. When performing the hypoxic maneuvers, subjects' HR and breathing rate increase as oxygen saturation decreases. These physiologic changes cause more distinct pulsations in the digits, which increase the signal-to-noise ratio. Conversely, the accuracy of all pulse oximeters diminishes as oxygen saturations deviate further from 100%.

Previous PPG reconstruction algorithms, such as [2, 15], have been tested under MA conditions but not concomitant hypoxia. This study illustrates the efficacy of OxiMA in a realistic scenario where both MA and oxygen saturation changes occur simultaneously.

The proposed OxiMA algorithm can be easily implemented in real-time. We have found that the algorithm takes only 180 msec on data divided into 8 second segments. Therefore, given the high accuracy of the proposed approach in estimating HR and SpO2 despite severe motion artifacts, this method has the potential for implementation on wearable devices such as smart watches and PPG-based fitness sensors. .

References

1. Laman, M., et al., Can clinical signs predict hypoxaemia in Papua New Guinean children with moderate and severe pneumonia? Ann Trop Paediatr, 2005. 25(1): p. 23-7.
2. Salehizadeh, S.M.A., et al., Photoplethysmograph Signal Reconstruction based on a Novel Motion Artifact Detection-Reduction Approach. Part II: Motion and Noise Artifact Removal. Annals of Biomedical Engineering, 2014. 42(11): p. 2251-2263.
3. Tamisier, R., et al., A new model of chronic intermittent hypoxia in humans: effect on ventilation, sleep, and blood pressure. J Appl Physiol (1985), 2009. 107(1): p. 17-24.
4. Jubran, A., Pulse oximetry. Crit Care, 1999. 3(2): p. R11-r17.

5. Maeda, Y., M. Sekine, and T. Tamura, Relationship between measurement site and motion artifacts in wearable reflected photoplethysmography. J Med Syst, 2011. 35(5): p. 969-76.
6. Thakor, N.V. and Y.S. Zhu, Applications of adaptive filtering to ECG analysis: noise cancellation and arrhythmia detection. IEEE Trans Biomed Eng, 1991. 38(8): p. 785-94.
7. Diniz, P., Adaptive filtering: algorithms and practical implementation. 2008: . Springer Science, Business Media L.L.C., .
8. Kalman, R.E., A New Approach to Linear Filtering and Prediction Problems Transactions of the ASME – Journal of Basic Engineering, 1960. Series D(82).
9. Morbidi, F., et al., Application of Kalman Filter to Remove TMS-Induced Artifacts from EEG Recordings. Control Systems Technology, IEEE Transactions on, 2008. 16(6): p. 1360-1366.
10. Seyedtabaii, S.S.a.L., Kalman filter based adaptive reduction of motion artifact from photoplethysmographic signal. World Academy of Science, Engineering and Technology, 2008. 37.
11. Comon, P., Independent component analysis, A new concept? Signal Processing, 1994. 36(3): p. 287-314.
12. Thompson, B., Canonical Correlation Analysis: Uses and Interpretation. 1984: SAGE Publications.
13. Jolliffe, I.T., Principal Component Analysis. 2 ed. Springer Series in Statistics. 2002: Springer-Verlag New York. 488.
14. Elsner, J.B. and A.A. Tsonis, Singular Spectrum Analysis: A New Tool in Time Series Analysis. 1996: Springer.
15. Kim, B.S. and S.K. Yoo, Motion artifact reduction in photoplethysmography using independent component analysis. IEEE Trans Biomed Eng, 2006. 53(3): p. 566-8.
16. Krishnan, R., B. Natarajan, and S. Warren, Two-Stage Approach for Detection and Reduction of Motion Artifacts in Photoplethysmographic Data. Biomedical Engineering, IEEE Transactions on, 2010. 57(8): p. 1867-1876.
17. Yao, J. and S. Warren, A short study to assess the potential of independent component analysis for motion artifact separation in wearable pulse oximeter signals. Conf Proc IEEE Eng Med Biol Soc, 2005. 4: p. 3585-8.
18. Fukushima, H., et al., Estimating heart rate using wrist-type Photoplethysmography and acceleration sensor while running. Conf Proc IEEE Eng Med Biol Soc, 2012. 2012: p. 2901-4.
19. Boreom Lee, J.H., Hyun Jae Baek, Jae Hyuk Shin, Kwang Suk Park and Won Jin Yi, Improved elimination of motion artifacts from a photoplethysmographic signal using a Kalman smoother with simultaneous accelerometry. Physiological Measurement, 2010. 31(12): p. 1585.
20. Zhilin, Z., P. Zhouyue, and L. Benyuan, TROIKA: A General Framework for Heart Rate Monitoring Using Wrist-Type Photoplethysmographic Signals During Intensive Physical Exercise. Biomedical Engineering, IEEE Transactions on, 2015. 62(2): p. 522-531.
21. Zhang, Z., Photoplethysmography-Based Heart Rate Monitoring in Physical Activities via Joint Sparse Spectrum Reconstruction. Biomedical Engineering, IEEE Transactions on, 2015. PP(99): p. 1-1.

22. Wang, H., et al., A high resolution approach to estimating time-frequency spectra and their amplitudes. Ann Biomed Eng, 2006. 34(2): p. 326-38.
23. Shi Z, J.G., Li T Pulse Oxyhemoglobin Desaturation Index for the Screening of Obstructive Sleep Apnea Syndrome. Scientific Reports, 2012. 233(1).
24. Reddy, K.A., et al. A Novel Method of Measurement of Oxygen Saturation in Arterial Blood. in Instrumentation and Measurement Technology Conference Proceedings, 2008. IMTC 2008. IEEE. 2008.
25. Reddy, K.A., et al., A Novel Calibration-Free Method of Measurement of Oxygen Saturation in Arterial Blood. Instrumentation and Measurement, IEEE Transactions on, 2009. 58(5): p. 1699-1705.

Chapter 10: SpaMA – A Novel Motion and Noise Artifact Reduction for HR Reconstruction from PPG Recordings

10.1. Introduction

In this chapter another time-frequency based signal reconstruction algorithm is presented that also use accelerometer information in frequency domain in order to compensate for the corruption that is caused by motion and noise artifact. Acceleration data are shown to be helpful to remove MA. For example, Fukushima et al. [24] suggested a spectral subtraction technique to remove the spectrum of acceleration data from that of a PPG signal. Acceleration data can be also used to reconstruct the observation model for Kalman filtering [25] to remove MA. Recently, Temko proposed an approach to HR estimation based on Wiener Filtering and the Phase Vocoder (WFPV) [28]. This work showed that WFPV on average can perform better than the JOSS algorithm. The main idea of WFPV is to estimate motion artifacts from accelerometer signals and then use a Weiner filter to attenuate the motion components in the PPG signal. Phase vocoder is also applied to overcome the limited resolution of the Fourier transform and to refine the initial dominant frequency estimation.

In this chapter, a new HR and also PPG signal reconstruction approach is presented using time-varying spectral analysis. The algorithm is called SpaMA and is comprised of five distinct stages: (1) time-varying power spectral density (PSD) calculation, (2) spectral filtering, (3) Motion Artifact detection, (4) HR reconstruction and (5) signal reconstruction. The idea is to calculate a window-segmented power spectral density of both PPG and accelerometer signals in real-time to scale each estimate of the PSD by the equivalent noise bandwidth of the window [29].

The simplest way to approach the first step, the PSD calculation, would be to employ a periodogram. However, it has the drawbacks that it is an inconsistent spectrum estimator, has high variance, and has leakage effects [29]. Thus, a dominant spectral peak can lead to an estimated spectrum that contains

power in frequency bands where there should be no power. However, both problems can be solved by down-sampling the raw signal and then using a sufficiently small frequency step by setting a large number of frequency points. Thus, in this study we resample the signal from the original sampling frequency to 1/4 of it and then we apply the periodogram algorithm with frequency resolution of 0.001. Next, we limit the spectrum to the heart rate frequency range of [0.5Hz – 3 Hz] and take the frequency and power information of the first three peaks in the PSD at each window and signal segment. We are assuming that the heart rate component in a typical clean (motion free) PPG signal is always the dominant frequency component in the time-varying power spectrum, thus, the highest peak of the spectrum corresponds to the HR frequency. Thus, when movement happens the dominant component can be replaced by movement components which shift the HR to the second or third peak in the spectrum. So the third phase of the SpaMA algorithm is to compare the first 3 peaks and corresponding frequencies of the PPG spectrum to the first peak and frequency of the accelerometers' spectra at each window and the idea is to choose the frequency components (out of three) that are different from the accelerometers' frequency. We are assuming that when there is coherence between a spectral peak in the PPG and the accelerometers' spectra this signifies a motion noise artifact in the PPG signal and that peak should be discarded in the HR reconstruction. After discarding these movement peaks in the spectrum, the next highest peak that is closest to the estimated HR of the previous window would be chosen at each window. By reconstructing the HR frequency at each window, simultaneously we can reconstruct the PPG signal by using the power, frequency and phase of the signal that corresponds to the HR frequency. That is, we reconstruct time-domain signals from the time-frequency domain. We will show in the Results section that the new SpaMA method not only provides PPG signal and HR reconstruction but also the potential to do heart rate variability analysis on the results. We will show that SpaMA can outperform the JOSS technique in heart rate estimation by providing less error to the reference, which yields higher accuracy.

10.2. Materials and Experiments

The SpaMA algorithm was evaluated on three different datasets. The first two datasets were provided for the IEEE Signal Processing Cup and are publically available. The three datasets are: 1.) 12 PPG training datasets (running on treadmill) from an IEEE signal processing competition [30] which was initially used in [26, 27], 2.) 11 PPG test datasets (e.g. arm exercise) from the IEEE signal processing competition and 3.) 10 PPG recordings from the Chon lab (running on treadmill).

IEEE Signal Processing Competition Training Dataset: A single-channel PPG signal, a three-axis acceleration signal, and an ECG signal simultaneously recorded from 12 Asian male subjects ranging in age from 18 to 35. For each subject, the PPG signal was recorded from their wrist using a pulse oximeter (PO) with green LED (wavelength: 609 nm). The acceleration signal was also recorded from their wrist using a three-axis accelerometer. Both the PO and the accelerometer were embedded in a wristband, which was comfortably worn. The ECG signal was recorded from the chest and it is used as the reference heart rate. All signals were sampled at 125 Hz.

IEEE Signal Processing Competition Test Dataset: The dataset consists of 11 five minute recordings which were collected from 19 to 58 year old subjects performing intensive arm movements (e.g. boxing). For each subject, PPG signals were recorded from their wrist using a pulse oximeter with green LEDs (wavelength: 515nm). The acceleration signal was also recorded from their wrist using a three-axis accelerometer. Both the PO and the accelerometer were embedded in a wristband. An ECG signal was recorded simultaneously from their chest using wet ECG sensors. All signals were sampled at 125 Hz and sent to a nearby computer via Bluetooth.

Chon Lab Dataset: This dataset was recorded in the Chon Lab from 10 healthy subjects (9 male/1 female), with ages ranging from 26 to 55. For each subject, the PPG signal was recorded from their forehead using a PO (developed in our lab) with red and infrared LED (wavelength: 660 and 940 nm). The acceleration signal was also recorded from their forehead using a three-axis accelerometer.

Table 10.1. PPG Datasets and Experiments Settings

Subject	Dataset	Activity Type	Pulse Oximeter Type	Subject's Age/Sex
1	1 (IEEE Cup)	Type (1)	Wrist: green LED (wavelength: 609nm)	18-38 y (All Male)
2				
3				
4				
5				
6				
7				
8				
9				
10				
11				
12				
13	2 (IEEE Cup)	Type (2)	Wrist: green LED (wavelength: 515nm)	19-58 y (9 Male, 1 Female)
14				
15				
16		Type (3)		
17				
18				
19				
20		Type (2)		
21		Type (3)		
22				
23		Type (2)		
24	3 (Chon Lab)	Type (4)	Forehead: Red and Infrared LED (wavelength: 660 nm, 940nm)	26-55 y (9 Male, 1 Female)
25				
26				
27				
28				
29				
30				
31				
32				
33				

Both the pulse oximeter and the accelerometer were embedded in a headband and the signals were sampled at 80 Hz. The ECG signal was recorded as a reference from the chest using ECG sensors, sampled at 400Hz. During data recording, subjects walked, jogged and ran on a treadmill with speeds of 3, 5 and 7 mph, respectively, for 9 min. At the end, all experimental subjects were asked to perform random arbitrary movements for 1 min.

For all three datasets, we down-sampled the data to ¼ of original sampling rate. This helps to increase the frequency resolution in time-frequency spectrum. Further details of this study's databases are given in Table (1). Four types of activities were involved:

Type (1): activity involved walking or running on a treadmill for intervals of 0.5m-1m-1m-1m-1m-0.5m with speeds of 1-2 km/h, 6-8 km/h, 12-15 km/h, 6-8 km/h, 12-15 km/h, 1-2 km/h, respectively. The subjects were asked to purposely move the hand with the wristband to generate motion artifacts.

Type (2): activity included various forearm and upper arm exercise which are common arm motions (e.g. shaking hands, stretching, pushing objects, running, jumping, and push-ups).

Type (3): activity consisted of intensive forearm and upper arm movements (e.g. boxing).

Type (4): activity involved 1 min rest, 1 min walking (3 mph), 1 min rest, 2 min jogging (5 mph), 1 min rest, 2 min running (7 mph), 1 min rest, 1 min arbitrary movement. The ECG-based reference HR was recorded in order to assess the performance of the algorithms being tested.

In summary, the first dataset includes only Type (1), the second dataset includes both Type (1) and (2) activities, and the third dataset includes only Type (4) activities.

10.3. Methodology

The procedure for our new HR monitoring algorithm during intensive movements is presented in Table (2). Details of each stage will be described in subsections 1 to 5.

10.3.1. Time-Varying Spectral Analysis of PPG and Accelerometer Data

We produce a time-varying spectrum by taking a T-sec window of the signal and computing the power spectral density (PSD) of the segment and then sliding the window through the whole dataset which yields a time-frequency matrix in which each array represents the power of the signal corresponding to a specific frequency and sliding time-step (shift) of S-sec.

Table 10.2. The proposed SpaMA algorithm: HR and PPG signal reconstruction

Stage 1. Time-Varying Spectral analysis

1.1. Down sample the PPG and Accelerometer signal to 20 Hz.
1.2. Compute the power spectral density of both PPG and Accelerometers [0-10 Hz].

Stage 2. Spectral Filtering

2.1. Assume HR to be in the frequency range of [0.5Hz – 3Hz], this accounts for both low and high heart rates.
2.2. The first highest three peaks and their corresponding frequencies in the PPG filtered spectrum are assumed to have HR information.
2.3. Only the largest frequency peak of the accelerometers' spectra is used for MA detection in stage 3.

Stage 3. Motion Artifact Detection

3.1. Compare the frequencies of the three peaks in the PPG spectrum with the frequency of the largest peak in the accelerometers' spectra. If the first or second largest peaks in the PPG spectrum are similar to that of the accelerometers' peaks, then motion artifact is present in the PPG.
3.2. If motion artifact is detected from 3.1, then the corresponding frequency peak (usually the first or second largest peak) in the PPG spectrum should be discarded.

Stage 4. Heart Rate Tracking and Extraction from PPG Spectrum

Case (1): From 3.1- if the spectrum is corrupted by movement and only the first largest peak is corrupted, then the HR frequency should be the frequency of the second peak in the spectrum.
Case (2): From 3.1- if the spectrum is corrupted by movement and both the first and second largest peaks have similar frequencies to those of the accelerometers' peaks, then the HR frequency should be the frequency of the third peak in the spectrum.
Case (3): Due to a gap between the pulse oximeter and a subject's skin, the HR frequency cannot be extracted from the spectrum and in this case the previous HR frequency is used or for offline implementation a cubic spline interpolation can be applied to fill in the missing HR information.

Stage 5. PPG Signal Reconstruction

6.1. The PPG signal is reconstructed by using the amplitude, frequency and phase information corresponding to the HR components (extracted in stage 4) that are calculated from the spectrum at each window.

- Heart Rate Variability Analysis

By using a sample-by-sample windowing strategy, HR can be extracted, from which dynamics of heart rate variability analysis can be obtained on the motion artifact-removed reconstructed HR time series.

The sliding process and frequency step specify the resolution and dimension of the time-frequency matrix. In this study, we take two different sliding window approaches depending on the application. For estimating either heart rates or heart rate variability, data are shifted sample-by-sample with no overlap for the entire dataset. This is because we are interested in capturing beat-to-beat dynamics of HRV which requires sample-to-sample estimation of PSD. Given our down-sampled data, each data point is shifted by 0.05 seconds. For estimating only the heart rates, we shift the data segment-by-segment rather than sample-by-sample. This coarse-grain windowing approach has less computational cost and it can provide good tracking of heart rates, but it cannot be used for HRV. The window segment length T was set to 8 seconds and was shifted (S) by 2 seconds. We chose the 8 second data segment and the shift of 2 seconds because one of the goals of this work is to compare our algorithm's results to other algorithms which have used this chosen data segment length and time shift. Moreover, the assumption of 8 second data length largely stems from the fact that heart rates do not change instantaneously, hence, an 8 second duration is a reasonable choice.

As a representative example, the resultant frequency components in the time-frequency matrix of recordings from subject #8 from the competition training dataset, for a window length of 8 seconds that is shifted by every 2 seconds, is shown in Fig. 1.

The panels of Fig. 1a and 1b show a PPG time series and the z-axis accelerometer data, respectively. From the upper left panel of Fig. 1c, which represents the time-frequency plot of the PPG signal, it is observed that there are three dominant frequency components - one of them represents HR and the other two are similar to those of the accelerometers' spectra shown in the upper right and lower left and right panels of Fig. 1c. This figure illustrates 4 motion artifact elements (A, B, C, D) that are present in exactly the same areas among all spectra.

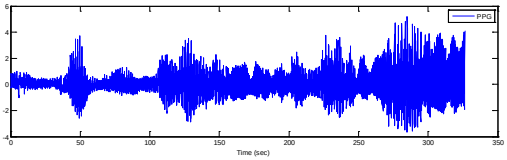

(a)

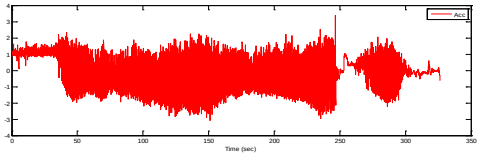

(b)

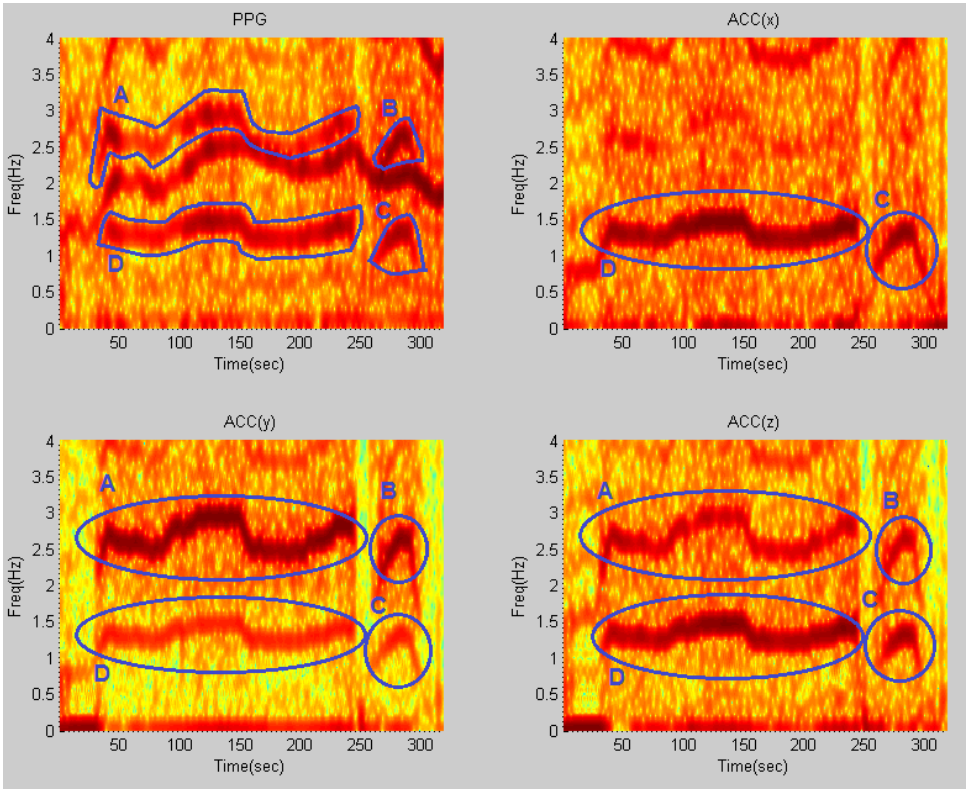

(c)

Figure 10.1 - Time-Frequency spectra of recording #8 from dataset (1) : (a) PPG signal, (b) simultaneous Accelerometer-Z signal, (c) (Top-Left) TF spectrum of PPG, (Top-Right) TF spectrum of ACC(x), (Bottom-Left) TF spectrum of ACC(y), (Bottom-Right) TF spectrum of ACC(z); all computed from stage (1) of the algorithm. Blue circles and letters represent movement elements in all four spectra.

By comparing the time-frequency (TF) spectrum of PPG to those of the accelerometers' spectra, we can detect that the marked dynamics (A, B, C and D) in the PPG spectrum shares the same frequency dynamics as those of the accelerometer spectra marked in circles. Hence, both the top and bottom marked

lines in the PPG spectrum most likely represent the motion artifacts, and the unmarked frequency represents the HR. The next section details how these motion artifact frequency dynamics are detected and filtered.

10.3.2. Spectral Filtering

After obtaining the power spectral density at each window, HR frequency is assumed to be confined in the range [0.5 Hz – 3 Hz], which takes into account both at rest and high HR due to either tachycardia or exercise scenarios. Hence, for HR estimation, the strategy is to eliminate frequencies that are outside of this HR frequency range as they are most likely due to motion artifacts or harmonics of the HR frequency.

In general, HR frequency in the power spectral density of PPG at each window can have three different scenarios: (1) PPG is devoid of MA and there is no spatial gap between the sensor and the subject's skin during recording, (2) PPG is corrupted by MA and there is no spatial gap between the sensor and the subject's skin during recording and (3) There is a spatial gap between the sensor and the subject's skin during recording. For the ideal case (1), HR can be extracted and it is most likely represented as the highest peak in the PPG spectrum. For case (2), MA dynamics can result in the dominant peak and HR frequency peak's magnitude become smaller than the MA frequency peak in the power spectrum. The frequency to the first highest peak in time-frequency of a MNA free PPG signal belongs to HR. When movement happens this highest peak can be replaced by motion frequency component and HR would be shifted to next peaks. Depending on the direction of movement at each time at most only two of three dimensions of movements changes the frequency of PPG which in worst case the first two highest peaks in the spectrum could belong to movement and so the HR will be the third one. The only scenario that makes it difficult to extract HR from the spectrum is scenario (3) when there is a spatial gap between the PPG sensor and the subject's skin during recording. In this scenario, assuming that the motion artifacts are short lasting, the missing HR values can be interpolated using the cubic spline approach.

Fig. 2 shows a representative filtered time-frequency spectral plot of a PPG signal. This step in the SpaMA process involves retaining only the three largest frequency peaks at each time point within

the defined HR range (30-180 bpm) and they are represented as blue, green and red colors, respectively. It is our opinion that retaining only the three largest frequency peaks at each time point is reasonable for the first two cases as outlined above.

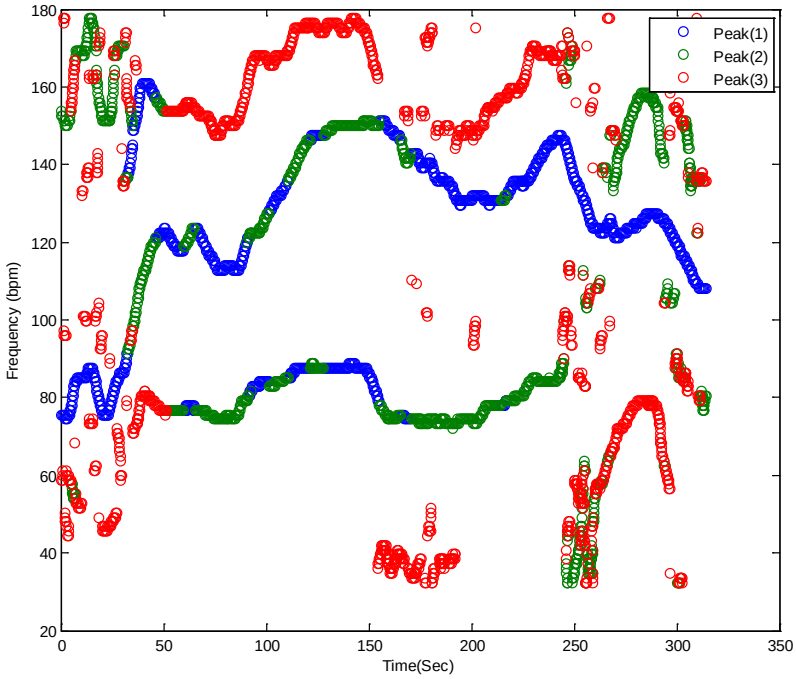

Figure 10.2 - Spectral Filtering. PPG time-frequency spectrum: Blue, Green and Red circles correspond to the first three highest peaks in the defined HR frequency range of (30-180 bpm), respectively, at each sliding window.

10.3.3. Motion Artifact Detection

Fig. 3a illustrates a PPG spectrum which is identical to Fig. 2, but it also identifies the frequencies associated with accelerometers, as marked by the shaded areas and the letters A-D, in the top left and two bottom panels of Fig. 1c. By removing the accelerometers' related frequencies in Fig. 3a, the remaining frequency dynamics which should represent HR frequency and its harmonics are shown in Fig. 3b.

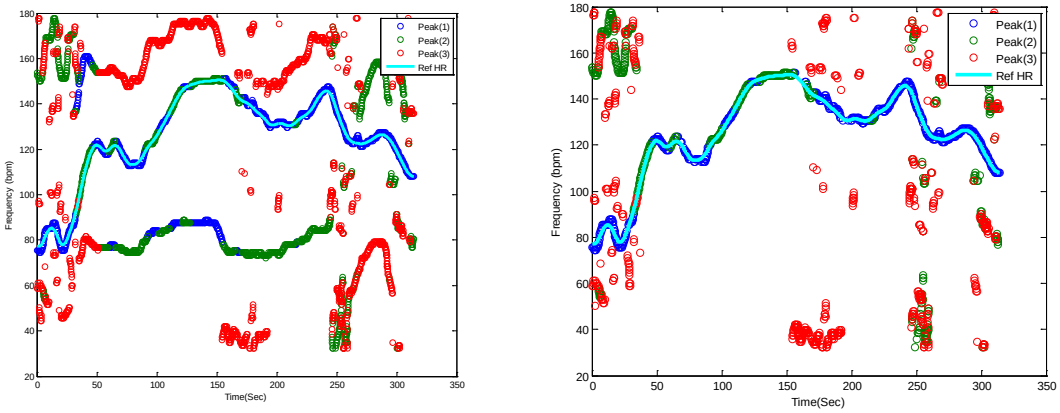

(a) (b)

Figure 10.3 - Motion Artifact Detection in the PPG spectrum. (a) Filtered PPG spectrum with movement and HR components: Shaded yellow elements (A, B, C, D) represent motion frequency components in the PPG spectrum, and the light blue line is the reference HR from clean reference ECG signal, (b) Filtered PPG spectrum after removing motion artifact frequency components.

10.3.4. Heart Rate Tracking & Extraction

The next step is to identify HR frequencies with time from Fig. 3b. Note that in Fig. 3b, there are three peaks at each time instance, thus, the question is how to identify which of the three peaks represents the HR at each time point. For the initial time window of 8 seconds, we require a clean data segment so that true HR can be determined. This scenario is case (1) described above in the spectral filtering section, and the detection of HR is simply the highest peak in the spectrum. The next step is to estimate HR for each sliding window of data. At this step of the algorithm, the goal is to choose a HR peak in the PPG spectrum with the knowledge of estimated HR values in previous time windows. In this step there are two main scenarios: (1) no peak exists in the spectrum that can represent HR, and (2) there is a spectral peak among the first three highest peaks of spectrum that belongs to the HR component. In case (1), where HR is not detectable in the window (e.g. due to spatial gap between the PO sensor and skin), in real-time implementation the algorithm takes the previous window's HR value as the current HR (or simply uses the moving average of several past HR beats or some other variant), however in offline processing, a cubic

spline interpolation can be used to fill in the missing HR information. In the more general case (2), where the HR peak is among the first three highest peaks in the spectrum, three possible scenarios can occur: (2-A) the windowed PPG signal is clean and the first highest peak in the spectrum represents the HR fundamental frequency, (2-B) the windowed PPG signal is corrupted by movement and at most two of the spectral peaks represent the accelerometers' frequency components, thus the second or the third peak corresponds to HR, (2-C) while the HR spectral peak is detectable, the difference between its value and that of the previous HR is more than 10 bpm, so it will be replaced by the most recent HR value from a previous window segment (or a moving average of several past HR beats or some other variant). We set a criterion that the HR value cannot change more than 10 BPM from a previous time window. In Fig. 3b, these cases are illustrated. For example, in most cases, the blue circle which represents the largest spectral peak is chosen but in other cases, either green or red circles are chosen for certain time points. For the HR peaks associated with either the green or red circles, they are chosen because either the first two highest peaks are related to accelerometers or the highest magnitude peak deviates more than 10 BPM from the previous HR value. Fig. 4 summarizes the flowchart of HR tracking and extraction procedures.

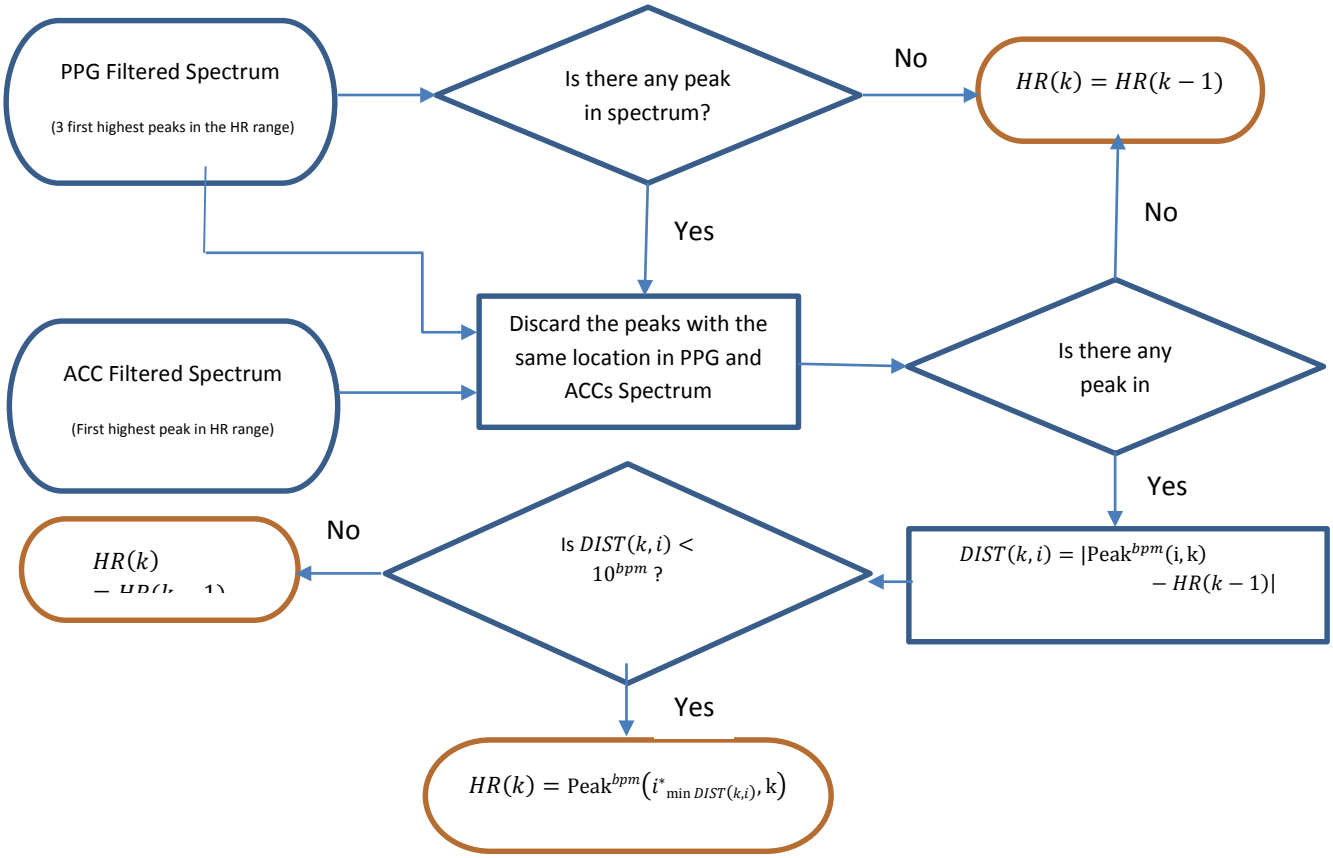

Figure 10.4 - Flowchart of HR Tracking and Extraction

Fig.5 shows the extracted HR (red color) from PPG spectra of recording#8 from the competition training dataset using our proposed approach along with the reference ECG-derived HR (black color). In order to calculate the performance of the SpaMA algorithm, the error value in each time window was calculated from the estimated HR to the reference ECG-derived HR. Two measurement indices of absolute error similar to the indices in [22] were used.

$$Error(1) = \frac{1}{W}\sum_{k=1}^{w}\left|HR_{SpaMA}(k) - HR_{ref}(k)\right| \quad (1)$$

$$Error(2) = \frac{1}{W}\sum_{k=1}^{w}\frac{\left|HR_{SpaMA}(k) - HR_{ref}(k)\right|}{HR_{ref}(k)} \times 100\% \quad (2)$$

where W is the total number of windows.

10.3.5. PPG Signal Reconstruction for HRV analysis

For HRV analysis application, the above-described procedures are identical but the only difference is the beat-by-beat shift of data rather than the 8 second data segment shift or its variant. The PPG signal can now be reconstructed using heart rate frequency, amplitude and phase changes, window-by-window using the sample-by-sample windowing process:

$$Rec_{Signal}(k) = A_{HR}(k) \times \sin\left(2\pi t(k) f_{HR}(k) + \varphi_{HR}(k)\right) \quad (3)$$

where $k = 1, \ldots, N$ and N is number of signal samples and total number of windows. $A_{HR}(k)$ and $\varphi_{HR}(k)$ are calculated according to the power of the signal for HR frequencies in the PSD and phase angles of complex elements in the FFT matrix that correspond to HR frequencies.

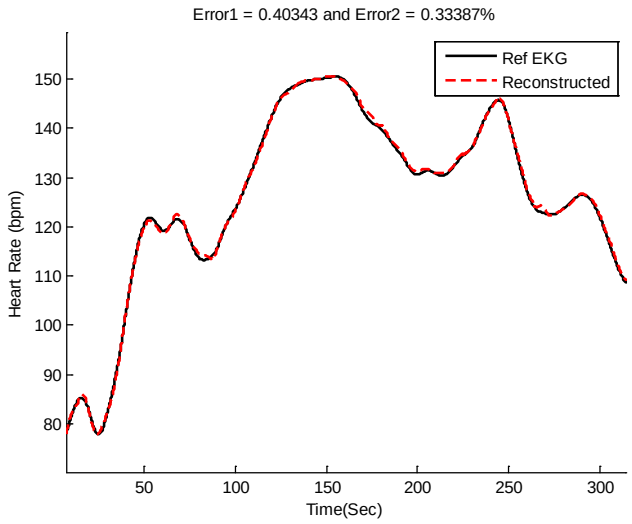

Figure 10.5 - Comparison of reconstructed HR obtained from SpaMA to reference HR obtained from simultaneous ECG recordings.

The left and right panels of Fig. 6 show the reconstructed PPG versus the original PPG and their HRV time series, respectively. Fig. 7 shows comparison of HRV spectra between the reference and the

reconstructed HRV time series from the MA-contaminated PPG signal for dataset #8. Note that for computing HRV, we are not concerned about matching the amplitude of the reference HR, as we are interested only in the dynamics of the fluctuations in the heart rates. Since we are tracking the beat-to-beat HR in time-frequency domain, we can only calculate the frequency-domain indices of HRV that is with the proposed method we are not able to provide time-domain HRV analysis like SDNN.

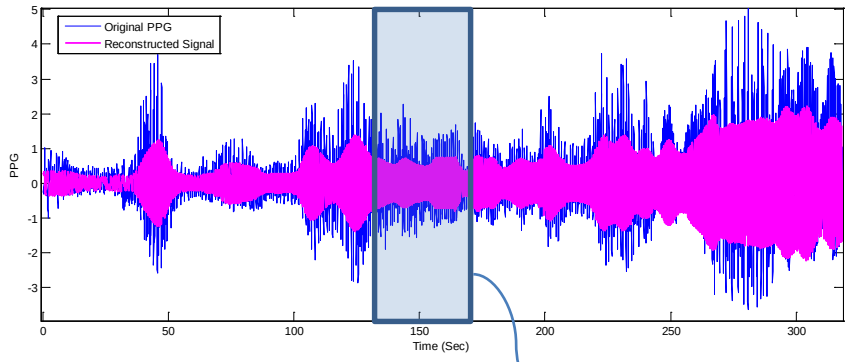

(a)

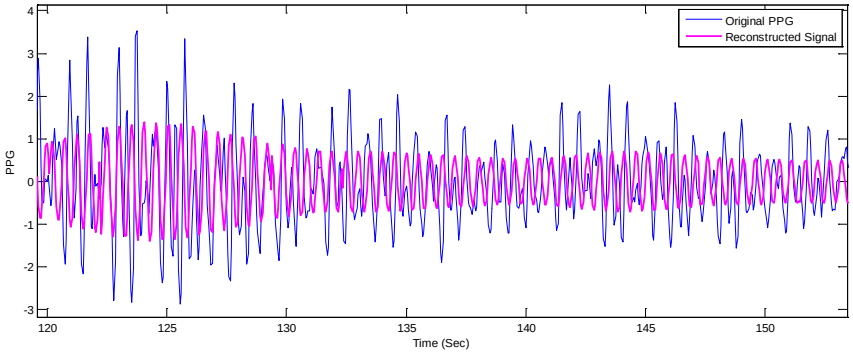

(b)

Figure 10.6 - PPG signal reconstruction. (a) Comparison between reconstructed PPG and original recording #8 from IEEE competition training dataset, (b) Zoomed-in version of (a)

Given that we are able to estimate quite accurate heart rates, it is not surprising to observe similar frequency dynamics between the reference and reconstructed HRV time series.

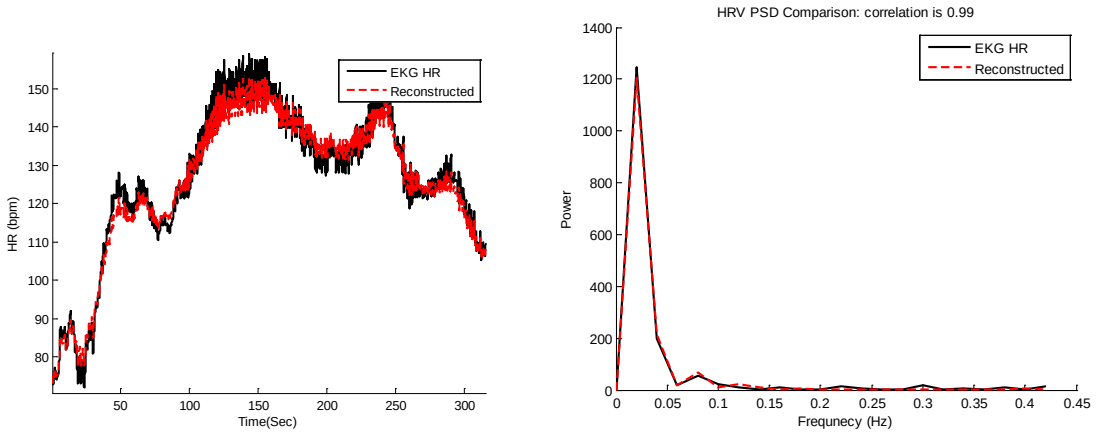

(a) (b)

Figure 10.7 - Heart Rate Variability Analysis (a) Time-domain comparison of reconstructed and reference HR. (b) Spectral comparison of heart rate variability between reconstructed HR and reference HR calculated from the reference ECG using Pan & Tompkins peak detection approach [31].

10.4. Results

Table 3 represents the average absolute error (E1) and the average absolute error percentage (E2) of the proposed SpaMA algorithm on all 3 datasets, respectively. Our SpaMA algorithm is compared to three recently-developed algorithms: TROIKA, JOSS and WFPV. The results in Table 3 show that SpaMA has better performance than JOSS and TROIKA for all 12 subjects in the first datasets. In comparison to WFPV, the proposed SpaMA approach outperforms WFPV on average across all 23 subjects in both datasets (1) and (2). The total average of E1 of SpaMA is less than 2 beats per minutes for all 33 subjects. The average of E1 across the treadmill experiment recordings (activity Type 1- IEEE dataset and Type 4- Chon Lab dataset) is around 1 beat per minute for all 22 subjects.

Figs. 8-10 show the reconstructed HR and corresponding PSD of a sample-sample windowed HR in comparison to the reference HR from ECG. The results for recording #9 from the first dataset (IEEE Competition Training dataset) and activity Type 1 (e.g. running on treadmill) are shown in Fig.8. We can

see that the E1 for this particular subject is as low as 0.4 bpm and the correlation between the PSD of reconstructed HR and reference HR is as high as 96%.

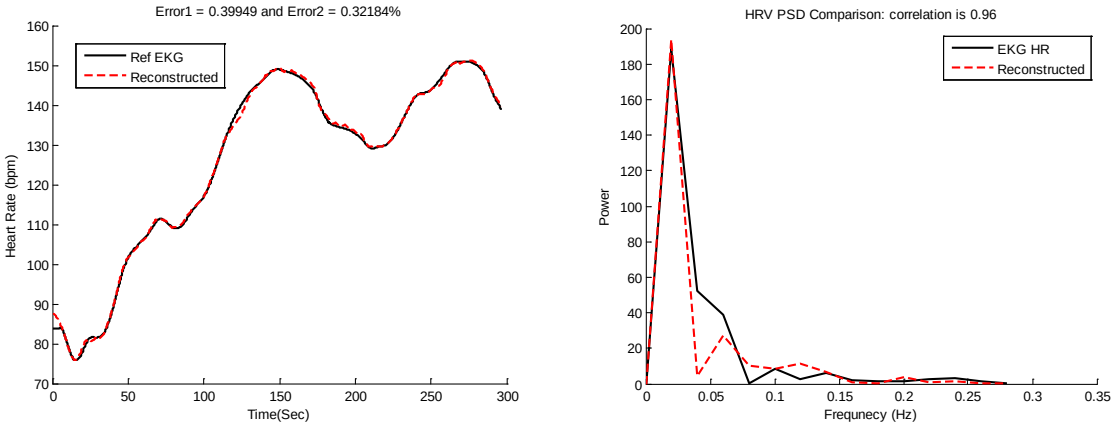

(a) (b)

Figure 10.8 - Subject 9 (IEEE Competition Training Dataset). (a) Reconstructed HR vs. reference HR. (b) Spectral comparison of reconstructed HR and reference HR (estimated from reference ECG)

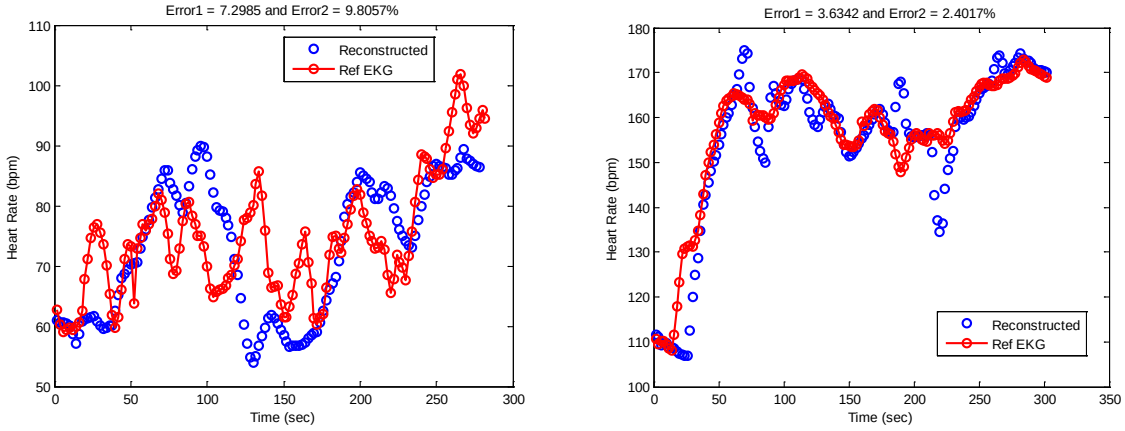

(a) (b)

Figure 10.9 - Reconstructed HR vs. reference HR: (a) Subject 14 (IEEE Competition Test Dataset). (b) Subject 16 (IEEE Competition Test Dataset).

Fig. 9a illustrates the comparison between the reconstructed HR and the reference HR for subject #14 which has the highest errors. Subject #14 belongs to the second dataset (IEEE Competition Test dataset) and Type 2 activities (e.g. jumping).

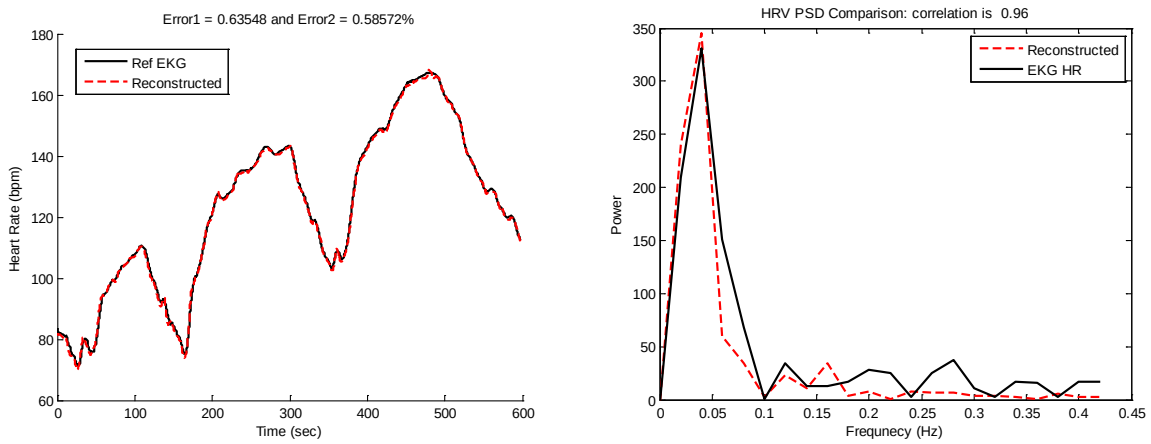

(a) (b)

Figure 10.10 - Subject 30 (Chon Lab Dataset). (a) Reconstructed HR vs. reference HR. (b) Spectral comparison of reconstructed HR and reference HR (estimated from reference ECG)

It can be seen that the largest error is obtained when both the physiological HR and the motion artifacts change rapidly so that the true HR cannot be reliably estimated. Fig. 9b shows the comparison results of reconstructed HR and reference HR for recording #16 of the second dataset (IEEE Competition Test dataset) which has the Type 3 activities (e.g. arm exercise).

The results for recording #30 from the third datasets (Chon Lab datasets) and activity Type 4 (e.g. running on treadmill) are shown in Fig. 10. It can be seen that the E1 for this subject is around 0.6 bpm and the correlation between the PSD of reconstructed HR and reference HR is as high as 99% for LF and 0.96 for HF frequency range. All subjects' results are provided in Table 4.

Table 4 represents the correlation and statistical difference using student t-test between PSD of estimated and reference HRV in both LF (0.04-0.15 Hz) and HF (0.15-0.4 Hz) frequency ranges. The correlation values in the table are calculated based on Pearson's linear correlation coefficient. Table 5 presents the time-domain HRV parameters of peak-to-peak intervals estimated from SpaMA in comparison to reference ECG R-R interval.

Table 10.3. SpaMA Algorithm Performance Comparison

Subject	Dataset	Activity Type	TROIKA		JOSS		WFPV		SpaMA	
			E1	**E2%**	**E1**	**E2%**	**E1**	**E2%**	**E1**	**E2%**
1	1 (IEEE Cup)	Type (1)	2.87	2.18	1.33	1.19	1.23	-	**1.23**	**1.14**
2			2.75	2.37	1.75	1.66	1.26	-	1.59	1.30
3			1.91	1.50	1.47	1.27	0.72	-	**0.57**	**0.45**
4			2.25	2.00	1.48	1.41	0.98	-	**0.44**	**0.31**
5			1.69	1.22	0.69	0.51	0.75	-	**0.47**	**0.31**
6			3.16	2.51	1.32	1.09	0.91	-	**0.61**	**0.45**
7			1.72	1.27	0.71	0.54	0.67	-	**0.54**	**0.40**
8			1.83	1.47	0.56	0.47	0.91	-	**0.40**	**0.33**
9			1.58	1.28	0.49	0.41	0.54	-	**0.40**	**0.32**
10			4.00	2.49	3.81	2.43	2.61	-	2.63	1.59
11			1.96	1.29	0.78	0.51	0.94	-	**0.64**	**0.42**
12			3.33	2.30	1.04	0.81	0.98	-	1.20	0.86
mean±std			2.42±0.8	1.82±0.5	1.28±0.9	1.02±0.6	1.04±0.5	-	**0.89±0. 6**	**0.65±0.4**
13	2 (IEEE Cup)	Type (2)					3.58	-	**3.41**	**4.25**
14							9.66	-	**7.29**	**9.80**
15							2.31	-	2.73	2.21
16		Type (3)					4.93	-	**3.18**	**2.11**
17							3.07	-	**3.01**	**2.52**
18							2.67	-	4.46	3.23
19							3.11	-	3.58	3.98
20		Type (2)					2.10	-	**1.94**	**1.66**
21		Type (3)					3.22	-	**2.56**	**2.02**
22							4.35	-	**3.12**	**3.28**
23		Type (2)					0.75	-	1.72	1.97
mean±std							3.61±2.2	-	**3.36±1.5**	**3.33±2.2**
Type (1,2) mean±std							2.27±2.0	-	**1.93±2.0**	**2.07±1.7**
24	3 (Chon Lab)	Type (4)							**0.88**	**0.91**
25									**1.03**	**0.83**
26									**1.10**	**0.90**
27									**1.64**	**1.54**
28									**1.41**	**1.12**
29									**0.82**	**0.70**
30									**0.63**	**0.58**
31									**4.78**	**3.87**
32									**0.95**	**0.79**
33									**0.62**	**0.52**
mean±std									**1.38±1.2**	**1.17±1.0**
Total: mean±std									**1.86±1.6**	**1.70±1.8**

Table 10.4. Frequency Domain HRV analysis Comparison: PSD of estimated vs. reference

Subjects	Correlation	
	LF[1]	HF
1	0.99	0.98
2	0.99	0.96
3	0.99	0.95*[2]
4	1.00	0.99
5	1.00	0.99
6	0.99	0.96*
7	0.98	0.92*
8	0.97	0.90*
9	1.00	0.99
10	1.00	0.99
mean	0.99	0.96

Table 10.5. Time Domain HRV analysis Comparison: estimated vs. reference HRV

Subjects	SDNN		meanNN		RMSSD*		pNN50	
	SpaMA	Reference	SpaMA	Reference	SpaMA	Reference	SpaMA	Reference
1	2620.75	2566.47	10481.89	10480.72	33.24	18.05	0.001	0.020
2	2115.44	2079.58	9908.00	10020.00	25.93	16.32	0.011	0.019
3	3173.73	3177.68	10764.20	10829.06	89.70	56.15	0.019	0.207
4	2517.78	2533.20	10376.95	10426.26	13.54	19.58	0.001	0.030
5	2654.42	2670.32	10846.04	10990.08	11.88	18.59	0.003	0.018
6	2012.53	1974.65	9737.35	9827.63	39.64	21.17	0.004	0.025
7	3056.36	2925.19	12519.74	13134.05	27.66	30.61	0.015	0.071
8	3133.76	2756.66	10504.00	10530.00	32.57	36.38	0.002	0.003
9	2195.08	2142.53	10499.81	10470.06	8.23	13.01	0.002	0.004
10	2454.57	2406.96	12936.62	12981.21	41.52	20.28	0.006	0.024
p-value	<0.05		<0.05		>0.05		<0.05	

10.5. Discussion

In this study, a new approach (SpaMA) based on time-varying spectral analysis of the PPG signal is introduced to address Heart Rate monitoring in the real world with challenges ranging from a subject who makes sudden movements but is otherwise sedate, to intensive physical activities. The idea behind the

[1] LF is [0.04-0.15] Hz and HF is [0.15-0.4] Hz
[2] (*) indicates significantly different (P-value>0.05)

proposed SpaMA approach is to compare spectral changes in PPG and accelerometer signals. Three different datasets have been used to verify the algorithm performance. Each dataset reflects different types of activities and movements. In all of the experiments, the reference HR was calculated from an ECG signal that was collected simultaneously with the PPG signal. The estimated HR was calculated from the spectrum of PPG in 8 second time windows. It has been shown in the results section that the proposed SpaMA algorithm can be used for tracking HR changes during severe motion artifacts with an average error of just 1.86 bpm compared to that of the reference ECG; these results are superior to three other algorithms tested: TROIKA, JOSS and WFPV [26, 27, 28].

Out of 33 recordings, 23 are from a wrist pulse oximeter, and the rest of the data were recorded by a forehead pulse oximeter. The results from Table 3 show that the SpaMA algorithm can be applied to monitor HR from both wrist and forehead pulse oximeters. By comparing the performance of the algorithm for treadmill experiments (dataset 1 and dataset 3), the error is lower by almost 1 beat using a wrist pulse oximeter. However, we cannot conclude from this result that the wrist PPG provides less error than the forehead, as the experiments used different subjects and were two separate studies. The prior algorithms (TROIKA, JOSS and WFPV) were tested using only the wrist-based PPG signals as the inventors of these algorithms did not have access to forehead PPG sensors. Our algorithm, tested on data from both PPG sensor locations, proved to be effective regardless of the location of the PPG sensor.

We made several observations while analyzing the data. The tracking ability of the SpaMA algorithm decreased as the frequency changes during recordings increased. This phenomenon mostly was observed while dealing with the second set of datasets from the IEEE competition, which involved Type (2) and Type (3) activities. These types of exercises involved more abrupt movements which consequently made it more difficult to track the HR-related frequencies in the spectrum. In the three datasets that have been analyzed, recordings #10 and 14 are examples of this phenomenon.

The strength of the PPG's LED is one of the most important factors determining the SpaMA algorithm performance. Movement induces much less spectrum corruption (shift) in the PPG if the LED is sufficiently strong. A reduction in the strength of the PPG signal can also be caused by ambient light leaking into the gap between a PPG sensor and the skin surface [27]. This is because the power of the signal is dependent on the depth and reflection of the light from the pulse oximeter to the subject's skin. This gap between skin and the planar substrate where the LEDs and PD are mounted may be the result of movement during physical activities or the shape of tissue that the sensors touch. Among the three datasets, low performance for recordings #16 and 31 is the result of a weak PPG signal most likely due to a gap between the sensor and skin caused by motion artifacts.

By using the sample-by-sample windowing process, the proposed SpaMA [32] algorithm can be utilized for both Heart Rate monitoring and HRV analysis in frequency domain. From the Results section, it can be observed that the algorithm is able to estimate the low frequency (0.04-0.15Hz) better than high frequency (0.15-0.4) modes of HRV spectrum. It has long been shown that during dynamic exercise, heart rate increases due to both a parasympathetic withdrawal and an augmented sympathetic activity [33, 34]. The relative role of the two drives depends on the exercise intensity [32, 35, 36]. Analysis of HRV permits insight into this control mechanism [37]. Also, being able to do HRV analysis from PPG even during movement and physical activities would be an advantage for detecting and diagnosing many cardiovascular diseases using only PPG recordings.

The proposed SpaMA algorithm can be implemented in real time. We have found that the algorithm takes only 110 msec on data divided into 8 second segments. Therefore, given the high accuracy of the proposed approach in estimating HR despite severe motion artifacts, this method has the potential to be applicable for implementation on wearable devices such as smart watches and PPG-based fitness sensors.

References

1. Deepak Vala , D.T.P., A Survey on Ambulatory ECG and Identification of Motion Artifact. International Journal of Engineering Research and Development, 2012. 1(7): p. 38-41.
2. Achten, J. and A.E. Jeukendrup, Heart rate monitoring: applications and limitations. Sports medicine (Auckland, N.Z.), 2003. 33(7): p. 517-538.
3. Laughlin, M.H., Cardiovascular response to exercise. Am J Physiol, 1999. 277(6 Pt 2): p. S244-59.
4. F. Yazicioglu, T.T., J. Penders, I. Romero, H. Kim, P. Merken, B. Gyselinckx, H.J. Yoo, C. Van Hoof. Ultra-low-power wireless sensor nodes. in Proceedings of the 31st Annual International Conference of the IEEE EMBS. 2009. Minneapolis: IEEE.
5. J. Penders, J.v.d.M., M. Altini, F. Yazicioglu and C. Van Hoof. A low-power wireless ECG necklace for reliable cardiac activity monitoring on-the-move. in Proceedings of the International Conference of the IEEE Engineering in Medicine and Biology Society. 2011. IEEE.
6. Aubert, A.E., B. Seps, and F. Beckers, Heart rate variability in athletes. Sports Med, 2003. 33(12): p. 889-919.
7. Kearney, K., C. Thomas, and E. McAdams. Quantification of Motion Artifact in ECG Electrode Design. in Engineering in Medicine and Biology Society, 2007. EMBS 2007. 29th Annual International Conference of the IEEE. 2007.
8. Friesen, G.M., et al., A comparison of the noise sensitivity of nine QRS detection algorithms. Biomedical Engineering, IEEE Transactions on, 1990. 37(1): p. 85-98.
9. Thakor, N.V. and Y.S. Zhu, Applications of adaptive filtering to ECG analysis: noise cancellation and arrhythmia detection. IEEE Trans Biomed Eng, 1991. 38(8): p. 785-94.
10. Webster, N.T.a.J. The origin of skin potential and its variations. in Proc. Ann. Conf. Eng. Biol. Med
    1978.
11. Edelberg, R., Local electrical response of the skin to deformation. J Appl Physiol, 1973. 34(3): p. 334-40.
12. Muhlsteff, J. and O. Such. Dry electrodes for monitoring of vital signs in functional textiles. in Engineering in Medicine and Biology Society, 2004. IEMBS '04. 26th Annual International Conference of the IEEE. 2004.
13. Comert, A. and J. Hyttinen, Investigating the possible effect of electrode support structure on motion artifact in wearable bioelectric signal monitoring. Biomed Eng Online, 2015. 14: p. 44.
14. Afonso, V.X., et al., Comparing stress ECG enhancement algorithms. Engineering in Medicine and Biology Magazine, IEEE, 1996. 15(3): p. 37-44.

15. P., A. Separating cardiac and muscular ECG components using adaptive modelling in time-frequency domain. in Proc. of the WACBE World Congress on Bioengineering. 2007.
16. Devlin PH, M.R., Ketchum JW., Detection electrode motion noise in ecg signals by monitoring electrode impedance. Computers in Cardiology, 1984: p. 51-56.
17. Hamilton, P.S., et al. Comparison of methods for adaptive removal of motion artifact. in Computers in Cardiology 2000. 2000.
18. Hamilton, P.S., M. Curley, and R. Aimi, Effect of adaptive motion-artifact reduction on QRS detection. Biomed Instrum Technol, 2000. 34(3): p. 197-202.
19. Tong, D.A., K.A. Bartels, and K.S. Honeyager. Adaptive reduction of motion artifact in the electrocardiogram. in Engineering in Medicine and Biology, 2002. 24th Annual Conference and the Annual Fall Meeting of the Biomedical Engineering Society EMBS/BMES Conference, 2002. Proceedings of the Second Joint. 2002.
20. Raya, M.A.D. and L.G. Sison. Adaptive noise cancelling of motion artifact in stress ECG signals using accelerometer. in Engineering in Medicine and Biology, 2002. 24th Annual Conference and the Annual Fall Meeting of the Biomedical Engineering Society EMBS/BMES Conference, 2002. Proceedings of the Second Joint. 2002.
21. Thakor, N.V. and Z. Yi-Sheng, Applications of adaptive filtering to ECG analysis: noise cancellation and arrhythmia detection. Biomedical Engineering, IEEE Transactions on, 1991. 38(8): p. 785-794.
22. Rahman, M.Z.U., R.A. Shaik, and D.V.R.K. Reddy. An Efficient Noise Cancellation Technique to Remove Noise from the ECG Signal Using Normalized Signed Regressor LMS Algorithm. in Bioinformatics and Biomedicine, 2009. BIBM '09. IEEE International Conference on. 2009.
23. Hashim, F.R., et al. Wavelet based motion artifact removal for ECG signals. in Biomedical Engineering and Sciences (IECBES), 2012 IEEE EMBS Conference on. 2012.
24. Hyvärinen, A. and E. Oja, Independent component analysis: algorithms and applications. Neural Networks, 2000. 13(4–5): p. 411-430.
25. Castells, F., A. Cebrian, and J. Millet, The role of independent component analysis in the signal processing of ECG recordings. Biomed Tech (Berl), 2007. 52(1): p. 18-24.
26. Heenam Yoon, H.K., Sungjun Kwon, Kwangsuk Park, An Automated Motion Artifact Removal Algorithm in Electrocardiogram Based on Independent Component Analysis, in The Fifth International Conference on eHealth, Telemedicine, and Social Medicine. 2013: Nice, France. p. 15-20.
27. Palaniappan R, K.T. Uni-channel PCA for noise reduction from ECG signals. 2004.
28. Chawla, M.P.S., A comparative analysis of principal component and independent component techniques for electrocardiograms. Neural Computing and Applications, 2009. 18(6): p. 539-556.

29. Jinseok, L., et al., Automatic Motion and Noise Artifact Detection in Holter ECG Data Using Empirical Mode Decomposition and Statistical Approaches. Biomedical Engineering, IEEE Transactions on, 2012. 59(6): p. 1499-1506.
30. Stoica, P. and R.L. Moses, Introduction to Spectral Analysis. 1997: Prentice Hall.
31. Yilmaz, T., R. Foster, and Y. Hao, Detecting Vital Signs with Wearable Wireless Sensors. Sensors, 2010. 10(12): p. 10837.
32. Cynthia A. Sanoski, Clinical, Economic, and Quality of Life Impact of Atrial Fibrillation FCCP, BCPS. Manag Care Pharm., 2009. 15(6-b): p. 4-9.
33. Pan J, T.W., A real-time QRS detection algorithm. IEEE Trans Biomed Eng, 1985. 32(3): p. 230-236.
34. Taji, B., et al., Impact of Skin– Electrode Interface on Electrocardiogram Measurements Using Conductive Textile Electrodes. Instrumentation and Measurement, IEEE Transactions on, 2014. 63(6): p. 1412-1422.
35. Iellamo, F., Neural mechanisms of cardiovascular regulation during exercise. Auton Neurosci, 2001. 90(1-2): p. 66-75.
36. Bernardi, L. and M.F. Piepoli, [Autonomic nervous system adaptation during physical exercise]. Ital Heart J Suppl, 2001. 2(8): p. 831-9.
37. Sarmiento, S., et al., Heart rate variability during high-intensity exercise. Journal of Systems Science and Complexity, 2013. 26(1): p. 104-116.
38. Roure, R., et al., Autonomic nervous system responses correlate with mental rehearsal in volleyball training. Eur J Appl Physiol Occup Physiol, 1998. 78(2): p. 99-108.
39. Perini, R., et al., The influence of exercise intensity on the power spectrum of heart rate variability. Eur J Appl Physiol Occup Physiol, 1990. 61(1-2): p. 143-8.
40. Posada-Quintero, H.F., et al., Low Impedance Carbon Adhesive Electrodes with Long Shelf Life. Ann Biomed Eng, 2015. 43(10): p. 2374-82.
41. Reyes, B.A., et al., Novel electrodes for underwater ECG monitoring. IEEE Trans Biomed Eng, 2014. 61(6): p. 1863-76.

Chapter 11: SegMA – A Novel Motion and Noise Artifact Reduction for HR Reconstruction from ECG Recordings

11.1. Introduction

The final algorithm that we present in this dissertation is SegMA that is ECG version of SpaMA with minor modifications.

Cardiovascular disease is the leading cause of death in the world. Considering the fact that a majority of such deaths due to cardiac arrest occur before the patient can get the needed medical care, the patient should be continuously monitored for real time detection of the events that can portend cardiac arrest [1]. The electrocardiogram (ECG) is the main measurement device for effectively diagnosing cardiovascular health, other cardio-respiratory related diseases and can be used as a guide for cardio-fitness therapy. For detecting infrequent and episodic cardiac arrhythmias, a Holter monitor is commonly used for continuous monitoring of ECG which can last more than several days. Additionally, to ensure that exercises are effective, during aerobic exercise, a heart-rate monitor provides the user with information such as the specific heart-rate zone, calories burned, and breathing rate. In addition, as a possible diagnostic outcome underlying many autonomic dysfunction, heart rate variability (HRV) information from wearable sensors including devices that use ECG will become more relevant as these wearable devices are personalized [2]. Increased HRV has been associated with lower mortality rates and is affected by both age and sex. During graded exercise, the majority of studies show that HRV decreases progressively up to moderate intensities, after which it stabilizes [3].

Wearable health monitoring systems (WHMS) enable continuous, reliable and long-term monitoring of vital signs and physiological signals during daily normal activities. Recently a variety of WHMS have also been introduced in an attempt to reduce size, improve comfort and accuracy, and extend the duration of monitoring. Product concepts and prototypes of ECG patches have been introduced by

several companies and research groups such as: Curvus, Corventis, iRhythm, Toumaz and Delta. Researchers in [4, 5] developed an ultra-low-power ECG platform and a low-power wireless ECG necklace. Samsung created a research WHMS prototype, Simband, for continuous monitoring of ECG and Electrocardiogram (ECG) signals [6]. Wearable and wireless devices allow delocalizing ECG monitoring from hospitals to home environments. Achieving reliable and high integrity recording however remains a challenge in ambulatory conditions due to the high level of noise introduced by motion artifacts. The effectiveness of WHMS can be significantly impaired by motion artifacts which contaminate the signal and that can lead to errors in estimation of cardiac parameters and trigger false alarms. For Holter systems, motion artifacts often lead to difficult interpretation of whether or not certain arrhythmia has truly occurred even when three or five different channels of ECG data are considered.

Reducing the motion artifact would extend the applicability of ambulatory monitors to situation of greater activity as encountered in most daily-life situations. Skin forms a physiological barrier for diffusion of water and ions and it is charged with a relatively high trans-dermal potential of typically -10 to -30 mV. The potential is generated by a constant ionic gradient and ionic potential of sweat glands [7]. The relatively thin (typically between 2 and 20μm) barrier has a very high resistance but allows a capacitive coupling at conventional ECG frequencies. The temporally and spatially varying skin potential accounts for the generation of low frequency noise and artifacts [7]. Noise and motion artifacts are also caused by several factors, such as baseline wander (BW), power-line interference (PLI), electromyography (EMG) noise and skin-electrode motion artifacts (MA) [8]. In practice MAs are difficult to remove because they do not have a predefined narrow frequency band and their spectrum often overlaps that of the ECG signal [9]. Several electrical models have been proposed to characterize skin-electrode interface [10-12]. The corruption introduced by motion artifacts are random variables which depend on the electrode properties, electrolyte properties, skin impedance, and the movement of the patient. Deformation in the skin produces changes in the impedance of the uppermost layers of the skin that are translated into changes in potential measured at the body surface [13]. In addition, relative motion of the electrode and skin under motion leads to a charge

deformation at the electrode-skin boundary. Consequently, development of algorithms capable of reconstructing the corrupted signal and removing artifacts is challenging.

Numerous methods for motion artifact detection and reduction have been proposed in literature. Traditional de-noising techniques are based on time averaging [14] and frequency analysis such as filter banks [14] or wavelet transforms [15]. In adaptive filtering, a filter is applied after adjusting its parameters to a time varying noise. This is particularly useful when the noise is non-stationary, like in the case of ambulatory motion artifacts. However, a reference signal has to be additionally recorded together with the ECG. Several adaptive filtering approaches have been proposed to obtain an adequate reference signal such as measurement of skin-electrode impedance [16, 17], skin stretching measured with optical sensors [17, 18] or accelerometers [19-21]. Raya and Sison [20] used an accelerometer to reduce the MA of ECG signals. However, the least mean square (LMS) and recursive least square (RLS) were unable to provide acceptable results. MA is difficult to detect because every movement of muscles are different for each person, thus a generalized algorithm that takes into account various MA features are difficult to develop. As sources of ECG and motion artifacts are uncorrelated, blind source separation (BSS) techniques could be used for separating both signals [24-26]. In order to apply BSS techniques, input signals should be linearly independent. In the case of ECG signals, a multi-lead ECG recording in which the leads are linearly independent is required. Principal Component Analysis (PCA) has been used for reducing noise in single lead ECG segmented in time intervals [27]. A combination of PCA and ICA was also proposed by Chawla [28] for ECG de-noising. Lee et al. used empirical mode decomposition (EMD) approach to detection of Motion and noise artifact for the purpose of detection of atrial fibrillation from ECG recordings [29]. The main issue with BSS algorithms is its heavy computational cost and that they are not suitable for real-time processing purposes.

In this chapter, an approach for HR and ECG signal reconstruction is presented using time-varying spectral analysis. The algorithm is called SegMA and is comprised of five distinct stages: (1) Taking derivative of downsampled ECG (2) time-varying power spectral density (PSD) calculation, (3) spectral

filtering, (4) HR reconstruction, (5) HRV analysis. The idea is to calculate a window-segmented power spectral density of both ECG and accelerometer signals in real-time to scale each estimate of the PSD by the equivalent noise bandwidth of the window [30]. The simplest way to approach the second step, the time-varying PSD calculation, would be to employ the Welch periodogram. However, it has the drawbacks that it is an inconsistent spectrum estimator, has high variance, and has leakage effects [30]. Thus, a dominant spectral peak can lead to an estimated spectrum that contains power in frequency bands where there should be no power. However, both problems can be solved by down-sampling the raw signal and taking the derivative of the data and then using a sufficiently small frequency step by setting a large number of frequency points. Thus, in this study we resample the signal from the original sampling frequency to 1/4 of it and then after taking derivative of downsampled signal we apply the periodogram algorithm with frequency resolution of 0.001. Next, we limit the spectrum to the heart rate frequency range of [0.5Hz – 3 Hz] and take the frequency and power information of the first three peaks in the PSD at each window and signal segment. We are assuming that the heart rate component in a typical clean (motion free) ECG signal is always the dominant frequency component in the time-varying power spectrum, thus, the highest peak of the spectrum corresponds to the HR frequency. Thus, when movement happens the dominant component can be replaced by movement components which shift the HR to the second peak in the spectrum. So the third phase of the SegMA algorithm is to first find two highest peaks and then choose the corresponding frequencies of the ECG to those highest powers in the spectrum. Then by adopting a tracking strategy the highest peak that is closest to the estimated HR of the previous window would be chosen at each window. We will show in the Results section that the new SegMA method not only provides ECG signal and HR reconstruction but also the potential to do heart rate variability analysis on the results. We will show that SegMA can improve HR estimations by almost 10 times better accuracy than without SegMA reconstruction.

11.2. Materials and Experiments

An experiment with a physically challenging protocol that includes 17-min ECG recordings from 10 healthy subjects was designed, in which each subject was asked to wear a wrist-worn ECG device as shown in Table (2). The wearable system is called NohChon and was custom designed in our laboratory. It consists of two wrist modules which are designed to fabricate a 1-channel ECG signal (Lead I configuration) on the top of right and left wrists. This device was designed and developed for ECG measurement based on two leads with virtual right-leg driven circuit and provides a frequency band at -3 dB from 0.05 to 150 Hz with second-order high-pass and low-pass filters to cover the full ECG range. In both modules, 3-axis accelerometric data were collected to reject MNAs using accelerometer (MMA8652FC, Freescale, TX, USA) which has a sensitivity of ±2 g. A wire was connected between both left and right wrist-based electrodes to produce an ECG signal and is threaded to a compression shirt for minimizing motion artifact than can be caused by wire movements. ECG signal was sampled at 360 Hz with 12-bit resolution over a range between 0 and 3.3 volts. Electrodes for ECG measurement are carbon black (CB) based film electrode [40, 41] as shown in Table (1) and (2). The electrode is consisted of adhesive so it enables collection of stable ECG signal even without hydrogel, and there was no complain about skin irritation from subjects. Each subject was asked to perform different types of physical activities (see Table (2)) during the experiment to investigate the performance of the algorithm in variety types of daily activities and movements. The reference ECG signals for evaluation of SegMA were recorded from a chest using Holter monitor. Table (3) present the most recent ECG wearable patches and devices in comparison to NohChon wearable module.

11.3. Methodology

The procedure for our HR monitoring algorithm during intensive movements is presented in Table (4). Details of each stage will be described in subsections 1 to 5.

Table 11.1. ECG Wearable Devices

Device	Piix (Corventis) [1]	iRhythm (Zio)	Imec ECG necklace [2]	NohChon ECG wrist
Appearance	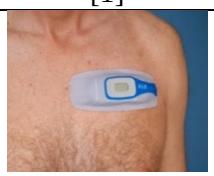		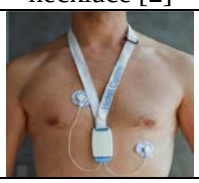	
Sensor modalities	ECG (1-lead), Respiration , Skin Temperature, Body fluids, Accelerometer	ECG (1-lead)	ECG (1-lead), Respiration, Accelerometer	ECG (1-lead), Electrodermal acitivity, Accelerometer
Sampling Frequency (ECG)	200 Hz	120 Hz	256 Hz	360 Hz
Analog front-end	Not disclosed	Not disclosed	imec ULP 1-ch ECG ASIC	Instrumentation amplifier
ADC resolution	10-bits	10-bits	12-bits	12-bits
Functionality	Event detection (Arrhythmia)	None	Beat-to-beat HR and HRV, seizure detection	Motion Artifact Reduction, Beat-to-beat HR and HRV
Wireless Connectivity	Event sent to z-link; and downloaded for off-line analysis	None	Real-time interface to mobile phone (using dongle)	Real-time interface to smart devices (using Bluetooth)
Power consumption	40 mW	Not disclosed	3 mW (data streaming); 7 mW (embedded data processing)	100 mW (data processing and transmitting via Bluetooth)
Form factor	Patch (160 mm x 60 mm)	Patch (123 mm x 53 mm)	Necklace (60 mm x 40 mm) + lead wires to disposable electrodes	Wrist bands + CB film electrodes (2.5mm x 2.5mm)
Usability	Disposable	Recycle	Disposable	Disposable

Table 11.2. ECG Datasets and Experiments Settings

Subject	Dataset	Activity Type	Setup	Subject's Age/Sex
1	3 (Chon Lab)	Depicted in Table (2)	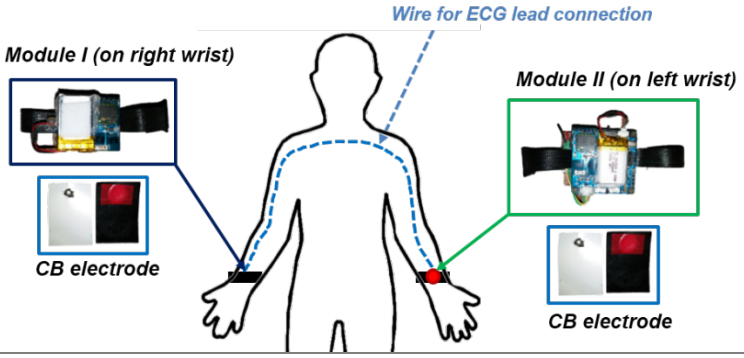	26-55 y (10 Males)
2				
3				
4				
5				
6				
7				
8				
9				
10				

Table (3) represents the experimental protocol of ECG data collection. A video of the activities each subject performed during the experiment is available from [3].

Table 11.3. Experiment Protocol

Activity Type	Rest (Supine Position)	Walking (2 mph) Jogging (4 mph) Running (6 mph)	Rest (Standing)	Standing/Sitting on a arm chair	Arm Movements (Up/Down) and (Left/Right)	Wrist Rotation/Shaking	Weight Lifting and Box Moving	Deep Breathing
Duration (min)	**5**	**1.5**	**0.5**	**0.5**	**3**	**3**	**3**	**0.5**

Table 11.4. The proposed SegMA algorithm: HR and ECG signal reconstruction

Stage 1. ECG Preprocessing

1.1. Down sample the ECG to ¼ of the original sampling rate

1.2. Compute the derivative of downsampled ECG signal.

Stage 2. Time-Varying Spectral analysis

2.1. Compute the power spectral density of preprocessed ECG data at each time window of 8 sec

Stage 3. Spectral Filtering

3.1. Assume HR to be in the frequency range of [0.5Hz – 3Hz], this accounts for both low and high heart rates.

3.2. The first highest two peaks and their corresponding frequencies in the ECG filtered spectrum are assumed to have HR information.

Stage 4. Heart Rate Tracking and Extraction from ECG Spectrum

Case (1): if the spectrum is corrupted by movement and only the first largest peak is corrupted, then the HR frequency should be the frequency of the second peak in the spectrum.

Case (2): Due to skin-electrode interface changes, the HR frequency cannot be extracted from the spectrum and in this case the previous HR frequency is used or for offline implementation a cubic spline interpolation can be applied to fill in the missing HR information.

Stage 5. Heart Rate Variability Analysis

By using a sample-by-sample windowing strategy, beat-to-beat HR can be extracted, from which dynamics of heart rate variability analysis can be obtained on the SegMA reconstructed HR time series.

11.3.1. ECG Preprocessing

The first step in SegMA algorithm is to resample ECG to ¼ of its original sampling rate. This improves the frequency resolution in the time-frequency spectrum. Next a derivative of the resampled ECG signal is computed so that the R-peaks are accentuated. The idea is by derivative of signal, motion and noise artifacts can be reduced to some extent as long as motion is not abrupt and the samples are uniformly corrupted by motion. Fig. 1 represents representative ECG recordings from both NohChon wrist device and a Holter. This figure shows the HR estimations from R-R interval of the reference and a wrist ECG. The

reference HR provides a clean and accurate HR and the estimated HR from wrist ECG signifies inaccurate HR estimation especially during running, wrist movements and weight lifting periods of experiment. This figure indicate the necessity of using a HR reconstruction approach.

11.3.2. Time-Varying Spectral Analysis of ECG data

We produce a time-varying spectrum by taking a T-sec window of the signal and computing the power spectral density (PSD) of the segment and then sliding the window through the whole dataset which yields a time-frequency matrix in which each array represents the power of the signal corresponding to a specific frequency and sliding time-step (shift) of S-sec. The sliding process and frequency step specify the resolution and dimension of the time-frequency matrix. In this study, we take two different sliding window approaches depending on the application. For estimating either heart rates or heart rate variability, data are shifted sample-by-sample with no overlap for the entire dataset. This is because we are interested in capturing beat-to-beat dynamics of HRV which requires sample-to-sample estimation of PSD. Given our down-sampled data of Fs = 20 Hz, each data point is shifted by 0.05 seconds. For estimating only the heart rates, we shift the data segment-by-segment rather than sample-by-sample. This coarse-grain windowing approach has less computational cost and it can provide good tracking of heart rates, but it cannot be used for HRV. The window segment length T was set to 8 seconds and was shifted (S) by 2 seconds. We chose the 8 second data segment and the shift of 2 seconds because one of the goals of this work is to compare our algorithm's results to other algorithms which have used this chosen data segment length and time shift. Moreover, the assumption of 8 second data length largely stems from the fact that heart rates do not change instantaneously, hence, an 8 second duration is a reasonable choice.

Hence the next step in SegMA, we compute the time-frequency spectrum of the derivative of resampled ECG. As a representative example, the resultant frequency components in the time-frequency matrix of recordings from subject #3 of the dataset, for a window length of 8 seconds that is shifted by every 2 seconds, is shown in Fig.2a. From the Fig.2b, time-frequency plot of the ECG signal, it is observed

that there are two major frequency components (A) and (B) in the time-frequency spectrum plot: one of them appears to represent HR and the other may represent the first harmonic of HR. In order to verify this conjecture we need to extract these components from time-frequency spectrum. To this end, in the phase of SegMA algorithm, we apply a filtering strategy to keep the major components of spectrum and remove the unnecessary information.

11.3.3. Spectral Filtering

Assuming that the HR frequency component is the dominant peak in the power spectral density (PSD) of each 8 sec window of a clean ECG signal, the filtered time-frequency spectrum using the first two largest peaks of PSD at each window can be extracted as shown in Fig. 3a. After obtaining the power spectral density at each window, HR frequency is assumed to be confined in the range [0.5 Hz – 3 Hz], which takes into account both at rest and high HR due to either tachycardia or exercise scenarios. Hence, for HR estimation, the strategy is to eliminate frequencies that are outside of this HR frequency range as they are most likely due to motion artifacts or harmonics of the HR frequency.

In general, HR frequency in the power spectral density of ECG at each window can have three different scenarios: (1) ECG is devoid of MA and there is no spatial gap between the electrode and the subject's skin during recording, (2) ECG is corrupted by MA and there is no spatial gap between the electrode and the subject's skin during recording and (3) There is a spatial gap between the electrode and the subject's skin during recording. For the ideal case (1), HR can be extracted and it is most likely represented as the highest peak in the ECG spectrum. For case (2), MA dynamics can result in the dominant peak and HR frequency peak's magnitude become smaller than the MA frequency peak in the power spectrum. The only scenario that makes it difficult to extract HR from the spectrum is scenario (3) when there is a spatial gap between the ECG electrodes and the subject's skin during recording. In this scenario, assuming that the motion artifacts are short lasting, the missing HR values can be interpolated using the cubic spline approach.

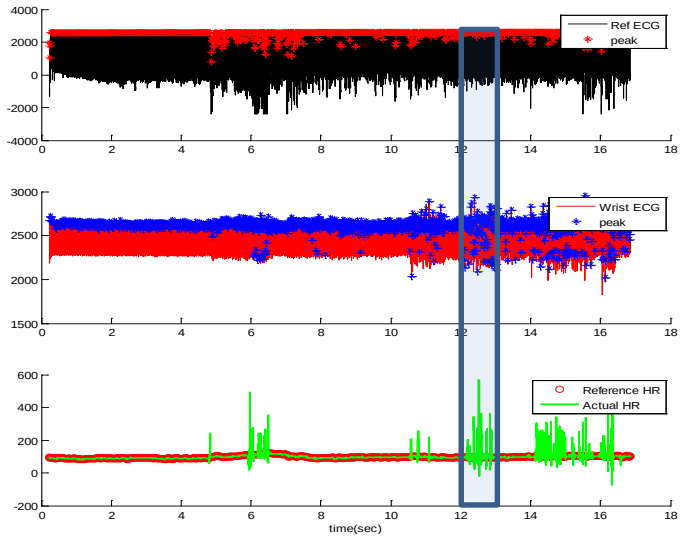

(a)

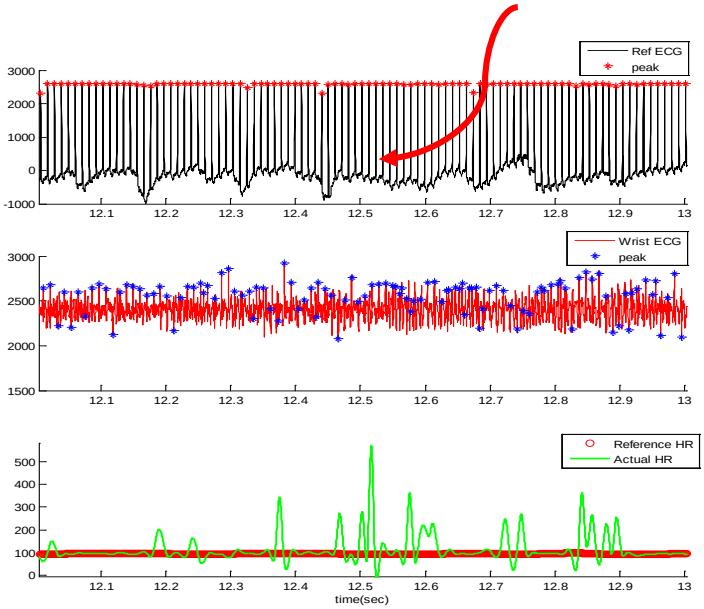

(b)

Figure 11.1 - ECG recordings and estimated HR from subject #3. (a) [top]: reference ECG, [middle]: Wrist ECG and [bottom] reference HR vs actual HR; (b) zoomed in version of (a)

Fig. 3a shows a representative filtered time-frequency spectral plot of an ECG signal. This step in the SegMA process involves retaining only the two largest frequency peaks at each time point within the defined HR range (30-180 bpm) and they are represented as blue and green colors, respectively. It is our opinion that retaining only the two largest frequency peaks at each time point is reasonable for the first two cases as outlined above. The component (A) is distinguishable from the filtered spectrum.

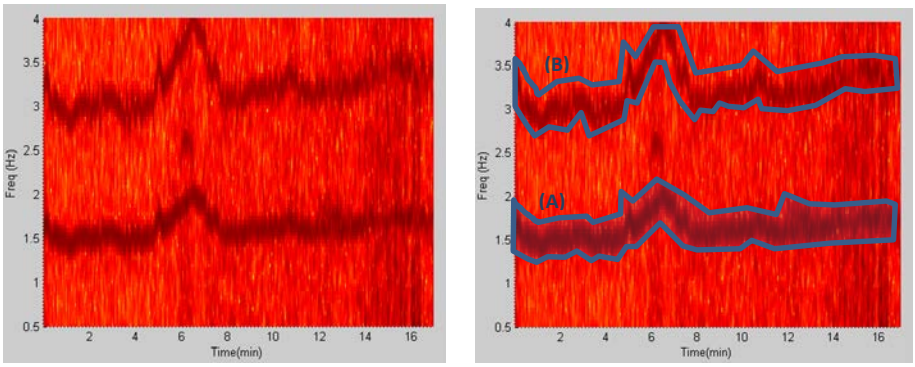

(a) (b)

Figure 11.2 - Time-Frequency spectra of recording #3: (a) ECG signal time-frequency spectra, (b) Blue areas and letters represent HR trace and its harmonic in the ECG spectra.

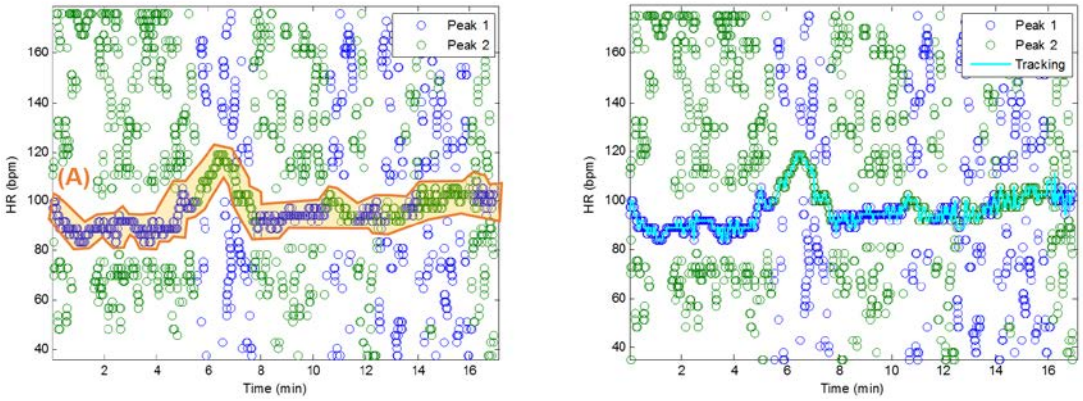

(a) (b)

Figure 11.3 - Spectral Filtering. (a) ECG time-frequency spectrum: Blue, Green circles correspond to the first two highest peaks in the defined HR frequency range of (30-180 bpm), respectively, at each sliding window. (b) Tracking of HR trace in the filtered ECG spectrum.

11.3.4. Heart Rate Tracking & Extraction

The next step is to extract HR frequencies with time from Fig. 3a. Note that in Fig. 3a, there are two peaks at each time instance, thus, the question is how to identify which of the two peaks represents the HR at each time point. For the initial time window of 8 seconds, we require a clean data segment so that true HR can be determined. This scenario is case 1 described above in the spectral filtering section, and the detection of HR is simply the highest peak in the spectrum. The next step is to estimate HR for each sliding window of data. At this step of the algorithm, the goal is to choose a HR peak in the ECG spectrum with the knowledge of estimated HR values in previous time windows. In this step there are two main scenarios: (1) no peak exists in the spectrum that can represent HR, and (2) there is a spectral peak among the first two highest peaks of spectrum that belongs to the HR component. In case (1), where HR is not detectable in the window (e.g. due to spatial gap between the ECG electrode and skin), in real-time implementation the algorithm takes the previous window's HR value as the current HR (or simply uses the moving average of several past HR beats or some other variant), however in offline processing, a cubic spline interpolation can be used to fill in the missing HR information. In the more general case (2), where the HR peak is among the first two highest peaks in the spectrum, two possible scenarios can occur: (2-A) the windowed ECG signal is clean and the first highest peak in the spectrum represents the HR fundamental frequency, (2-B) the windowed ECG signal is corrupted by movement and the second peak corresponds to HR, (2-C) while the HR spectral peak is detectable, the difference between its value and that of the previous HR is more than 15 bpm, so it will be replaced by the most recent HR value from a previous window segment (or a moving average of several past HR beats or some other variant). We set a criterion that the HR value cannot change more than 15 BPM from a previous time window. It can be observed from Fig.3b that in most cases, the blue circle which represents the largest spectral peak is chosen but in other cases, green circles are chosen for certain time points. For the HR peaks associated with the green, they are chosen because either the first highest peak is related to MA or the highest magnitude peak deviates more than 15

BPM from the previous HR value. Fig.4 illustrates the tracking of reconstructed HR comparing to the reference during different activities involved in the experiment.

Fig.5 shows the SegMA reconstructed HR (red color) from ECG spectra of recording#3 using our proposed approach along with the 8-sec moving average of reference ECG-derived HR (black color). In order to calculate the performance of the SegMA algorithm, the error value in each time window was calculated from the estimated HR to the reference ECG-derived HR.

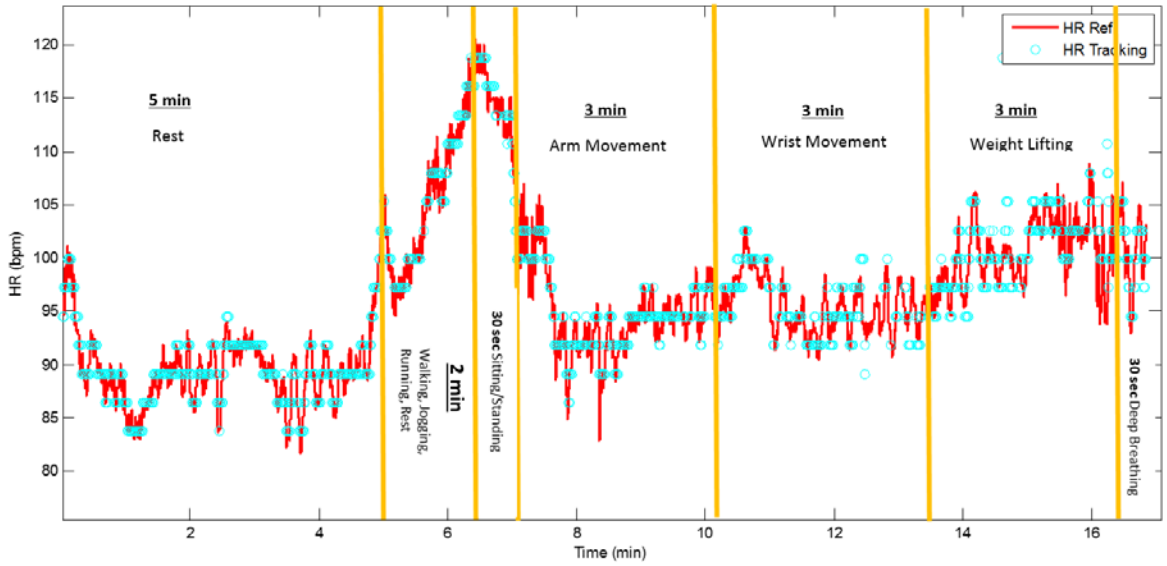

Figure 11.4 - Comparison of reference HR to the HR tracking from filtered time-frequency spectrum of ECG recordings from subject #3 labeled with type of activities.

Two measurement indices of absolute error similar to the indices in [22] were used.

$$Error(1) = \frac{1}{W}\sum_{k=1}^{w}\left|HR_{SegMA}(k) - HR_{ref}(k)\right| \quad (1)$$

$$Error(2) = \frac{1}{W}\sum_{k=1}^{w}\frac{\left|HR_{SegMA}(k) - HR_{ref}(k)\right|}{HR_{ref}(k)} \times 100\% \quad (2)$$

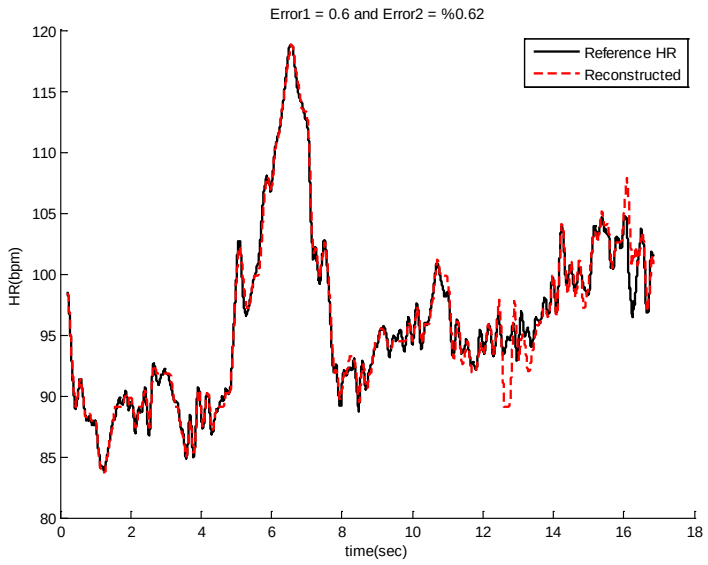

Figure 11.5 - Comparison of reconstructed HR obtained from SegMA to reference HR estimated from simultaneous ECG recordings#3.

11.3.5. Heart Rate Variability analysis

For HRV analysis application, the above-described procedures are identical but the only difference is the beat-by-beat shift of data rather than the 8 second data segment shift or it's variant. Fig. 6a illustrate the beat-by-beat reconstruction of HR using SegMA. The power spectral density of reconstructed HR is illustrated in Fig. 6b. It can be observed that the correlation between PSD of estimated SegMA and reference HRV in frequency range of [0-0.4] Hz is almost 100%.

11.4. Results

Table (5) represents the average absolute error (E1) and the average absolute error percentage (E2) of HR estimations of the proposed SegMA algorithm on the dataset. Our SegMA algorithm is compared to the HR estimations before applying the reconstruction algorithm, where both before and after reconstruction estimations are compared to the reference HR from ECG, and reference SpO2 from Masimo commercial device. The forth column in Table (5) show that SegMA on average improves the HR

estimations with almost 1000% comparing to those estimations before reconstruction. Improvement rate was calculated as follow

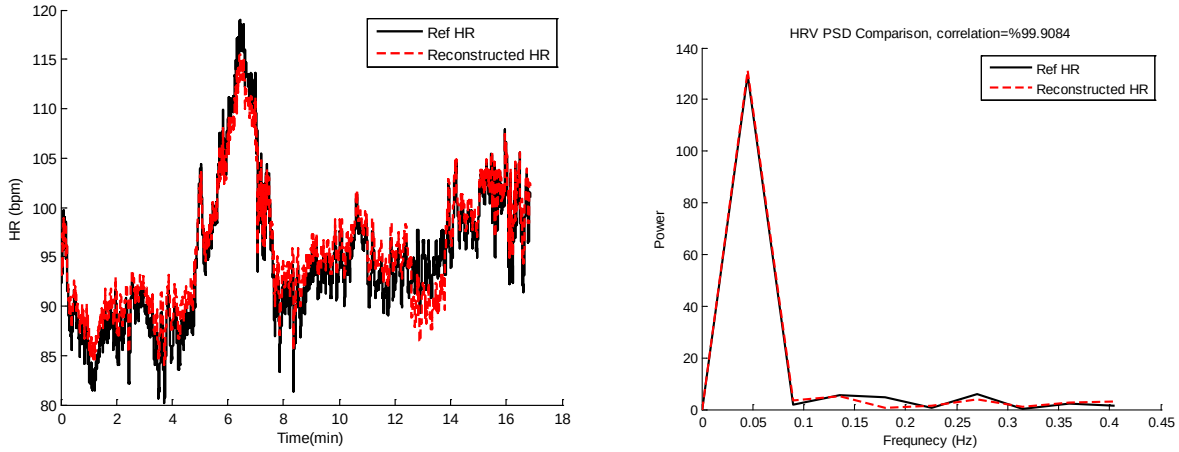

(a) (b)

Figure 11.6 - Heart Rate Variability Analysis (a) Time-domain comparison of reconstructed and reference HR. (b) Spectral comparison of heart rate variability between reconstructed HR and reference HR calculated from the reference ECG using Pan & Tompkin peak detection approach [4].

$$ImRate1(\%) = \frac{1}{W}\sum_{k=1}^{w}\frac{\left|Error1_{SegMA}(k) - Error1_{Act}(k)\right|}{Error1_{SegMA}(k)} \times 100\% \quad (3)$$

$$ImRate2(\%) = \frac{1}{W}\sum_{k=1}^{w}\frac{\left|Error2_{SegMA}(k) - Error2_{Act}(k)\right|}{Error2_{SegMA}(k)} \times 100\% \quad (4)$$

Table 11.5. SegMA Algorithm Performance Comparison

Subject	Actual HR estimation error		SegMA HR estimation error		SegMA Improvement Rate	
	E1	E2%	E1	E2%	ImRate1%	ImRate1%
1	13.66	13.98	**1.31**	**1.46**	943.1	857.5
2	22.69	24.37	**2.05**	**2.16**	1006.9	1028.2
3	8.66	8.71	**0.60**	**0.62**	1343.3	1304.8
4	15.32	15.06	**1.64**	**1.78**	834.4	746.1
5	33.32	31.87	**4.87**	**5.50**	584.20	479.4
6	20.84	21.56	**2.43**	**2.61**	757.66	726.05
7	26.85	23.93	**2.61**	**2.31**	928.7	935.9

8	16.15	16.66	**0.97**	**1.00**	1582.3	1582.8
9	10.19	10.83	**0.72**	**0.75**	1315.7	1344.2
10	9.43	9.37	**0.84**	**0.93**	1022.6	907.5
mean±std	17.71±8.1	17.63±7.6	1.80±1.3	1.91±1.4	1031.9±300.8	991.2±332.4

Figures 7-9 show the reconstructed HR and corresponding PSD of a sample-sample windowed HR in comparison to the reference HR from ECG. The results for recording #8 are shown in Fig.8. We can see that the E1 for this particular subject is as low as 0.97 bpm and the correlation between the PSD of reconstructed HR and reference HR is as high as 97%.

Fig. 8 illustrates the comparison between the reconstructed HR and the reference HR for subject #5 and 7 that have the highest errors. Higher error from recording #7 can be due to rapid changes of physiological HR and the motion artifacts during the activities. In case of subject #5 it can be observed that the error is due to losing track of HR during weight lifting activity. This could be due to skin-electrode interface gap.

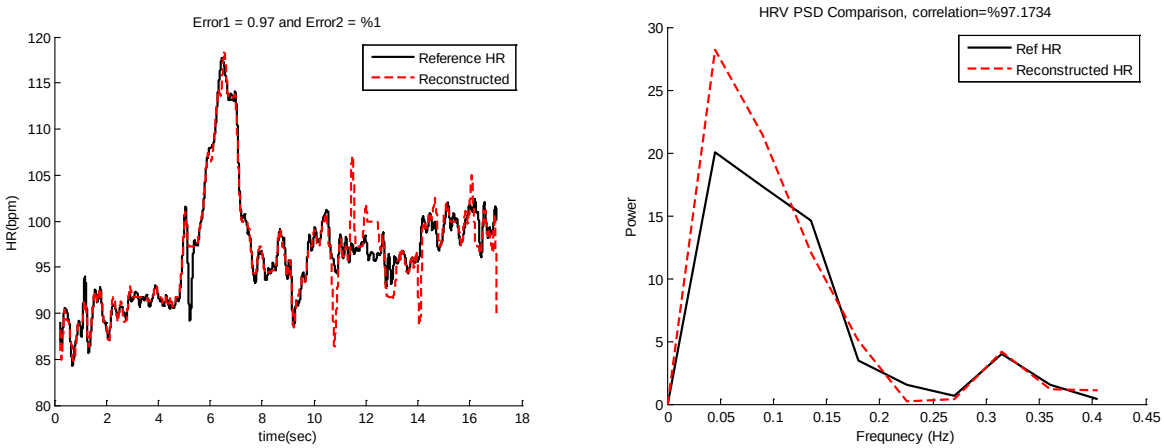

(a) (b)

Figure 11.7 – Results of Subject 8. (a) Reconstructed HR vs. reference HR. (b) Spectral comparison of reconstructed HR and reference HR (estimated from reference ECG)

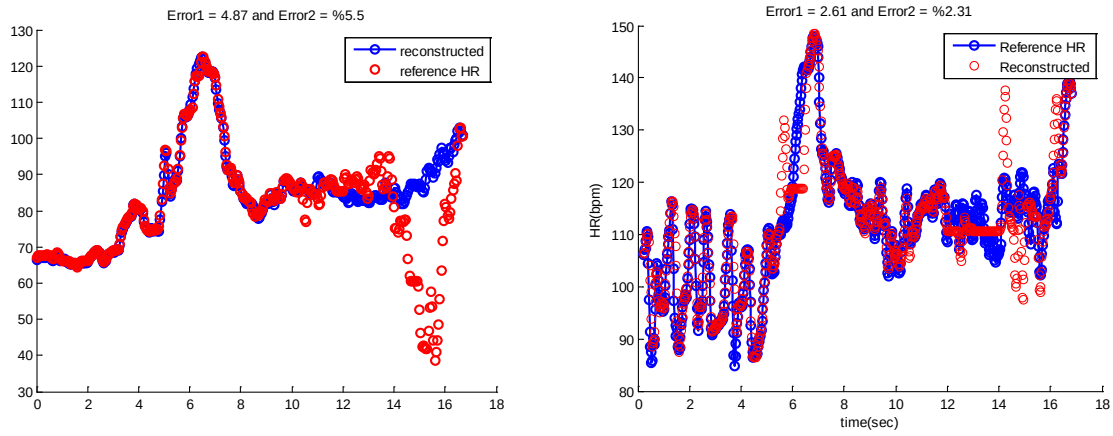

(a) (b)

Figure 11.8 – Reconstructed HR vs. reference HR (a) Subject 5. (b) Subject 7.

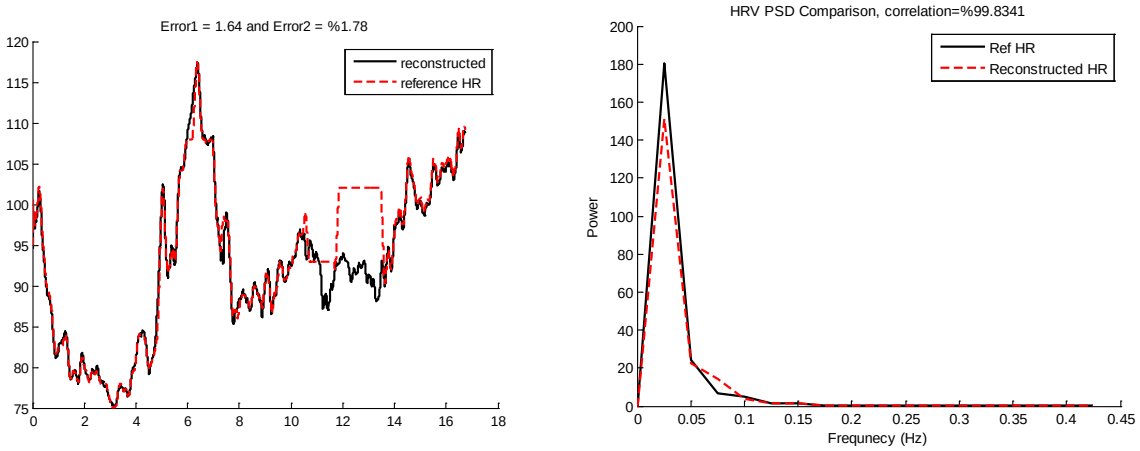

(a) (b)

Figure 11.9 – Results of Subject 4. (a) Reconstructed HR vs. reference HR. (b) Spectral comparison of reconstructed HR and reference HR (estimated from reference ECG)

The results for recording #4 are shown in Fig. 9. It can be seen that the E1 for this subject is around 1.7 bpm and the correlation between the PSD of reconstructed HR and reference HR is as high as 99%. All subjects' results are provided in Table (6). Table 6 represents the correlation between PSD of estimated and reference HRV in the frequency range of 0-0.4 Hz. The correlation values in the table are calculated based on Pearson's linear correlation coefficient. The results clearly indicate that the proposed algorithm has great potential in HRV analysis applications.

Table 11.6. Correlation between PSD of estimated SegMA and reference HRV

Subjects	1	2	3	4	5	6	7	8	9	10	Average
Correlation	0.98	0.96	1.00	1.00	0.86	0.94	0.92	0.97	1.00	0.99	0.96

A video of the real-time implementation of SegMA algorithm is available from [3].

11.5. 4. Discussion

Wearable sensors have recently enjoyed much public attention and interests. This is well deserved as many wrist-worn devices promise to provide reasonable estimates of heart rates and other health related information including the calories burned based on the number of steps or activities taken throughout the course of a day. More importantly, these devices provide an attractive feature where for the first time individuals can track and manage their own health-related data. In spirit of these recent development in wrist-worn sensors, the objective of our work was to develop a robust and accurate algorithm that can mitigate motion artifact so that more accurate heart rates and other relevant diagnostic information can be estimated. Certainly, this is challenging since wrist-worn devices are especially prone to more challenging and varied motion artifacts when compared to sensors placed on other parts of the body.

While wearable ECG devices are normally worn as either a Holter monitor or a patch on the chest, recent advances in non-contact capacitive and dry electrodes has resulted in textile worn ECG measurements. The form factor and locations of these textile-based ECG sensors can be found from the traditional ECG electrode placements around the chest area to electrodes incorporated directly into a belt [40, 41]. Most recently, Samsung Corporation has developed a wrist-based ECG measurement device called Simband, which holds much promise for a wide adoption by the general public due to its convenient form factor. Similarly, we also developed a wrist-worn ECG device using our own dry flexible electrodes [40, 41], and this is the device that was used to collect experimental data as detailed in the Methods section.

Our algorithm, SegMA, based on time-varying spectral analysis of the ECG signal is introduced to combat motion artifacts. To fully test the robustness of the SegMA algorithm, the design of the type of

motion artifacts introduced for our experiment was cognizant of the wide variety movements subjects might encounter during their daily activities. In all of the recordings, the reference HR was calculated from an ECG signal that was collected simultaneously with the ECG signal. The estimated HR was calculated from the spectrum of ECG in 8 second time windows. It was shown that the proposed SegMA algorithm can be used for tracking fast HR changes as they varied more than 70 beats/min in less than 2 minutes and despite severe motion artifacts since the subjects were running at a full speed on a treadmill, the average error of just 1.80 bpm was found when compared to that of the reference ECG. This average error also includes when subjects were introducing challenging motion artifacts by performing wrist shaking and bending exercises.

The results from Table 5 show that the SegMA algorithm can be effectively applied to monitor HR from ECG wrist wearable devices. We made several observations while analyzing the data. The tracking ability of the SegMA algorithm decreased as the dynamics of the motion artifact increased. This phenomenon mostly was observed while dealing with the subject #7 and is due to fast changing HR and abrupt movements which consequently made it more difficult to track the HR-related frequencies in the spectrum.

The main sources of noise and corruption during recording ECG signal using NohChon wrist band was (1) movement of wire inside of tight suit, (2) electromyogram (EMG) interference when subjects were either shaking or bending the wrist, and (3) contact issues with the skin-electrode interface during movements. We showed that SegMA is able to address the first two type of noise and motion artifacts. However the third noise type which can be due to gaps or poor contact between skin-electrode interfaces is the most challenging scenario for any motion artifact reconstruction algorithm. This is because a gap between electrode and skin, ECG signal strength would decrease due to impedance mismatch [34], and if severe, it can lead to loss of signal. The electrodes we used in this study were a thin flexible film type made out of carbon black powder adhered to a skin with adhesive [40, 41], but it can wrinkle or loose contact with the skin when subjected to severe bending or flexing motions. Certainly, this type of noise could be

minimized if we choose electrodes that have thicker foam electrodes that cannot deformed easily. However, the tradeoff is that certain flexible exercises are possible with these thicker electrodes as they may all together pop off the skin depending on the severity of the flexing exercises. Among the 10 recordings datasets, the lowest performance seen for recordings #5 is most likely due to a gap between the ECG electrode and skin caused by the bending and reflexing motion artifacts.

By using the sample-by-sample shifting windowing approach, the proposed SegMA algorithm can be effectively utilized for HRV analysis. Using this approach, we have shown that that both the low- (0.04-0.15Hz) and high frequency (0.15-0.4) bands can be reliably estimated when compared to Holter-derived HRV spectrum. We found high cross-correlation values between our SegMA algorithm and Holter monitor derived HRV spectra, as shown in Table 6 for all subjects. It has long been shown that during dynamic exercise, heart rate increases due to both parasympathetic withdrawal and an augmented sympathetic activity [35, 36]. The relative role of the two drives depends on the movement intensity [37-39]. Analysis of HRV permits insight into these control mechanisms [6]. HRV analysis from ECG during severe movements and physical activities has been problematic in the past. With SegMA, missing portions of corrupted data during severe motion artifacts can reconstructed with a good confidence.

The proposed SegMA algorithm can be implemented in real time. We have found that the algorithm takes around 75 msec on data segmented into 8 seconds. Therefore, given the high accuracy of the proposed approach in estimating HR despite severe motion artifacts, this method has the potential to be applicable for real-time implementation on wearable devices such as smart watches and ECG-based fitness sensors.

References

42. Deepak Vala , D.T.P., A Survey on Ambulatory ECG and Identification of Motion Artifact. International Journal of Engineering Research and Development, 2012. 1(7): p. 38-41.
43. Achten, J. and A.E. Jeukendrup, Heart rate monitoring: applications and limitations. Sports medicine (Auckland, N.Z.), 2003. 33(7): p. 517-538.
44. Laughlin, M.H., Cardiovascular response to exercise. Am J Physiol, 1999. 277(6 Pt 2): p. S244-59.

45. F. Yazicioglu, T.T., J. Penders, I. Romero, H. Kim, P. Merken, B. Gyselinckx, H.J. Yoo, C. Van Hoof. Ultra-low-power wireless sensor nodes. in Proceedings of the 31st Annual International Conference of the IEEE EMBS. 2009. Minneapolis: IEEE.
46. J. Penders, J.v.d.M., M. Altini, F. Yazicioglu and C. Van Hoof. A low-power wireless ECG necklace for reliable cardiac activity monitoring on-the-move. in Proceedings of the International Conference of the IEEE Engineering in Medicine and Biology Society. 2011. IEEE.
47. Aubert, A.E., B. Seps, and F. Beckers, Heart rate variability in athletes. Sports Med, 2003. 33(12): p. 889-919.
48. Kearney, K., C. Thomas, and E. McAdams. Quantification of Motion Artifact in ECG Electrode Design. in Engineering in Medicine and Biology Society, 2007. EMBS 2007. 29th Annual International Conference of the IEEE. 2007.
49. Friesen, G.M., et al., A comparison of the noise sensitivity of nine QRS detection algorithms. Biomedical Engineering, IEEE Transactions on, 1990. 37(1): p. 85-98.
50. Thakor, N.V. and Y.S. Zhu, Applications of adaptive filtering to ECG analysis: noise cancellation and arrhythmia detection. IEEE Trans Biomed Eng, 1991. 38(8): p. 785-94.
51. Webster, N.T.a.J. The origin of skin potential and its variations. in Proc. Ann. Conf. Eng. Biol. Med
1978.
52. Edelberg, R., Local electrical response of the skin to deformation. J Appl Physiol, 1973. 34(3): p. 334-40.
53. Muhlsteff, J. and O. Such. Dry electrodes for monitoring of vital signs in functional textiles. in Engineering in Medicine and Biology Society, 2004. IEMBS '04. 26th Annual International Conference of the IEEE. 2004.
54. Comert, A. and J. Hyttinen, Investigating the possible effect of electrode support structure on motion artifact in wearable bioelectric signal monitoring. Biomed Eng Online, 2015. 14: p. 44.
55. Afonso, V.X., et al., Comparing stress ECG enhancement algorithms. Engineering in Medicine and Biology Magazine, IEEE, 1996. 15(3): p. 37-44.
56. P., A. Separating cardiac and muscular ECG components using adaptive modelling in time-frequency domain. in Proc. of the WACBE World Congress on Bioengineering. 2007.
57. Devlin PH, M.R., Ketchum JW., Detection electrode motion noise in ecg signals by monitoring electrode impedance. Computers in Cardiology, 1984: p. 51-56.
58. Hamilton, P.S., et al. Comparison of methods for adaptive removal of motion artifact. in Computers in Cardiology 2000. 2000.
59. Hamilton, P.S., M. Curley, and R. Aimi, Effect of adaptive motion-artifact reduction on QRS detection. Biomed Instrum Technol, 2000. 34(3): p. 197-202.

60. Tong, D.A., K.A. Bartels, and K.S. Honeyager. Adaptive reduction of motion artifact in the electrocardiogram. in Engineering in Medicine and Biology, 2002. 24th Annual Conference and the Annual Fall Meeting of the Biomedical Engineering Society EMBS/BMES Conference, 2002. Proceedings of the Second Joint. 2002.
61. Raya, M.A.D. and L.G. Sison. Adaptive noise cancelling of motion artifact in stress ECG signals using accelerometer. in Engineering in Medicine and Biology, 2002. 24th Annual Conference and the Annual Fall Meeting of the Biomedical Engineering Society EMBS/BMES Conference, 2002. Proceedings of the Second Joint. 2002.
62. Thakor, N.V. and Z. Yi-Sheng, Applications of adaptive filtering to ECG analysis: noise cancellation and arrhythmia detection. Biomedical Engineering, IEEE Transactions on, 1991. 38(8): p. 785-794.
63. Rahman, M.Z.U., R.A. Shaik, and D.V.R.K. Reddy. An Efficient Noise Cancellation Technique to Remove Noise from the ECG Signal Using Normalized Signed Regressor LMS Algorithm. in Bioinformatics and Biomedicine, 2009. BIBM '09. IEEE International Conference on. 2009.
64. Hashim, F.R., et al. Wavelet based motion artifact removal for ECG signals. in Biomedical Engineering and Sciences (IECBES), 2012 IEEE EMBS Conference on. 2012.
65. Hyvärinen, A. and E. Oja, Independent component analysis: algorithms and applications. Neural Networks, 2000. 13(4–5): p. 411-430.
66. Castells, F., A. Cebrian, and J. Millet, The role of independent component analysis in the signal processing of ECG recordings. Biomed Tech (Berl), 2007. 52(1): p. 18-24.
67. Heenam Yoon, H.K., Sungjun Kwon, Kwangsuk Park, An Automated Motion Artifact Removal Algorithm in Electrocardiogram Based on Independent Component Analysis, in The Fifth International Conference on eHealth, Telemedicine, and Social Medicine. 2013: Nice, France. p. 15-20.
68. Palaniappan R, K.T. Uni-channel PCA for noise reduction from ECG signals. 2004.
69. Chawla, M.P.S., A comparative analysis of principal component and independent component techniques for electrocardiograms. Neural Computing and Applications, 2009. 18(6): p. 539-556.
70. Jinseok, L., et al., Automatic Motion and Noise Artifact Detection in Holter ECG Data Using Empirical Mode Decomposition and Statistical Approaches. Biomedical Engineering, IEEE Transactions on, 2012. 59(6): p. 1499-1506.
71. Stoica, P. and R.L. Moses, Introduction to Spectral Analysis. 1997: Prentice Hall.
72. Vvv Yilmaz, T., R. Foster, and Y. Hao, Detecting Vital Signs with Wearable Wireless Sensors. Sensors, 2010. 10(12): p. 10837.
73. Cynthia A. Sanoski, Clinical, Economic, and Quality of Life Impact of Atrial Fibrillation FCCP, BCPS. Manag Care Pharm., 2009. 15(6-b): p. 4-9.

74. Pan J, T.W., A real-time QRS detection algorithm. IEEE Trans Biomed Eng, 1985. 32(3): p. 230-236.
75. Taji, B., et al., Impact of Skin– Electrode Interface on Electrocardiogram Measurements Using Conductive Textile Electrodes. Instrumentation and Measurement, IEEE Transactions on, 2014. 63(6): p. 1412-1422.
76. Iellamo, F., Neural mechanisms of cardiovascular regulation during exercise. Auton Neurosci, 2001. 90(1-2): p. 66-75.
77. Bernardi, L. and M.F. Piepoli, [Autonomic nervous system adaptation during physical exercise]. Ital Heart J Suppl, 2001. 2(8): p. 831-9.
78. Sarmiento, S., et al., Heart rate variability during high-intensity exercise. Journal of Systems Science and Complexity, 2013. 26(1): p. 104-116.
79. Roure, R., et al., Autonomic nervous system responses correlate with mental rehearsal in volleyball training. Eur J Appl Physiol Occup Physiol, 1998. 78(2): p. 99-108.
80. Perini, R., et al., The influence of exercise intensity on the power spectrum of heart rate variability. Eur J Appl Physiol Occup Physiol, 1990. 61(1-2): p. 143-8.
81. Posada-Quintero, H.F., et al., Low Impedance Carbon Adhesive Electrodes with Long Shelf Life. Ann Biomed Eng, 2015. 43(10): p. 2374-82.
82. Reyes, B.A., et al., Novel electrodes for underwater ECG monitoring. IEEE Trans Biomed Eng, 2014. 61(6): p. 1863-76.

Chapter 12: Discussion, Conclusions and Future Work

12.1. Discussion and Conclusions

Wearable sensors have recently enjoyed much public attention and interests. This is well deserved as many fitness tracker and medical wearable devices promise to provide reasonable estimates of heart rates and other health related information including the calories burned based on the number of steps or activities taken throughout the course of a day. More importantly, these devices provide an attractive feature where for the first time individuals can track and manage their own health-related data. In spirit of these recent development in wearable sensors, the objective of our work was to develop robust and accurate algorithms that can detect and mitigate motion artifact so that more accurate vital sign information can be estimated. Certainly, this gets more challenging since wearable devices are prone to random and varied motion artifacts where thrives to develop signal processing algorithms to be addressed.

In this thesis eight different algorithm presented to address the problem motion and noise artifacts in wearable sensors and vital sign monitoring. Three general category of applications were considered in this study: (1) Motion and noise corrupted data removal, (2) MA corrupted signal usability index measurement, and (3) Motion and noise corrupted data reconstruction. Three methods (TDV, RepMA and RAFMA) were introduced for the first category, one algorithm (TifMA) was presented from second category and 4 different methods were proposed to motion and noise corrupted data reconstruction.

TDV is a real-time MA detection algorithm that was developed based on time-domain statistical features of PPG signal. Four features were adopted by TDV algorithm to address the problem of MA detection in PPG recordings: (a) standard deviation of peak-to-peak intervals (b) standard deviation of peak-to-peak amplitudes (c) standard deviation of systolic and diastolic time ratios, and (d) mean-standard deviation of pulse shapes. Finally the feature were fed as inputs to a support vector machine learning. We use these parameters since motion corrupted PPG signals are observed to have noticeably different values and have large variations for successive pulses compared to clean PPG signals [37]. We evaluated our

proposed algorithm by comparing it to four other detection methods based on kurtosis (K), Shannon entropy (SE), Hjorth 1 (H1), and Hjorth 2 (H2) metrics. The results demonstrated that our proposed SVM-based MNA detection algorithm has offered higher classification accuracy as well as lower HR and SpO2 errors compared to the conventional detection methods.

The main issue with statistical MA detection methods are they may misclassify a PPG signal with fast changing frequency (HR) as corrupted signals and also they might misclassify a PPG recordings from a patient with Atrial Fibrillation or a patient is hemorrhage shock as MA corrupted recordings which is not desirable. That is why we came up with an idea of looking into time-time or time-frequency domain rather than only time domain would improve the accuracy of MA detection algorithm. RepMA and RAFMA for instance are two algorithms that were developed according to distinctive features in time-time recurrence plot of PPG/ECG signals. The idea behind RepMA and RAFMA was to transform the one dimensional PPG/ECG data into a 2 dimensional image using recurrence plot quantification. The main point is MA corrupted data is easier to be detected when we look into the recurrence features of PPG in its recurrence plot. We showed that RepMA can provide more accurate results on both lab-controlled and UMASS datasets when compared to three other MA detection method: (1) Hjorth, (2) KSE and (3) TDV. Concomitantly, the accuracy, sensitivity and specificity values on average of our proposed method were significantly higher than other methods. The proposed RepMA algorithm can be implemented in real time. We have found that the algorithm takes only 0.47 sec on PPG recordings of 60 sec. RAFMA algorithm was based on time-time recurrence analysis of the ECG signal that is proposed to address Atrial Fibrillation detection in the presence motion and noise artifacts. We showed in time-time domain the AF episodes of MNA free and MNA corrupted ECG signals are easier to be distinguished. Two datasets has been used to verify the algorithm performance. The second dataset reflects different types of activities and movements. In all of the recordings of dataset (2), the reference HR was calculated from an ECG signal that was collected simultaneously with the ECG signal. It has been shown in the results section that the proposed RAFMA algorithm can be used for MNA detection in ECG recordings with performance around 90% from 10 healthy subjects and detection of AF episodes in the signal with accuracy of

97% from 33 subjects. It may be possible that RAFMA can be applied to respiratory rate estimation and autonomic nervous function assessment as well.

By moving forward to MA corrupted signal usability index category, we proposed one method (TifMA) using VFCDM time-frequency spectrum of PPG. TifMA uses dynamic characteristics of the corrupted PPG derived via the VFCDM. The algorithm has two phases: (1) MA detection and (2) Usability detection. The efficacy of the detection phase was validated using contrived motion data from healthy subjects and unconstrained MNA data from participants recruited from a hospital-setting. The second phase of the algorithm was tested on HR varying scenario where subjects were asked to walk/jog/run for 9 min on a treadmill. For MA detection several key features associated with MAs derived from the VFCDM-based time-frequency spectrum. By transforming the PPG time series into the time-frequency domain, we were able to better capture time-varying characteristics of the MAs. Specifically, we recognized that PPG's clean signal dynamics are largely concentrated at the heart rate and its harmonic frequency bands. Hence, we surmised that the presence of large amplitudes in the other frequency bands must be associated with MAs. The detection accuracy on both lab-controlled and UMMC datasets using TifMA outperformed the other three detection methods: Hjorth, TDV-SVM, and KSE. Furthermore we showed that by applying the second phase of TifMA algorithm on MA corrupted PPG, it was able to discriminate between the usable and non-usable segments of PPG for HR estimations.

Finally, since the ultimate goal of this study was to recover the corrupted vital signs (ECG, PPG, HR, SpO_2, etc.) during motion and noise artifacts and estimate a more accurate values we dedicated the second half of this dissertation to motion and noise corrupted signal reconstruction. Starting from IMAR, we investigated the problem of motion and noise artifacts using a blind source separation technique, singular spectrum analysis (SSA). IMAR method was introduced to reconstruct MA contaminated segments of PPG data. In IMAR, we basically used the most adjacent prior clean data segment and used its dynamics to derive the MNA contaminated segment's heart rates and oxygen saturation values. Hence, the key assumption with our IMAR technique is that signal's dynamics do not change abruptly between the MNA contaminated segment and its most adjacent prior clean portion of data. However there are some scenarios in which the above assumption does not hold. Thus, clearly if this assumption is violated, the IMAR's ability to reconstruct the dynamics of the signal will be compromised. The other issue with IMAR was it cannot be implemented in real-time since the complexity of the algorithm is high. Later in Chapter (7) we investigated

the regression modeling and prediction algorithms based on sinusoidal frequency and AR basis functions. We showed in that chapter that the algorithm works perfectly with synthetic simulated MA corrupted PPGs. The main problem with the approaches proposed in Chapter (7) is if the corruption takes longer than 10 sec the accuracy of the method degrades accordingly. This was the point where we move forward with time-frequency reconstruction methods and rather than reconstructing the PPG itself we were concentrated in reconstructing the HR from Spectrogram time-frequency of PPG and ECG by introducing two algorithms (SpaMA and SegMA) and another algorithm (OxiMA) for reconstructing both HR and SpO_2 values during movement using VFCDM time-frequency of PPG signal. We also were able to reconstruct the PPG signal around HR frequency band too.

In Chapter (9), OxiMA a new approach based on VFCDM analysis of the PPG signal was introduced to address SpO2 and HR monitoring during motion artifacts. The idea behind the proposed OxiMA approach was to extract the accurate HR from MA corrupted PPG signals and then use the VFCDM components with closes frequency to the estimated HR to reconstruct the red and infrared PPG signals. Finally the reconstructed red and infrared we applied to estimate accurate MA free SpO^2 signals.

The accuracy of HR estimations using OxiMA was improved by using time-varying spectral analysis of PPG and ECG based on fast Fourier transform and periodogram power spectral density estimations instead of complex demodulation of data. Chapter (10) and (11) presented the two algorithms SpaMA and SegMA for accurate HR estimations during exercise and physical activities using PPG and ECG signals respectively.

The idea behind SpaMA approach was to compare spectral changes in PPG and accelerometer signals. Three different datasets have been used to verify the algorithm performance. Each dataset reflects different types of activities and movements. In all of the experiments, the reference HR was calculated from an ECG signal that was collected simultaneously with the PPG signal. The estimated HR was calculated from the spectrum of PPG in 8 second time windows. It has been shown in the results section that the proposed SpaMA algorithm can be used for tracking HR changes during severe motion artifacts with an average error of just 1.86 bpm compared to that of the reference ECG; these results are superior to three other algorithms tested: TROIKA, JOSS and WFPV. We made several observations while analyzing the data. The proposed SpaMA algorithm can be implemented in real time. We have found that the algorithm takes only 110 msec on data divided into 8 second segments. Therefore,

given the high accuracy of the proposed approach in estimating HR despite severe motion artifacts, this method has the potential to be applicable for implementation on wearable devices such as smart watches and PPG-based fitness sensors.

The tracking ability of the SpaMA algorithm decreased as the frequency changes during recordings increased. This phenomenon mostly was observed while dealing with the second set of datasets from the IEEE competition, which involved Type (2) and Type (3) activities. These types of exercises involved more abrupt movements which consequently made it more difficult to track the HR-related frequencies in the spectrum. The strength of the PPG's LED is one of the most important factors determining the SpaMA algorithm performance. Movement induces much less spectrum corruption (shift) in the PPG if the LED is sufficiently strong. A reduction in the strength of the PPG signal can also be caused by ambient light leaking into the gap between a PPG sensor and the skin surface. This is because the power of the signal is dependent on the depth and reflection of the light from the pulse oximeter to the subject's skin. This gap between skin and the planar substrate where the LEDs and PD are mounted may be the result of movement during physical activities or the shape of tissue that the sensors touch.

In chapter (11), in order to fully test the robustness of the propsoed SegMA algorithm, the design of the type of motion artifacts introduced during ECG recordings in our experiment was cognizant of the wide variety movements that subjects might encounter during their daily activities. The estimated HR was calculated from the spectrum of ECG in 8 second time windows. It was shown that SegMA can be used for tracking fast HR changes as they varied more than 70 beats/min in less than 2 minutes and despite severe motion artifacts since the subjects were running at a full speed on a treadmill, the average error of just 1.80 bpm was found when compared to that of the reference ECG. This average error also includes when subjects were introducing challenging motion artifacts by performing wrist shaking and bending exercises. Although we could not get such results using SpaMA on PPG recordings from IEEE test dataset that includes weight lifting, wrist movement and jumping activities. This is reasonable since R-peaks in ECG are less vulnerable to motion that peaks of PPG signal.

However, the tracking ability of SegMA like SpaMA decreased in scenarios where HR is changing fast or when the movement is abrupt which consequently made it more difficult to track the HR-related frequencies in the spectrum.

We also showed that SegMA algorithm like SpaMA can be implemented in real time. We have found that the algorithm takes around 75 msec on data segmented into 8 seconds. Thus, given the high accuracy of the proposed approach in estimating HR despite severe motion artifacts, this method has the special potential to be applicable for real-time implementation on wearable devices such as smart watches and ECG-based fitness sensors.

Using both SpaMA and SegMa, we showed that both algorithms are capable of estimating accurate beat-to-beat HR values for heart variability applications. We have shown that both the low- (0.04-0.15Hz) and high frequency (0.15-0.4) bands can be reliably estimated when compared to Holter-derived HRV spectrum. We found high cross-correlation values (>95%) between our SpaMA and SegMA algorithm and Holter monitor derived HRV spectra. It has long been shown that during dynamic exercise, heart rate increases due to both parasympathetic withdrawal and an augmented sympathetic activity. The relative role of the two drives depends on the movement intensity. Analysis of HRV permits insight into these control mechanisms. HRV analysis from ECG/PPG during severe movements and physical activities has been problematic in the past. With SpaMA and SegMA, missing portions of corrupted data during severe motion artifacts can reconstructed with a good confidence.

Table 12.1 and Figure 12.1 present the algorithms proposed in this dissertation and comparison between the proposed techniques according to their applications and level of complexity and strength in solving the motion and noise artifact problem. We investigated the problem in three levels and proposed solutions by analyzing the recordings during movement and physical activities in three domains: Time, Tim-Time and Time-Frequency domain.

Table 12.1. Comparison of Motion and Noise Artifact Algorithms presented in this Thesis

	Applications and Scenarios							
Methods	**Level**	**Domain**	**HR**	**SpO2**	**PPG/ECG**	**HRV**	**AF Detection**	**Real-Time**
TDV	Motion Artifact Detection	Time-Domain	Yes (Partial)	Yes (Partial)	No	Yes (Partial)	No	Yes
RepMA		Time-Time	Yes (Partial)	Yes (Partial)	No	Yes (Partial)	No	Yes
RAFMA		Time-Time	Yes (Partial)	Yes (Partial)	No	Yes (Partial)	Yes	Yes
TifMA	MA Detection and Usability Index	Time-Frequency	Yes (Almost)	Yes (Partial)	No	NA	NA	Yes
IMAR	Motion Corrupted Vital Sign Reconstruction	Time-Domain	Yes (Almost)	Yes (Almost)	Yes	Yes (Partial)	Yes	No
DyParam		Time-Domain	Yes (Partial)	Yes (Partial)	Yes (Partial)	Yes (Partial)	No	Yes
OxiMA		Time-Frequency	Yes	Yes	Yes	NA	Yes	Yes
SpaMA		Time-Frequency	Yes	Yes	Yes	Yes	Yes	Yes
SegMA		Time-Frequency	Yes	NA	NA	Yes	Yes	Yes

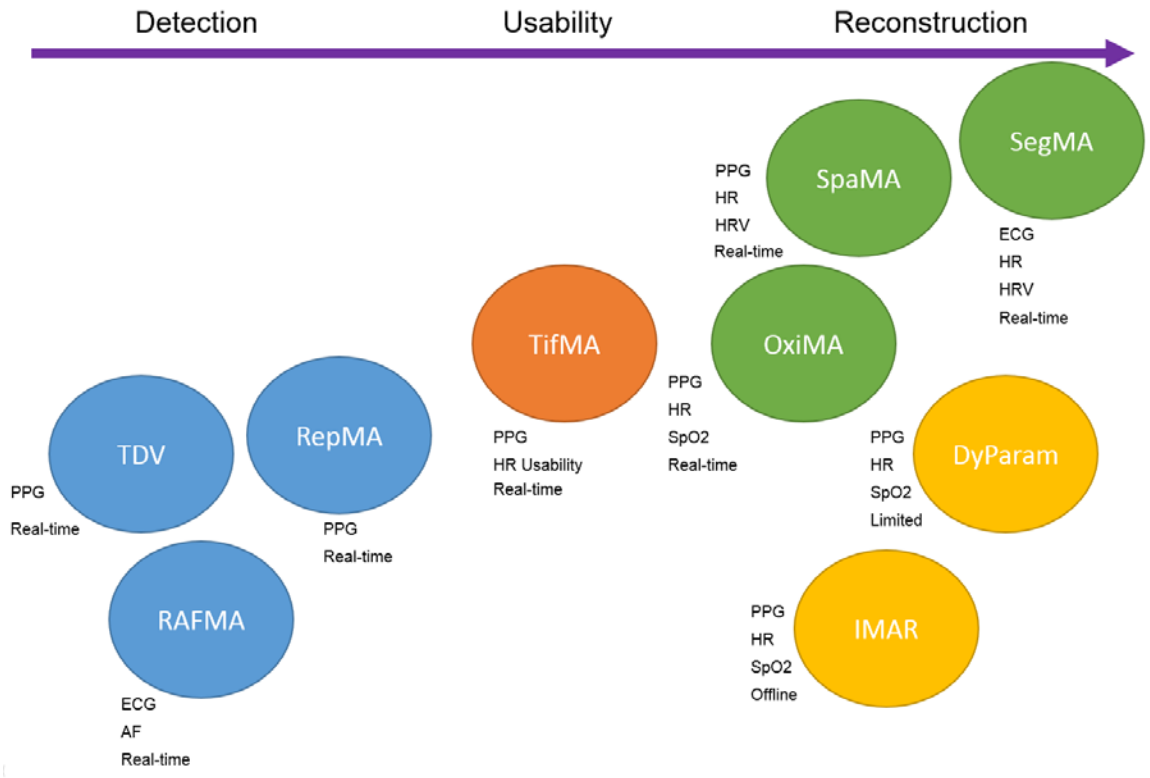

Figure 12.1 – Algorithms Presented in this thesis to address Motion and Noise Artifact Problem.

Acknowledgments

This work was supported in part by the US Army Medical Research and Materiel Command (USAMRMC) under Grant No. W81XWH-12-1-0541.